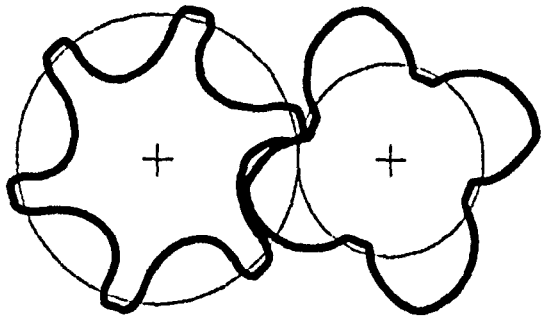

COMPUTER AIDED DESIGN OF TWIN SCREW COMPRESSORS

by
Yan Tang

Thesis Submitted to the
University of Strathclyde
for the Degree of
Doctor of Philosophy

Department of Mechanical Engineering
University of Strathclyde
Glasgow, UK

February 1995

Acknowledgement

I wish to express my deep sense of gratitude to my supervisor Dr. John S. Fleming for suggesting this research work and for the guidance he provided throughout the project.

I gratefully acknowledge the support and help of Howden Compressors Ltd., especially in supplying many pieces of data required for the verification of the CAD programs. It has been a great honour and priviledge for me to have had the opportunity of reading many reports and using measured data records of the Howden company which occupies an historic place in the development of the twin screw compressor. My knowledge of compressors has been extended greatly. I wish to thank H. Anderson, G. Cook, W. Young and my other friends in the Company for many helpful discussions.

Many thanks are also due to all my colleagues and friends for their help during the work and for their pleasant company throughout the period of this research.

I am thankful to my parents for their continuous courage.

Many thanks to my wife L. Li for looking after my daughter alone for two years and for providing me with continuous support.

Indeed I want to thank my daughter Jie and feel very sorry for leaving so little spare time to her.

ABSTRACT

The twin screw refrigeration compressor is required to run over a large range of working conditions. In order to design an advanced and high-efficiency compressor economically, computer aided design techniques are required. This thesis presents such techniques, which include profile generation, geometrical characteristic calculation, working process simulation, rotor cutter blade calculation and optimisation techniques.

All the basic theory and equations and the derived equations are presented. Four important computer programs, ie the profile generation program, the geometrical characteristics calculation program, the working process simulation program and the cutter blade calculation program, are developed and presented in the thesis. A few other support programs are also developed by the author to display the calculated results. All the programs developed form a program library for the CAD of twin screw compressors. All the programs except the profile generation program are *universal*, which means that they can be used for any shape of rotor profile.

For the working process simulation program, only refrigeration twin screw compressors are considered, but it is easy to extend the use of the programs to other kinds of compressor. The thermodynamic effects of the following are discussed and taken into account: internal leakage of gas through all paths; oil, injected and drained from bearings; refrigerant injection, both gaseous and liquid; the flashing of injected refrigerant and that dissolved in oil; friction effects, in both end and main casings; the use of measured performance data in the determination of essential empirical coefficients in the mathematical model.

The application of the programs and the design optimisation technique are presented, which include leakage analysis, compressor geometrical parameter optimisation, rotor-to-rotor clearance distribution optimisation and cutter blade shape optimisation etc. The author believes that the research work presented in this thesis is of practical value. Further, it presents new knowledge: of the compression start blow hole and its influence; of leakage quantitative analysis; of

compressor design optimisation; of the quantitative analysis of the influence of different determination procedures of inter-rotor clearances.

CONTENTS

Chapter 1 INTRODUCTION 1

1.1 Development and Application of the Twin Screw Compressor 1

1.2 Basic Compression Principle of the Twin Screw Compressor 3

1.3 The Procedure of Computer Aided Design 6

1.4 Review of Literature 9

1.4.1 Geometrical Analysis Programs 10

1.4.2 Working Process Simulation Programs 11

1.5 References 14

Chapter 2 THE SRM PROFILES AND THEIR GENERATION PROGRAM 18

2.1 SRM Profile Analysis 18

2.2 Mathematical Analysis of Profiles 22

2.3 Profile Generation Program 23

2.4 Comparison with Practically Used Profiles 25

2.5 References 34

Chapter 3 COMPUTER AIDED ANALYSIS OF THE GEOMETRICAL CHARACTERISTICS OF A TWIN SCREW COMPRESSOR 36

3.1 Introduction 36

3.2 The Cross-Sectional Area and the Cavity Volume 37

3.2.1 The Cross-Sectional Area 37

3.2.2 The Cavity Volume and the Overlap Constant 38

3.3 The Suction and Discharge Port Areas 39

3.3.1 The Axial and Radial Suction Port Areas 39

3.3.2 The Axial Discharge Port Area 41

3.3.3 The Radial Discharge Port and Slide-Valve by-Pass Port Area 43

3.4 The Sealing Line Lengths of a Cavity Volume 44

3.4.1 The Contact Line Length between the Rotors 44
3.4.2 The Rotor Tip Sealing Line Lengths 44
3.4.3 The Rotor End Face Sealing Line Lengths 45
3.5 The Blow Hole Areas 46
3.5.1 The Blow Hole Area on the High Pressure Side 47
3.5.2 The Blow Hole Area on the Low Pressure Side 48
3.6 The Injection Port Areas 49
3.7 The Geometrical Characteristics Calculation Program 50
3.8 References 53

Chapter 4 SIMULATION OF THE WORKING PROCESS OF A MODERN REFRIGERATION TWIN SCREW COMPRESSOR 56

4.1 Introduction 56
4.2 Characteristics of a Modern Refrigeration Compressor 57
4.3 Leakage Paths in a Twin Screw Compressor 60
4.4 Mathematical Model 63
4.4.1 The Basic Equations dor the Control Volume 65
4.4.2 Gas Flow through Suction, Discharge and Slive Valve by-Pass Ports 67
4.4.3 Gas Flow through the Leakage Paths 71
4.4.4 Liquid Refrigerant Injection 73
4.4.5 Gas from the Superfeed 75
4.4.6 Friction Power Calculation Model 75
4.4.7 Oil Supply and Refrigerant Dissolved in Oil 78
4.4.8 Heat Exchange with the Gas in Control Volume 81
4.4.9 Work Exchanged by the Gas in Control Volume 83
4.4.10 Property Equations of Refrigerant 84
4.4.11 Compressor Efficiencies and the Other Performance Parameters .. 85
4.4.12 Determination of the Important Coefficients 87
4.5 Computer Program for the Mathematical Model 89
4.5.1 Input for the Simulation Program 89
4.5.2 Thermodynamic Property Subroutines of the Simulation 90

4.5.3 Output from the Simulation Program 93
4.5.4 Limitations of the Working Process Simulation Program 94
4.6 An Example of Working Process Simulation 95
4.6.1 Specification of the Simulated Compressor 95
4.6.2 Running Conditions of the Simulated Compressor 96
4.6.3 Comparison between Predictions and Test Results 96
4.6.4 Analysis of Simulation Results 97
4.7 Simulation and Test Results Compared 101
4.7.1 Simulation and Test Performances for Various Speeds 102
4.7.2 Simulation and Test Performances for a Full Loaded Compressor 109
4.7.3 Simulation and Test Performances for Partially Loaded Compressors 116
4.7.4 Simulation and Test Performances for Liquid Refrigerant Injection 121
4.7.5 p-V Diagrams for Different Working Conditions 128
4.8 References 129

Chapter 5 CUTTER BLADE SHAPE DETERMINATION AND OPTIMISATION 132
5.1 Introduction 133
5.2 Cutter Geometry and Determination of Inter-Rotor Clearance 135
5.3 Computer Program for Cutter Shape 138
5.4 Comparison of the Two Methods of Clearance Determination 140
5.4.1 The Equidistant Lobe Profile Method 140
5.4.2 The Equidistant Helical Surface Method 141
5.4.3 Clearance Distributions of the Two Methods 142
5.4.4 Timing Gear Accuracy 145
5.4.5 Leakage Influence on Thermodynamic Performance 146
5.5 Determination of Optimum Clearance Distribution 148
5.6 The Optimisation of Cutter Shape 152
5.7 References 156

Chapter 6 DISCUSSION OF THE USE OF THE PROGRAMS IN

THE OPTIMISATION OF COMPRESSOR DESIGN 159
6.1 Introduction 159
6.2 Leakage Analysis of a Twin Screw Compressor 161
6.2.1 Influences of Leakage Paths on Compressor Performance 163
6.2.2 Application of Leakage Analysis Results 169
6.3 Optimisation of Geometrical Parameters of a Profile 173
6.3.1 The Blow Hole Constant and the Contact Line Constant 173
6.3.2 A Method of Reducing the Blow Hole Area 175
6.4 Determination of the Discharge Port Position 177
6.5 Rotor Parameters and Compressor Performance 180
6.6 Optimisation of Slide Valve Definition Parameters 184
6.6.1 With and without Slide Valve 184
6.6.2 Slide Stop and Adjusting Characteristics of a Slide Valve 188
6.7 References 190

Chapter 7 CONCLUSIONS 192

Chapter 8 SUGGESTIONS FOR FURTHER WORK 199

Appendix A BASIC EQUATIONS FOR PROFILE ANALYSIS .. 203

Appendix B PARAMETER EQUATIONS OF THE SRM D-PROFILE 208

Appendix C THE FIRST DERIVATIVES OF THE D-PROFILE EQUATIONS 228

Appendix D KEY POINT COORDINATES OF A SRM D-PROFILE 233

Appendix E THERMODYNAMIC PROPERTY EQUATIONS .. 235

Appendix F SYSTEM DIAGRAM OF MEASUREMENT RIG .. 247

Appendix G CALCULATION OF CUTTER GEOMETRY 248
G.1 The Zero Clearance Cutter Blades 248
G.2 The Equidistant Lobe Profile Method 252

G.3 The Equidistant Helical Surface Method 253

BIBLIOGRAPHY 256

LIST OF FIGURES

1.1 Standard SRM D-profile 4
1.2 Twin screw compressor principle 5
1.3 The procedure flow diagram 9
2.1 A symmetrical circular profile 19
2.2 A SRM A-profile 20
2.3 A SRM D-profile 21
2.4 The flow diagram of profile generation program 24
2.5 Illustrative profiles generated by the program 27
2.6 Comparison with the practical A-profile 30
2.7 Comparison with the practical D-profile 33
3.1 Cross-sectional area vs rotational angle 37
3.2 Cavity volume vs rotational angle 38
3.3 Theoretical shape of a suction port 39
3.4 Axial suction port area vs rotational angle 40
3.5 Radial suction port area vs rotational angle 41
3.6 Theoretical shape of an axial discharge port 42
3.7 Axial discharge port area vs rotational angle 42
3.8 Areas vs rotational angle 43
3.9 Contact line length vs rotational angle 44
3.10 Tip sealing line lengths vs rotational angle 45
3.11 End plane sealing line lengths vs rotational angle 46
3.12 Area of blow hole on high pressure side vs rotational angle 48
3.13 Area of blow hole on low pressure side vs rotational angle 49
3.14 The injection port areas vs rotational angle 50
3.15 The flow diagram of the geometrical calculation program 51
4.1 Leakage paths of a cavity in a twin screw compressor 62
4.2 The schematic diagram of leakage paths 64
4.3 A simplified control volume of a screw compressor 65

4.4 A practical used suction port 68
4.5 Process calculation flow program 90
4.6 p-V diagram 97
4.7 Pressure in the cavity vs the rotational angle of the male rotor 98
4.8 Gas temperature in the cavity vs the rotational angle of the male rotor . 99
4.9 Gas mass in the cavity vs the rotational angle of the male rotor 100
4.10 Mach No through the suction and discharge ports vs the rotational angle of the male rotor 100
4.11 Oil and gas temperatures in the cavity vs cavity volume 101
4.12 Comparison of predicted results with measured data ($p_2/p_1 = 3.0$) 104
4.13 Comparison of predicted results with measured data ($p_2/p_1 = 5.0$) 106
4.14 Comparison of predicted results with measured data ($p_2/p_1 = 8.0$) 107
4.15 Comparison of predicted results with measured data ($p_2/p_1 = 12.0$) ... 109
4.16 Comparison of predicted results with measured data ($V_{ir} = 2.6$) 111
4.17 Comparison of predicted results with measured data ($V_{ir} = 3.6$) 113
4.18 Comparison of predicted results with measured data ($V_{ir} = 5.0$) 115
4.19 Prediction and test volumetric efficiency vs capacity 116
4.20 Prediction and test volumetric efficiency vs capacity 117
4.21 Prediction and test volumetric efficiency vs capacity 118
4.22 Prediction and test volumetric efficiency vs capacity 118
4.23 Prediction and test volumetric efficiency vs capacity 119
4.24 Prediction and test volumetric efficiency vs capacity 119
4.25 Prediction and test volumetric efficiency vs capacity 120
4.26 Prediction and test volumetric efficiency vs capacity 121
4.27 Comparison of predicted results with measured data ($V_{ir} = 2.6$) 123
4.28 Comparison of predicted results with measured data ($V_{ir} = 3.6$) 125
4.29 Comparison of predicted results with measured data ($V_{ir} = 5.0$) 127
4.30 p-V diagrams 129
5.1 The flow diagram of the cutter calculation program 140
5.2 A zero clearance lobe profile and its equidistant real profile 141
5.3 The zero clearance and real cutter blades to produce equidistant lobes . 142

5.4 The zero clearance and real lobe profiles deriving from the equidistant helical surface method 143
5.5 The zero clearance and real cutter blades to produce an equidistant helical surface 144
5.6 The clearance distributions along the contact line 145
5.7 A zero clearance profile and its two real profiles 146
5.8 Predicted and test results for a compressor with oil and liquid refrigerant injection—two clearance schemes compared 148
5.9 Predicted results of a compressor with oil and liquid refrigerant injection—optimized and equidistant profile schemes compared 151
5.10 The influence on cutter shape of the angle between the cutter and rotor axes 153
5.11 The influence of offset angle on the cutter shape 155
5.12 The cutter blades for the proposed improved profile 156
6.1 The leakage flow rate through each leakage path 165
6.2 Leakage tables for different running conditions 167
6.3 Reduced volumetric and isentropic indicated efficiencies: leakage along each path compared with zero leakage 168
6.4 A proposed improved profile 171
6.5 Reduced volumetric and isentropic indicated efficiencies: for a new proposed compressor having a 5/7 lobe combination 172
6.6 Blow hole area reduction 176
6.7 The total and indicated efficiencies vs p_d/p_i 178
6.8 p-V diagrams for different p_d/p_i ratios 179
6.9 Efficiencies vs the wrap angle of the male rotor 181
6.10 The overlap constant vs the wrap angle of the male rotor 183
6.11 Efficiencies vs the length/diameter ratio of rotors 183
6.12 Indicated efficiency vs volume ratio of radial discharge port 185
6.13 Discharge Mach Nos vs rotation angle of the male rotor 186
6.14 p-V diagrams 187
6.15 Stop and position parameters of a slide valve 188

6.16 Adjusting characteristics of different slide stops 189
6.17 Adjusting characteristics of different slide stops 189
6.18 Adjusting characteristics of different volume ratios 190
A.1 Coordinate systems for profile analysis 203
B.1 SRM D-profile and its symboles 210
G.1 Coordinates systems of a rotor and its cutter 249

LIST OF TABLES

6.1 The measured and simulated efficiencies 165
6.2 The measured and simulated efficiencies 181
6.3 The measured and simulated efficiencies 186
E.1 Constants for Liquid Density Equation 235
E.2 Constants for Vapour Pressure Equation 236
E.3 Constants for Equation of State 237
E.4 Constant X for the Enthalpy Equation 238
E.5 Constants for the Enthalpy Equation 239
E.6 Constant Y for the Entropy Equation 240
E.7 Constants for Equation of State 244
E.8 Constants for Enthalpy Equation of Vapour 246

NOMENCLATURE

The symbol definitions used are those given below unless otherwise stated, and then only in the section where the definition is declared.

A The center distance of the rotors, $A = r_M + r_F$, $[mm]$.

A_{axial} The axial discharge port area, $[m^2]$.

A_{flow} The minimum flow area, $[m^2]$.

A_{LRI} The liquid refrigerant injection port area, $[m^2]$.

A_{LRImax} The maximum liquid refrigerant injection port area, $[m^2]$.

A_{OD1} The area of oil draining port from the suction end casing, $[m^2]$.

A_{OD1max} The maximum area of oil draining port from the suction end casing, $[m^2]$.

A_{OD2} The area of oil draining port from the discharge end casing, $[m^2]$.

A_{OD2max} The maximum area of oil draining port from the discharge end casing, $[m^2]$.

A_{OI} The area of oil injection ports, $[m^2]$.

A_{OImax} The maximum area of oil injection ports, $[m^2]$.

A_b Blow hole area, $[m^2]$.

A_r Relative blow hole area.

A_{radial} The radial discharge port area, $[m^2]$.

A_{SF} The superfeed port area, $[m^2]$.

A_{SFmax} The maximum superfeed port area, $[m^2]$.

A_1 An area shown in Fig. 4.4, $[m^2]$.

A_2 An area shown in Fig. 4.4, $[m^2]$.

A_{01} The cross-sectional area bounded by the male rotor profile and the housing bore, $[m^2]$.

A_{02} The cross-sectional area bounded by the female rotor profile and the housing bore, $[m^2]$.

$A_{oil\leftrightarrow}$ Surface area of the droplets of the oil in the control volume, $[m^2]$.

C_o Overlap constant of the compressor.

C_{oil} Oil specific heat, $[J/kgK]$.

c_{area} Modification coefficient for the calculated minimum flow areas.

c_{LRI} Flow rate coefficient through the liquid refrigerant injection port.

c_{main1} Coefficient one used for the friction power generated from the main casing.

c_{main2} Coefficient two used for the friction power generated from the main casing.

c_{OI} Flow rate coefficient through the oil injection ports.

c_{SF} Flow rate coefficient through the superfeed port.

c_{speed} Modification coefficient for the calculated flow speeds which go through the calculated minimum flow area.

D_{1out} The nominal outer diameter of the male rotor, $[mm]$.

D_{2out} The nominal outer diameter of the female rotor, $[mm]$.

D_{shaft} The diameter of the shaft which goes through the shaft seal, $[mm]$.

$H_{drained-gas}$ The enthalpy of the gas drained together with the oil from the suction and discharge end case, $[J]$.

$H_{inlet-gas}$ The enthalpy of the gas through the suction port, $[J]$.

$H_{leak-in-gas}$ The enthalpy of the gas leaking into the control volume, $[J]$.

$H_{leak-out-gas}$ The enthalpy of the gas leaking out off the control volume, $[J]$.

$H_{LRI:flash-gas}$ The enthalpy of the gas flashed from the liquid refrigerant injected, $[J]$.

$H_{oil:flash-gas}$ The enthalpy of the gas flashed from the injected or drained oil, $[J]$.

$H_{outlet-gas}$ The enthalpy of the gas through the discharge port, $[J]$.

$H_{superfeed}$ The enthalpy of the gas through the superfeed port, $[J]$.

$H_{SV:by-pass-gas}$ The enthalpy of the gas through the by-pass port of the slide valve, $[J]$.

h The gas specific enthalpy, $[J/kg]$.

h_1 The suction specific enthalpy, $[J/kg]$.

h_2 The discharge enthalpy, $[J/kg]$

h_{gas} The enthalpy of the gas in the control volume, $[J/kg]$.

h_{LR} The enthalpy of the refrigerant dissolved in the oil and corresponding to the temperature of the oil, $[J/kg]$.

h_{LRI} The enthalpy of liquid refrigerant before the injection port, $[J/kg]$.

h_{OD} The enthalpy of flashed gas before the drained ports, $[J/kg]$.

h_{OI} The enthalpy of liquid refrigerant dissolved in oil before all the injection ports, $[J/kg]$.

h_{SF} The gas enthalpy at the superfeed port, $[J/kg]$.

$h_{upstream}$ The enthalpy of the gas in the cavity from which the gas leaks into the control volume, $[J/kg]$.

i The transmission ratio from the male rotor to the female rotor.

k The ratio of A to r_F, $k = 1 + i$.

L Work exchanged by the gas in the control volume with the surroundings through the control surface area, $[J]$.

L_r Length of the male rotor or the female rotor, $[mm]$.

$L_{sealing}$ Sealing line length, $[mm]$.

l_c Length of contact line per lobe in the $X - Y$ plane, $[m]$.

l_r Relative contact line length per lobe.

m The mass of the gas which goes through any port and leakage path in the compressor, $[kg]$.

$m_{drained-gas}$ The mass of the gas which is drained together with the oil drained from the suction and discharge end casings, $[kg]$.

m_{gas} The mass of the gas in the control volume, $[kg]$.

$m_{inlet-gas}$ The mass of the gas which goes through the suction port, $[kg]$.

$m_{leak-in-gas}$ The mass of the gas which leaks into the control volume, $[kg]$.

$m_{leak-out-gas}$ The mass of the gas which leaks out off the control volume, $[kg]$.

m_{LR} The mass of liquid refrigerant still dissolved in the oil, but ready to flash, $[kg]$.

$m_{LRI:port}$ The mass of liquid refrigerant through the liquid refrigerant injection port, $[kg]$.

$m_{LRI:flash-gas}$ The mass of the gas which is flashed from the liquid refrigerant inject, $[kg]$.

m_{LRI} The mass of the liquid refrigerant injected in the control volume, $[kg]$.

m_{OD} The mass of the oil drained from the end casings, $[kg]$.

m_{OI} The mass of the oil injected into the cavity, $[kg]$.

m_{oil} The mass of the oil in the control volume, $[kg]$.

$m_{oil:flash-gas}$ The mass of the gas which is flashed from the oil injected or drained, $[kg]$.

$m_{outlet-gas}$ The mass of the gas which goes through the discharge port, $[kg]$.

$m_{superfeed}$ The mass of the gas which goes through the superfeed port, $[kg]$.

$m_{SV:by-pass-gas}$ The mass of the gas which goes through the by-pass port of the slide valve, $[kg]$.

$P_{bearing}$ The friction power of the bearings, $[kw]$.

$P_{endcasing}$ The total friction power of the two end casings, $[kw]$.

$P_{isentropic}$ Isentropic compression power of compressor, $[kw]$.

P_{ind} Indicated power of compressor, $[kw]$.

$P_{maincasing}$ The total friction power generated from the main casing, $[kw]$.

P_{piston} The friction power of the balance pistons, $[kw]$.

$P_{shaftseal}$ The friction power of the shaft seal, $[kw]$.

P_{input} Input power of compressor, $[kw]$.

p Pressure in the control volume, $[bar]$.

p_1 The suction pressure of the compressor, $[bar]$.

p_2 The discharge pressure of the compressor, $[bar]$.

$p_{endcasing}$ The pressure in the end casings, $[bar]$.

p_i Internal pressure at the end of compression process, $[bar]$.

p_{oil} The oil pressure before all the injection ports, $[bar]$

p_{vapour} Saturated vapour pressure, $[bar]$.

Q Heat exchanged with the gas in the control volume due to the drained or injected oil and due to the friction power in the cavity, $[J]$.

$Q_{FG:endcasing}$ The flow rate of the flashed gas from the two end casing, $[kg/min]$.

$Q_{leaking-in-gas}$ Total leaking inflow rate of a leakage path, $[kg/min]$.

$Q_{leaking-out-gas}$ Total leaking outflow rate of a leakage path, $[kg/min]$.

Q_{LRI} The total flow rate of the liquid refrigerant injected, $[kg/min]$.

$Q_{LRI:flash-gas}$ The total flash rate of the liquid refrigerant injected, $[kg/min]$.

Q_{LR} The flow rate of ready-to-flash refrigerant from the oil in the control volume, $[kg/min]$

Q_{mass} Mass capacity of compressor, $[kg/min]$

$Q_{netoutflow}$ The net outflow rate of a leakage path, $[kg/min]$.

Q_{OD} Total drained oil flow rate from the end casings, $[kg/min]$.

Q_{OI} Total injected oil flow rate directly into the main casing, $[kg/min]$.

Q_{oil} Equivalent oil flow rate through the compressor, $[kg/min]$.

$Q_{oil:flash-gas}$ Total flash rate of refrigerant dissolved in the oil in the cavity volume, $[kg/min]$.

$Q_{oil\leftrightarrow gas}$ Heat exchanged between the gas and the oil in the control volume, $[J]$.

Q_{SF} The total gas flow rate through the superfeed port, $[kg/min]$.

r_F The radius of the pitch circle of the female rotor, $[mm]$.

r_M The radius of the pitch circle of the male rotor, $[mm]$.

s_{gas} The entropy of the gas in the control volume, $[J/kg\ K]$.

t The generally used parameter used in geometrical analysis, $[mm$ or $rad]$.

t Temperature used in the mathematical model, $[°C]$.

t_{gas} The temperature of the gas in the control volume, $[°C]$.

t_{OD} The oil temperature before the oil drained ports, $[°C]$.

t_{OI} The oil temperature before all the oil injection ports, $[°C]$.

t_{oil} The temperature of the oil in the control volume, [°C].

U_{gas} The internal energy of the gas in the control volume, $[J]$.

u Specific internal energy, $[J/kg]$.

V Cavity volume, $[m^3]$.

V_{ia} Volume ratio for axial discharge port.

V_{ir} Volume ratio for radial discharge port.

V_{liquid} The cavity volume taken up by the liquids, such as oil and liquid refrigerant, $[m^3]$.

V_r The real maximum cavity volume of the compressor, $[mm^3]$.

v_1 Suction specific volume, $[m^3/kg]$.

v_{gas} The specific volume of the gas in the control volume, $[m^3/kg]$.

v_{liquid} The specific volume of liquid refrigerant, $[m^3/kg]$.

W Fluid flow speed through the minimum flow area, $[m/s]$.

W_{sound} The local sound speed at the minimum flow area, $[m/s]$.

W_1 The rotational speed of the male rotor, $[rev/min]$.

z_1 The number of lobes of the male rotor.

z_2 The number of grooves of the female rotor.

α_{1s} Suction stop angle on the male rotor side, [°].

α_{2s} Suction stop angle on the female rotor side, [°].

$\alpha_{oil \rightarrow gas}$ Heat transfer coefficient of oil to gas or gas to oil, $[W/(m^2 \cdot K)]$.

β_{ftip} Screw angle at the tip of female rotor, $[rad]$.

β_{pitch} Screw angle on the pitch circle, $[rad]$.

ΔH_{lat} Latent heat of vaporization, $[J/kg]$.

δ Gap clearance in the main casing, $[mm]$.

η_{ind} Isentropic indicated efficiency of compressor, $[percentage]$.

$\eta_{mechanical}$ Mechanical efficiency of compressor, $[percentage]$.

η_{total} Total efficiency of compressor, $[percentage]$.

η_{vol} Volumetric efficiency, $[percentage]$.

ξ Ratio of the mass of the liquid refrigerant dissolved in oil to the total mass of the mixture.

ρ Working fluid density, $[kg/m^3]$.

ρ_{LR} Density of liquid refrigerant, $[kg/m^3]$.

ρ_{oil} Oil density, $[kg/m^3]$.

φ_1 The rotational angle of the male rotor, [°].

$\varphi_{1dis.start}$ The rotational angle of the male rotor corresponding to the end of the compression process, [°].

φ_{1max} The rotational angle of the male rotor corresponding to the end of the discharge process, [°].

$\varphi_{1suc.stop}$ The rotational angle of the male rotor corresponding to the end of the suction process, [°].

φ_2 The rotation angle of the female rotor, [°].

ω_1 The rotational angular speed of the male rotor, $[°/s]$.

ω_2 The rotational angular speed of the female rotor, $[°/s]$.

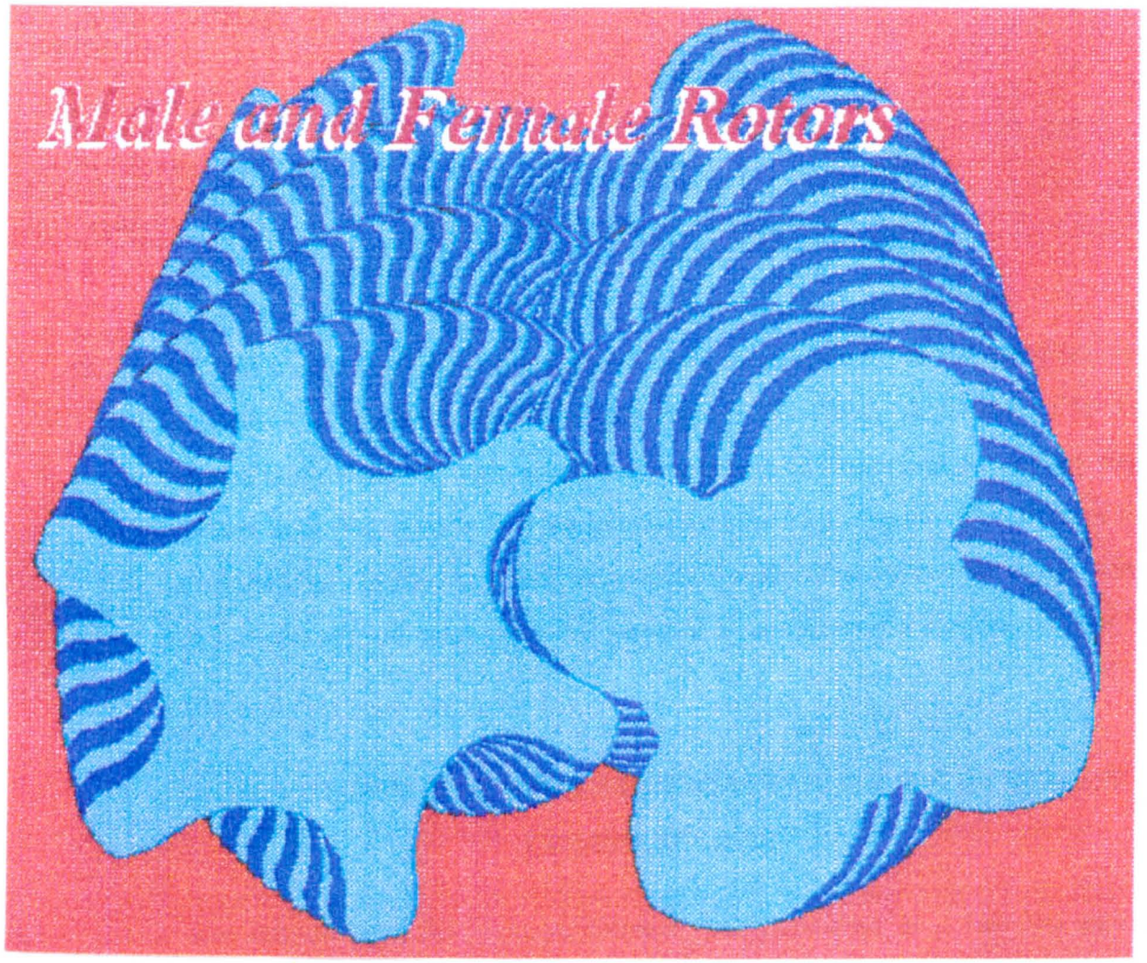

3D rotor diagram generated by the author's program

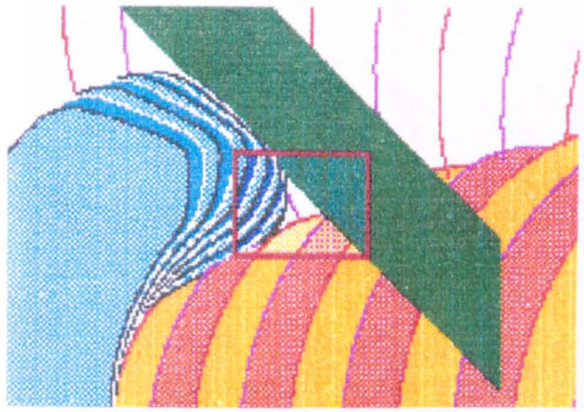

Blow hole of a twin screw compressor (generated by the author's program)

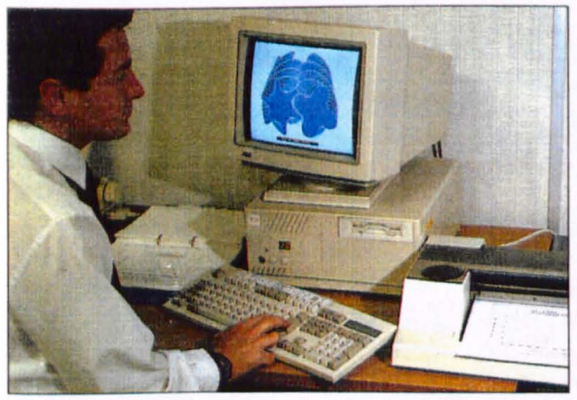

The author's twin screw compressor CAD program library is used in Howden Compressors Ltd.

COMPRESSION CYCLE

In a screw compressor, compression is achieved by the intermeshing of two helical rotors as shown in the following illustrations. (Diagrammatic only).

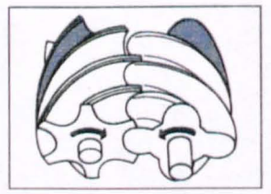

Figure 1
Gas is drawn in to fill the interlobe space between adjacent lobes.

Figure 2
As the rotors mesh, the gas is trapped between the rotors and the casing.

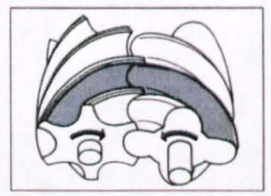

Figure 3
Continued rotation progressively reduces the space occupied by the gas causing compression.

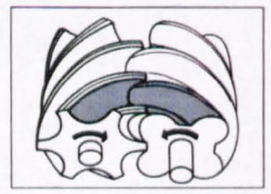

Figure 4
Compression continues until the interlobe space becomes exposed to the outlet port, through which the gas is discharged.

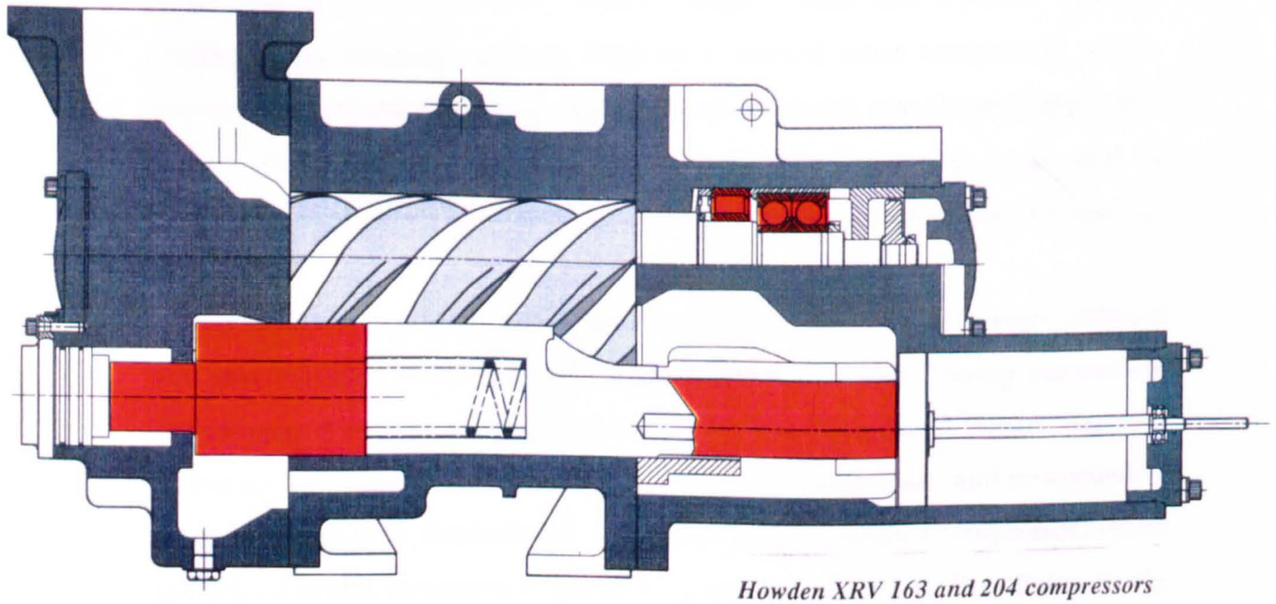

Howden XRV 163 and 204 compressors

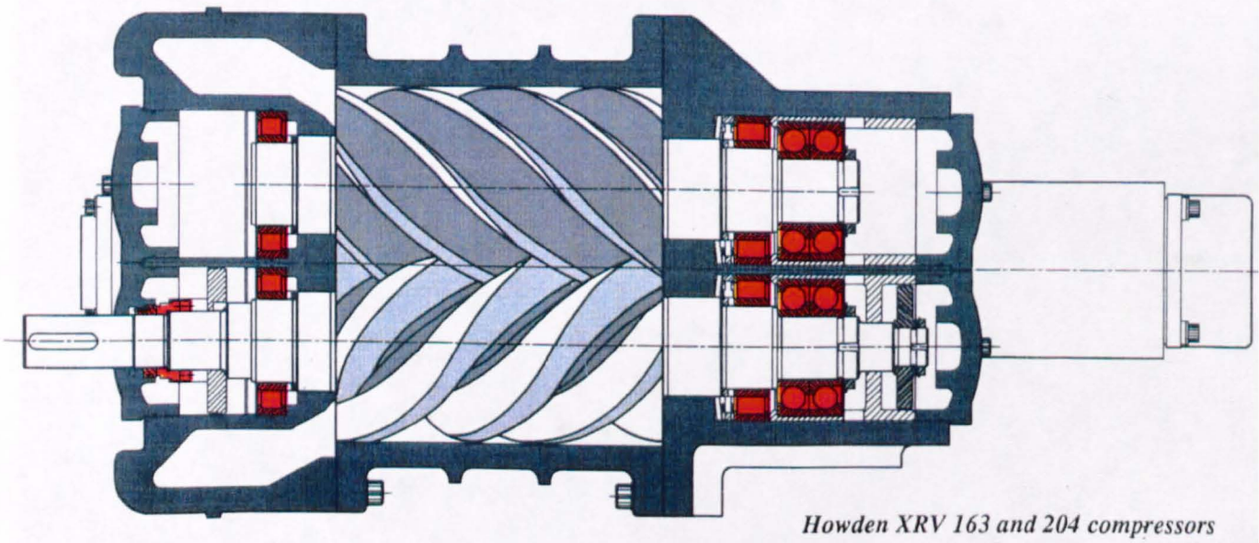

Howden XRV 163 and 204 compressors

Plate 1 Typical cross sections of a modern screw compressor

Chapter 1
INTRODUCTION

In this chapter the development and application of twin crew compressors are presented. Their basic compression principle is described. A procedure for the computer aided design of twin screw compressors is an important part of the work presented here. An outline is given in this introductory chapter. The work of the other researchers in the same field is described with comments on its significance. Plate 1 shows typical cross sectional views of a modern screw compressor and its rotors.

1.1 DEVELOPMENT AND APPLICATION OF TWIN SCREW COMPRESSORS

The original idea for a screw 'blower' was embodied in a German patent granted to Heinrich Krigar of Hannover as early as 1878, and one such compressor is believed to have been manufactured. Further work on the concept was done by General Motors in the USA, without much success, and a patent was also granted to the Swedish company IMO for a 'conical screw compressor' which, however, was not manufactured. Around 1928, academic gear theories applicable to compression were developed by Nahuse of Tohoku University, Japan, and by Novikov of Russia, but these were not used practically in compressor technology at the time.

The first practical screw compressor was not developed until the early 1930s; it was later patented by the Swedish engineer, Alfred Lysholm. During gas turbine development work at the Ljungstrm Steam Turbine Company, Lysholm was concerned by the occurrence of 'surge' in a centrifugal compressor, and proceeded to developed a positive-displacement rotary machine. Lysholm's compressor, which had a $3+3$ profile combination (three lobes on the male rotor, three flutes on the female rotor), was produced in 1934; by 1937, a $4+6$ profile combination machine

had been developed, and in 1938, such a compressor was manufactured, in collaboration with Lysholm, by James Howden & Company of Glasgow, Scotland. The first development work was described in the *Proceeding of the Institution of Mechanical Engineers*, vol. 150, 1943 (1). From this work was derived the most widely applied form of screw compressor for gas compression used today. In more recent times the Ljungstrm Company was renamed Svenska Rotor Maskiner AB (SRM) and most screw compressors for process gas compression today are manufactured under licence from this company (2).

One of the main features of the early screw compressor was the fact that it was oil-free. The description 'oil-free' implies that the gas compression space is entirely free from oil contamination, although in most cases the bearings and seals of such compressors are supplied with oil under pressure. The compressor rotors were designed to mesh with each other without surface-to-surface contact, one rotor driving the other through timing gears, which synchronize their rotation.

During the 1950s another development occurred, i.e. the elimination of the timing gears by injecting oil and allowing one rotor to drive the other directly like a pair of gears. The oil also improved the sealing and cooled the compressed gas but required the use of an oil separator in the discharge line, to make the gas usable. The idea for an oil-injected compressor was first developed by SRM in early 1950s, but the first practically operating machine was tested by the Scottish engineer Duncan Laing, at James Howden & Company in 1955. This type of screw compressor was at first intended for portable use, but was later followed by stationary versions of similar capacity and by special purpose units such as refrigeration compressors. In oil injected screw compressors, the compressor rotors are designed so that one drives the other directly and metal-to-metal contact of the rotor surfaces is prevented by a hydrodynamic oil film. This design is the major technological breakthrough in the history of twin screw compressors. As used in this thesis, "oil-injected" means that a quantity of oil much greater than necessary for proper lubrication is supplied to the compression chamber. This additional oil seals the clearances between the rotors and compression chamber walls, reduces the discharge temperature of the gas being compressed, and allows

the use of simpler mechanical designs.

Nowadays the helical screw compressor is used for refrigeration in the food and process industries and for gas compression in the petrochemical and process industries and increasingly, for general air compression duty. It competes with the medium to large sizes of reciprocating compressors and the smaller dynamic compressors. Ironically enough, what the screw compressor originally was designed for — to replace dynamic compressors in gas turbines — is an application where it is not used at all these days.

Its use has advanced steadily if fairly slowly from its invention in the 1930s until a few years ago when its market share began to increase significantly. This acceleration in popularity has been due to the machine's inherent virtues becoming apparent to users, most particularly its ability to handle a range of running conditions and its reliability and robustness—it can tolerate the ingestion of liquid for example on a scale which would cause catastrophe damage to a reciprocating machine. However, there is a considerable art and science to be mastered in the design and manufacturing processes if these machines are to come close to their potential. There may be only two moving parts, but their shapes are not symmetrical and are helical. As a consequence, the deformations due to gas loads and temperature effects are difficult to predict and set severe problems for the designers. Equally the manufacture of the rotors tests the ingenuity of the production engineers. In recent years the development of more sophisticated computerized models of the compressor structure and of its thermo-fluid behaviour have greatly aided the designers. These advances combined with advances in specialized machine tools have made the production of reliable high performance helical screw compressors more certain than before, but the tasks are still very demanding.

1.2 BASIC COMPRESSION PRINCIPLE OF TWIN SCREW COMPRESSORS

The helical screw compressor is a positive displacement compressor, the working cavity of which is enclosed by the housing bores, housing end plates and the helical surfaces of the male and female rotors. As a result of the rotation of the

rotors, the volume of the working cavity varies from zero to its maximum and from its maximum to zero periodically. As a consequence of this periodic variation, the compressor completes its suction, compression and discharge processes. Helical screw compressors contain only two moving parts, a male rotor and a female rotor. Fig. 1.1 shows a standard SRM D-profile for the male and female rotors. The rotor with lobes which are outside the pitch circle, is called the male rotor, and the rotor with lobes which are inside the pitch circle, is called the female rotor. The male has a large addendum, the female a large dendendum.

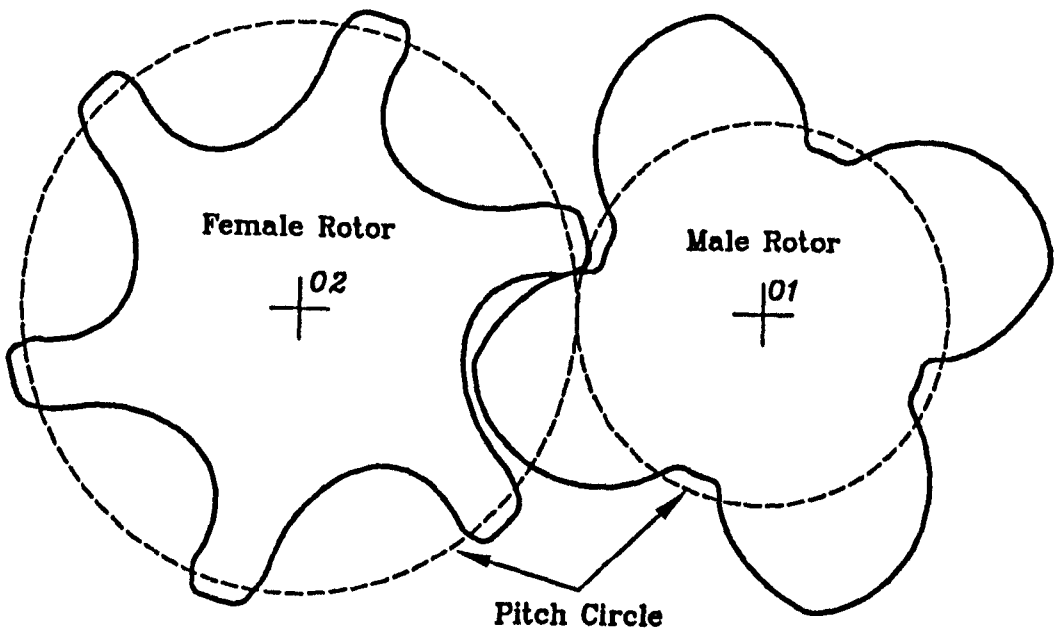

Fig. 1.1 A standard SRM D-profile (generated by the author's program)

The screw compression principle involves a highly skewed three-dimensional mechanism having a series of adjacent spaces which are confined by the meshed crests and roots of the rotors and the compression chamber walls. Fig. 1.2 depicts this mechanism as a series of two-dimensional S-shaped projections moving diagonally from left to right on a plane along the periphery of the female rotor. To understand this analogy, it is essential to assume that the casing seals the gas paths all around, even through the meshing of the rotors plays a large part in this respect. On this simplified basis, the principle features of the screw compression sequence can be described as follows:

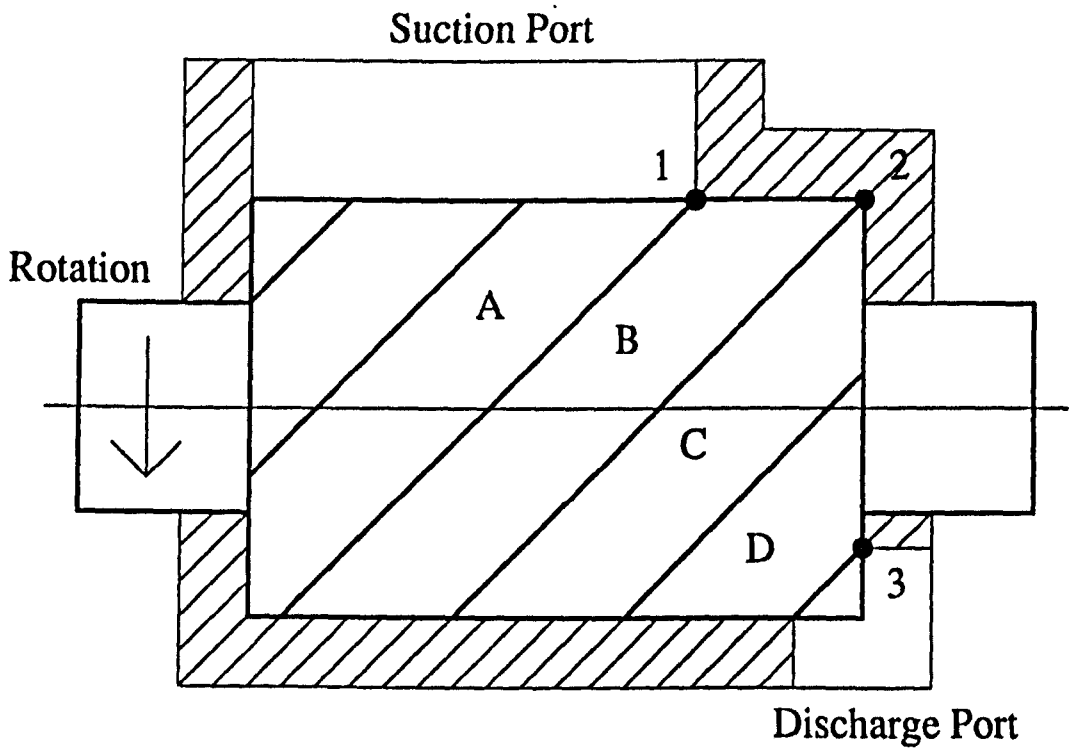

Fig. 1.2 Twin screw compressor principle

1. As the screws unmesh, a cavity is created and its size A increases until its maximum size B is exposed. During this interval, suction gas is drawn continuously into the expanding cavity.
2. When the crest between A and B reaches point **1**, the finite volume of gas B is cut off from both the suction and the discharge openings of the compression chamber (The chamber walls will fully shroud the rotors just before **1** is reached, to avoid the uncontrolled expulsion of some gas back to the suction). This volume represents the ideal maximum suction volume called the "Theoretical Displacement" or, more commonly, simply "Displacement".
3. When the crest between B and C passes point **2**, the volume of the cavity begins to decrease and continues to decrease C until this crest reaches point **3** which delimits the minimum volume D. During this interval, the pressure of the gas is increased due to the decrease in volume from B to D.

4. When the leading crest of D passes point **3**, the cavity opens to the compressor discharge and the gas is expelled due to the continuing rotation of the rotors. Because the preceding cavity is still being vacated, a continuous discharge results.

1.3 THE PROCEDURE OF COMPUTER AIDED DESIGN

The performance of the compressor is influenced greatly by its fundamental geometry, i.e the male and female lobe profiles, rotor length to diameter ratio and wrap angle; and also the detailed geometry of the suction and discharge ports and the slide valve. In a good compressor these factors must be optimized to suit running conditions whilst simultaneously providing rotors which are easy and cheap to machine, which requires computer aided techniques for its design, and especially for predicting its thermodynamic behaviour. Earlier design techniques relied on the designer's experience and many geometrical characteristics were obtained by hand calculation, plotting and planimetry, all of which was very time-consuming. Further, the designer did not know if the performance of the new machine was adequate or not before the prototype was tested. If the test results of the prototype were not satisfactory, the design and the machining of the prototype had to be repeated, which was both very time-consuming and very expensive. The development of computer aided design programs has not only made it possible to obtain the best performance from the machine but has also greatly reduced the cost of the design process.

For the purpose of computer aided design for twin screw compressors, the following computer programs including their result display and support programs are developed by the author:

Profile Generation Program This program (see Chapter 2) is a profile library which can generate any profile within the definitions of the symmetrical circular, the SRM A and the SRM D. The profile generation program is the basis of all the research work. It calculates and outputs its calculated results into differents data files, which are required by other programs developed

by the author for the compressor geometrical characteristics calculations, cutter blade calculations, etc.

Geometrical Characteristic Calculation Program This program (see Chapter 3) calculates all the required geometrical characteristics and parameters for both the working process simulation and design purposes. Many of the geometrical characteristics are expressed as a function of the male rotor rotation angle, especially those which are used in the working process simulation program.

Working Process Simulation Program This program (see Chapter 4) simulates working processes of a refrigeration twin screw compressor which may run under various conditions, such as partial loading, oil injection, liquid refrigerant injection, gaseous refrigerant superfeeding and different refrigerants etc. The program calculates the thermodynamic properties in the cavity as a function of the male rotor rotational angle or the cavity volume, and also the derived parameters and efficiencies describing the behaviour of the compressor.

Cutter Blade Calculation Program This program (see Chapter 5) is used to calculate: the zero clearance and real profiles of both the male and female lobes; the zero clearance and real cutter blades for male and female; the variation of the total clearance both normal to the profile and to the helical surface along the length of the contact line. It also gives desirable manufacturing parameters and the average clearance between the male and female rotors, which is required by the working process simulation program of the compressors.

With the exception of the profile generation program, all the programs developed by the author are *universal.* This means that they can be used for any shape of profile, if the suitable data files similar to those generated by the author's profile generation program are available.

The flow diagram for the computer aided design process is shown in Fig. 1.3. The profile generation program is a profile library. The basic parameters and coordinates of the new generated profile are output into different data files, which

provide the input to the geometrical characteristic calculation program. The geometrical characteristic calculation program calculates all the geometrical characteristics in terms of the male rotor rotation angle for the length and wrap angle chosen for the male rotor. Its output is read by the working process simulation program, which predicts the performance of the proposed machine. If the performance does not match the chosen criteria, basic parameters of the profile or the rotors should be changed and the above steps repeated until the required performance is obtained. The cutter blade calculation program may now be run to calculate the cutter blades for the male and female rotors with the clearance between the two rotors determined as described by the author (**3** & **4**). The shapes of the cutter blades have a considerable influence both on the machining cost and the meshing accuracy of the rotors so if the shapes are poor from this practical point of view the basic parameters of the profile should be modified and the above steps repeated until the shapes are acceptable. During the process many useful plots and curves for the design may be drawn by a plotter or shown on a monitor.

In Chapter 6 the four computer programs developed to facilitate the work described here are used to optimise a twin screw compressor design. Its internal and external leakages are analysed. A method for optimising the basic geometrical parameters of the rotor profile, the rotor geometrical parameters, the position of the discharge port and the slide valve definition parameters etc. is presented. The optimisation technique described in that chapter is very useful for the practical design of a twin screw compressor.

Although this thesis is concerned mainly with a refrigeration twin screw compressor, the working fluid of which is *R*22, the computer aided design and optimisation technique described can be applied to a twin screw compressor compressing a working fluid which can be a pure substance or a mixture of several substances e.g. air, refrigerant, several refrigerants, several gases with or without oil. The property relations for the gas or mixture would require to be known together with some measured data from a test compressor to permit the determination of certain essential empirical coefficients needed in the thermodynamic performance

simulation model (see Chapter 4).

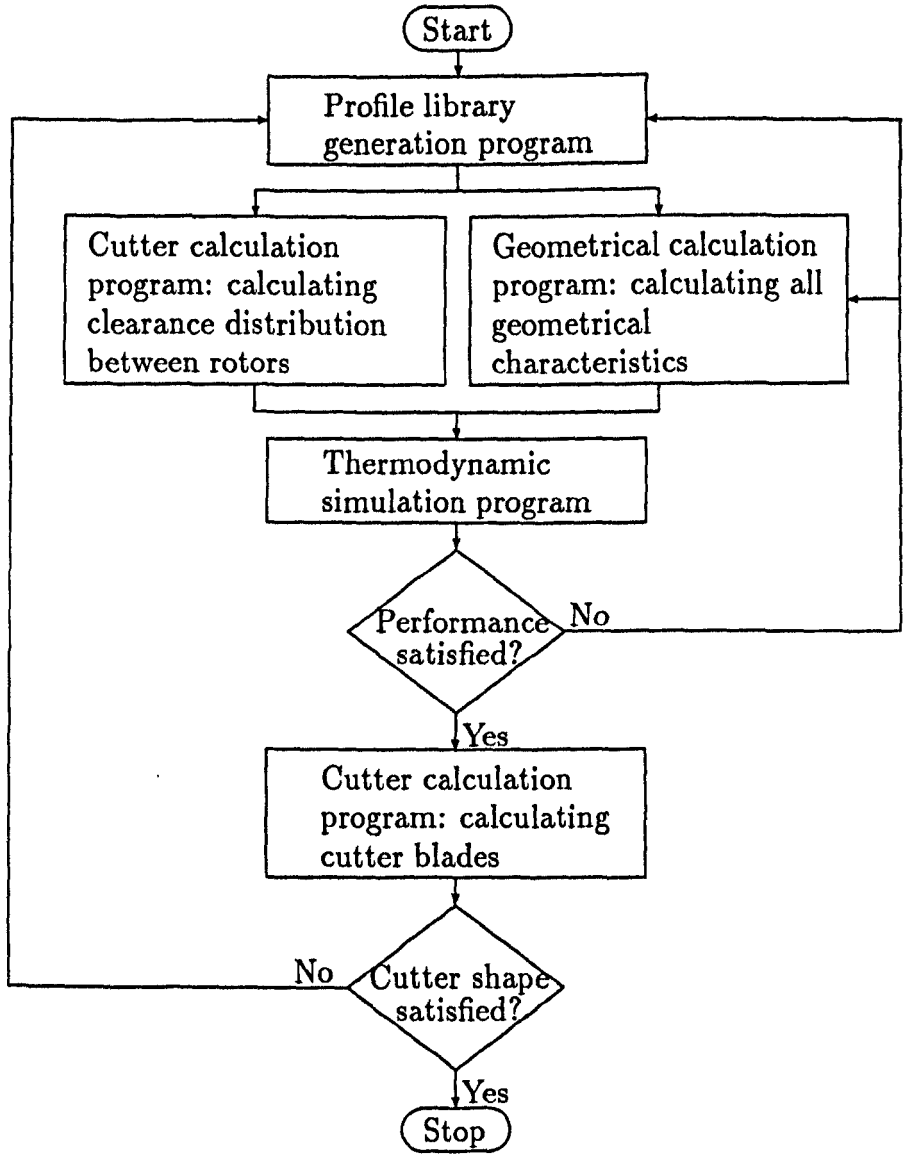

Fig. 1.3 The procedure flow diagram

1.4 REVIEW OF LITERATURE

There are three remarks of a general nature which may be made concerning the published work on twin screw compressors as follows:

1. Its comparative scarcity. Compared with the papers on other major engineering components like turbines or transformers say, the total number of published papers is small.

2. Of the papers written in English the majority are conference papers, short on technical detail and in inaccessible places such as bound conference proceedings without ISBN numbers. The number of papers in archived journals is actually very small.
3. Germany is the world's biggest producer of twin screw compressors and a substantial level of research and development work is known to go on there. It has led to a reasonable literature, virtually all of it in German and consequently not readily available to a non German reader like the author of this work. The VDI Schraubenmaschinen conference proceedings are a good example.

The scarcity of the literature and its lack of detail is explained by the desire of the developers to avoid giving anything of a commercially valuable nature away. The release of valuable information could occur inadvertently when discussing a machine in which small changes to profile geometry, for example, are capable of improving performance. However, papers are published and the increasing effort devoted to computer aided design of twin screw compressors is seen in the published work of the last ten or so years. This work concentrates on profile generation, geometrical design and simulating the thermodynamic behaviour of the compressor. Although there have been very few papers on the optimisation of clearance distribution between rotors or on cutter blade shapes, it is safe to assume that every manufacturer has been paying much attention to the cutter blade calculation and the optimisation of cutter blade and clearance distribution. The absence of published work on this topic is due to its commercially sensitive nature and the competition between manufacturers.

1.4.1 Geometrical Analysis Programs

In order to simulate the working processes of a twin screw compressor, the profile should be generated and the required geometrical characteristics such as cavity volume, sealing line lengths and blow hole area etc. should be calculated first. The geometrical analysis programs also give the compressor designer all the

required design parameters besides the geometrical parameters which are input to the simulation program. Some of geometrical analysis programs are developed from the equations for a given profile, and their applications are quite limited. Some of them are universal, which means that they can be used for any shape of profile.

An important paper on profile generation and geometrical analysis was published by Singh and Onuschak in 1984 (5). A comprehensive and computerized approach to twin screw rotor profile generation and analysis was presented. Using the method, a user, starting with a rough sketch, can generate a profile, determine all important geometrical parameters such as leakage lengths, blow hole area and discharge port area, and analyze a machine's performance using this profile. The method can be used for new profile generation, adjustment of existing profiles, parametric studies and profile optimisation. The programs described, of course, are universal, but for a refrigeration compressor the program is not powerful enough, as some important geometrical characteristics such as slide valve by-pass port area, superfeed port area, liquid refrigerant injection port area and sealing line lengths at the suction and discharge ends of rotors, are not given by the program.

Fujiwara and Kasuya etc. presented their work for the geometrical calculation in (6). Their program can calculate volume curve, sealing line length and discharge port area etc. A numerical procedure was used in their program.

Jonsson described in outline a comprehensive program library in 1986 (7). The programs calculate the following geometrical parameters: volume curve, inlet port area vs. rotation angle, outlet port area vs. rotation angle, rotor-rotor sealing line length vs. rotation angle, male and female lobe tip sealing line length vs. rotation angle and blow hole area. The results are input to the simulation program. All the programs have a set of profile coordinates as input and they do not deal with analytical profile definitions. This means that they can be used for all types of profiles. Significantly, all of these workers presented their papers at conferences in short papers without detail.

1.4.2 Working Process Simulation Programs

Since 1980, a number of twin screw compressor researchers have published papers on the simulation of the working process. The compressors have been oil-free or oil-injected, and the working fluid of the machine is a refrigerant, air or another gas.

Firnhaber and Szarkowicz published a paper on the simulation of the working process of the twin screw compressor in 1980 (**8**). Their model was very simple. Expansion through leakage paths and the effects of coolant injection were not considered, and ideal gas behaviour was assumed. A more sophisticated model was reported by Fukazawa and Ozawa in (**9**), in which the effects of internal leakage are considered and the thermodynamic properties of a refrigerant are treated as a real gas.

At the International Compressor Engineering Conference at Purdue in 1982, two papers on working process simulation were published. Bráblik and Praha published an analytical model of an oil-free screw compressor, in which the working fluid is treated as an ideal gas, and the geometrical parameters are calculated by an analytical method (**10**). However the model presented by Sångfors (**11**) is even more advanced. The model can handle oil-free or oil-injected machines, and leakage through leakage paths, friction losses due to oil in the leakage paths and heat exchange between oil and gas are considered in the model. A comparison between computed and measured pressure in the cavity was presented and showed good agreement. More detail of the mathematical model is described in (**12**).

Fujiwara and Kasuya etc. developed a model for an oil injected screw compressor (**6**), based on the laws of thermodynamics for perfect gases. The effects of internal leakage, heat exchange between gas and oil, and the flow resistance at suction and discharge ports are included in the model. Later, Fujiwara and Kasuya obtained flow and heat transfer characteristics for their model (**13**). The heat transfer coefficient is determined from the experimental relation between the volumetric efficiency and the inlet temperature. Flow coefficients are obtained

from the efficiency-clearance curves. Singh and Patel also developed a model for oil injected screw compressors in which the working fluid is considered as a perfect gas (**14**). The program accounts for all leakages, viscous shear losses, oil cooling, and inlet and discharge losses. It uses some empirical coefficients which have been developed based on extensive test data. The program's results have been extensively checked against test data and have been shown to give a good agreement over a wide tip speed range and for several different machines having different rotor profiles and lobe number combinations.

The thermodynamic efficiency of the compression process in oil injected screw compressors depends greatly on the oil-gas heat transfer process. The magnitude of heat transfer is a function of many parameters such as mode of oil injection, oil inlet temperature etc. In 1986 Singh and Bowman published a paper which describes a mathematical model which calculates this heat transfer, assuming that the oil is injected in the form of spherical droplets which do not interact with each other(**15**). Person published his research results on the same topic in 1987 (**16**), but the model is more general as water injection is considered in addition to oil injection. The injected liquid is considered to atomize into a uniform spray. For oil injection, transient heat transfer air-oil has been studied. For water injection, transient heat and mass transfer, ie evaporation cooling, has been studied. Stošić and Milutinović later published two papers on the same topic (**17** & **18**). Some results of mathematical modeling and experimental investigation of the influence of oil injection upon the screw compressor working process are presented. Several parameters that characterize oil injection were varied over ranges that were initially determined from a computer model. These include: oil flow rate, inlet temperature, droplet atomization, positions in the casing at which the oil was injected.

Also in 1986 Singh and Bowman published a paper about some optimisation results of the main design parameters of an oil flooded screw compressor such as rotor profile, number of rotor lobes, rotor L/D ratio, wrap angle, geometrical clearances, quantity and location of oil injection, discharge port size and tip speed (**19**). Knowledge of the effect of these parameters can help a designer to select the

best performing machine for a given application. Proprietary computer programs (**5** & **15**) are used to calculate the geometrical characteristics of the rotors and compressor performance.

Jonsson published a paper which presented a brief description of a computer program for the simulation of a twin screw compressor for refrigeration purposes in 1987 (**20**). The effect of evaporation of refrigerant, dissolved in the injected oil, is considered in the computations. Economizer arrangements are also considered in the model.

Stošić and Milutinović etc. published two papers about their computer model and computer aided design for twin screw compressors (**21** & **22**). The model was developed to serve as a basis for computer-aided design and optimisation of compressors. The heat exchange of the working fluid with the injected oil, the rotors and the housing are taken into account in the model, and nine refrigerants are considered.

Alday and Hood reported a computer program which provides a quick, simple, and accurate environment for modeling and analyzing the performance of a rotary screw compressor (**23**). The program utilizes performance data measured during dynamometer testing of a compressor to develop a mathematical model of the compressor's performance. This model has been developed from many measured results and as a consequence, is not a true thermodynamic model. It is important to appreciate however, that even the most sophisticated thermodynamic model requires empirical coefficients derived from measured data.

1.5 REFERENCES

1 **Lysholm, A.J.R.** New Rotary Compressor. *Proc. Instn mech. Engrs*, 1943, **150**, pp.11–16.

2 **Arbon, Ian M.** The Design and Application of Rotary of Rotary Twin-Shaft Compressors in the Oil and Gas Process Industry. *Mechanical Engineering Publications Ltd, London*, 1994.

3 **Tang, Yan** and **Fleming, John S.** Clearances between the Rotors of Helical Screw Compressors: Their Determination, Optimisation and Thermodynamic Consequences. *Proc I Mech E Vol 208 Part E, Journal of Process Mechanical Engineering*, 1994.

4 **Fleming, John S. Tang, Yan Young, W.** and **Anderson, H.** The Calculation and Optimisation of Cutter Blade Shapes for the Manufacture of Helical Screw Compressor Rotors. *Proceedings of IMechE European Conference on Developments in Industrial Compressors and their Systems*, London, U.K., 1994, pp.17–25.

5 **Singh, Pawan J.** and **Onuschak, Anthony D.** A Comprehensive, Computerized Method for Twin-Screw Rotor Profile Generation and Analysis. *Proceedings of International Compressor Engineering Conference at Purdue*, Purdue University, U.S.A., 1984, pp.519–527.

6 **Fujiwara, M., Kasuya, K., Matsunaga, T.** and **Watanabe, M.** Computer Modeling for Performance Analysis of Rotary Screw Compressor. *Proceedings of International Compressor Engineering Conference at Purdue*, Purdue University, U.S.A., 1984, pp.536–543.

7 **Jonsson, S.** Computer Calculation for Design and Analysis of Screw Compressors. *Royal Institute of Technology, Department of Thermal Engineering*, Stockholm, Sweden, Trita åtk 860907, 1986.

8 **Firnhaber, M.A.** and **Szarkowicz, D.S.** Modeling and Simulation of Rotary Screw Compressor. *Proceedings of International Compressor Engineering Conference at Purdue*, Purdue University, U.S.A., 1980, pp.305–308.

9 **Fukazawa, Yoshimitsu** and **Ozawa, Utaka** Small Screw Compressors for Automobile Air-Conditioning Systems. *Proceedings of International Compressor Engineering Conference at Purdue*, Purdue University, U.S.A., 1980, pp.323–330.

10 **Bráblik, J.** and **Praha, Č** Analytical Model of an Oil-Free Screw Compressor. *Proceedings of International Compressor Engineering Conference at Purdue*, Purdue University, U.S.A., 1982, pp.356–364.

11 **Sångfors, B.** Analytical Modeling of Helical Screw Machine for Analysis and Performance Prediction. *Proceedings of International Compressor Engineering Conference at Purdue*, Purdue University, U.S.A., 1982, pp.135–139.

12 **Sångfors, B.** Computer Simulation of the Oil Injected Twin Screw Compressor. *Proceedings of International Compressor Engineering Conference at Purdue*, Purdue University, U.S.A., 1984, pp.528–535.

13 **Fujiwara, M.** and **Osada, Y.** Performance Analysis of Oil-Injected Screw Compressors and its Applications. *Proceedings of International Compressor Engineering Conference at Purdue*, Purdue University, U.S.A., 1990, pp.51–60.

14 **Singh, Pawan J.** and **Patel, Ghanshyam C.** A Generalized Performance Computer Program for Oil Flooded Twin-Screw Compressors. *Proceedings of International Compressor Engineering Conference at Purdue*, Purdue University, U.S.A., 1984, pp.544–553.

15 **Singh, Pawan J.** and **Bowman, James L.** Heat Transfer in Oil-Flooded Screw Compressors. *Proceedings of International Compressor Engineering Conference at Purdue*, Purdue University, U.S.A., 1986, pp.135–151.

16 **Person, J.-G.** Heat-Exchange in Liquid-Injected Screw-Compressors. **VDI** *BERICHTE NR. 640*, 1987, pp.121–135.

17 **Stošić, N. Milutinović, Lj. Hanjalić, K.** and **Kovačević** Invetigation of the Influence of Oil Injection Upon the Screw Compressor Working Process. *Int. J. Refrig.*, 1992, Vol 15, No 4, pp.206–220.

18 **Stošić, N. Kovačević, A. Hanjalić, K.** and **Milutinović, Lj.** Mathematical Modeling of the Oil Influence upon the Working Cycle of Screw

Compressors. *Proceedings of International Compressor Engineering Conference at Purdue*, Purdue University, U.S.A., 1988.

19 **Singh, Pawan J.** and **Bowman, James L.** Effect of Design Parameters on Oil-Flooded Screw Compressor Performance. *Proceedings of International Compressor Engineering Conference at Purdue*, Purdue University, U.S.A., 1986, pp.71–89.

20 **Jonsson, S.** Performance Simulation of Twin-Screw Compressors for Refrigeration Purpose. **VDI** *BERICHTE NR. 640*, 1987, pp.187–207.

21 **Stošić, N.** and **Hanjalić, K.** etc. Mathematical Modeling of Screw Compressor Working Process. *Technic-Science-Engineering*, 20(1989)4, pp.7–13.

22 **Stošić, N.** and **Hanjalić, K.** etc. Computer Aided Design of Screw Compressors. *Technic-Science-Engineering*, 20(1989)4, pp.23–29.

23 **Alday, J.H.** and **Hood, J.A.** A Program for Mathematical Modeling and Analysis of Rotary Screw Compressor Performance. *Proceedings of International Compressor Engineering Conference at Purdue*, Purdue University, U.S.A., 1992, pp.249–258.

Chapter 2

THE SRM PROFILES AND THEIR GENERATION PROGRAM

Generation of practically used profiles is the basis of the research work presented in this thesis. This chapter introduces the three most commonly used rotor profiles, ie the symmetrical circular profile, the SRM A-profile and the SRM D-profile. The program used to generate these three profiles has been developed and presented. Any shape of profile under the symmetrical circular, A and D definitions can be generated by the program. In order to test the profile generation program, the standard profiles generated by the program are compared with those applied in practical compressors.

2.1 THE SRM PROFILES

There has been extensive rotor profile development over the years and the three most commonly used rotor profiles are the symmetrical circular profile, the SRM A-profile and SRM D-profile. Ownership of all patent rights for development and manufacture of rotors with such profiles rests with Svenska Rotor Maskiner AB (SRM). In this thesis, the author generates these profiles and does some optimisation for the basic geometrical parameters of the profiles, to illustrate the design technique only.

The symmetrical circular profile, or the symmetrical circular Nilsson-profile, is the first successful profile of SRM (Fig. 2.1). Compared with very theoretical "basic Lysholm-profile", it is a much more practical profile. Although it is old, the symmetrical circular profile is still widely used due to its simplicity and reliability. Its blow hole is large. According to the author's calculated results for the same size compressors, its blow hole area in the plane formed by two cusp points and one

contact line tip point (see Section 3.5) is about three times of the blow hole area of the A-profile. However if the above area is projected onto a plane normal to the female rotor tip helix, which has the same tangent as the gas leakage streamline according to the definition of Singh and Onuschak for the "throat" blow hole area (1), the blow hole area of the symmetrical circular profile is only about ten percent higher that the A-profile. The contact line of the symmetrical circular profile is short, and the length is about ninety percent of the A-profile. Operating at a low pressure ratio (less than 3.0), the machine with the symmetrical circular profile has almost the same performance as the machine with the A-profile, but as the pressure ratio increases, the efficiencies of the symmetrical circular profile become lower than those of the A-profile. The volumetric efficiency of the symmetrical profile is about five percent lower than the A-profile at 6.0 pressure ratio. The higher the pressure ratio, the bigger the difference (2 & 3).

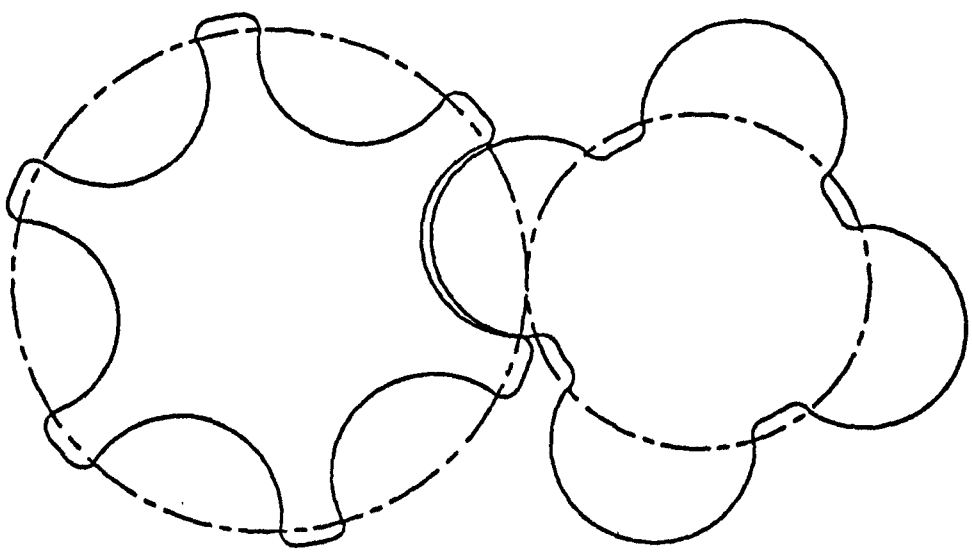

Fig. 2.1 A symmetrical circular profile (generated by the author's program)

From the theoretical "basic Lysholm-profile", through the more practical "symmetrical circular Nilsson-profile" the development led to the asymmetrical

SRM A-profile. As the screw compressor was finding its way into new fields, so the demands on the rotor profiles were changing. The A-profile is a "milestone" in the field of profile development. Fig. 2.2 shows a SRM A-profile. The A-profile is very successful due to its good performance, operation reliability and low manufacturing cost.

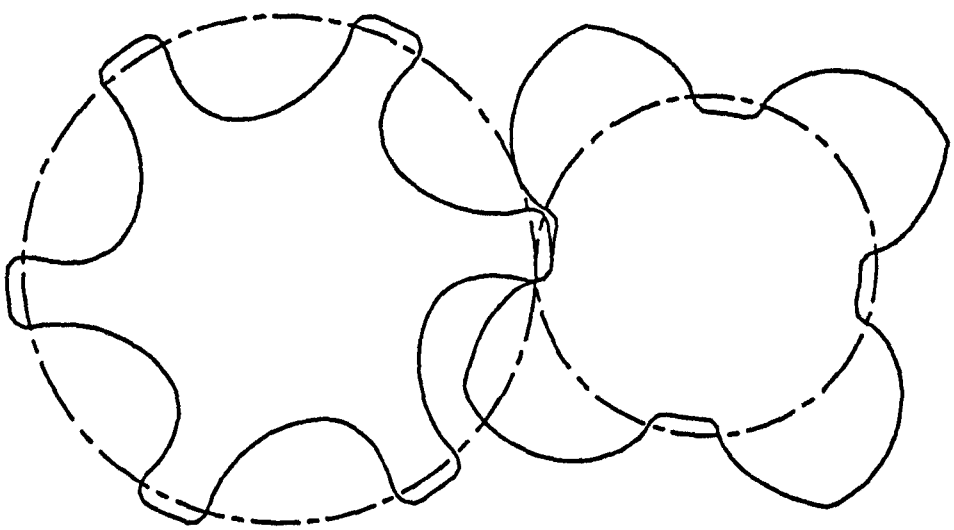

Fig. 2.2 A SRM A-profile (generated by the author's program)

To be able to better fill the needs in the ever changing screw compressor world, the D-profile system has been brought forward by SRM. The D-profile is in fact a profile system and not just a single profile since its geometry can give rise to profiles sufficiently different from each other that distinct compressor characteristics result (4). A change of any basic parameter will result in a change in the shape of the profile produced. Fig. 2.3 shows a SRM D-profile. SRM D-profiles have no point-generated curves and typically have the following desirable features: manufacturing advantages, better sealing characteristics, good performance for both oil-injected and dry machines, favourable conditions for female rotor drive and built-in design flexibility to allow optimisation for specific conditions. Under the

definition of the D-profile, a few standard D-profiles have been issued to its licensees by SRM for different applications, ranging in size from around $40mm$ to over $800mm$, and used for wet, semi-dry and dry machines.

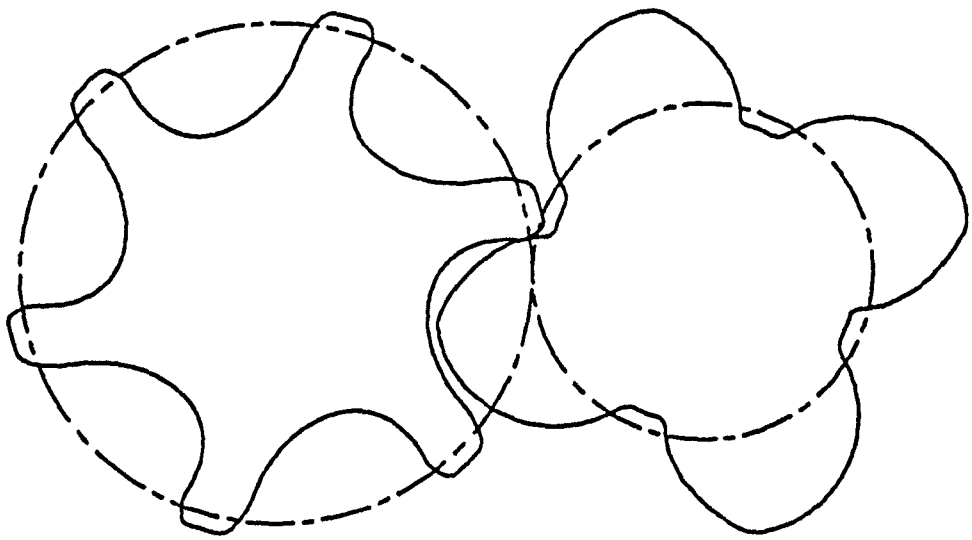

Fig. 2.3 A SRM D-profile (generated by the author's program)

It is worth mentioning here that the SRM B-profile is a profile which has been patented, but has never been used in practice. The SRM C-profile is a profile which is a development from the A, and its application is very limited as it is a special profile used only for hobbing manufacture and for small compressors.

There are many patented rotor profiles, and some of them are very successful. Generation of a new profile is very different from development of a successful profile. In this thesis, the main purpose of all the programs presented are for computer aided design of twin screw compressors, and of course they can be used to predict the performance of a new profile. But besides the prediction of the performance, there are many more things which need to be done to develop a new profile. The theory must be transformed to real rotors, and the rotors have to be tested and evaluated. Very often the prediction by even a good model could be

be very different from the measured results as many factors, besides the blow hole area and sealing line lengths, influence the coefficients and parameters used in the model and could thus result in totally different predicted results. Behind any successful profile, especially those standard profiles, are many predictions, manufacturing processes, tests and evaluations derived from experience.

2.2 MATHEMATICAL ANALYSIS OF PROFILES

The purposes of the mathematical description and analysis of a profile are to ensure that the mating segments of the profiles of the male or female rotors mate geometrically and to calculate the contact points between them in terms of rotor rotational angle. Parametric equations of a segment of a profile are derived and their limits of application are set, and then the parameter equations of the mating segment, which is a conjugate of the original curve, are generated. During this process, the contact points between the two rotor profiles and the corresponding rotational angles can be calculated. The theory on which the profile mathematical analysis is based can be found in many textbooks on gears and also in many textbooks on industrial mathematics. Compared with the geometrical theory used for single screw compressors, the geometrical theory used for twin screw compressors is simple. In order to be convenient to the reader of this thesis, the basic equations are listed in Appendix A. The equations are from (5), (6) and (7). They can also be found in (8) and (9).

The symmetrical circular profile is described in (9). The SRM A-profile is described in (10), and its mathematical analysis is an important part of (11). A practically used A-profile, ie the standard A-profile, is a little different from the profile presented in (10) and (11). The author has also developed the parameter equations for the symmetrical circular profile and the A-profile, as the books (9) and (11), which would have been of greatest help, were written in German and Russian, both of which the author can not read. Based on the standard symmetrical circular and A- profiles, the parameter equations are developed according to the basic equations listed in Appendix A (3).

The basic definition of the SRM D-profile is presented in (**12**), but practically used profiles for different purposes differ from the basic definition. The parameter equations for all the segments of the SRM D-profile are developed and presented in Appendix B, and again the most basic equations for the development are those listed in Appendix A. Appendix C gives the first derivatives of the parameter equations, which are also the basic equations for the profile generation and the cutter blade calculation. The author develops and presents in mathematical form the SRM patent for the D-profile (**12**) which to his knowledge has not been published in English. His main purpose in making the presentation is to draw attention to some special procedures used during the analysis which others may find useful practically. The geometry of the D-profile system is defined by seven circular arcs and their mating curves combined with a few different tip shapes, which makes it more complex than some others. Its great popularity makes it a very important profile in the field of rotor profile development.

2.3 PROFILE GENERATION PROGRAM

Making use of the results of the mathematical analyses of the symmetrical circular, the A- and the D- profiles (**3**, Appendix B & C), a generation program, which is used to generate various profiles within the definitions of these profiles, has been developed. The flow diagram of the profile generation program is shown in Fig. 2.4.

All the basic parameters for standard versions of SRM profiles are built into the program and are quickly and easily generated by the user when the program is run. The user also has the choice of entering the basic parameters needed to generate any shapes of profiles to the SRM symmetrical circular, A- and D-definitions besides the range of standard SRM profiles commonly used (**3** & **4**).

The basic parameters of the profile should be chosen to suit the operating conditions, for example, for high or low pressure ratio and male or female drive etc., and to optimize the basic parameters and the design of the compressors. Choosing different basic parameters will result in different shapes of profiles. The

basic parameters have a great influence on the length of the contact line between the male and female rotors, on the sizes of the the blow hole areas, the efficiencies of the machine and the manufacturing cost of the rotors etc. The optimisation processes for the basic geometrical parameters are described in Chapter 6 of this thesis. The profile generation program is the base of all the research work.

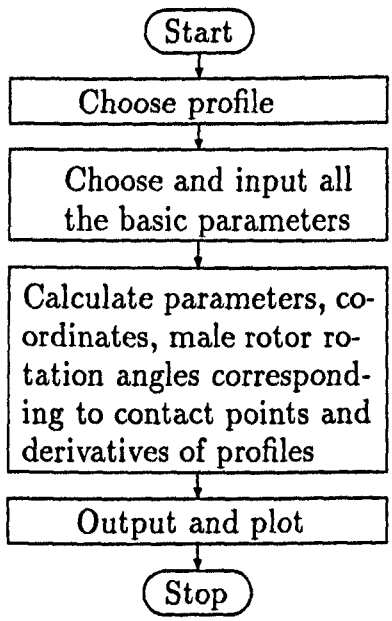

Fig. 2.4 The flow diagram of profile generation program

The program is composed of two main parts. The first part is used to calculate all the parameters which define all the segments of the profile, including their range of application. The second part is used to generate the profile and its first derivatives according to a definite sequence using the parametric equations of the segments. Some parametric limits of segments are the basic parameters which are entered or chosen by the user, but the others need to be calculated based on the basic parameters entered or chosen.

The first part of the program calculates all the parameters which define all the segments of the profile. The derived geometrical parameters together with the basic geometrical parameters are output and stored in a data file.

Making use of the equations, which describe the profile and its derivatives, and the envelop condition equations, the second part of the profile generation program calculates and outputs the following results into different data files:

1. The coordinates of the end profiles of the male and female rotors.

2. The rotation angles of the male rotor corresponding to the contact points between the end profiles.
3. The derivatives of the end profiles.

They are required by other programs developed by the author for the geometrical characteristic calculation, cutter blade calculation, etc. During the profile generation, the program ensures that the maximum distance between any two adjacent points on the generated profiles is not greater than a value entered by the user. For practical purposes, this maximum distance is suggested to be 0.4 *mm* according to the author's experience. The above data files with this accuracy can be used for any purposes including manufacturing in practice. For the academic purpose, the maximum distance could be larger to save the running time of the program and the other programs using the data files.

A display program has been developed to show the generated profile to normal or large scales on a plotter or on a monitor. A few support programs, which are used to show the meshing process between the male and female rotors in 2 or 3 dimensions, also have been developed.

2.4 COMPARISON BETWEEN PRACTICALLY USED PROFILES AND PROFILES GENERATED BY THE AUTHOR'S PROGRAM

Fig. 2.5 illustrates various profiles generated by the profile generation program.

The profile generation is the basis of the research work presented in this thesis in the sense that nothing else is possible without it. In the working process simulation program (Chapter 4), modification coefficients are derived from measured data of Howden Compressors Ltd. As a consequence, it is very important to generate a profile which is used practically. Based on the correct profile generation, the geometrical characteristics, such as the cavity volume curve, the blow hole areas and the sealing line lengths etc. can be calculated correctly, and thus the measured data can be used to derive the modification coefficients.

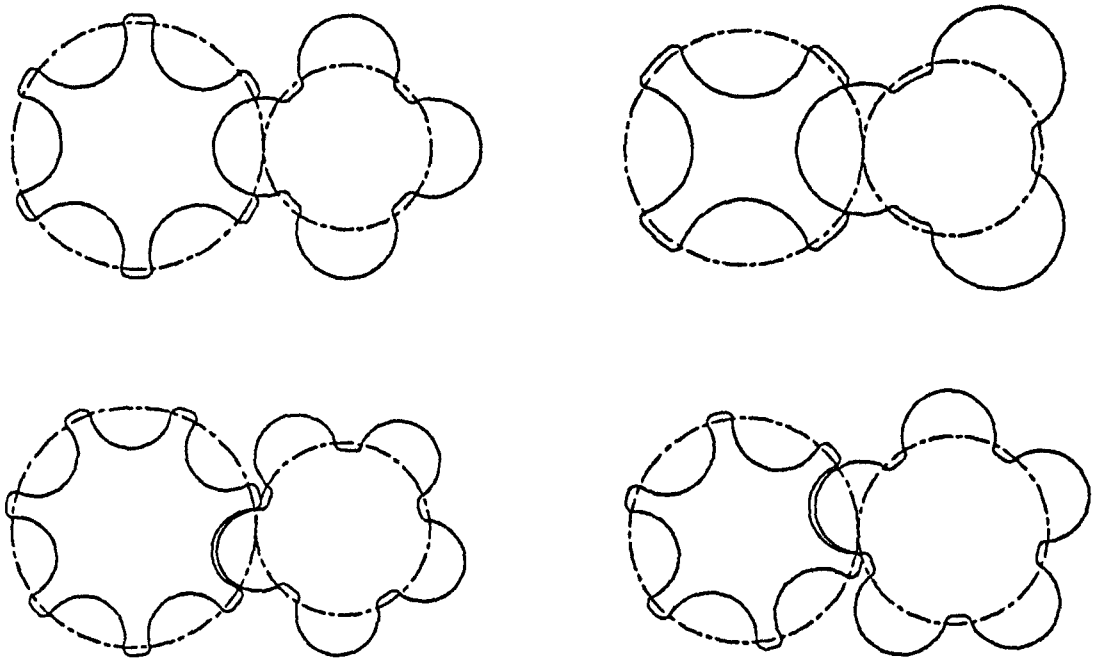

Fig. 2.5 (a) Various symmetrical circular profiles

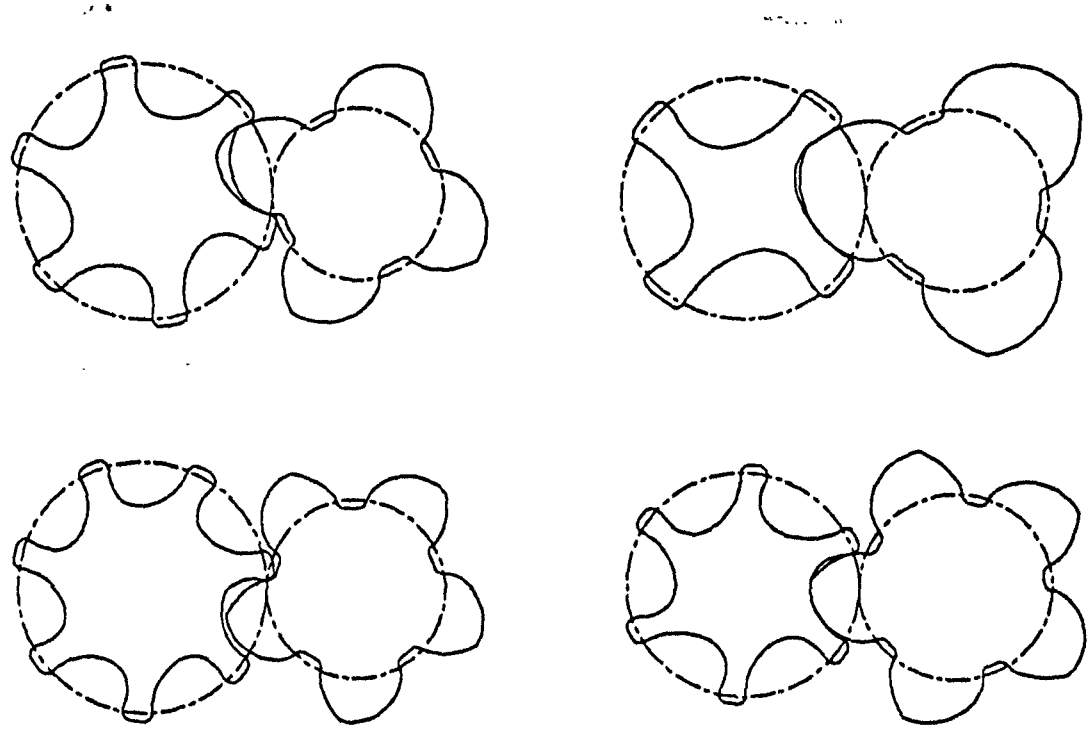

Fig. 2.5 (b) Various SRM A-profiles

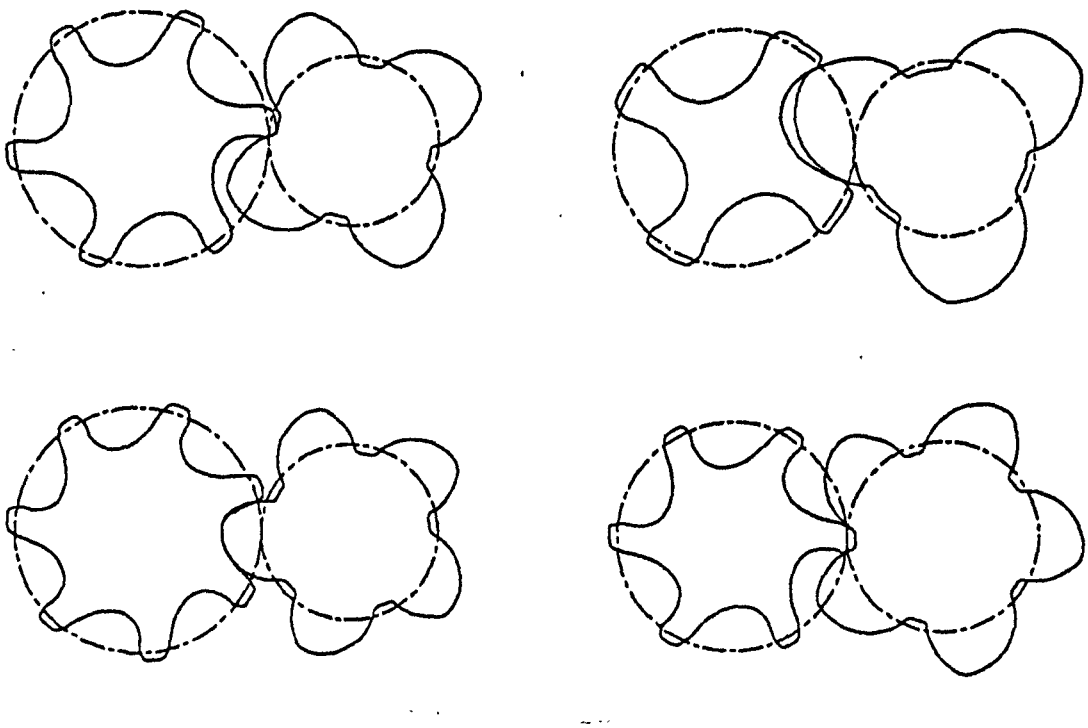

Fig. 2.5 (c) Various SRM D-profiles

Fig. 2.5 Illustrative profiles generated by the profile generation program

Fig. 2.6 shows the comparison of a practically used A-profile (standard) and the profile generated by the author's profile generation program. On this scale they coincide. Its two enlarged partial areas, ie Areas A and B, are shown in Fig. 2.6 (b) and (c). The agreement is excellent. The small difference is due to an insufficient number of points used to describe the practical profile. Fig. 2.6 (d) is the female rotor profile, and again the practical profile and the profile generated by the author's program coincide on this scale. Its two enlarged partial areas, ie Areas A and B, are illustrated in Fig. 2.6 (e) and (f). The agreement is excellent, and the difference is also due to the insufficient number of points used to describe the practical profile.

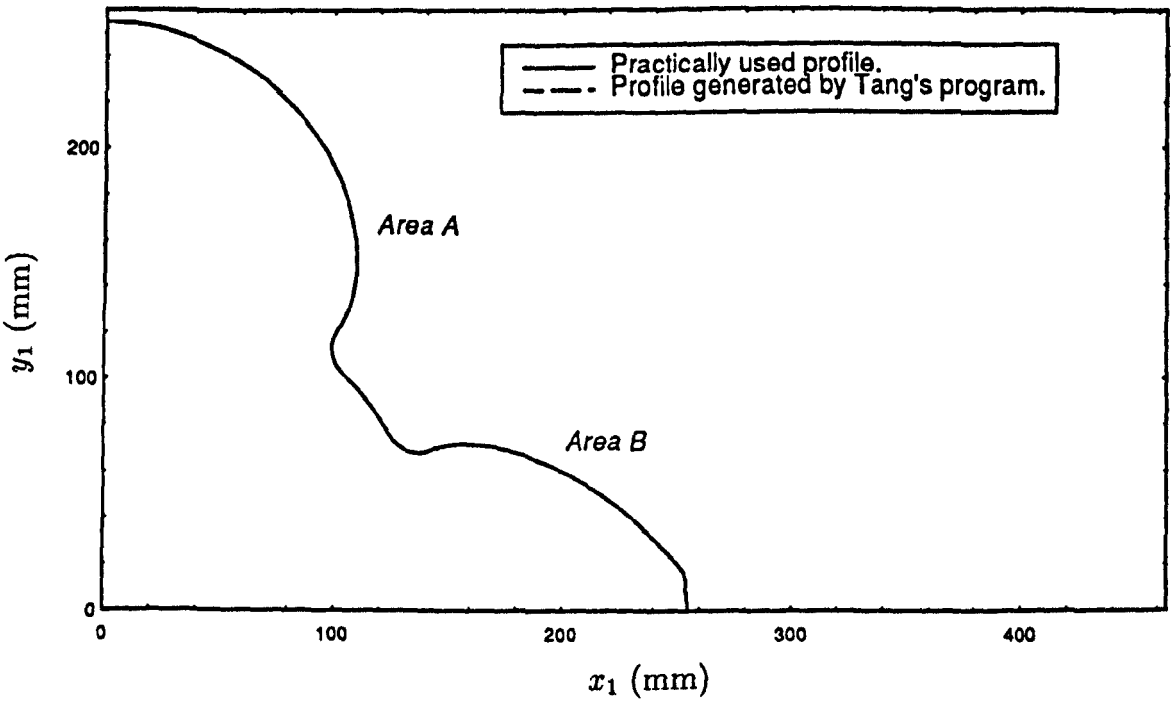

Fig. 2.6 (a) The male rotor profile

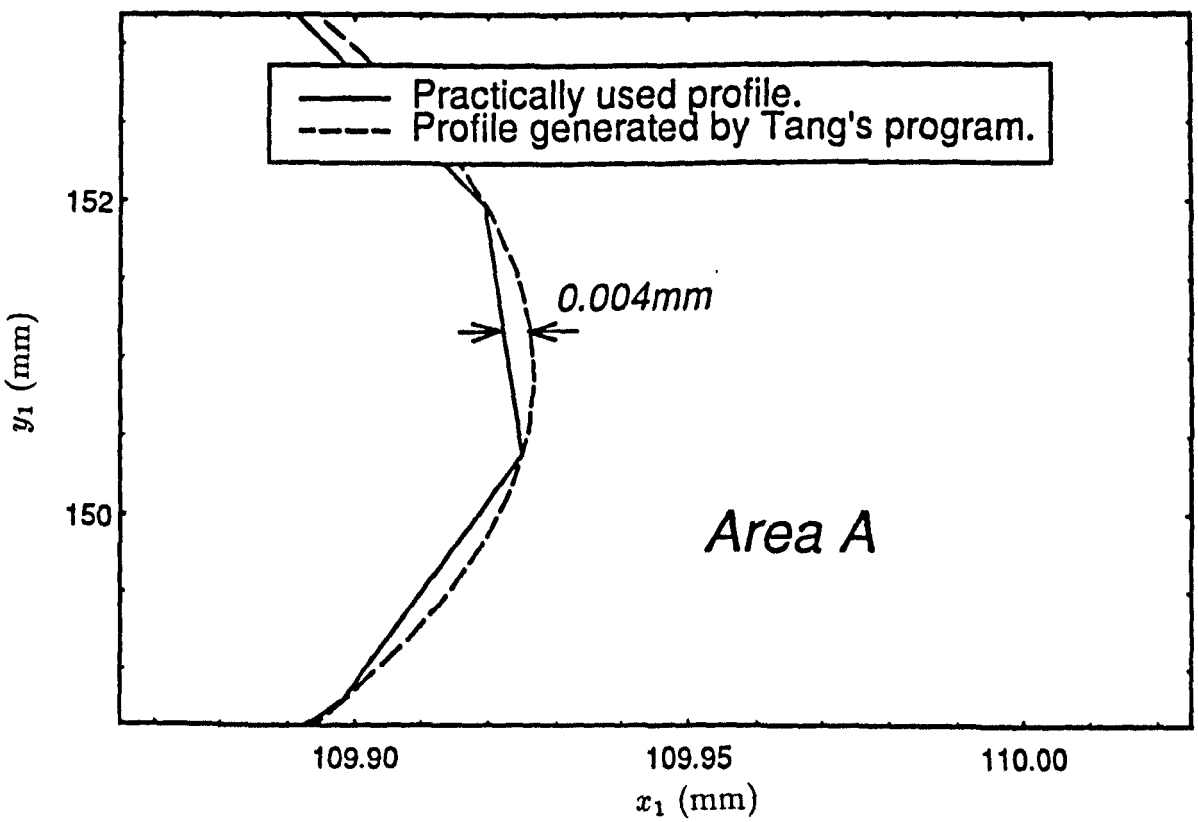

Fig. 2.6 (b) Area A of the male rotor profile

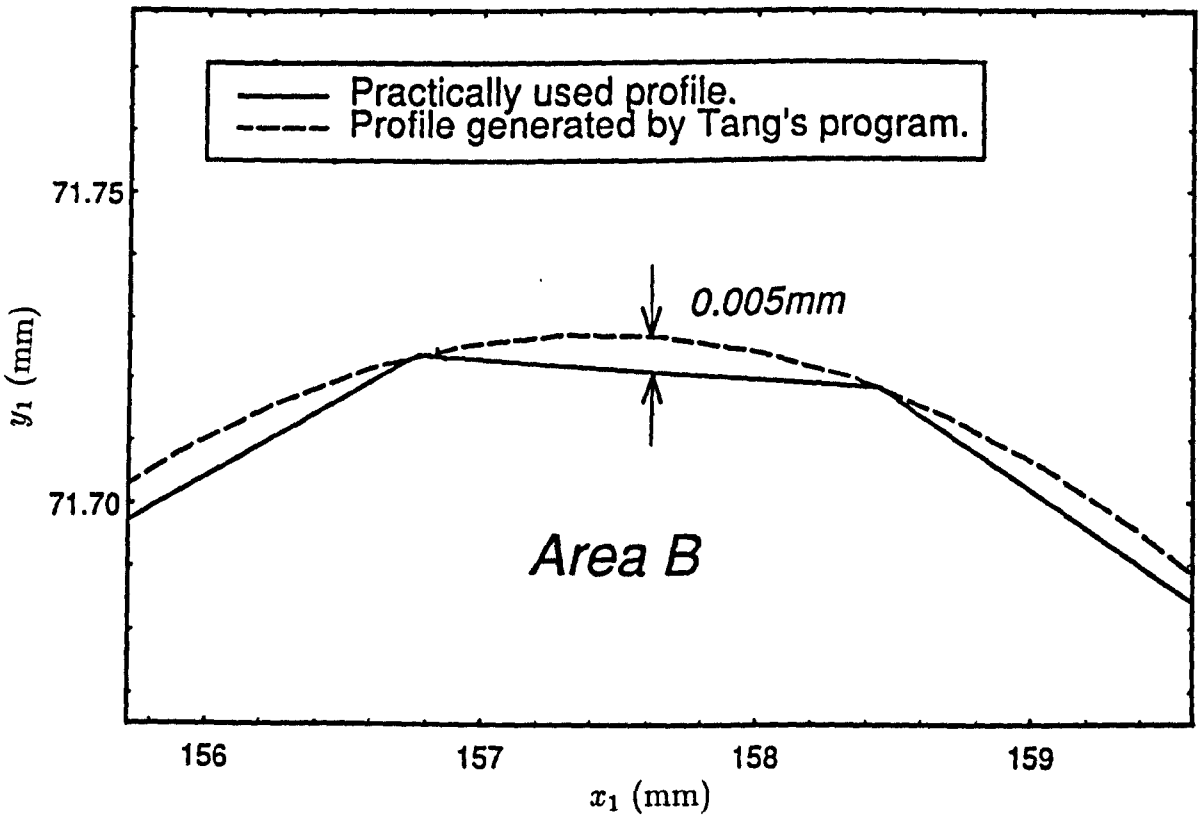

Fig. 2.6 (c) Area B of the male rotor profile

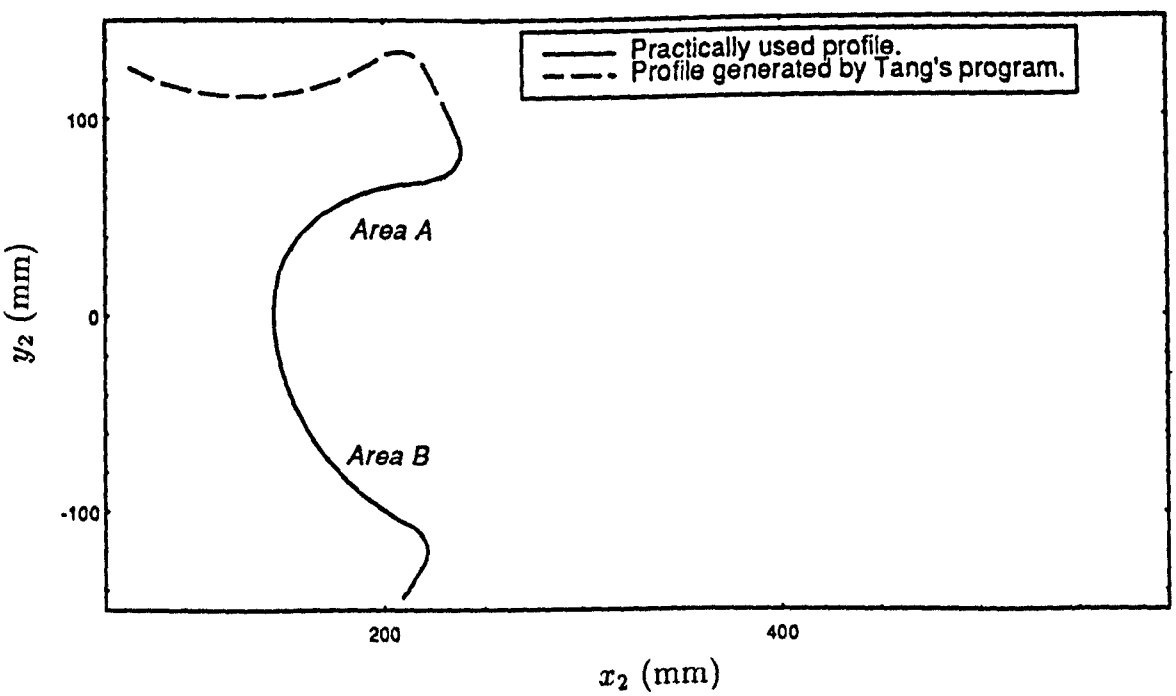

Fig. 2.6 (d) The female rotor profile

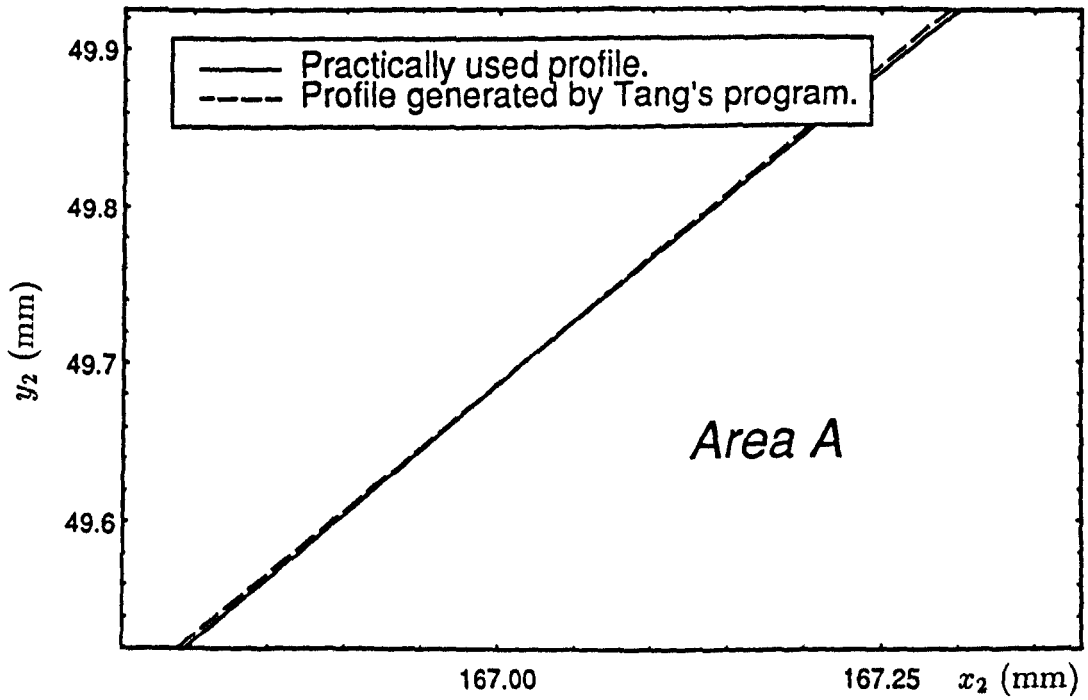

Fig. 2.6 (e) Area A of the female rotor

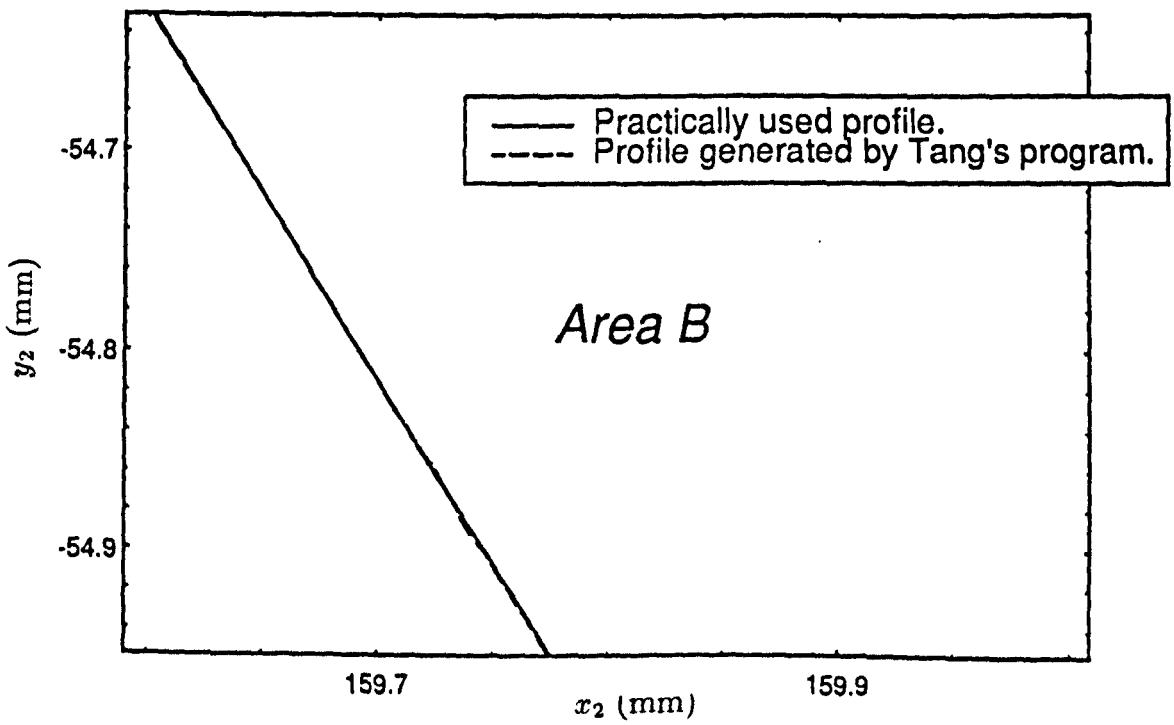

Fig. 2.6 (f) Area B of the female rotor

Fig. 2.6 Comparison with the practical A-profile

Fig. 2.7 shows the comparison of a practical D-profile (standard) and the profile generated by the author's profile generation program. The agreement is excellent, and the difference is also due to the insufficient number of points used

to describe the practical profile. The comparison for coordinate values of the key points on a standard D-profile is also presented in Appendix D. The coordinates generated by the author's program are identical with the practical coordinates.

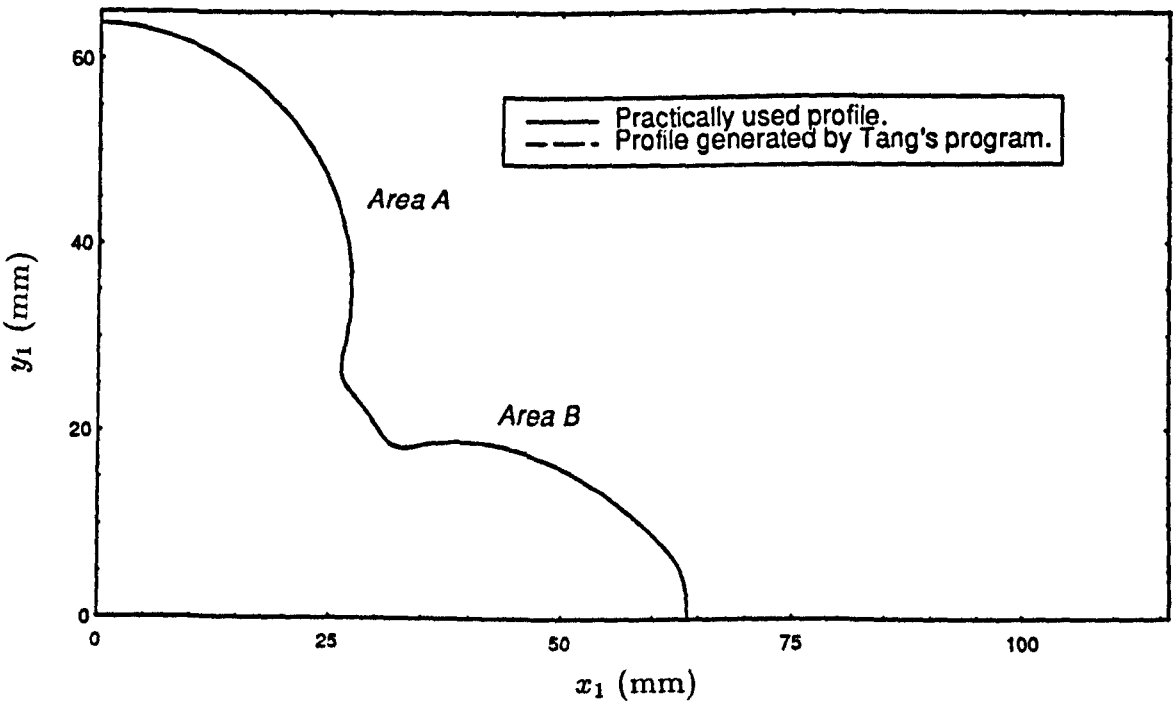

Fig. 2.7 (a) The male rotor profile

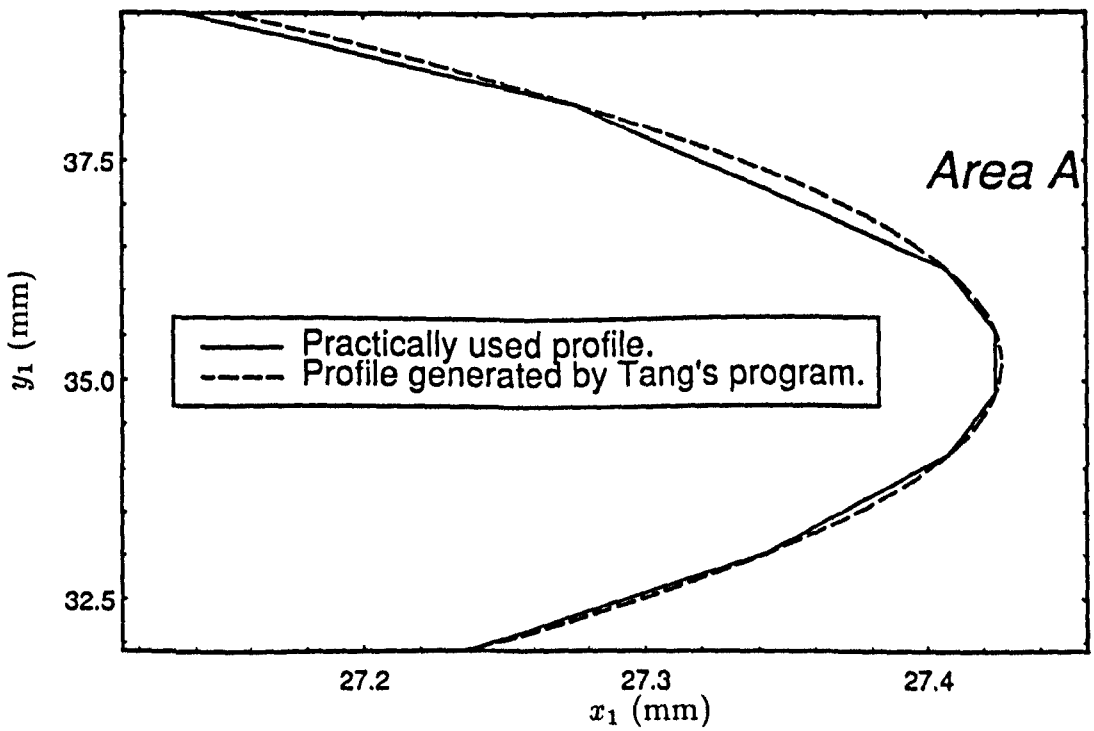

Fig. 2.7 (b) Area A of the male rotor profile

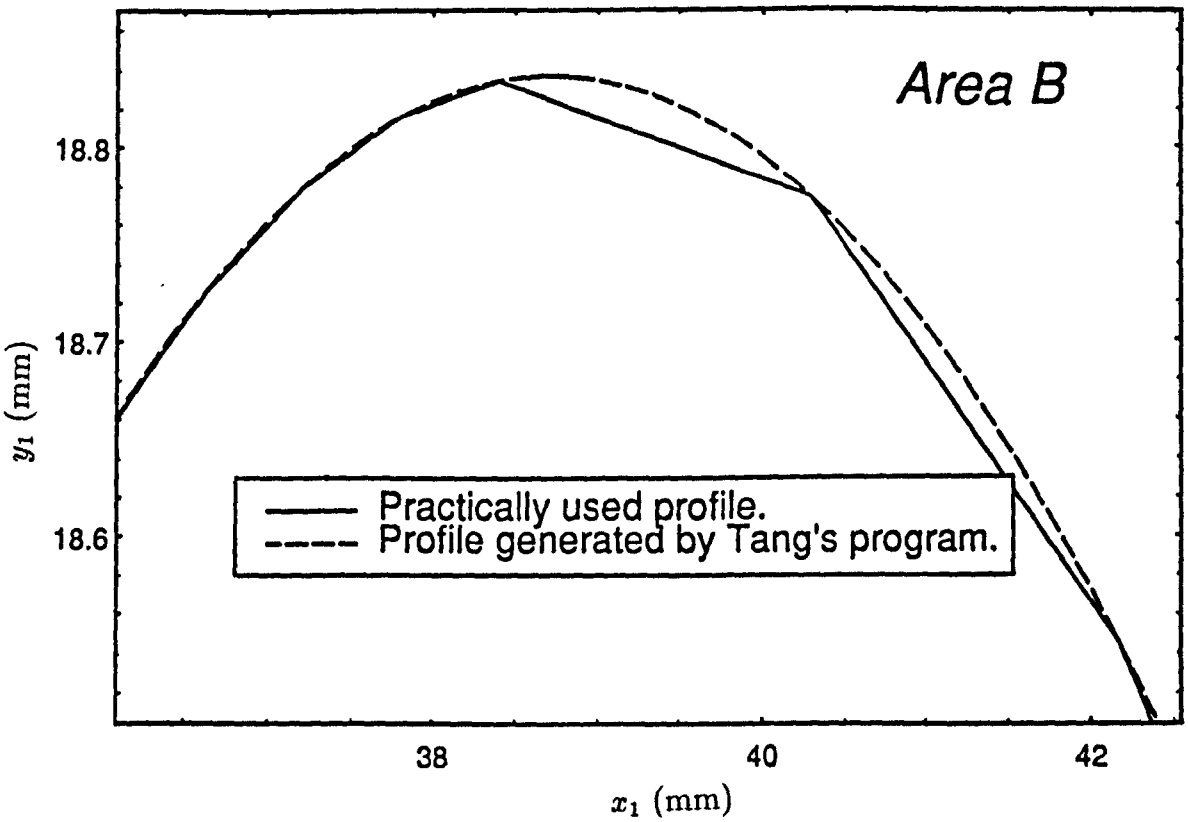

Fig. 2.7 (c) Area B of the male rotor profile

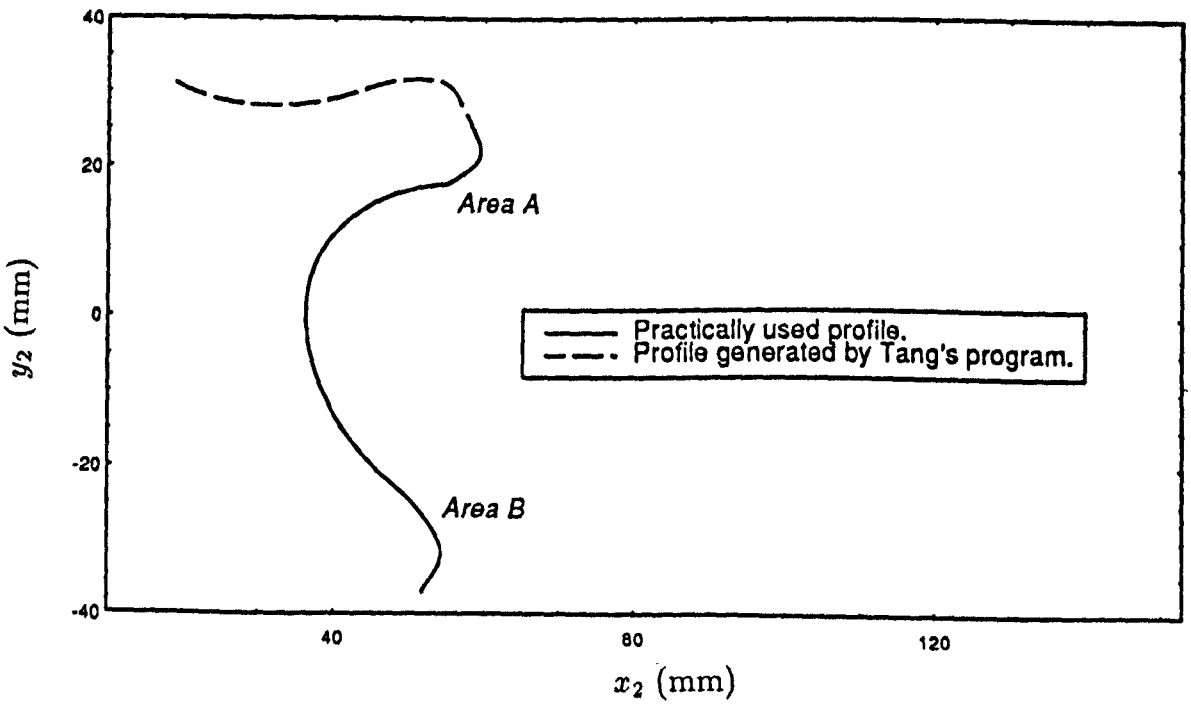

Fig. 2.7 (d) The female rotor profile

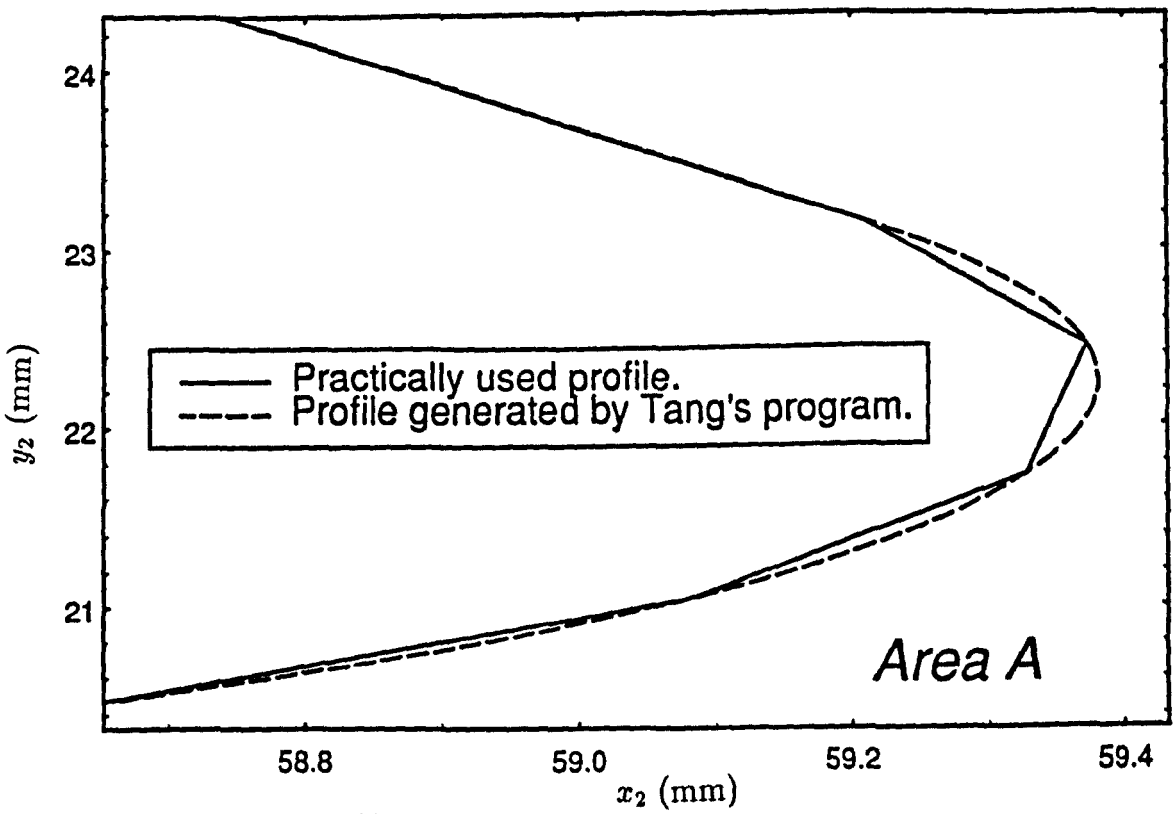

Fig. 2.7 (e) Area A of the female rotor

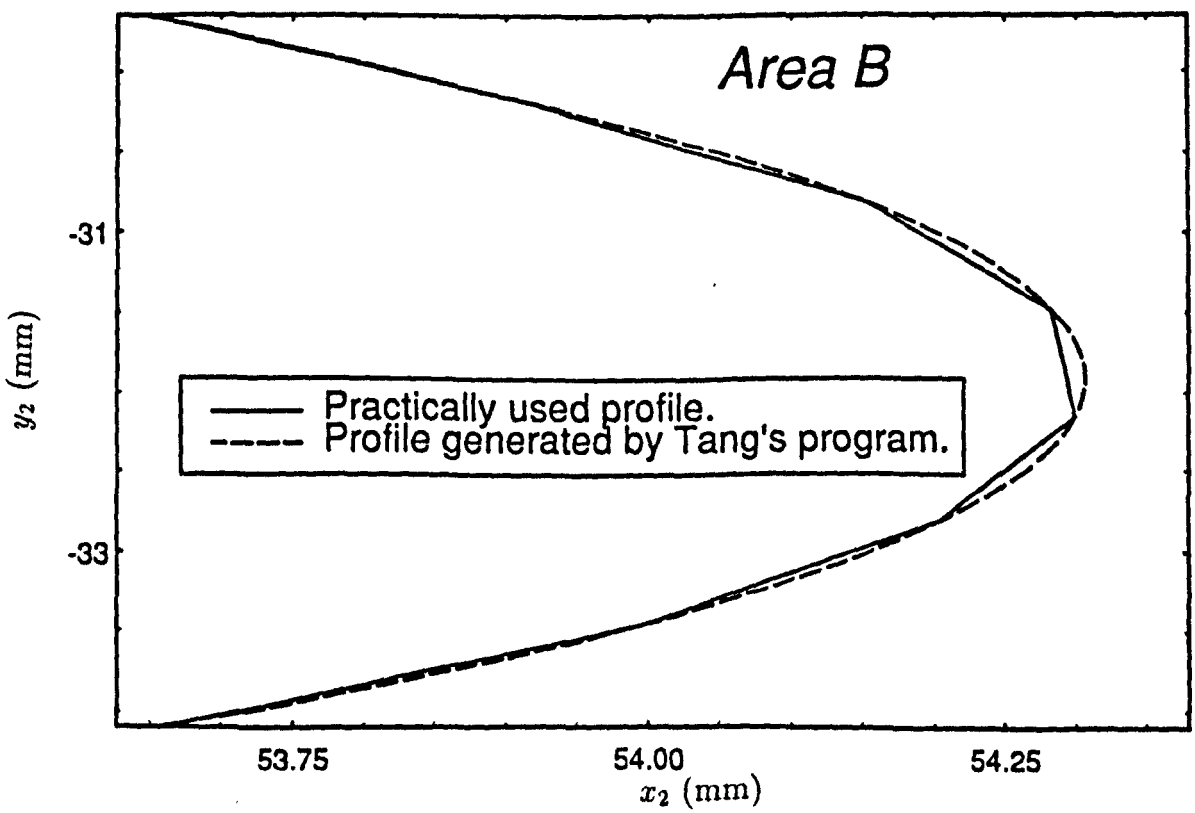

Fig. 2.7 (f) Area B of the female rotor

Fig. 2.7 Comparison with the practical D-profile

2.5 REFERENCES

1 **Singh, Pawan J.** and **Onuschak, Anthony D.** A Comprehensive, Computerized Method for Twin-Screw Rotor Profile Generation and Analysis. *Proceedings of International Compressor Engineering Conference at Purdue*, Purdue University, U.S.A., 1984.

2 **Howden Compressors Ltd., Glasgow, UK** Measured Data Books.

3 **Tang, Yan** and **Fleming, John S.** The SRM A-Profile and Symmetrical Circular Profile: there Basic Construction, Analysis and Generation. *Research Report 11*, April, 1994.

4 **Tang, Yan** and **Fleming, John S.** The SRM-D Profile: its Basic Construction, Analysis and Use in Twin Screw Compressor Design. *Research Report 7*, Nov., 1993.

5 **Buckingham, E.** Analytical Mechanics of Gears. *McGraw-Hill Book Company, Inc.*, 1949.

6 **Wu, Xu-Tang** Mating Theory of Gears (in Chinese). *Mechanical Industry Book Company*, Beijing, 1982.

7 **Nutbourne, A.W.** Differential Geometry Applied to Curve and Surface Design (Volume 1: Foundations). *Ellis Horwood Ltd.*, Chichester, 1988.

8 Сакун, И. А.: Винтовые компрессоры. МАШГИЗ, 1960.

9 Амосов, П. Е.: Винтовые Компрессорные машины (Справочник). МАШГИЗ. 1977.

10 UK Patent GB 1 197 432.

11 **Rinder, L.** Schraubenverdichter. *Springer*, Vienna, Austria, 1974.

12 UK Patent GB 2 092 676 B.

Chapter 3

COMPUTER AIDED ANALYSIS OF THE GEOMETRICAL CHARACTERISTICS OF A TWIN SCREW COMPRESSOR

In this chapter a *universal* program developed by the author is introduced. It is described as a universal program because the rotor end profile may be of any practical shape. Its function is to calculate all the geometrical relationships and characteristics of a helical screw compressor which are needed by a designer. The geometrical relationships include those which are needed in a thermodynamic model for simulating the working processes of the compressor, such as, the cross-sectional area bounded by the two rotors and the housing bores, the cavity volume, the axial and radial discharge port areas, the contact line length, the blow hole areas along the two cusps of the housing bores, the tip to bore sealing line lengths and the leakage path widths on the rotor end faces at suction and discharge, all of which are expressed in terms of the rotation angle of the male rotor. The geometrical parameters include those which are needed both in the thermodynamic model and for the geometric design of the compressor, such as, the overlap constant, the full thread cross-sectional area, the theoretical and real cavity volumes, the suction-stop angle and discharge port opening angles, and the suction and discharge pocket volumes, etc. The definitions of these geometrical relationships and parameters and the mathematical procedures for their calculations are presented.

3.1 INTRODUCTION

It is not easy to optimize the geometrical parameters of helical screw compressors manually. Fortunately, modern computers are so powerful that the cal-

culations for all the geometrical relationships and parameters for the design, performance prediction and cutter blade shapes can be completed in a few seconds, if correct calculation procedures are used and suitable software is developed.

A few researchers have published papers concerning the calculations of geometrical relationships and parameters, but none of them include *all* the geometrical relationships and parameters needed for design and performance prediction purposes. For example, the blow hole on the low pressure side has been neglected by all other workers but it can have an influence on the volumetric efficiency. Leakage through it can reduce volumetric efficiency by over one per cent (1).

The definitions of the geometrical relationships and the mathematical procedures for their calculation are presented in this chapter. In order to calculate the geometrical characteristics in numerical procedures, the end lobe profiles of the rotors of a helical screw compressor should be defined by a large number of separate points, in the region of 1500. The profile generation program can generate any lobe profile within the symmetrical circular, A- and D- definitions (see Chapter 2). The profile generation program calculates and outputs the results into different data files which are required by the geometrical characteristic calculation program presented in this chapter.

The geometrical characteristic calculation program developed by the author is a *universal* program, which means that it can be used to calculated the geometrical characteristics of a compressor having any profile and not just those mentioned in Chapter 2. When it is applied to the other profiles, the same data files as those generated by the author's profile generation program, should also be generated first to describe the chosen profile by a similar program.

The geometric features demonstrated in this chapter are those of a refrigeration compressor with SRM D-profile rotors and the following specification:

- Lobe profile—SRM D standard.
- Bore diameters (equal): $204mm$.
- Male rotor wrap angle: 300°.
- Length/diameter ratio: 1.65.

3.2 THE CROSS-SECTIONAL AREA AND THE CAVITY VOLUME

3.2.1 The Cross-Sectional Area

The cross-sectional area is the area bounded by the rotor end profiles and the housing bores, which varies with the rotational angle of the male rotor. At any rotational angle, the cross-sectional area can be calculated by a numerical method according to those separate points which define the profiles and the housing bores. In the geometrical characteristic calculation program developed by the author in the integration procedure a polynomial of degree three is used in the curve fit to calculate all the relevant areas. Fig. 3.1 shows the relationship between the cross-sectional area and the rotational angle of the male rotor. The maximum cross-sectional area is the sum of A_{01} and A_{02}, and these areas are shown in Fig. 4.4.

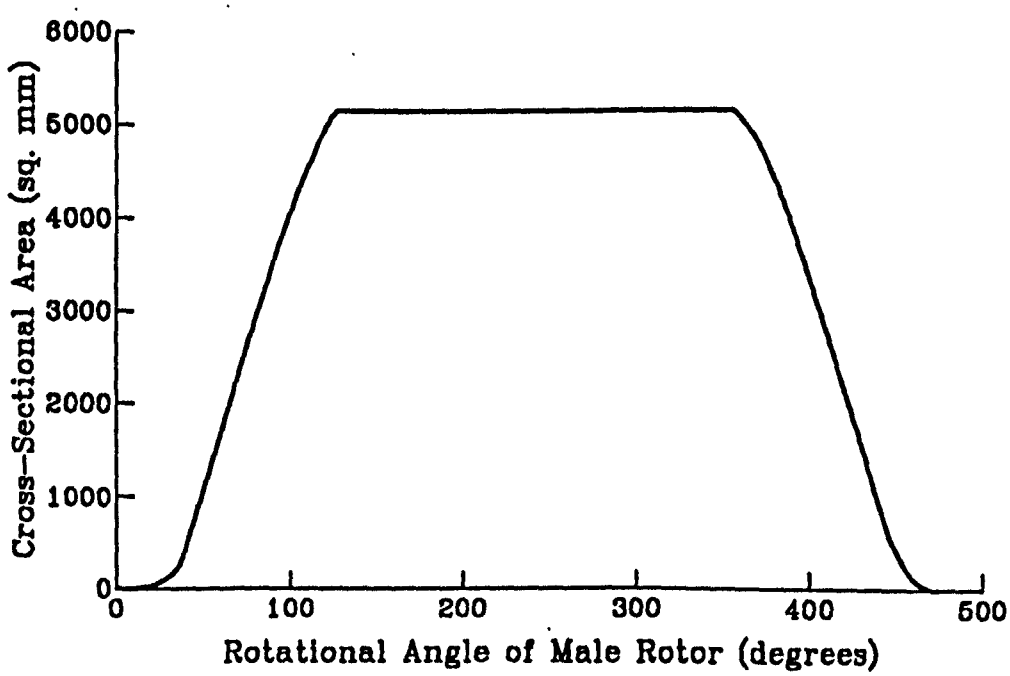

Fig. 3.1 Cross-sectional area vs rotational angle

In this chapter all the geometrical characteristics, which will be used in the working process simulation model, are expressed in terms of the rotational angle

of the male rotor. The start angle is the angle where the cavity volume equals zero.

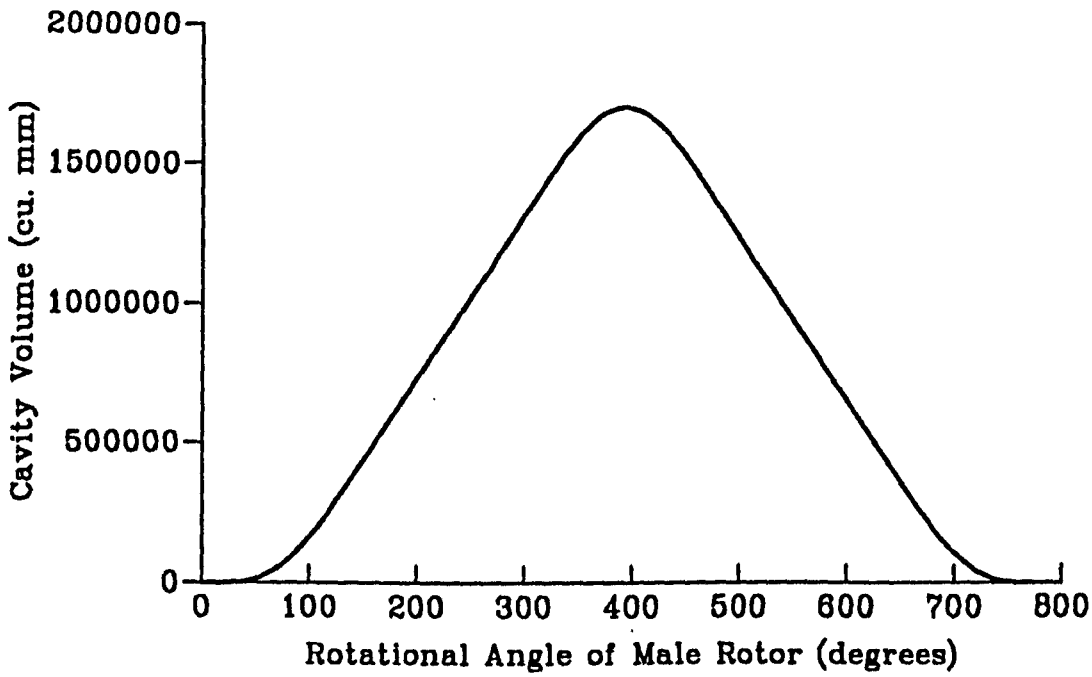

Fig. 3.2 Cavity volume vs rotational angle

3.2.2 The Cavity Volume and the Overlap Constant

The cavity volume is the volume surrounded by the helical surfaces of the male and female rotors, the housing bores and the end planes of the compressor. As the male rotor rotates the cavity volume changes from zero to its maximum and from its maximum to zero. This permits the compressor to execute its working processes. that is, suction, compression and discharge. The cavity volume is calculated by integrating the curve of the cross-sectional area. For the integration, the rotational angle should be transformed to rotor length along the rotor axis, and of course the integration limits should be less than or equal to the wrap angle of the male rotor. Fig. 3.2 shows the relationship between the cavity volume and the rotational angle of the male rotor. The real maximum cavity volume

is represented by V_r. The overlap constant of the compressor is defined and calculated by the following equation:

$$C_o = \frac{V_r}{(A_{01} + A_{02})L_r} \tag{1}$$

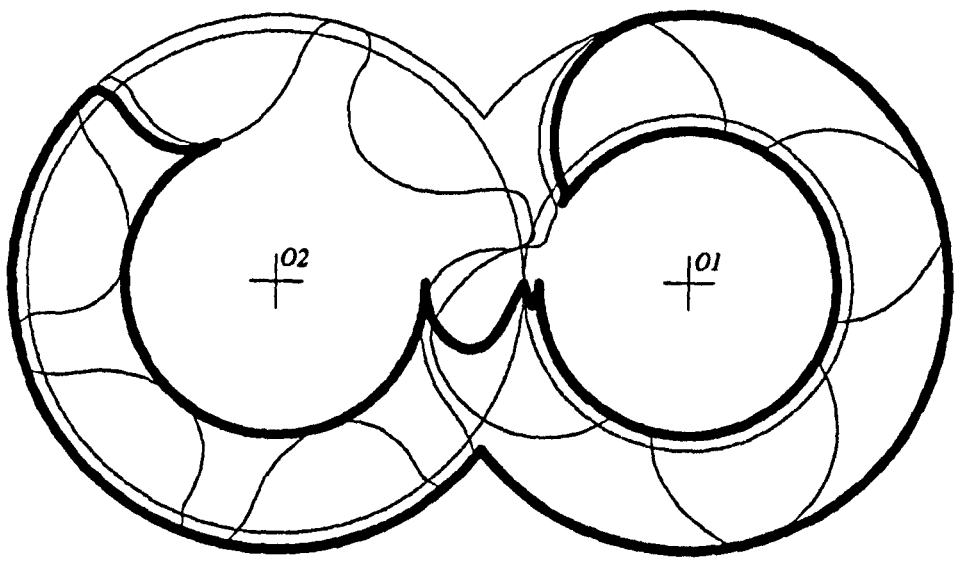

Fig. 3.3 Theoretical shape of a suction port (view from the suction end and generated by the author's program)

3.3 THE SUCTION AND DISCHARGE PORT AREAS

3.3.1 The Axial and Radial Suction Port Areas

Fig. 3.3 shows a theoretical shape of an axial suction port, which is determined theoretically by the meshing line on the end plane and the rotational angle of the male rotor at which the cavity volume becomes a maximum.

It is believed that in real compressor designs the suction stop position on the female rotor side is chosen in a range, but theoretically and strictly there

only exists one definite suction stop angle on the female rotor side, which can be calculated by the following equation:

$$\alpha_{2s} = \alpha_{1s}\frac{z_1}{z_2} + \frac{360^\circ}{z_2} \tag{2}$$

Any angle less than or more than the above given suction stop angle should result in reducing both the indicated efficiency and the volumetric efficiency slightly. Fig. 3.4 shows the relationship between the axial suction port area and the rotational angle of the male rotor.

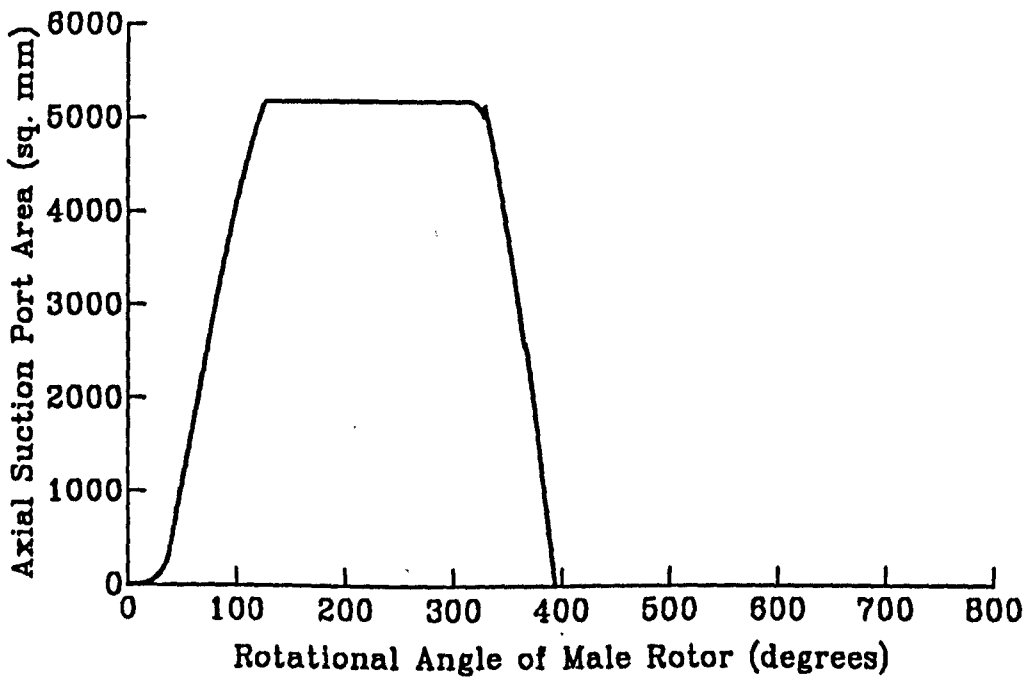

Fig. 3.4 Axial suction port area vs rotational angle

The nature of the geometry of the twin screw compressor dictates that the axial suction port area is much larger that the axial discharge port area. As consequence, suction resistance is low, and it can be reduced further by introducing a radial suction port. In oil flooded machines the introduction of a radial suction port can also reduce the area for viscous friction drag between the rotor tips and the housing bores. Fig. 3.5 shows the relationship between the available maximum radial suction port area and the rotational angle of the male rotor.

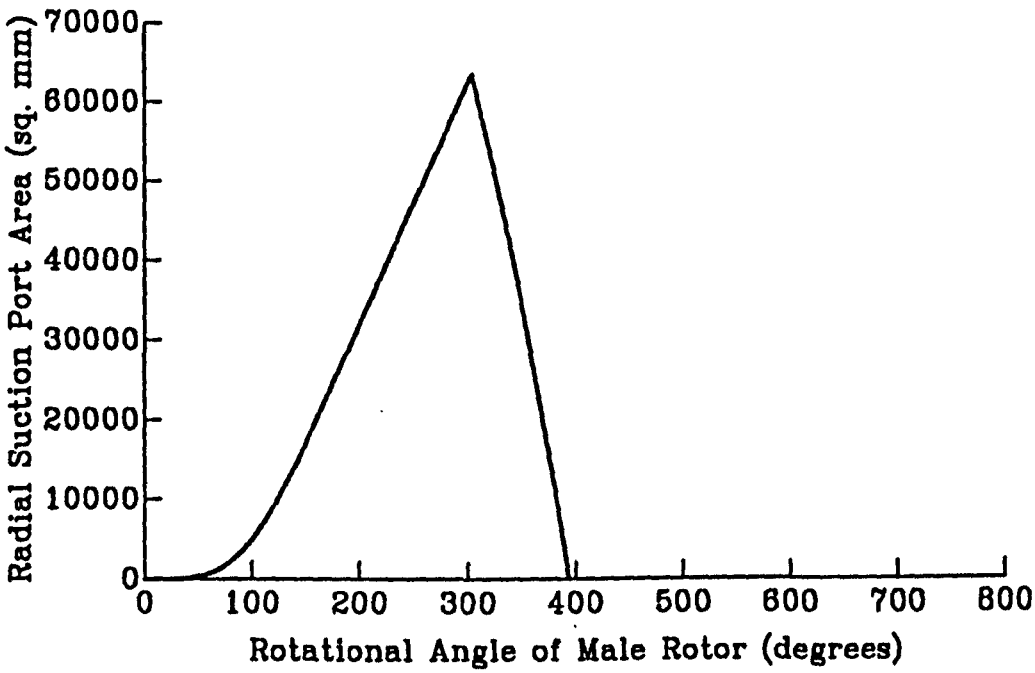

Fig. 3.5 Radial suction port area vs rotational angle

3.3.2 The Axial Discharge Port Area

Fig. 3.6 shows a theoretical shape of an axial discharge port, which is determined by the meshing line on the end plane and the designed volume ratio. Usually the volume ratio for the axial discharge port is larger than the volume ratio for the radial discharge port in refrigeration compressors due to the use of a slide valve applied to adjust capacity. Commonly it is equal in air compressors due to the absence of a slide valve. Fig. 3.7 shows the relationship between the axial discharge port area and the rotational angle of the male rotor.

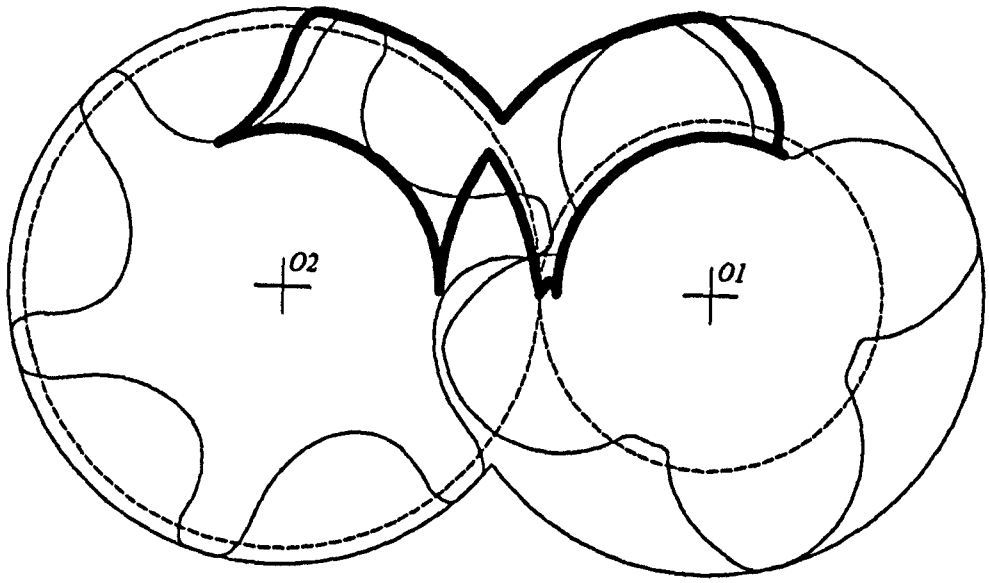

Fig. 3.6 Theoretical shape of an axial discharge port (view from the discharge end and generated by the author's program)

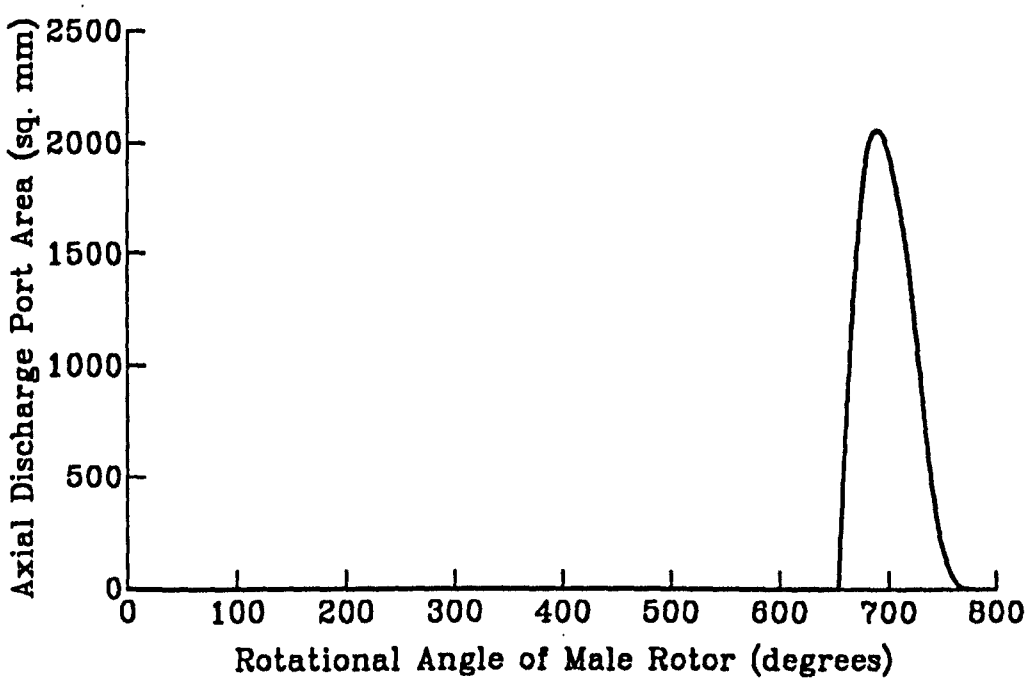

Fig. 3.7 Axial discharge port area vs rotational angle

3.3.3 The Radial Discharge Port and Slide-Valve by-Pass Port Area

A radial discharge port can reduce discharge flow resistance considerably. In refrigeration compressors the slide valves are applied to adjust capacity. The shape, and thus the area, of the radial discharge port varies with the position of the slide valve.

On the full-load condition, the slide-valve by-pass port is closed, and its area equals zero. On the partial-load condition, the by-pass port is part opened. Fig. 3.8 shows the relationships between areas of the radial discharge port and the slide-valve by-pass port and the rotational angle of the male rotor when the compressor is on partial-load condition (about 50 percent of capacity here).

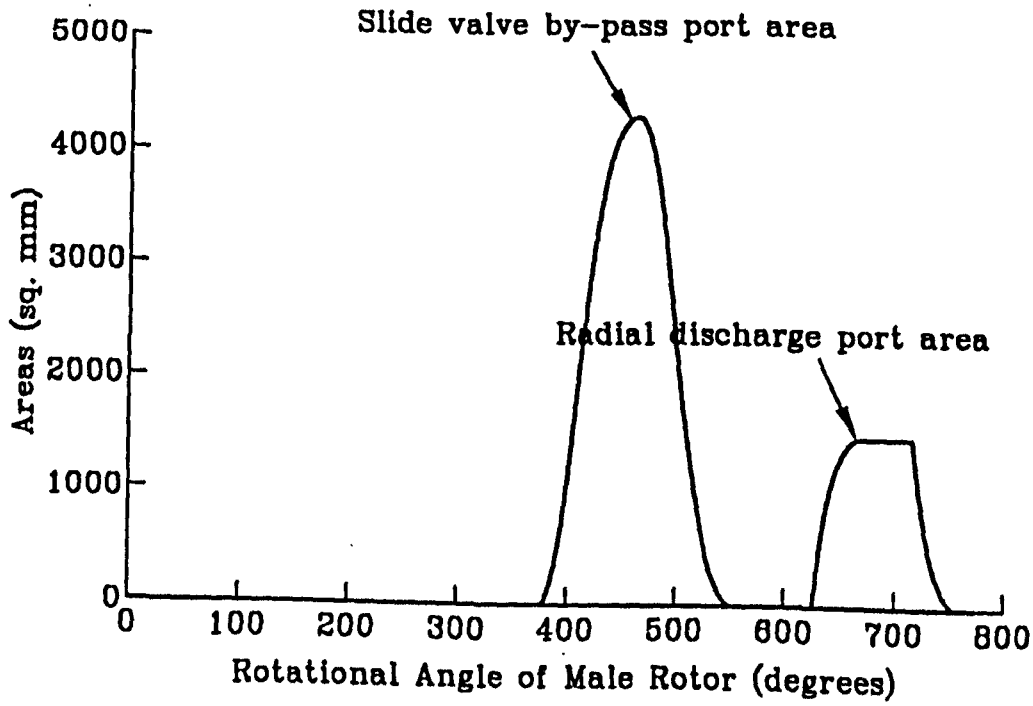

Fig. 3.8 Areas vs rotational angle

3.4 THE SEALING LINE LENGTHS OF A CAVITY VOLUME

3.4.1 The Contact Line Length between the Rotors

The leakage path across the contact line length between the male and female rotors is the most important leakage path. At any rotational angle, the leakage area can be obtained by multiplying the contact line length by the average clearance between the rotors. The contact line length varies with the rotational angle. Fig. 3.9 shows this relationship.

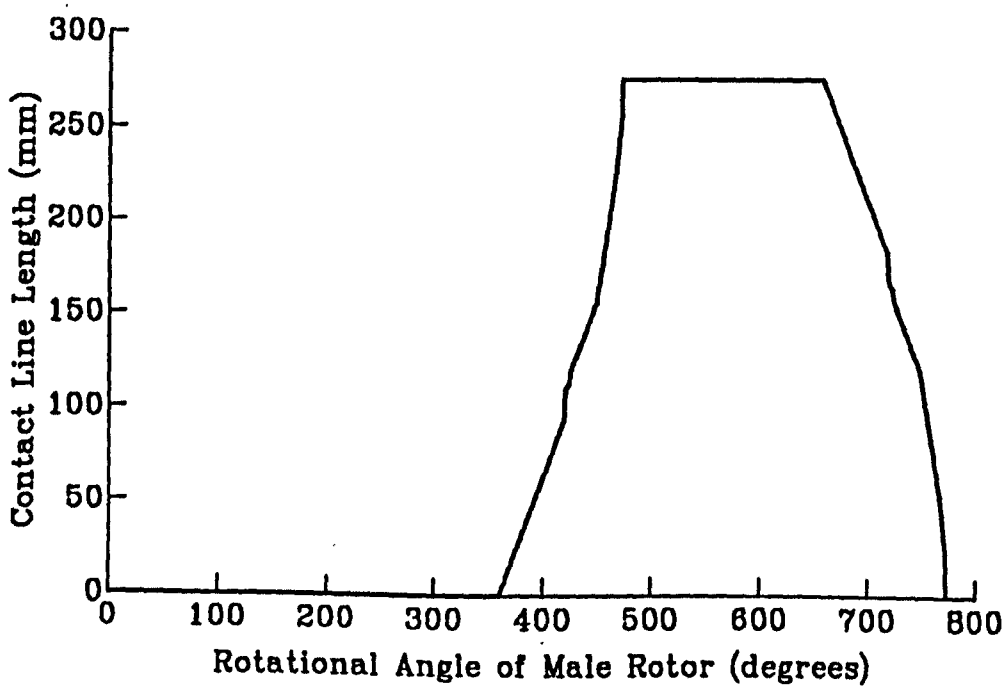

Fig. 3.9 Contact line length vs rotational angle

3.4.2 The Rotor Tip Sealing Line Lengths

The rotor tip sealing line lengths are the sealing line lengths between the rotor tips of the male or female rotors and the housing bore. They vary with the rotational angle of the male rotor. Fig. 3.10 shows this variation.

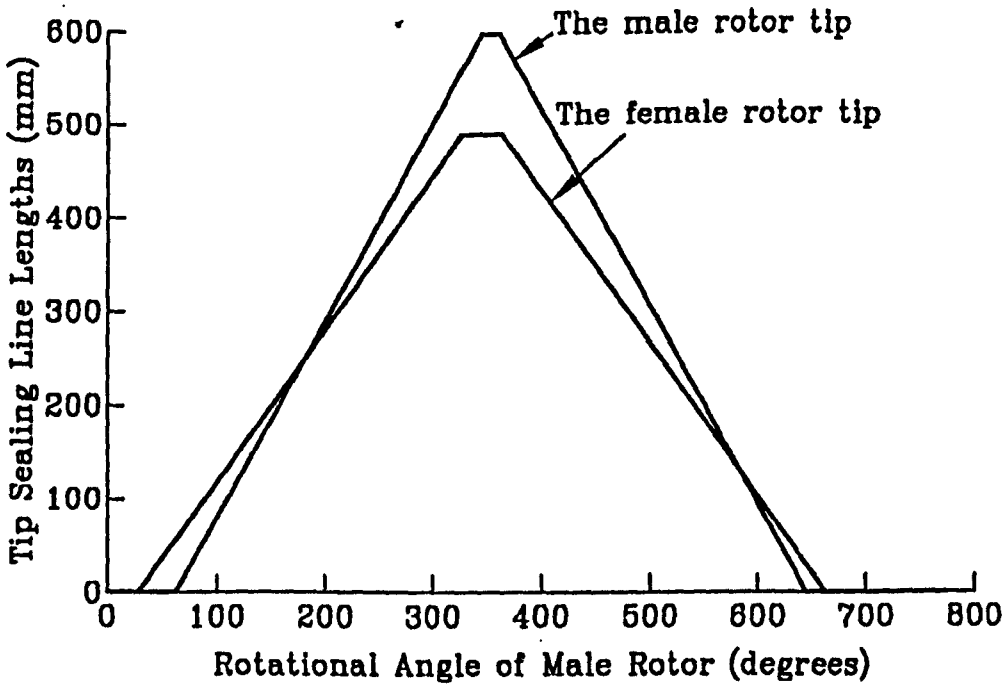

Fig. 3.10 Tip sealing line lengths vs rotational angle

3.4.3 The Rotor End Face Sealing Line Lengths

At the beginning of the compression process the compressed gas in the compression cavity can leak to suction pressure across the rotor end face at the suction end. A relationship between the rotor end face sealing line length at the suction end and the rotational angle of the male rotor is shown in Fig. 3.11 (curve 1).

At the discharge end the situation of leakage across the rotor end face is more complicated. The compressed gas leaks from the leading cavity volume to the following one, and the length of the sealing line between them is shown as curve 2 in Fig. 3.11. Gas also leaks from the discharge chamber to the enclosed cavity during the early stage of the compression process, and its sealing line length is shown as curve 3 in Fig. 3.11. Gas also leaks from the cavity volume in discharge process or from the discharge chamber to suction pressure directly, and its sealing line length is shown as curve 4 in Fig. 3.11.

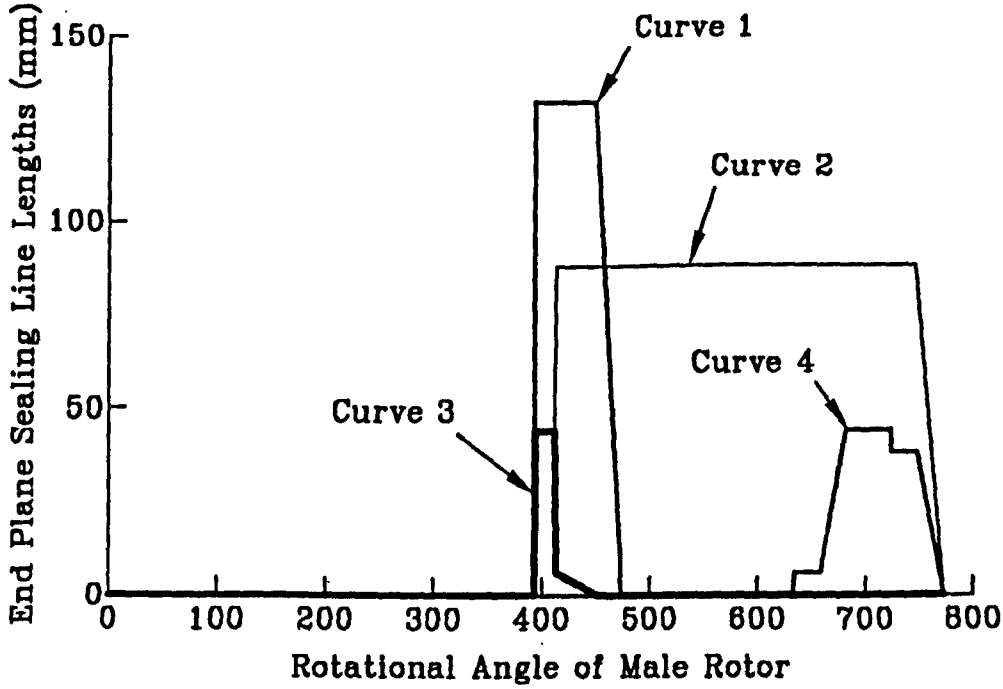

Fig. 3.11 End plane sealing line lengths vs rotational angle

3.5 THE BLOW HOLE AREAS

The blow hole, which is sometimes called the leakage triangle — as it has a shape like a distorted triangle — is formed between the tips of the male and female lobes and the cusp of the housing, and permits leakage between adjacent threads.

A helical screw compressor has two "sides", the "low pressure side" and the "high pressure side". Practically almost the whole length of the "low pressure cusp" is exposed to the suction pressure of the compressor, so that most of the threads meeting at that cusp are under the same pressure. Thus most of triangles formed on that side are not "leakage triangles". This is why on the low pressure side the designer is more free to give the profile a form that leads to a short sealing line. If the wrap angle of the male rotor is large enough, for example, 300°, part of the length of the "low pressure cusp" will be adjacent to a cavity beginning its compression, so that a leakage triangle is formed which can be called the blow

hole on the low pressure side or the compression start blow hole. It results in leakage of gas from the leading high pressure cavity to the suction pressure during the start period of the compression process. Although it exists during a small range of the rotational angle of the male rotor, it reduces the volumetric efficiency by about one percent for a wrap angle of 300° as its area is very large.

On the "high pressure side" only small part of the length of the "high pressure cusp" is exposed to the discharge pressure of the compressor. The blow hole on this side exists during the whole compression process, so that it has a great influence on both the volumetric and indicated efficiencies. As a consequence, an objective of the designer should be to reduce the size of the blow hole.

3.5.1 The Blow Hole Area on the High Pressure Side

The blow hole on the high pressure side is a small triangular-shaped area formed by the housing cusp on the high pressure side and the male and female rotor tips. Different definitions are used in the literature for the blow hole area. The definition of Singh and Onuschak (2) is used to calculate the "throat" blow hole area normal to the streamlines in the leakage flow which is constrained by the tip geometry to be along the helix of the female rotor. The blow hole area is computed by locating the three vertices of the "triangle"; two of which are where the male and female rotors "contact" the housing cusp and they are connected by a straight line (the cusp) while the third point is one of the nearby male-female contact points. These three points lie in a plane, which intersects the male and female rotor tips to obtain the two curved sides of a curvilinear triangle. The area of the curvilinear triangle is calculated by a numerical procedure. In the geometrical characteristics calculation program a numerical scheme automatically scans all the contact points in the cusp's vicinity, calculates the two curved sides and the areas, and then identifies the minimum area. This minimum area is projected to a plane normal to the female rotor tip helix, which has the same tangent as the (presumed) gas leakage streamline, to yield the final blow hole area. Fig. 3.12 shows the relationship between the blow hole area and the rotational angle of the male rotor.

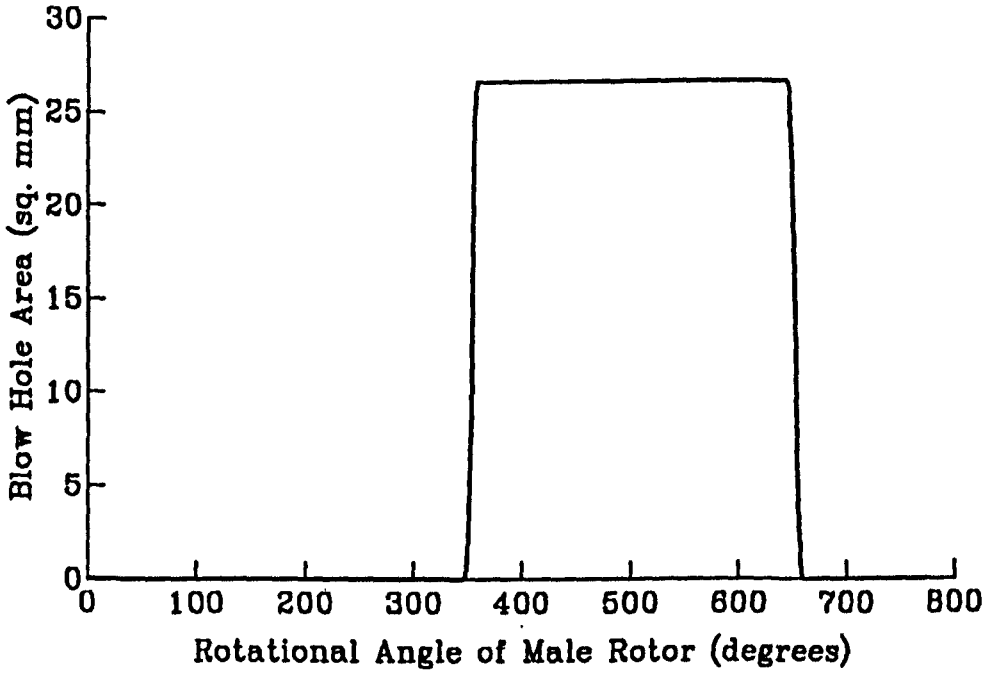

Fig. 3.12 Area of blow hole on high pressure side vs rotational angle

3.5.2 The Blow Hole Area on the Low Pressure Side (the Compression Start Blow Hole Area)

The blow hole on the low pressure side has the same definition as the blow hole on the high pressure side, and the same method is used to calculated its area. The introduction of the asymmetrical profile resulted in a larger blow hole on the low pressure side which differs from the blow hole on the high pressure side, and only exists during the early stage of the compression process. However, it has a noticeable influence on the performance of the compressor since its area is ten to twenty times as large as the area of the blow hole on the high pressure side, and the larger the wrap angle, the larger the influence. According to the leakage analysis (3) carried out by the author for an SRM-D standard profile and a wrap angle of 300° the blow hole on the low pressure side will reduce the volumetric efficiency by about one percent. Fig. 3.13 shows the relationship between the blow hole area on the low pressure side and the rotational angle of the male rotor.

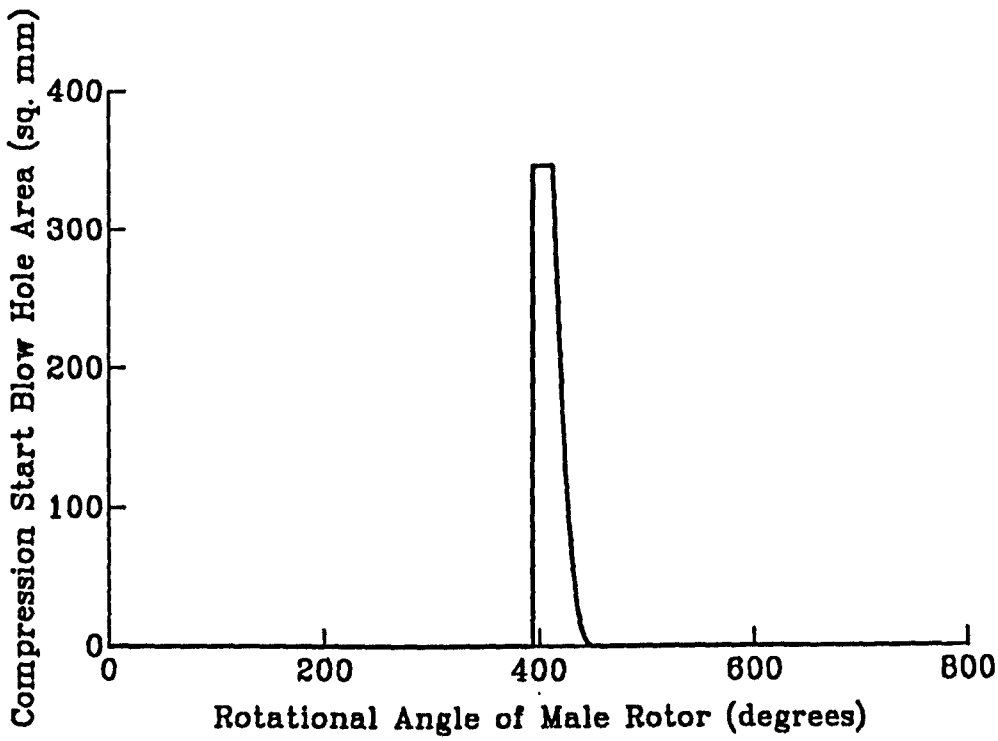

Fig. 3.13 Area of blow hole on low pressure side vs rotational angle

3.6 THE OIL INJECTION, LIQUID REFRIGERANT INJECTION AND SUPERFEED PORT AREAS

In modern refrigeration helical screw compressors, there are a few holes in the housing in addition to the suction and discharge ports. The oil is injected into the cavity volume from the oil injection port in the housing or from the small oil injection holes in the slide valve, depending on the compressor arrangement in use. The oil is also drained into the cavity volume from two or more ports which connect the cavity volume to the suction end casing or to the discharge end casing. Further, liquid refrigerant and gas from the superfeed are also, for some applications, injected into the cavity volume simultaneously. The geometrical characteristic calculation should also include the calculations of the areas of these injection ports in terms of the rotational angle of the male rotor. The port positions may vary from machine to machine in order to obtain an optimised performance. The geometrical characteristic calculation program is capable of

calculating the curves of all the port areas vs the male rotor rotational angle according to the compressor arrangement. Fig. 3.14 shows the relationships between the oil injection port area (curve 1), the liquid refrigerant injection port area (curve 2), the superfeed port area (curve 3) and the rotational angle of the male rotor.

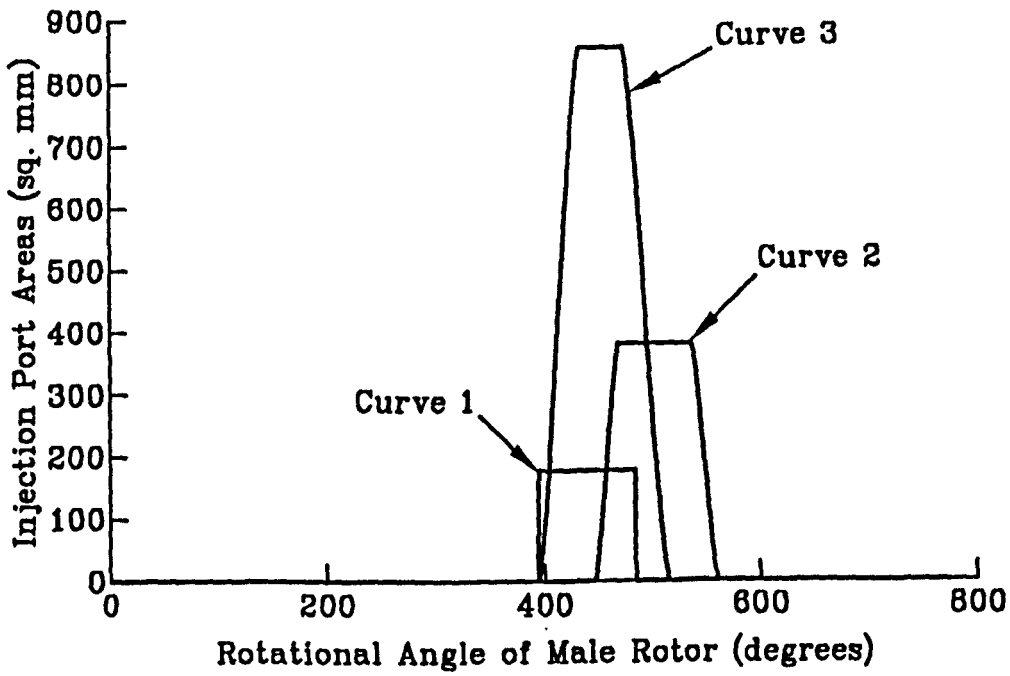

Fig. 3.14 The injection port areas vs rotational angle

3.7 THE GEOMETRICAL CHARACTERISTICS CALCULATION PROGRAM

The flow diagram of the geometrical characteristics calculation program is shown in Fig. 3.15. Before this program is run the profile generation program should be run first to obtain all the required data files. For any profile under the definitions of the symmetrical circular, the SRM A and D, the profile generation program (see Chapter 2) developed by the author can be used to generate those data files. For other profiles a similar computer program should be developed to generate the same required data files. The geometrical characteristic calculation

program is called a *universal* geometrical characteristics calculation program, because it can be used to calculate all the geometrical characteristics of a twin screw compressor fitted with rotors having *any* profile.

The geometrical calculation program reads the data files generated by the profile generation program. In addition, the following data are needed for the geometrical characteristics calculations and must be entered by the user in the places requested by the program:

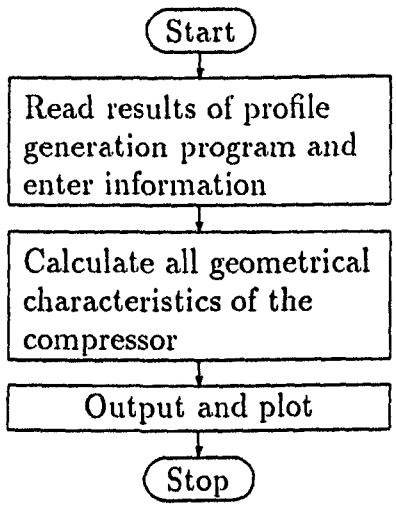

Fig. 3.15 The flow diagram of the geometrical calculation program

1. Choice of the compressor arrangement. There are six compressor arrangements which can be chosen by the user of the program, such as "dry machine with slide valve", "dry machine without slide valve, "wet machine with slide valve" and "wet machine without slide valve" etc. These machine arrangements cover all the applications of twin screw compressors, although in this thesis only the refrigeration compressors are involved.
2. The screw lead of the male rotor.
3. The wrap angle of the male rotor.
4. The diameters and position parameters of all the oil injected and oil drained ports.
5. The diameter and position parameters of the liquid refrigerant injection port. If liquid refrigerant injection into the compression cavity during the

compression process is used and the relationship between the liquid refrigerant port area and the rotational angle of the male rotor is required, these parameters should be entered.

6. The diameter and position parameters of the superfeed port. If the refrigeration system has a superfeed and the gas from it is injected into the compression cavity and the relationship between the superfeed port area and the rotational angle of the male rotor is required, these parameters should be entered.
7. The volume ratio for the axial discharge port, which is the ratio of the maximum cavity volume to the cavity volume at the moment at which the cavity begins to connect with the axial discharge port.
8. The volume ratio for the radial discharge port, which is the ratio of the maximum cavity volume to the cavity volume at the moment at which the cavity begins to connect with the radial discharge port.
9. The construction parameters of the slide valve. If a sliding valve is not fitted to the compressor, these parameters do not need to be entered.
10. The stop and position parameter of the slide valve. If a sliding valve is not fitted to the compressor, these parameters do not need to be entered.

The geometrical calculation program calculates all the required geometrical characteristics and parameters for both the working process simulation and design purposes (4). Many geometrical characteristics are expressed as a function of the male rotor rotation angle, especially those which will be used in the working process simulation program. The start angle is the angle where the cavity volume equals zero. The following geometrical characteristics in terms of the male rotor rotation angle can be calculated and output as data files:

1. The cross-sectional area bounded by the two rotors and the housing bores.
2. The cavity volume and built-in volume ratio.
3. The axial and radial suction port areas.
4. The axial and radial discharge port areas.
5. The slide-valve by-pass port area.

6. The contact line length between the rotors.
7. The blow hole and the compression start blow hole areas.
8. The male and female rotor tip sealing line lengths.
9. The rotor end face sealing line length at the suction end.
10. The rotor end face sealing line lengths at the discharge end between the leading and following cavities and between the discharge and suction pressures.
11. The oil injection, oil draining, liquid refrigerant injection and superfeed port areas.

In addition to the above geometrical relationships the program outputs all the geometrical parameters which a compressor designer or a compressor researcher needs, to a new data file (**5**).

A display program has been developed to show the calculated results of the geometrical calculation program or to make required hard copies. All the diagrams in this chapter can be shown on the monitor by the display program. Some hard copies made by the program can form the starting point for design of machines in practice.

3.8 REFERENCES

1 **Tang, Yan** and **Fleming, John S.** Obtaining the Optimum Geometrical Parameters of a Refrigeration Helical Screw Compressor. *Proceedings of International Compressor Engineering Conference at Purdue*, Purdue University, U.S.A., 1992, pp. 221-227.

2 **Singh, Pawan J.** and **Onuschak, Anthony D.** A Comprehensive, Computerized Method for Twin-Screw Rotor Profile Generation and Analysis. *Proceedings of International Compressor Engineering Conference at Purdue*. Purdue University, U.S.A., 1984.

3 **Fleming, John S. Tang, Yan Young, W.** and **Anderson, H.** Leakage Analysis of a Helical Screw Compressor. *Proceedings of I Mech E European Conference on Developments in Industrial Compressors and their Systems*, London, U.K., 1994, pp. 1–8.

4 **Tang, Yan** and **Fleming, Johs S.** Computer Aided Geometrical Analysis of the Geometrical Characteristics of a Helical Screw Compressor. *International Compressor Engineering Conference at Xi'an*, Xi'an Jiaotong University, Xi'an, China, 1993, pp.399–407.

5 **Tang, Yan** and **Fleming, John S.** Computer Aided Analysis of the Geometrical Characteristics of a Twin Screw Compressor. *Research Report 8*, Dec., 1993.

Chapter 4

SIMULATION OF THE WORKING PROCESS OF A MODERN REFRIGERATION TWIN SCREW COMPRESSOR

In this chapter a mathematical model for the working process of a refrigeration helical screw compressor is presented and discussed. The manner in which geometric parameters such as cavity volume, sealing line length, blow hole area, discharge port area etc. are related to rotation angle is established and used in the thermodynamic model which is based on real gas laws for the working fluid. The influence of factors such as oil injection, liquid refrigerant injection, vapour charge from the economizer, different pure fluid refrigerants and partial loading etc., can be considered simultaneously or separately in the model. The structure of the computer program is described. All the subroutines used to calculate the required thermodynamic properties of the refrigerants considered are also described in this chapter. In order to validate the computer model its predictions must be compared with results derived from compressor tests. In this chapter the predictions for R22 are compared with measured values and the agreement is good.

4.1 INTRODUCTION

An accurate computerized mathematical model capable of simulating the working process of a helical screw compressor is a very useful tool. Such a model can be used for the following purposes:

1. *To optimise the design of a compressor*

   Many geometrical parameters of a twin screw compressor have a strong

influence on the efficiency of the compressor. When a new machine is designed, its many geometrical parameters, such as the rotor profile parameters, the rotor parameters and the discharge port position etc. should be optimised so that the machine obtains the highest total efficiency for the required operating conditions. The working process simulation program is the most important program for carrying out this optimisation process.

2. *Saving test time and costs*

   When a new machine is produced, physical tests on a prototype require both time and money. This is especially true of a refrigeration compressor which must be connected to a refrigeration plant which by its nature has a long settling time. The working process simulation program can not, on its own, be used to replace the physical prototype tests entirely since important coefficients in the mathematical model are determined by some test results, but it can be used to *reduce* greatly the number of physical tests, so saving time and money.

3. *Choosing a machine suitable for a certain operating condition*

   When a compressor is requested for a particular running condition and it is felt that a completely new design is not justified, then the working process simulation program can be used to determine which of the existing designs would be most suitable.

4. *Other applications*

   The working process simulation program can be used for other purposes. For example, it can be used to pursue the following research interests: leakage analysis, the optimum clearance pattern between the male and female rotors, choosing the most economic cutter blade shape, analysing the thermal- and dynamic-distortion of the rotors, the determination of gas torque and bearing forces, investigation of the performance of compressors using pure or binary or ternary substitutes for the ozone depleting refrigerants, etc.

Modern refrigeration helical screw compressors are required to work under a wide range of operating conditions whilst maintaining a high energy efficiency.

To achieve this a number of modifications to the basic compressor have been introduced, such as the injection of oil and liquid and gaseous refrigerant into the compression cavities, and the use of different refrigerants and partial loading etc. In order to make the working process simulation program capable of handling any operating condition to which a modern refrigeration helical screw compressor may be applied, the quantitative influence of all these factors must be considered simultaneously and separately in the model. The model requires the calculation of the thermodynamic properties of refrigerants, which must be based on real gas laws if realistic predictions are to result. Unlike a reciprocating compressor, where piston rings effectively seal a working chamber, a helical screw compressor has many leakage paths which should be considered carefully in the working process simulation program.

In this chapter a mathematical model for the working process of a refrigeration helical screw compressor is presented and discussed. The friction loses in the compressor are considered in the model, and the influence of factors such as oil draining from the bearings, oil injected into the cavity, liquid refrigerant injection, liquid refrigerant flashed from the injected or drained oil, vapour charge from the economizer, different refrigerants and partial loading etc., are also considered simultaneously or separately in the model. The computer programs are described in the chapter. All the leakage paths are considered in the program. All the subroutines used to calculate all the required thermodynamic properties of the refrigerants considered are described in the chapter. The property equations used in the program for the refrigerants considered are presented in Appendix E. In order to validate the computer model the performance predicted by it is compared with the results from compressor tests run on R22. The results are compared for compressors of different sizes and for different operating conditions.

4.2 CHARACTERISTICS OF A MODERN REFRIGERATION HELICAL SCREW COMPRESSOR

The helical screw compressors, which are applied in process refrigeration systems, usually operate over a range of conditions. They have the following common

characteristics:

1. A quantity of oil much greater than the minimum quantity needed for proper lubrication is supplied to the compression chamber. This additional oil seals the clearances between the rotors and compression cavity walls, affects the discharge temperature, and permits the simple mechanical arrangement of one rotor driving the other. With oil injection, screw compressors can work at higher compression ratios. This has permitted their application to process refrigeration. The oil can come into the working cavity by the following three routines:
   (a) The oil is injected into the cavity directly through the oil injection port in the housing or through the oil injection holes in the slide valve.
   (b) The oil is injected into the suction end casing, lubricates the shaft seal and bearings first, and then is drained into the cavity through a port provided for the purpose.
   (c) The oil is injected into the discharge end casing, lubricates the balance piston and the radial and thrust bearings first, and then is drained into the cavity through another port.

   The oil before the oil injection port has almost the same pressure as the discharge, but the oil drained from suction end casing has only a pressure a little higher than the suction. The oil drained from the discharge end casing can have a low or high pressure, depending on the design of the compressor.
2. Many refrigerants unfortunately dissolve in the oil, which results in the dilution of the oil, and when the oil is injected into the compression cavity, part of the dissolved refrigerant will flash as the oil pressure drops suddenly on entering the cavity. The dissolved refrigerant also flashes in the suction end casing and the discharge end casing, so that the drained oil actually is a mixture of the oil and the flashed vapour.
3. Liquid refrigerant is injected directly into the oil/refrigerant stream flowing through the compressor. As the liquid refrigerant enters the compression cavity its pressure drops suddenly and it is heated by the compressing gas/oil mixture. As a result it evaporates and cools both the oil and the

vapour being compressed, thus eliminating the need for separate oil cooling. The vapour discharge temperature is reduced as are the temperatures of the rotors and the compressor housing, which makes possible very small clearances between the male and female rotors and between the rotors and the housing and between the rotors and the end plates, which increases the performance of the compressor. Liquid refrigerant injection is not used in place of oil injection, but in conjunction with it.

4. The vapour generated in superfeed (economizer), normally called flash, is injected into the compression cavity through a port in the compressor casing, the site of which is chosen to ensure that injection takes place at an early stage in the compression process. The purpose of the application of superfeed is to obtain a higher COP of the refrigeration system. The superfeed circuits are similar in design to the economizers often used in multi-stage compression systems to cool the liquid refrigerant from the condenser prior to its being supplied to the evaporators.

5. Capacity control is needed to enable the helical screw compressor to meet the wide range of load demands which are a feature of modern refrigeration plants. The most common method makes use of a slide valve which allows a measured quantity of the compressed cavity volume to "blow out" back to suction.

6. Many fluids are used as working fluids, i.e refrigerants, in modern refrigeration plants. The compressors must handle these refrigerants. The refrigerants often used in process refrigeration systems, such as R12, R22, R717, and R134a etc., cannot be considered as perfect gases. The real gas equations must be used to calculate their properties for use in the mathematical model. Due to the increasing concern about the direct global warming impact of the HCFC substitutes for the ozone depleting refrigerants, more and more new refrigerants will come into use, which means that the helical screw compressor will be required to handle more and more refrigerants. So far the binary and ternary refrigerants are not widely used, but the signs are that they will increasingly replace the established refrigerants with the re-

sult that the helical screw compressor will be used to compress an increasing variety of mixtures.

Simulating the working process of a refrigeration helical screw compressor involves all the above important considerations. If *all* the characteristics of the modern helical screw compressors can be handled by the mathematical model of the working process and its corresponding computer program, the working process simulation program will be powerful and very useful for the purposes mentioned in section 4.1.

4.3 LEAKAGE PATHS IN A TWIN SCREW COMPRESSOR

The working cavity of a helical screw compressor is bounded by the housing bores, housing end faces and the helical surfaces of the male and female rotors. The relative sliding movement between the two rotors and between the rotors and the housing casing, and the unavoidable imperfections in the design of a lobe profile result in many leakage paths through which the working fluid leaks in or out of a working cavity.

Considering a given cavity volume the following are the leakage paths through which the working fluid leaks in or out (Fig. 4.1):

Path 1: *The contact line between the male and female rotors*

The working fluid leaks to suction pressure from the considered cavity across the contact line between the male and female rotors. At any rotational angle, the leakage area can be obtained by the contact line length times the average clearance between the rotors. The contact line length is calculated by the geometrical calculation program (see Chapter 3), and the average clearance between the rotor can be calculated by the cutter blade calculation program (see Chapter 5). If the wrap angle of the male rotor is large enough the fluid may leak to the considered cavity from a high pressure cavity at the beginning of the compression process or it may leak to a low pressure cavity from the considered cavity at the end of compression process or discharge process due to the overlap of rotor threads.

Path 2: *The sealing lines between the rotor tips and the housing bores*

The working fluid leaks to the following cavity or suction pressure from the considered cavity across the following sealing lines between the rotor tips of the male or female rotors and the housing bores. It also leaks to the considered cavity from the leading cavity or discharge pressure across the leading tip-to-bore sealing lines. At any rotational angle, the leakage areas can be obtained by the tip sealing line lengths times the tip-to-bore clearances. The calculation of the tip sealing line lengths is described in Chapter 3. It should be noted that the clearances between the housing bores and the rotor tips are usually different for the male and female rotors.

Path 3: *The cusp blow hole*

The working fluid leaks to the following cavity or suction pressure through the following cusp blow hole. It also leaks to the considered cavity from the leading cavity or discharge pressure through the leading cusp blow hole. The definition and the calculation have been presented in the previous chapter.

Path 4: *The compression start blow hole*

The working fluid leaks to suction pressure through the compression start blow hole, which is a blow hole along the housing cusp on the low pressure side. Its definition and the calculation have been presented in the last chapter.

Path 5: *The clearance between the end plate and the rotor end face at the suction end*

The working fluid leaks to suction pressure across the rotor end face at the suction end during the early stage of the compression process. The suction end clearance, which includes the allowance of the axial thermal expansion of the rotors, is the biggest clearance in a compressor. The pressure ratio or difference across this leakage path is small, but the leakage rate through it and the reduction to the volumetric efficiency of the compressor is not negligible like the situation for a compression start blow hole. The width of the leakage path is also calculated by the geometrical characteristic calculation program presented in the previous chapter.

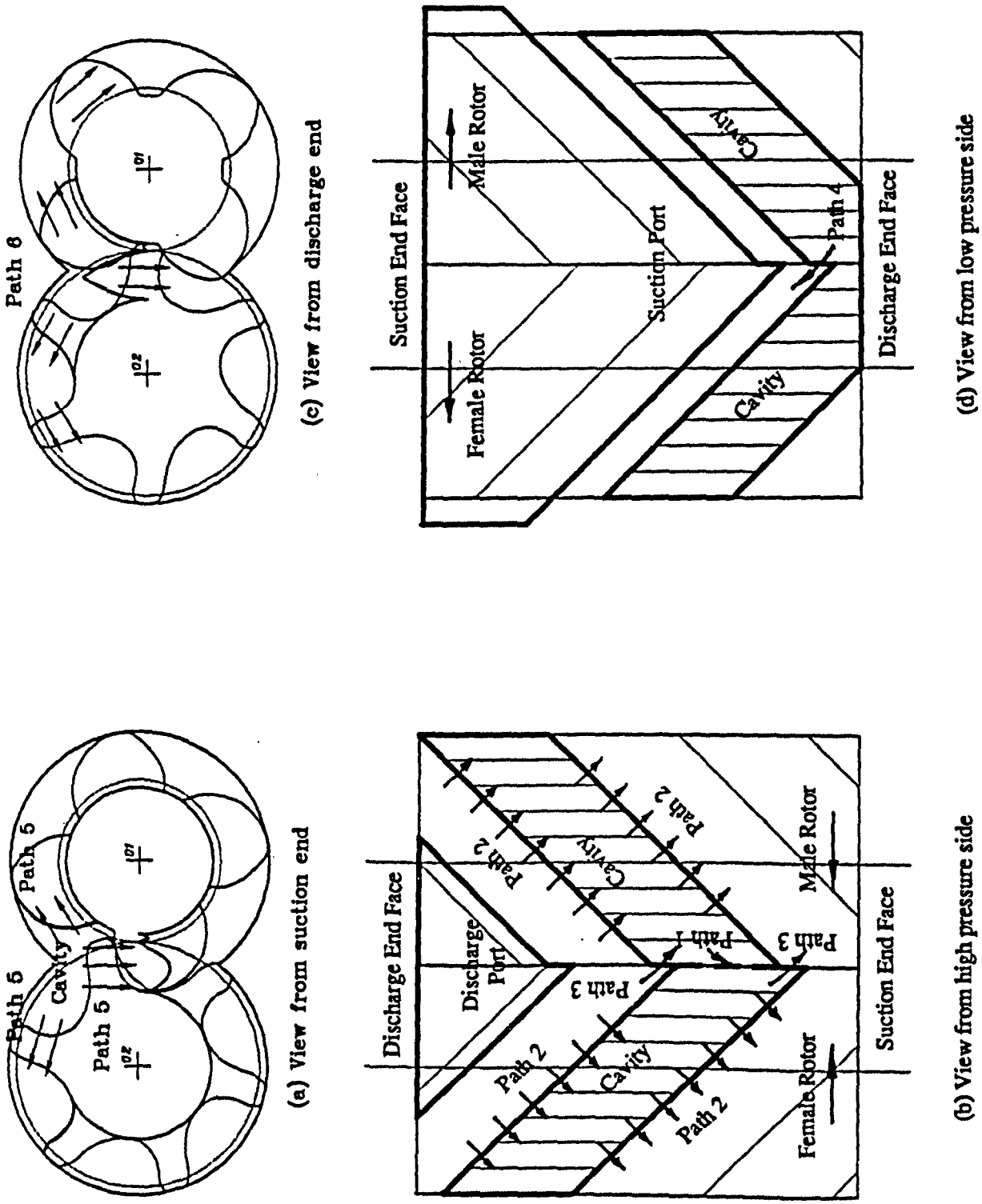

Fig. 4.1 Leakage paths of a cavity in a twin screw compressor

Path 6: *The clearance between the end plate and the rotor end face at the discharge end*

At the discharge end the situation of leakage across the rotor end face is more complicated. Strictly speaking, there are the following three leakage paths across the discharge end faces of the rotors:

1. The working fluid leaks to the following cavity from the considered cavity, or leaks into the considered cavity from the leading cavity or discharge plenum.
2. During the late stages of the compression process or during the discharge process the working fluid can leak to suction pressure directly across the discharge end faces between the two rotor axes.
3. During early stage of the compression process the working fluid can leak into the enclosed cavity across the discharge end faces between the two rotor axes.

The widths of the above three leakage paths are also calculated by the geometrical characteristic calculation program. They have the same clearance, ie the discharge end clearance, so that in this thesis they are grouped into one leakage path — Path 6, the leakage path across the discharge end.

In common arrangements 2–3 enclosed cavities between the suction and discharge ports exist, which are simultaneously in compression. Not all the leakage paths exist for the whole period of the compression and discharge processes. Further, for the duration of their existence the leakage areas of most paths vary in a complex manner with male rotor angle. In the author's working process simulation program, all the leakage paths have been taken into account. A schematic diagram of leakage paths is shown in Fig. 4.2.

4.4 MATHEMATICAL MODEL

The mathematical model should consider all the characteristics of modern refrigeration helical screw compressors mentioned in Section 4.2, and all the leakage paths described in the last section. This section presents the mathematical model used to simulate the working processes of a refrigeration twin screw compressor.

Path 1: contact line between rotors.
Path 2: rotor tip sealing lines.
Path 3: cusp blow hole.
Path 4: compression start blow hole.
Path 5: rotor suction end.
Path 6: rotor discharge end.

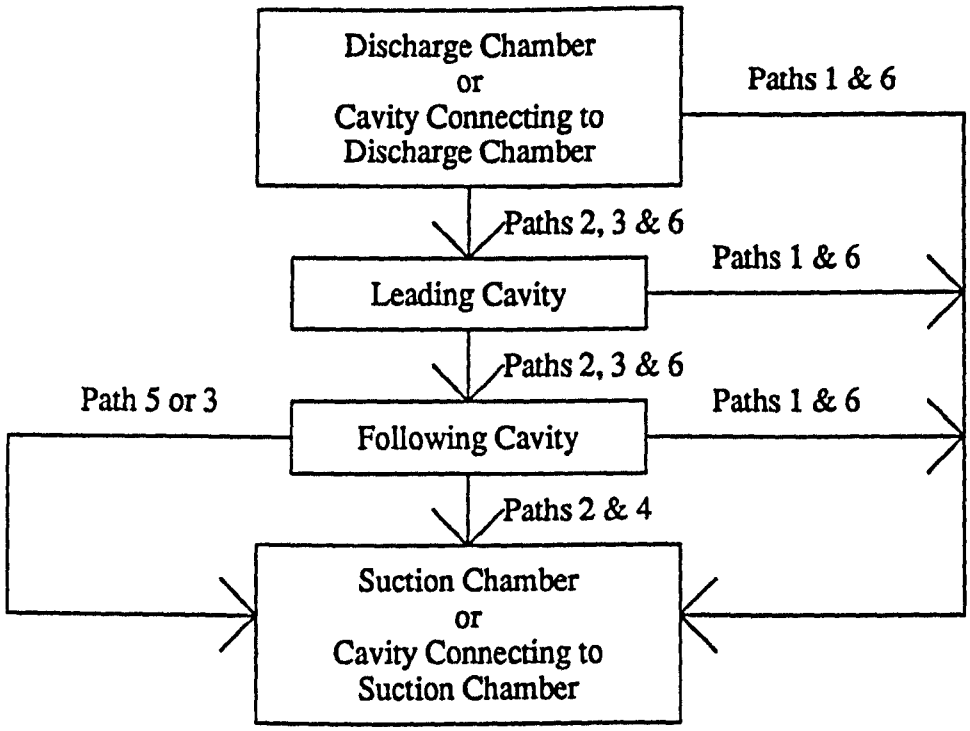

Fig. 4.2 The schematic diagram of leakage paths

The basic assumptions for the mathematical model are as follows:

1. The vapour flow through the suction port, discharge port, superfeed port, slide valve by-pass port and every leakage path is treated as being isentropic (modified as indicated in some cases by coefficients), and in the vapour flow through the suction and slide valve by-pass ports compressibility effects are taken as being negligible since flow velocities are well below the sonic velocity.
2. The pressures in the suction and discharge chambers and before the superfeed port, liquid refrigerant port and oil injection port are constant.

3. Refrigerant gas, oil and liquid refrigerant are assumed to be separate fluids, and gas leakage through any leakage path does not result in significant mass changes of oil or liquid refrigerant in the control volume.

4.4.1 The Basic Equations for the Control Volume

The control volume of a screw compressor is its cavity volume. A simplified control volume is shown in Fig. 4.3, in which an analogy is drawn with a reciprocating compressor, also a positive displacement machine but simpler to represent.

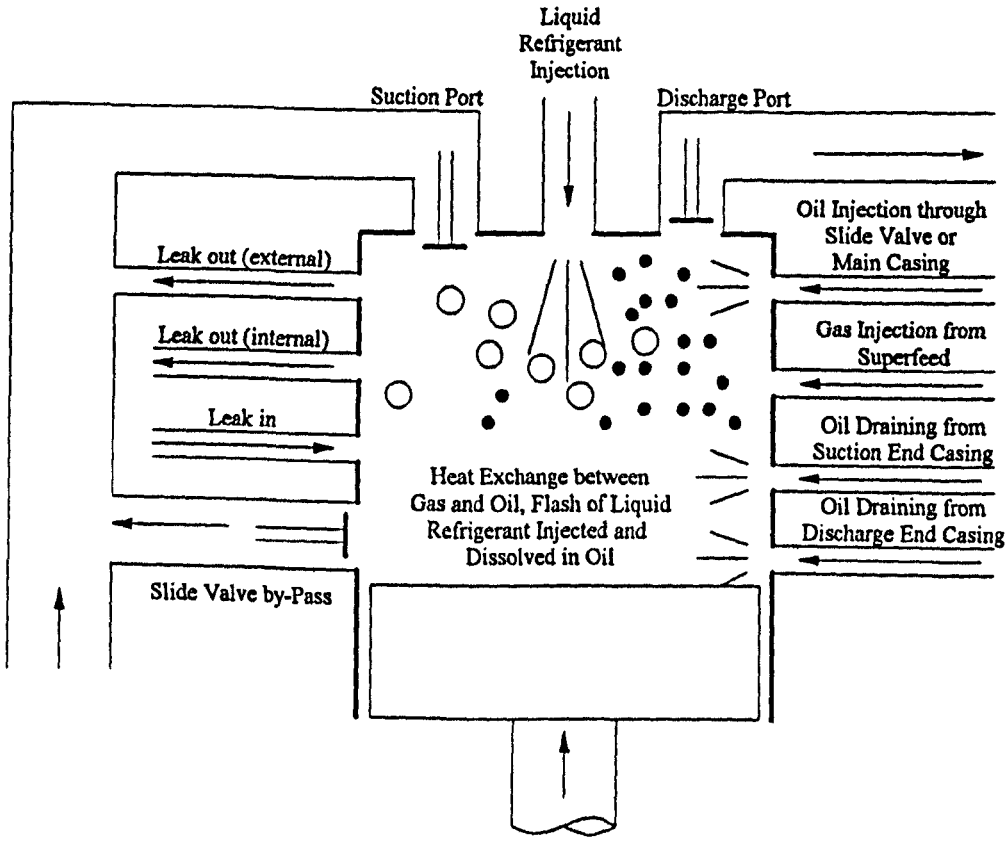

Fig. 4.3 A simplified control volume of a screw compressor

For the control volume of a screw compressor the conservation equation for gas internal energy in terms of the rotation angle of the male rotor can be written. Different working processes have different items in the conservation equation for internal energy. which is presented as follows (here i = integer):

Suction process

$$\frac{dU_{gas}}{d\varphi_1} = \frac{dH_{inlet-gas}}{d\varphi_1} + \sum_{i=1}^{6} \frac{dH_{leak-in-gas}}{d\varphi_1}\Big|_i + \frac{dH_{oil:flash-gas}}{d\varphi_1} + \frac{dH_{drained-gas}}{d\varphi_1} + \frac{dQ}{d\varphi_1} - \frac{dL}{d\varphi_1} \tag{3}$$

Compression process

$$\frac{dU_{gas}}{d\varphi_1} = \sum_{i=1}^{6} \frac{dH_{leak-in-gas}}{d\varphi_1}\Big|_i - \sum_{i=1}^{6} \frac{dH_{leak-out-gas}}{d\varphi_1}\Big|_i + \frac{dH_{SF}}{d\varphi_1} + \frac{dH_{LRI:flash-gas}}{d\varphi_1} - \frac{dH_{SV:by-pass-gas}}{d\varphi_1} + \frac{dH_{oil:flash-gas}}{d\varphi_1} + \frac{dH_{drained-gas}}{d\varphi_1} + \frac{dQ}{d\varphi_1} - \frac{dL}{d\varphi_1} \tag{4}$$

Discharge process

$$\frac{dU_{gas}}{d\varphi_1} = -\frac{dH_{outlet-gas}}{d\varphi_1} - \sum_{i=1}^{6} \frac{dH_{leak-out-gas}}{d\varphi_1}\Big|_i + \frac{dH_{LRI:flash-gas}}{d\varphi_1} + \frac{dH_{oil:flash-gas}}{d\varphi_1} + \frac{dQ}{d\varphi_1} - \frac{dL}{d\varphi_1} \tag{5}$$

The conservation equation for the gas mass in the control volume in terms of the rotation angle of the male rotor can be written. Different working processes also have different items in the conservation equation for the mass, which is presented as follows:

Suction process

$$\frac{dm_{gas}}{d\varphi_1} = \frac{dm_{inlet-gas}}{d\varphi_1} + \sum_{i=1}^{6} \frac{dm_{leak-in-gas}}{d\varphi_1}\Big|_i + \frac{dm_{oil:flash-gas}}{d\varphi_1} + \frac{dm_{drained-gas}}{d\varphi_1} \tag{6}$$

Compression process

$$\frac{dm_{gas}}{d\varphi_1} = \sum_{i=1}^{6} \frac{dm_{leak-in-gas}}{d\varphi_1}\Big|_i - \sum_{i=1}^{6} \frac{dm_{leak-out-gas}}{d\varphi_1}\Big|_i + \frac{dm_{SF}}{d\varphi_1} + \frac{dm_{LRI:flash-gas}}{d\varphi_1} - \frac{dm_{SV:by-pass-gas}}{d\varphi_1} + \frac{dm_{oil:flash-gas}}{d\varphi_1} + \frac{dm_{drained-gas}}{d\varphi_1} \tag{7}$$

Discharge process

$$\frac{dm_{gas}}{d\varphi_1} = -\frac{dm_{outlet-gas}}{d\varphi_1} - \sum_{i=1}^{6} \frac{dm_{leak-out-gas}}{d\varphi_1}\Big|_i + \frac{dm_{LRI:flash-gas}}{d\varphi_1} + \frac{dm_{oil:flash-gas}}{d\varphi_1} \tag{8}$$

The conservation equations for the gas mass and internal energy in the control volume are the basic equations of the mathematical model. From these two equations the temperature and pressure of the gas can be calculated, and so can the other properties. The fourth-order Runge-Kutta procedure and the recursion procedure are used to solve the equations (1). The calculated results are accepted after the iteration procedure has given a difference between two consecutive pressure volume graphs which is smaller than a small value prescribed in advance (0.01 *bar*). The calculation of every item in the above equations and the other necessary equations in the mathematical model are explained in the following sections.

4.4.2 Gas Flow through the Suction Port, Discharge Port and Slide Valve by-Pass Port

The gas flow through the suction and slide valve by-pass ports can be considered as incompressible as the Mach number is usually small. The following one-dimensional equation is used to calculate the flow speeds through the suction and slide valve by-pass ports:

$$WdW + \frac{dp}{\rho} = 0 \tag{9}$$

The gas flow rate through the suction port is calculated by the following continuity equation:

$$\frac{dm_{inlet-gas}}{d\varphi_1} = c_{area} c_{speed} \rho W A_{flow} / \omega \tag{10}$$

In the above equation, two modification coefficients are used, c_{area} and c_{speed}. Coefficient c_{area} provides an area change caused by the difference between the calculated and real areas. For the suction process, the axial suction port area is used in the place of A_{flow} in equation 10 as the suction port shown as Fig. 4.4 is used for the compressors which the author is due to simulate. A modification coefficient, greater than one, is used to modify the calculated area according to the theoretical suction port shown as Fig. 3.3. The coefficient is decided by the

following simple equation:

$$c_{area} = \frac{A_{01} + A_{02} + A_1 + A_2}{A_{01} + A_{02}} \tag{11}$$

where the areas A_{01}, A_{02}, A_1 and A_2 are shown in Fig. 4.4.

The other modification coefficient used in equation 10 is c_{speed}, which is applied to account for irreversibilities reducing the flow speed calculated by equation 9. When equation 9 is used to calculate the flow speed through the suction port, it is assumed that the flow is isentropic and one-dimensional, which are not truly the case, so that in equation 10 a modification coefficient, ie c_{speed}, is used to modify the calculated speed.

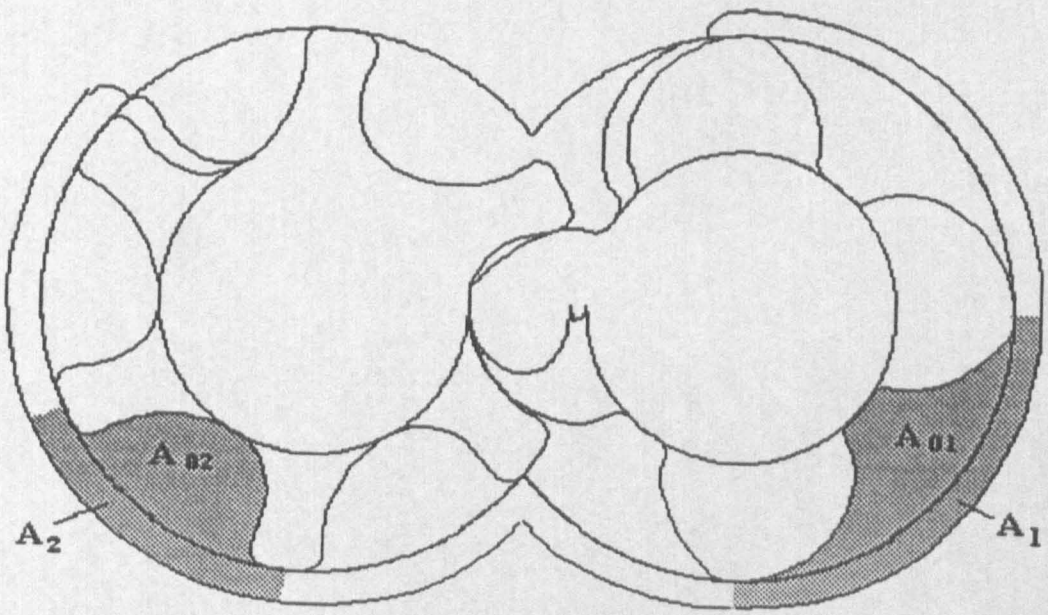

Fig. 4.4 A practical used suction port

The closing angle of the suction port is usually set at the maximum cavity volume. For the compressors running under big pressure ratios and low rotational speeds, the performance could be improved a little if the port is closed slightly earlier. For the compressors running under low pressure ratios and high rotational speeds, an improved performance could be obtained if the suction port has a later

closing angle. The optimum closing angle of the suction port depends on the balance between the gas sucked and the gas leaking into the cavity during the last stage of the suction process, and the optimum closing angle is the angle where the flow speed equals zero at the end of the suction process. For a given closing angle, at the end of the suction process, the gas pressure in the control volume can be equal to, higher than or lower than the suction pressure. In equation 10, if the pressure in control volume is lower than the suction pressure, ie the gas flow is from the suction chamber into the cavity, the flow speed W is set to positive. Otherwise it is negative. $\frac{dH_{inlet-gas}}{d\varphi_1}$ in equation 3 can be calculated by the following equations:

$$\begin{cases} \frac{dH_{inlet-gas}}{d\varphi_1} = \frac{d(m_{inlet-gas}h_1)}{d\varphi_1} & W > 0 \\ \frac{dH_{inlet-gas}}{d\varphi_1} = 0 & W = 0 \\ \frac{dH_{inlet-gas}}{d\varphi_1} = \frac{d(m_{inlet-gas}h_{gas})}{d\varphi_1} & W < 0 \end{cases} \tag{12}$$

The gas flow rate through the slide valve by-pass port is also calculated by the following continuity equation:

$$\frac{dm_{SV:by-pass-gas}}{d\varphi_1} = c_{area}c_{speed}\rho W A_{flow}/\omega \tag{13}$$

Coefficient c_{area} in the above equation is set to 1.0 in the author's working process simulation program. The gas goes back to the suction pressure always. $\frac{dH_{SV:by-pass-gas}}{d\varphi_1}$ in equation 4 can be calculated by the following equations:

$$\frac{dH_{SV:by-pass-gas}}{d\varphi_1} = \frac{d(m_{SV:by-pass-gas}h_{gas})}{d\varphi_1} \tag{14}$$

During the discharge process, the pressure in the control volume can be equal to, higher than or lower than the discharge pressure because the compressor can run under the normal compression, over compression and under compression. The pressure difference between the discharge pressure and the pressure in the control volume could be very large. When this happens, the gas flow can not be considered as incompressible because the Mach number could be quite large, and the following one-dimensional and isentropic energy conservation equation is used to calculate the flow speed through the discharge port:

$$WdW + dh = 0 \tag{15}$$

In the working process simulation program, after the pressure difference across the discharge port is reduced to a value less than 0.1 *bar*, equation 9 is used to calculate the flow speed, ie the flow is assumed to be incompressible.

The gas flow rate through the discharge port is calculated by the following continuity equation:

$$\frac{dm_{outlet-gas}}{d\varphi_1} = c_{area}c_{speed}\rho W A_{flow}/\omega \tag{16}$$

The flow speed W in the above equation is set to positive if the flow is out of the control volume, otherwise it is negative.

The gas flow through the discharge port can not be consider as along the axial direction or along the radial direction. A total discharge port area, ie A_{flow} in equation 16, should be calculated according the calculated axial and radial discharge port areas (see Chapter 3). It can be simply calculated by the following equation:

$$A_{flow} = A_{axial} + A_{radial} \tag{17}$$

and a modification coefficient, ie c_{area}, less than one is used. However, due to the application of the slide valve, the volume ratio for the radial discharge port differs from the ratio for the axial discharge port very often. A constant modification coefficient may not be reasonable. In the working process simulation program, the author sets c_{area} to equal one, and uses the following equation to calculate an equivalent total discharge port area:

$$A_{flow} = A_{axial}\cos(\arctan\frac{D_{1out}}{L_r}) + A_{radial}\sin(\arctan\frac{D_{1out}}{L_r}) \tag{18}$$

The above equation is based on the assumption that the discharge flow is along the direction of the diagonal of the male rotor. In a real compressor, the flow through the discharge port does go along the diagonal, or very nearly. As a consequence, the equivalent total discharge port area is assumed to be the sum of the axial and radial area projected into the diagonal direction.

The energy transfer rate $\frac{dH_{outlet-gas}}{d\varphi_1}$ in equation 5 can be calculated by the

following equations:

$$\begin{cases} \dfrac{dH_{outlet-gas}}{d\varphi_1} = \dfrac{d(m_{outlet-gas}h_{gas})}{d\varphi_1} & W > 0 \\ \dfrac{dH_{outlet-gas}}{d\varphi_1} = 0 & W = 0 \\ \dfrac{dH_{outlet-gas}}{d\varphi_1} = \dfrac{d(m_{outlet-gas}h_2)}{d\varphi_1} & W < 0 \end{cases} \tag{19}$$

4.4.3 Gas Flow through the Leakage Paths

The gas flow through any leakage path is considered as compressible, although the flow through the compression start blow hole or across the suction end faces of the rotors can be considered as incompressible because the leakage through these two paths happens during the very early stage of the compression process and the pressure difference across them is usually very small. The flow speeds through all the leakage paths are calculated by the one-dimensional and isentropic energy conservation equation 14. At the minimum area of the leakage path, the maximum flow speed can be obtained. The speed through some leakage paths such as the contact line and the discharge end faces of the rotors can approach the local sound speed if the pressure difference over the path is large enough. The local speed of sound is calculated by the following differential equation:

$$W_{sound} = \sqrt{\left(\frac{\partial p}{\partial \rho}\right)_s} \tag{20}$$

For the suction and discharge ports, the local speed of sound is also calculated according to the above equation in order to obtain the Mach numbers for the suction and discharge processes. The working process simulation program also calculates the local speed of sound through all the leakage paths.

The following continuity equations are used to calculate the leakage rate through any leakage path:

$$\begin{cases} \dfrac{dm_{leak-in-gas}}{d\varphi_1}|_{i=1\sim6} = c_{area}c_{speed}\rho W A_{flow}/\omega & W < W_{sound} \\ \dfrac{dm_{leak-in-gas}}{d\varphi_1}|_{i=1\sim6} = c_{area}c_{speed}\rho W_{sound} A_{flow}/\omega & W \geq W_{sound} \\ \dfrac{dm_{leak-out-gas}}{d\varphi_1}|_{i=1\sim6} = c_{area}c_{speed}\rho W A_{flow}/\omega & W < W_{sound} \\ \dfrac{dm_{leak-out-gas}}{d\varphi_1}|_{i=1\sim6} = c_{area}c_{speed}\rho W_{sound} A_{flow}/\omega & W \geq W_{sound} \end{cases} \tag{21}$$

In the above equations, the minimum flow areas for the blow hole (Path 3) and the compression start blow (Path 4) are described and calculated in Chapter 3. The definition of Singh and Onuschak (2) of the blow hole area seems to be good and reasonable for the A- and D-profiles. However, according to the definition, the blow hole area of the symmetrical circular profile is only ten percent bigger than that of the A-profile. Consequently, it is surprising that when the pressure ratio becomes a little higher the performance of the symmetrical circular profile becomes much worse than that of the A-profile, particularly when one considers that the contact line length of the symmetrical circular profile is 10 percent *less* than that of the A-profile. For the symmetrical circular profile, the author suggests that an area in the plane containing the two cusps of the housing be used in equation 18, so that the prediction results can be improved.

The flow areas for the contact line (Path 1), the rotor tip sealing lines (Path 2), the rotor suction end face (Path 5) and the rotor discharge end face (Path 6) are calculated by the following equation:

$$A_{area}\,|_{i=1,2,5,6} = \delta \times L_{sealing}(\varphi_1) \tag{22}$$

The sealing line lengths of different leakage paths have been described and calculated in Chapter 3.

As mentioned earlier in this chapter, coefficient c_{area} provides an area change caused by the difference between the calculated and real areas. It is mainly used to account for three quite distinct physical effects as follows:

1. the tendency of the oil in the compressor to seal the leakage gaps;
2. the changes caused to nominal clearances by the cavity pressure under load;
3. the changes caused to nominal clearances by the temperature distribution of the rotors and housing under load.

The influence of the above factors on the blow hole area and the compression start blow hole area is very small, so that in the working process simulation program coefficient c_{area} for areas of these two leakage paths are set to one. However, the influence of the above factors on the leakage area of the other paths could be considerable. Although, the author has developed some computer programs such

as the force analysis program and the rotor deflection program, which could help to work out the clearances under load, much more research work needs to be done, as determination of the clearances under load involves many other factors such as the calculation of the thermal expansion of the rotors and housing, and the clearances in radial and thrust bearings etc. Different operation conditions result in different clearances under load. Only at the stage where the clearances under load have been determined, could coefficient c_{area} become a function of the total oil rate. In the existing working process program, coefficients c_{area} for Paths 1, 2, 5 and 6 are also set to one. For the machines for which measured clearances are known, the measured clearances are used in the program, otherwise the nominal design clearances are input. For the contact line between the male and female rotors, an average clearance normal to the rotor helical surface, calculated by the cutter blade calculation program (see Chapter 5), is used.

The energy transfer rate through any leakage path can be calculated by the following equations:

$$\begin{cases} \dfrac{dH_{leak-in-gas}}{d\varphi_1}\Big|_{i=1\sim6} = \dfrac{d(m_{leak-in-gas}h_{upstream})}{d\varphi_1}\Big|_{i=1\sim6} \\ \dfrac{dH_{leak-out-gas}}{d\varphi_1}\Big|_{i=1\sim6} = \dfrac{d(m_{leak-out-gas}h_{gas})}{d\varphi_1}\Big|_{i=1\sim6} \end{cases} \tag{23}$$

4.4.4 Liquid Refrigerant Injection

When liquid refrigerant is injected into a low pressure or high temperature open space, it flashes. The refrigerant vapour in the control volume now becomes superheated vapour with liquid refrigerant droplets in suspension. The phenomenon that happens in the control volume cannot be described by equilibrium thermodynamics and presents a challenge to modern heat transfer theory. The flash needs take a finite time before all the injected liquid refrigerant evaporates or flashes to vapour as happens in an area of fog-style flow in an evaporator (3 and 4). This flash time should be a function of the pressure and temperature of liquid refrigerant before the injection port, the vapour temperature and pressure in the control volume and the geometry of the injection port. As the vapour

temperature and pressure in the control volume changes very rapidly with the male rotor rotational angle, the flash time should also change in a related manner.

In the mathematical model, an average flash time for the flash of the injected liquid refrigerant during the compression and discharge processes is introduced. An average flash time, 0.02 seconds, is used for R22 in the model, which is obtained according to the time of persistence of fog-style flow in an evaporator (3 and 4). The tip speed for an oil flooded twin screw compressor should be within the range 15 - 40 m/s. For a medium size compressor, the compression time will then be roughly 0.003 - 0.015 seconds. Consequently, the injected liquid refrigerant can not be totally flashed during the compression process, leaving liquid refrigerant to continue flashing in the discharge line.

The flash rate of the injected liquid refrigerant is calculated by the equation as follows:

$$\frac{dm_{LRI:flash-gas}}{d\varphi_1} = \frac{60 \times m_{LRI}}{360 \times T_{LRI:flash} W_1} \tag{24}$$

Two procedures are used to calculate the liquid refrigerant flow rate through the injection port. If the total liquid refrigerant average flow rate is known, the following equation is used to calculate the flow rate through the injection port as a function of rotation angle:

$$\frac{dm_{LRI:port}}{d\varphi_1} = \frac{Q_{LRI}}{360 \times W_1} \times \frac{A_{LRI}(\varphi_1)}{A_{LRImax}} \tag{25}$$

The above equation is based on the assumption that the liquid refrigerant flow rate through the injection port is uniform. Practically the flow rate is varied as the pressure difference across the injection port is varied. If the total liquid refrigerant flow rate is unknown, equation 9 can also be used to calculate the flow speed through the injection port. The flow rate is calculated by the following equation:

$$\frac{dm_{LRI:port}}{d\varphi_1} = c_{LRI} \rho W A_{LRI} / \omega \tag{26}$$

The flow rate coefficient c_{LRI} in the above equation can be determined according to the measured total flow rate easily. The liquid refrigerant mass in the control volume is calculated by the equation as follows:

$$m_{LRI} = \int_0^{\varphi_1} \frac{dm_{LRI:port}}{d\varphi_1} d\varphi_1 - \int_0^{\varphi_1} \frac{dm_{LRI:flash-gas}}{d\varphi_1} d\varphi_1 \tag{27}$$

The energy transfer rate due to flash of the liquid refrigerant injected is calculated by the following equation:

$$\frac{dH_{LRI:flash-gas}}{d\varphi_1} = h_{LRI:beforeport}\frac{dm_{LRI:flash-gas}}{d\varphi_1} \tag{28}$$

The heat transfer between the gas and the liquid refrigerant droplets in the control volume is negligible, compared with the energy transfer due to the flash.

4.4.5 Gas from the Superfeed

Two procedures are used to calculate the gas flow rate from the superfeed through the superfeed port. If the total flow rate is known, the following equation is used to calculate the flow rate through the port:

$$\frac{dm_{SF}}{d\varphi_1} = \frac{Q_{SF}}{360 \times W_1} \times \frac{A_{SF}(\varphi_1)}{A_{SFmax}} \tag{29}$$

The above equation is based on the assumption that the gas flow rate through the superfeed port is uniform for different rotational angles. Practically the flow rate is varied as the pressure difference across the superfeed port is varied. If the total liquid refrigerant flow rate is unknown, equation 15 is used to calculate the flow speed through the superfeed port. The flow rate is then calculated by the following equation:

$$\frac{dm_{SF}}{d\varphi_1} = c_{SF}\rho W A_{SF}/\omega \tag{30}$$

The flow rate coefficient c_{SF} in the above equation can be determined according to the measured total flow rate easily.

The energy transfer rate due to the gas injection from the superfeed is calculated by the following equation:

$$\frac{dH_{SF}}{d\varphi_1} = h_{SF}\frac{dm_{SF}}{d\varphi_1} \tag{31}$$

4.4.6 Friction Power Calculation Models

In a twin screw compressor frictional or viscous shear losses result from the end casings, such as from the shaft seal, the radial and thrust bearings and the balance pistons etc. They also results from the main casing, such as the friction losses due to the presence of oil in small gaps and due to the viscosity of the compressed gas etc. The friction losses between the compressed gas and the rotors or housing are much smaller than those resulting from oil viscous friction in the small gaps in the compressor as the viscosity of the gas is much smaller than that of the oil. The viscous friction loss due to oil between the rotor tips and housing is generally predominant unless a seal strip is used to minimize the shear area (**5**) and a nominal or real radial suction port is used.

In a refrigeration screw compressor the friction losses from end casings have an indirect influence on the working process in the main casing. The lubrication oil is heated due to the friction losses, and the dissolved refrigerant flashes due the pressure decrease and temperature increase. Then the mixture of the oil and the flashed gas is drained into the cavity through the drain ports. The bearing power losses and the shaft seal losses are calculated using bearing and shaft seal loss data or charts supplied by the manufacturers (**6** and **7**). For example, the following equations are developed by the curve fitting procedure from the data supplied by the shaft seal manufactures (**6**), and are used for the calculation of the balanced shaft seal losses in the model:

$$
\begin{cases}
P_{shaftseal} = (-1.43 \times 10^{-5} p_{oil}^2 + 0.00354 p_{oil} + 0.0467) \times W_1 \\
\qquad D_{shaft} = 40, p_{oil} = 0 \sim 80 \\
P_{shaftseal} = (1.88 \times 10^{-5} p_{oil}^2 + 0.00436 p_{oil} + 0.0946) \times W_1 \\
\qquad D_{shaft} = 60, p_{oil} = 0 \sim 80 \\
P_{shaftseal} = (3.23 \times 10^{-5} p_{oil}^2 + 0.00749 p_{oil} + 0.152) \times W_1 \\
\qquad D_{shaft} = 80, p_{oil} = 0 \sim 80 \\
P_{shaftseal} = (4.30 \times 10^{-5} p_{oil}^2 + 0.00126 p_{oil} + 0.190) \times W_1 \\
\qquad D_{shaft} = 100, p_{oil} = 0 \sim 80 \\
P_{shaftseal} = (1.33 \times 10^{-4} p_{oil}^2 + 0.0218 p_{oil} + 0.372) \times W_1 \\
\qquad D_{shaft} = 120, p_{oil} = 0 \sim 80
\end{cases}
\tag{32}
$$

As there are no friction loss measured results for the balance pistons, the friction

losses of the balance pistons are also calculated by the above equations approximately. The total friction losses in both the suction and discharge end casings can be presented as follows:

$$P_{endcasing} = P_{bearing} + P_{piston} + P_{shaftseal} \tag{33}$$

According to an energy balance and assuming that the heat transfer between the end casings and the environment is negligible, the oil temperature at the oil drain ports can be calculated by the following equation:

$$t_{OD} = t_{OI} + \frac{1000 \times P_{endcasing} - Q_{FG:endcasing}(h_{OD} - h_{OI})/60}{(Q_{OD} - Q_{FG:endcasing})C_{oil}/60} \tag{34}$$

In spite of the difference of the pressure in the suction and discharge end casings which can exist in reality, in the model it is assumed that the oil from both the casings has the same state before it drains into the control volume.

The gas flow rate due to the refrigerant flash in the end casings is calculated by the following equation:

$$\frac{dm_{drained-gas}}{d\varphi_1} = \frac{Q_{FG:endcasing}}{360 \times W_1} \times \frac{A_{OD1}(\varphi_1) + A_{OD2}(\varphi_1)}{A_{OD1max} + A_{OD2max}} \tag{35}$$

The above equation is based on the assumption that the gas flow rate through the oil drain ports is uniform for different rotational angles. This is reasonable as during the end stage of the suction process and the early stage of the compression process the pressure in the control volume remains nearly constant. The energy transfer rate due to the gas from the end casings is calculated by the following equation:

$$\frac{dH_{drained-gas}}{d\varphi_1} = h_{OD}\frac{dm_{drained-gas}}{d\varphi_1} \tag{36}$$

The friction power in the main casing is generated due to many factors. Every item can be considered as in proportion to the square of the male rotor tip speed (8). The following simplified equation is used to calculate the friction power in the main casing by the author:

$$P_{maincasing} = c_{main1}c_{main2}\left(\frac{\pi D_{1out}W_1}{6 \times 10^4}\right)^2 \tag{37}$$

The above equation has two coefficients. Coefficient c_{main1} is a basic coefficient, which is a function of the viscosity of the drained or injected oil, the viscosity of

the compressed gas, the gap clearances in the main casing and the geometry of the compressor etc., and it is decided according to the measured adiabatic total efficiency or the measured power absorbed by the compressor for the given oil flow rate. The author discovered from measured data that the friction power in the main casing is very sensitive to the oil flow rate through the compressor. According to the measured results (**9**), the following equation representing the relationship between coefficient c_{main2} and the equivalent oil flow rate is obtained by the curve fitting procedure:

$$\begin{cases} c_{main2} = -7.16 \times 10^{-11} Q_{oil}^4 + 1.84 \times 10^{-7} Q_{oil}^3 - 1.37 \times 10^{-4} Q_{oil}^2 + \\ \qquad 0.0468 Q_{oil} - 0.253 \\ Q_{oil} = 10 \sim 500 \end{cases} \tag{38}$$

The equivalent oil flow rate in the above equation is calculated by the following equation:

$$Q_{oil} = Q_{OD} + c_{OI} Q_{OI} \tag{39}$$

Coefficient c_{OI} in the above equation is decided according to the oil injection port position, and it is the ratio of the injected oil duration to the drained oil duration in the control volume. If the injection port has the same male rotor rotational angle as the oil drained ports, coefficient c_{OI} equals one.

4.4.7 Oil Supply and Refrigerant Dissolved in Oil

The twin screw compressor and its oil system circulate a solution of oil with refrigerant instead of pure oil owing to the solubility of refrigerant in oil. The refrigerant dissolved in the oil reduces the viscosity of the oil and worsens the sealing between the gaps, and it is a source of additional volumetric and energy losses in the compressor. Halogenated hydrocarbons dissolve in oil better than does ammonia. Much attention has been paid to analyzing the influence of the refrigerant-oil solubility characteristics on the behaviour of screw compressors.

Although there are published papers on refrigerant-oil interaction such as (**10**, **11** and **12**), in the author's mathematical model the data supplied by the oil man-

ufacturer is used (6). According to the supplied data, the following relationships have been obtained for the oil by a curve fitting procedure:

1. Viscosity vs mass ratio and temperature.
2. Mass ratio vs temperature and pressure.
3. Density vs mass ratio and temperature.
4. Specific heat vs mass ratio and temperature.

The oil solubility with ammonia is treated as being negligible in the model. Due to the relative small variation of the oil density and specific heat with temperature and mass ratio, they are treated as constants in the working process simulation program, and the density and specific heat before the injection ports are used.

The following example shows how important the refrigerant disolved in the oil is for the working process of the compressor. A medium size compressor handles *R22* and has 120 *kg/min* drained oil flow rate. The oil temperature before the injection ports is 45 $^{\circ}C$, and the delivery temperature is 70 $^{\circ}C$. The oil pressure before the injection is 13 *bar*, and the delivery pressure is 13.55 *bar*. Before the injection ports, the mass ratio of refrigerant to total mass is 30 percent, and after the delivery, ie after the separation from the gas, the mass ratio becomes 17 percent. 15.6 *kg/min* of *R22* will flash to gas, which can result in a heat removal rate of about 50 *kw* from the oil, the compressed gas and the friction mechanisms. During the same process the oil, actually the liquid mixture of oil and *R22*, results in a heat absorption rate of about 85 *kw*. Unlike the heat absorbed by the oil, most of which is absorbed in the discharge line, about half of the heat transfer due to the flash happens in the end and main casings of the compressor.

Although the oil state could be different depending on its entry point, as it enters the control volume, its temperature, pressure etc. are treated as uniform everywhere. The uniform pressure is the pressure of the compressed gas in the control volume. The uniform oil temperature and mass in the control volume is calculated according to the following energy and mass conservation equations for the oil in the control volume:

$$\frac{dU_{oil}}{d\varphi_1} = C_{oil}t_{OD}\frac{dm_{OD}}{d\varphi_1} + C_{oil}t_{OI}\frac{dm_{OI}}{d\varphi_1} - C_{oil}t_{oil}\frac{dm_{oil:outletport}}{d\varphi_1} + \frac{dQ_{oil\leftrightarrow gas}}{d\varphi_1} \quad (40)$$

$$\frac{dm_{oil}}{d\varphi_1} = \frac{dm_{OD}}{d\varphi_1} + \frac{dm_{OI}}{d\varphi_1} - \frac{dm_{oil:outletport}}{d\varphi_1} - \frac{dm_{oil:flash-gas}}{d\varphi_1} \tag{41}$$

The above equations are used for the suction, compression and discharge processes, and for different processes some items can be equal to zero. When under-compression happens, the oil in the discharge chamber could re-enter the control volume, which is not considered in the existing program. The flash of the refrigerant dissolved in oil could absorb heat from the oil, but in the program it is assumed that it absorbs heat from the compressed gas only. In energy equation 40, the item due to the friction heat is not included, and in the existing working process simulation program, the oil temperature after the discharge is modified according to the calculated $P_{maincasing}$ by a simple energy balance equation. However, the friction heat in the main casing warms up the injected oil during the working processes, and a mathematical model uesd to described this heating process needs to be developed in the future. In the above equations, the oil flow rate through the oil drain ports is calculated by the following equation:

$$\frac{dm_{OD}}{d\varphi_1} = \frac{Q_{OD} - Q_{FG:endcasing}}{360 \times W_1} \times \frac{A_{OD1}(\varphi_1) + A_{OD2}(\varphi_1)}{A_{OD1max} + A_{OD2max}} \tag{42}$$

Two procedures are used to calculate the injected oil flow rate through the injection port or ports. If the total flow rate is known, the following equation is used to calculate the flow rate:

$$\frac{dm_{OI}}{d\varphi_1} = \frac{Q_{OI}}{360 \times W_1} \times \frac{A_{OI}(\varphi_1)}{A_{OImax}} \tag{43}$$

The above equation is based on the assumption that the oil flow rate through the injection port or ports is uniform for different rotational angles. In reality, the flow rate varies as the pressure in the control volume varies. If the total oil injection flow rate is unknown, equation 15 is used to calculate the flow speed through the injection port. The flow rate is then calculated by the following equation:

$$\frac{dm_{OI}}{d\varphi_1} = c_{OI}\rho_{oil}WA_{OI}/\omega \tag{44}$$

The flow rate coefficient c_{OI} in the above equation can be determined according to the measured total flow rate easily. The oil outlet rate through the discharge

port is calculated by the equation as follows:

$$\frac{dm_{oil:outletport}}{d\varphi_1} = \frac{m_{OIL}}{m_{gas}} \times \frac{dm_{outlet-gas}}{d\varphi_1} \tag{45}$$

The same method as used for the calculation of the flash rate of the injected liquid refrigerant is also used to calculate the refrigerant flash rate from the oil in the control volume, that is, an average flash time is used for the calculation of the flash rate as follows:

$$\frac{dm_{oil:flash-gas}}{d\varphi_1} = \frac{60 \times m_{LR}}{360 \times T_{LRI:flash} W_1} \tag{46}$$

In the above equation, m_{LR} is the mass of liquid refrigerant which is still dissolved in oil, but is ready to flash due to the variation of the oil state. It is calculated by the following equation:

$$m_{LR} = \int_0^{\varphi_1} m_{oil} \left(-\frac{d\xi}{d\varphi_1}\right) d\varphi_1 - \int_0^{\varphi 1} \frac{dm_{oil:flash-gas}}{d\varphi_1} d\varphi_1 \tag{47}$$

Due to the short time of the compression process, not all the ready-to-flash refrigerant dissolved in oil can flash to gas during the compression process. However the oil injected into the end casing has a relatively longer dwell time. Consequently, in the model the ready-to-flash refrigerant in the end casing is considered as 100 percent flashed before the drained ports, based on which $Q_{FG:endcasing}$ is calculated.

The energy transfer rate due to the flash of the refrigerant dissolved in oil is calculated by the equation as follows:

$$\frac{dH_{oil:flash-gas}}{d\varphi_1} = h_{LR} \frac{dm_{oil:flash-gas}}{d\varphi_1} \tag{48}$$

4.4.8 Heat Exchanged with the Gas in Control Volume

In the mathematical model, heat transfer between the gas and the compressor rotors or housing is treated as being negligible since it is much smaller than the energy exchanges which occur within the cavity as a result of the compression process and the flashing of refrigerant, whether injected as neat liquid or dissolved

in the injected lubricating oil (**13**). The calculation of the energy transfer rates due to the flash of the refrigerant injected and dissolved in oil has been described in 4.4.4 and 4.4.7. In addition, the compressed gas exchanges heat with the oil injected or drained into the control volume, and it also absorbs part of the friction heat generated in the main cavity. In the existing mathematical model, it is assumed that all the friction loss in the main casing goes into heating the oil (**8**), so that the heat transfer rate $\frac{dQ}{d\varphi_1}$ in energy equations 3 – 5 is only equal to $-\frac{d_{oil\leftrightarrow gas}}{d\varphi_1}$, that is the heat transfer rate between the gas and oil, which can be calculated by the following equation:

$$\frac{d_{oil\leftrightarrow gas}}{d\varphi_1} = \frac{A_{oil\leftrightarrow gas}\alpha(t_{gas} - t_{oil})}{\omega} \tag{49}$$

The injected oil can be assumed to be in the form of a uniform spray of spherical droplets (**14** and **15**). From the average diameter of droplets the following heat transfer area can be calculated easily. The droplet sizes can be calculated by the equations presented in (**14** – **16**). Different injection nozzles can result in very different sizes of droplets. The higher the injection pressure, the smaller the oil droplets. However if a high degree of atomization is required to reduce the compression work, ie to make the compression process approach an isothermal process, a pneumatic nozzle with a very high power consumption would be required, so that Persson concludes in his paper (**15**) that in high-speed screw compressors, any significant reduction of the specific work for compression cannot be obtained by the injection of a very fine oil spray. Due to the internal turbulence and centrifugal action, the droplets injected will rapidly form a liquid film on the compressor casing. The main advantage of liquid injection will therefore be the improved sealing of the clearances, the improved cooling of rotors and casing, and the lubricating film in the rotor mesh. By improved cooling of the metal parts, thermal distorsions will be reduced but will be combined with a higher working fluid temperature. In addition, a much higher stage pressure ratio can then be achieved, than is possible for dry screw compressor.

If the oil droplet flow through the compressor is considered as Stokes flow, the heat transfer coefficient between the oil and the compressed gas can be calculated by the equations presented in (**14** and **15**).

For the compressors simulated here, part of oil is drained from the end casing, and the pressure difference across the ports is only about 0.5 *bar* usually, so that the degree of atomization is very low. Part of oil is injected into the compressor, and the atomization could be better, depending on the position of the oil injection port. Very often there is no direct oil injection at all, only oil drained from the bearings. The flash process of the refrigerant dissolved in the oil can strengthen the heat transfer, which is similar to the physical events of two phase flow. However, in the mathematical model equation 49 is still used to calculate the heat transfer rate between the existing oil and the compressed gas. The average diameter of droplets is chosen according to (**15** and **16**), the correct choice of which is not necessarily very important in obtaining a correct numerical answer since the heat transfer coefficient used in the equation is obtained according to the measured discharge temperature.

When twin screw compressors are operating under the partial loading condition, part of the drained or injected oil is re-circulated through the slide valve by-pass port to the suction chamber and then through the suction port into the compression cavity again. This oil re-circulation could warm up the suction gas. In the mathematical model, the possibility of this oil re-circulation is not taken into account.

4.4.9 Work Exchanged by the Gas in Control Volume

The oil and liquid refrigerant in the control volume are treated as incompressible, and they take up part of the compression cavity. Usually the oil volumetric flow rate is about 0.25 – 1.0 percent of the volumetric capacity of the compressor. During the early stage of the compression process, the influence of the oil volume on the compression process is very small and can be neglected. However during the end stage of the compression process, its influence becomes bigger, and for a compressor with a volume ratio of 5.0, up to 5 percent of the cavity volume could be taken up by the oil before the discharge process begins. If a compressor has liquid refrigerant injected, the unflashed liquid also takes up some cavity volume,

although this is usually much smaller than that taken up by the oil. The volume taken up by the oil and liquid refrigerant in the control volume is calculated according to their masses and densities. Then the specific volume of the gas in the control volume can be calculated by the following formula:

$$v_{gas} = \frac{V - V_{liquid}}{m_{gas}} \tag{50}$$

The pressure in the control volume is calculated according to the above specific volume.

The gas work exchange rate in the control volume is calculated by the following equation:

$$\frac{dL}{d\varphi_1} = p\frac{d(V - V_{liquid})}{d\varphi_1} \tag{51}$$

4.4.10 Property Equations of Refrigerants

In addition to the equations mentioned above, many equations used to calculate the thermodynamic properties of refrigerants in the mathematical model are needed. These equations are:

- Equation of liquid density: $\rho_{LR} = f(t)$.
- Equation of vapour pressure: $p_{vapour} = f(t)$.
- Equation of state: $p = f(t, v_{gas})$.
- Equation of latent heat of vaporization: $\Delta H_{lat} = f(t, \rho_{LR}, v_{gas})$.
- Equation of vapour enthalpy: $h_{gas} = f(t, v_{gas})$.
- Equation of vapour entropy: $s_{gas} = f(t, v_{gas})$.

The specific internal energy of a refrigerant can be presented as follows:

$$u_{gas} = h_{gas} - pv_{gas} = f(t, v_{gas}) \tag{52}$$

The specific volume of the gas in the cavity can be calculated by equation 50, and the specific internal energy can be calculated following integration of equations 3 - 8. From the above equation the gas temperature can be solved, and then the gas pressure can be calculated by the state equation.

The thermodynamic property equations are different for different refrigerants. At the request of the Howden Compressors Ltd. four refrigerants, R12, R22, R143a and R717 (ammonia), are considered in the model, but the simulation program is structured in such a way that it is very easy to include other refrigerants including binary refrigerants if the required property equations or the required property calculation subroutines are known.

The thermodynamic property equations for the considered refrigerants are presented in Appendix E. Martin-Hou equations are used to calculate the thermodynamic properties of R12 and R22 in the mathematical model (17). The thermodynamic property equations of R134a is provided by the refrigerant manufacturers (6), and the thermodynamic property equations of R717 is from (18).

4.4.11 Compressor Efficiencies and the other Performance Parameters

The leaking outflow, leaking inflow and net leaking outflow rates for every leakage path are calculated by the following equations:

$$Q_{leak-in-gas}\,|_{i=1\sim6} = z_1 W_1 \int_{\varphi_{1suc.stop}}^{\varphi_{1max}} \frac{dm_{leak-in-gas}}{d\varphi_1}\,|_{i=1\sim6}\, d\varphi_1 \tag{53}$$

$$Q_{leak-out-gas}\,|_{i=1\sim6} = z_1 W_1 \int_{0}^{\varphi_{1max}} \frac{dm_{leak-out-gas}}{d\varphi_1}\,|_{i=1\sim6}\, d\varphi_1 \tag{54}$$

$$Q_{netoutflow}\,|_{i=1\sim6} = Q_{leak-out-gas}\,|_{i=1\sim6} - Q_{leak-in-gas}\,|_{i=1\sim6} \tag{55}$$

Leakage into a cavity during the suction process is treated as external leakage.

The mass capacity of the compressor is calculated as follows:

$$Q_{mass} = z_1 W_1 \left(\int_0^{\varphi_{1suc.stop}} \frac{dm_{inlet-gas}}{d\varphi_1} d\varphi_1 - \int_{\varphi_{1suc.stop}}^{\varphi_{1max}} \frac{dm_{SV:by-pass-gas}}{d\varphi_1} d\varphi_1 \right) \tag{56}$$

or

$$\begin{aligned} Q_{mass} = z_1 W_1 \Big(& \int_{\varphi_{1dis.start}}^{\varphi_{1max}} \frac{dm_{outlet-gas}}{d\varphi_1} d\varphi_1 - \int_{\varphi_{1suc.stop}}^{\varphi_{1dis.start}} \frac{dm_{SE}}{d\varphi_1} d\varphi_1 - \\ & \int_0^{\varphi_{1dis.start}} \frac{dm_{drained-gas}}{d\varphi_1} d\varphi_1 - \int_0^{\varphi_{1max}} \frac{dm_{oil:flash-gas}}{d\varphi_1} d\varphi_1 - \\ & \int_{\varphi_{1suc.stop}}^{\varphi_{1max}} \frac{dm_{LRI:flash-gas}}{d\varphi_1} d\varphi_1 \Big) \end{aligned} \tag{57}$$

The total oil injection flow rate, drained oil flow rate, gas flow rate from superfeed and injected liquid refrigerant flow rate are calculated by the following equations respectively:

$$Q_{OI} = z_1 W_1 \int_0^{\varphi_{1max}} \frac{dm_{OI}}{d\varphi_1} d\varphi_1 \tag{58}$$

$$Q_{OD} = z_1 W_1 \int_0^{\varphi_{1dis.start}} \frac{dm_{OD}}{d\varphi_1} d\varphi_1 + \int_0^{\varphi_{1dis.start}} \frac{dm_{drained-gas}}{d\varphi_1} d\varphi_1 \tag{59}$$

$$Q_{SF} = z_1 W_1 \int_{\varphi_{1suc.stop}}^{\varphi_{1dis.start}} \frac{dm_{SF}}{d\varphi_1} d\varphi_1 \tag{60}$$

$$Q_{LRI} = z_1 W_1 \int_{\varphi_{1suc.stop}}^{\varphi_{1max}} \frac{dm_{LRI:port}}{d\varphi_1} d\varphi_1 \tag{61}$$

The following equations calculate the total refrigerant flash rate from the injected liquid refrigerant, the total refrigerant available for flashing from the oil and flash rate from the oil respectively:

$$Q_{LRI:flash-gas} = z_1 W_1 \int_{\varphi_{1suc.stop}}^{\varphi_{1max}} \frac{dm_{LRI:flash-gas}}{d\varphi_1} d\varphi_1 \tag{62}$$

$$Q_{LR} = z_1 W_1 \int_0^{\varphi_{1max}} \frac{dm_{LR}}{d\varphi_1} d\varphi_1 \tag{63}$$

$$Q_{oil:flash-gas} = z_1 W_1 \int_0^{\varphi_{1max}} \frac{dm_{oil:flash-gas}}{d\varphi_1} d\varphi_1 \tag{64}$$

The indicated and total powers of the compressor are calculated by the following two equations respectively:

$$P_{ind} = \frac{z_1 W_1}{60 \times 1000} \oint pdV \tag{65}$$

$$P_{input} = P_{ind} + P_{endcasing} + P_{maincasing} \tag{66}$$

The volumetric, indicated, total and mechanical efficiencies of the compressor are defined as follows:

$$\eta_{vol} = \frac{Q_{mass} v_1}{z_1 W_1 V_r \times 10^{-9}} \times 100\% \tag{67}$$

$$\eta_{ind} = \frac{P_{isentropic}}{P_{ind}} \times 100\% \tag{68}$$

$$\eta_{total} = \frac{P_{isentropic}}{P_{input}} \times 100\% \tag{69}$$

$$\eta_{mechanical} = \frac{P_{ind}}{P_{input}} \times 100\% \tag{70}$$

Many other equations, such as the equation used to calculate the total input torque, the input torque due to gas pressure, the isentropic power, and the volumetric efficiency reductions due to leakage through every leakage path etc., are easy to develop and are not listed here.

4.4.12 Determination of the Important Coefficients

In the mathematical model, important coefficients are used. Some of them have different values depending on circumstances, others, are constants. These coefficients could be modified in the future as more measured data becomes available and as analytical technique progresses. The structure of the existing program gives some scope for this.

Measured p-V diagrams were not available to the author in order to test the $p - V$ diagrams generated by the mathematical model as was done by other research workers (**14**, **19** and **20**). The author believes that this is very important and should be done at the earliest opportunity. However the measured performance data of many years from Howden Compressors Ltd. and the geometrical details for the tested machines gave the author the opportunity of determining the most important coefficients used in the mathematical model and of testing the corresponding simulation program developed for different sized machines with different profiles and working under different working conditions.

Coefficient c_{speed} is used to modify the flow speed calculated based on the assumption of the isentropic and one-dimensional flow. This coefficient is determined according to the measured volumetric efficiency. Theoretically for different flowing paths in the twin screw compressor, this coefficient could be different due to their different shapes. The leakage paths across the rotor tips are like an orifice plate if sealing strips exist, the leakage paths across the rotor suction and discharge end faces are like a narrow passage between two parallel plates and the others are like nozzles. The author applied two procedures to determine the coefficient. The first treats the coefficient not to be equal for different flowing paths,

and the second uses the same coefficient for all paths. In the first procedure, it is difficult to decide the difference between the coefficients used for different flowing paths. Although the measured or theoretical data for standard orifices and turbine nozzle flow coefficients are available, they are supposed to be used for dry gas or steam only. In the second procedure, the coefficient is much easier to determine, and comparing the predicted volumetric efficiency with the measured volumetric efficiency, it can be decided. In the existing program, coefficient c_{speed} is decided by the second procedure, and the agreement between the predicted and measured results is good, although it is to be expected that the predicted leakage *distribution* will be less good then that derived from non-constant coefficients.

The heat transfer coefficient between the oil and gas in the control volume is decided according to the gas discharge temperature. The real gas temperature in the discharge chamber is important for this procedure. Usually the discharge temperature is measured in the discharge line just after the discharge chamber, which is not the real discharge temperature due to the following two reasons: heat transfer continues in the discharge line and an oil film will probably exist on the sensing element of the thermometer. The real gas temperature in the discharge chamber must be higher than the measured discharge temperature. In the procedure to decide the heat transfer coefficient, the measured discharge temperature is increased by $20 - 30°C$ to account for these effects. For future work, the author suggests that a model be developed to simulate the flowing process in the discharge chamber and line and also that corresponding measurement be made.

The heat transfer coefficient has a weak influence on the volumetric efficiency but a strong influence on the discharge temperature. As a result, the following procedure was adopted: (i) Beginning with a guessed heat transfer coefficient according to experience (**3** and 4), c_{speed} is varied until the model predicts the measured volumetric efficiency; (ii) Making use of the new c_{speed} obtained by (i), the heat transfer coefficient is then varied until the model predicts the (adjusted) measured discharge temperature. Making use of the new heat transfer coefficient (i) is then repeated and then (ii) etc. In fact this iterative process converges very rapidly due to the weak coupling between the heat transfer and leakage effect as

described above. At this stage, it is supposed that the correct $p - V$ diagrams and the indicated power of the compressor can be calculated, and then according to the difference between the calculated indicated power and the measured total input power coefficient c_{main1} is determined.

The above important coefficients are determined on a medium size machine which has a medium ratio of diameter to length, medium volume and pressure ratios and medium rotational speed, and then the simulation program is checked against measured results for various size machines and various working conditions. The coefficients are influenced by working fluid, profile and the oil used.

4.5 COMPUTER PROGRAM FOR THE MATHEMATICAL MODEL

In accordance with the foregoing theory and mathematical model, a computer program has been developed, and its flow diagram is shown in Fig. 4.5. Before this program is run the program which calculates the geometrical characteristics of the compressor should be run first (see Chapter 3), as the simulation program needs to read all the required data files from the outputs of the geometrical characteristic calculation program.

4.5.1 Input for the Simulation Program

The simulation program reads following data files generated by the geometrical characteristic calculation program:

1. The contact line length between the rotors.
2. The blow hole areas.
3. The male and female rotor tip sealing line lengths.
4. The rotor end face sealing line length at the suction end.
5. The rotor end face sealing line lengths at the discharge end between the leading and following cavities and between the discharge and suction pressures.

6. The oil draining and injection, liquid refrigerant injection and superfeed port areas.
7. The slide-valve by-pass port area.
8. The cavity volume.
9. The axial and radial suction port areas.
10. The axial, radial discharge port areas and the equivalent discharge port area.

The clearances in the compressor, operating conditions and other parameters must be entered by the user in the places requested by the program (**21**).

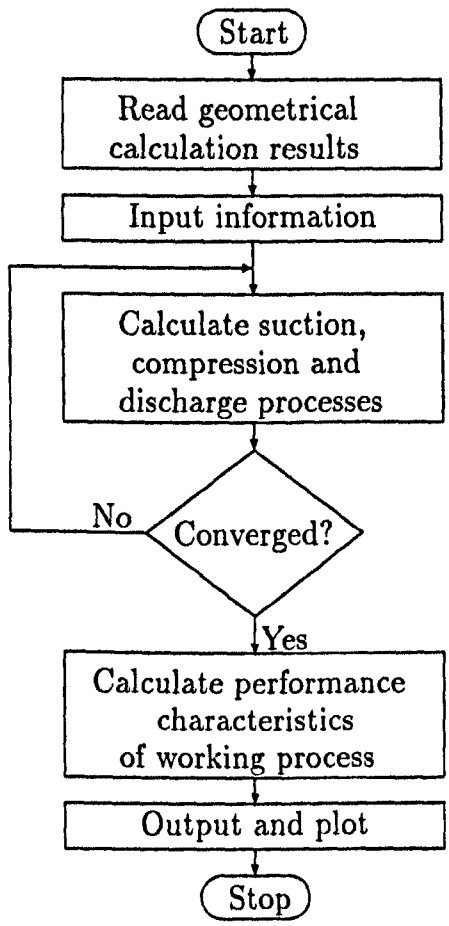

Fig. 4.5 Process calculation flow diagram

4.5.2 Thermodynamic Property Subroutines of the Simulation Program

Many thermodynamic properties of refrigerants are required by the working process mathematical model, and these thermodynamic properties are calculated by subroutines in the working process simulation program. So far four refrigerants, that is, R12, R22, R134a and R717, are considered in the program, and the thermodynamic property equations described in Appendix E are used in the subroutines to calculate the required properties. The structures of the working process simulation program and the property calculation subroutines make it very easy to include other refrigerants including binary refrigerants if the required property equations or the required property calculation subroutines are known. The following subroutines are used to calculate the properties of different refrigerants in the simulation program:

1. **PROP1**(p_{vapour}, t, $fluid$)

   This subroutine is used to calculate the saturated vapour pressure of the chosen refrigerant from the given saturated vapour temperature. The vapour pressure equation for every refrigerant is used in the subroutine.

2. **PROP2**(v_{gas}, p, t_{gas}, $fluid$)

   This subroutine is used to calculate the specific volume from the given vapour pressure and temperature. The equation of state is used in the subroutine.

3. **PROP3**(p, t_{gas}, v_{gas}, $fluid$)

   This subroutine is used to calculate the vapour pressure from the given vapour temperature and specific volume. The equation of state is used in the subroutine.

4. **PROP4**(h_{gas}, p, t_{gas}, v_{gas}, $fluid$)

   This subroutine is ued to calculate the vapour enthalpy of the chosen refrigerant from the given vapour pressure, temperature and specific volume. The property equation for enthalpy of vapour is used in the subroutine.

5. **PROP5**(s_{gas}, t_{gas}, v_{gas}, $fluid$)

   This subroutine is used to calculate the vapour entropy of the chosen refrigerant from the given vapour temperature and specific volume. The property equation for entropy of vapour is used in the subroutine.

6. **PROP6**(t_{gas}, p, s_{gas}, *fluid*)

   This subroutine is used to calculate the vapour temperature of the chosen refrigerant from its given vapour pressure and entropy. The property equation for entropy of vapour is used in the subroutine.

7. **PROP7**(t, p_{vapour}, *fluid*)

   This subroutine is used to calculate the saturated vapour temperature from the given saturated vapour pressure. The vapour pressure equation is used in the subroutine.

8. **PROP8**(t_{gas}, p, v_{gas}, *fluid*)

   This subroutine is used to calculate the vapour temperature from the given vapour pressure and specific volume. The equation of state is used in the subroutine.

9. **PROP9**(u, t_{gas}, v_{gas}, *fluid*)

   This subroutine is used to calculate the vapour internal energy of the chosen refrigerant from the given vapour temperature and specific volume. The property equation for enthalpy of vapour is used in the subroutine.

10. **PROP10**(v_{liquid}, t, *fluid*)

    This subroutine is used to calculate the liquid specific volume of the chosen refrigerant from its given liquid temperature. The property equation for liquid density is used in the subroutine.

11. **PROP11**(H_{lat}, p_{vapour}, t, v_{gas}, v_{liquid}, *fluid*)

    This subroutine is used to calculate the vaporisation latent heat of the chosen refrigerant from its given saturated pressure, saturated temperature, specific volume of saturated vapour and specific volume of saturated liquid. The property equation for latent heat is used in the subroutine.

12. **PROP12**(t_{gas}, v_{gas}, u, *fluid*)

    This subroutine is used to calculate the vapour temperature from the given vapour specific volume and internal energy. The property equation for enthalpy of vapour is used in the subroutine.

There is another subroutine which is used to calculate the maximum flow speed through any leakage path, and also local sound speed and Mach number.

This subroutine calls the above property calculation subroutines, but it does not need to be changed when other refrigerants are considered. This subroutine greatly lengthens the computer running time.

4.5.3 Output from the Simulation Program

Before the calculated results have acceptable accuracy, ie the iteration procedure has given a difference between two consecutive pressure volume graphs which is smaller than a small value prescribed in advance, for example, $0.01bar$ in the simulation program, three to four calculation loops are required. During the first loop the leakage through any leakage path is not considered. The purpose of the first loop of calculation is to get the initial values for the second loop of calculation.

Mach number is an important thermodynamic parameter for the suction, discharge and for every leakage process etc. In the working process simulation program the local speed of sound and Mach number are calculated for the suction, discharge and for every leakage process. If the pressure difference is big enough across a leakage path, the flow speed at the position of the minimum area along the leakage path may reach the speed of sound. When this happens, the speed of sound will be used to calculate the leakage rate through the leakage path, and the leakage rate is then at its maximum.

The working process simulation program calculates all the parameters and efficiencies (volumetric, isentropic indicated and total efficiencies) etc. to describe the behaviour of the compressor, which may be required by a designer or researcher, and outputs them into a data file (**21**). In this thesis all the performance prediction results are obtained by this program.

The working process simulation program calculates and outputs the following gas thermodynamic properties in the control volume in terms of rotational angle of male rotor or cavity volume and outputs them into different data files:

1. The pressure of the compressed gas.
2. The specific volume of the compressed gas.

3. The temperature of the compressed gas.
4. The entropy of the compressed gas.
5. The total internal energy of the compressed gas in the control volume.
6. The total mass of the compressed gas in the control volume.
7. The speed of sound in the control volume.
8. The flow speed of the suction and discharge processes.
9. Mach number of the suction and discharge processes.
10. The temperature of the oil in the control volume.

A display program has been developed to show the results of the simulation program on a monitor. This program can show the following diagrams on the monitor:

1. The p-V diagram.
2. Pressure in the cavity vs the rotational angle of the male rotor.
3. Gas temperature in the cavity vs the cavity volume.
4. Gas temperature in the cavity vs the rotational angle of the male rotor.
5. Total gas mass in the cavity vs the cavity volume.
6. Total gas mass in the cavity vs the rotational angle of the male rotor.
7. Gas entropy in the cavity vs the cavity volume.
8. Gas entropy in the cavity vs the rotational angle of the male rotor.
9. Mach number of the suction and discharge flow vs the rotational angle of the male rotor.
10. The temperature of the oil in the cavity vs the cavity volume.

4.5.4 Limitations of the Working Process Simulation Program

If the vapour in the cavity is compressed into its two-phase region, the working process simulation program will not continue the simulation for the compression process. When this happens, an error message will appear on the monitor and the program stops. Usually the vapour in the cavity cannot be compressed into

two-phase area, but if some input parameters describing the operating condition of the compressor are not physically reasonable, it could happen. For example, too much liquid refrigerant injection or too much oil injection can result in the vapour in the cavity being compressed into its two-phase region.

All the parameters input to the program should be physically reasonable, otherwise errors may appear.

4.6 AN EXAMPLE OF WORKING PROCESS SIMULATION

This section presents an example of working process simulation. The simulation results are explained, analysed, and compared with the test results. The analysis of the simulation results helps the understanding of the behaviour of the compressor.

4.6.1 Specification of the Simulated Compressor

The specification of the simulated twin screw compressor is as follows:

- Refrigeration twin screw compressor—Mk. 1/XRV 204/16526/002P made by Howden Compressors Ltd.
- Rotor lobe profile—SRM D standard.
- Male and female rotor diameters (equal): 203.92mm.
- Male rotor wrap angle: 299.2°.
- Length/diameter ratio: 1.65.
- Volume ratio for the axial discharge port: 5.00.
- Volume ratio for the radial discharge port on the slide valve: 2.60.

4.6.2 Running Conditions of the Simulated Compressor

The running conditions of the simulated compressor are as follows:

- Refrigerant: $R22$.

- Speed of male (driven) rotor: 3000 rev/min.
- Condensing temperature: 25°C (saturation pressure: 10.44 bar).
- Evaporating temperature: −5°C (saturation pressure: 4.21 bar).
- Suction superheat degrees: 30°C.
- Oil injected and drained.
- No liquid refrigerant injected.
- The superfeed is not on duty.
- The compressor is on full load.

4.6.3 Comparison between Predictions and Test Results

When the working process simulation program is run, it reads the required calculation results of the geometrical characteristic calculation program automatically. The geometrical characteristics are calculated according to the specification of the simulated compressor. The working process simulation program simulates the suction, compression and discharge processes of the compressor. The simulation results are output into a data file after the iteration procedure has given a maximum difference between two consecutive pressure volume graphs which is smaller than 0.01bar. Three loops are needed for the given operating condition.

The system diagram of the measurement rig used by Howden Compressors Ltd. is shown in Appendix F (9). Compressor MK.1/XRV 204/16526/002P has the following test results for the given running conditions (9):

- Volumetric efficiency: 91.8–94.5%.
- Total efficiency: 74%.
- Absorbed power: 173kw.

The predicted results for the same machine are as follows:

- Volumetric efficiency: 93.5%.
- Total efficiency: 75.2%.
- Isentropic indicated efficiency: 82.6%

- Mechanical efficiency: 91.0%
- Absorbed power: 170kw.
- Isentropic power: 127.8kw.
- Indicated power: 154.74.

Compared with the measured results, the volumetric efficiency difference is +0.35% (average measured value is used for the comparison), total efficiency +1.2% and absorbed power −1.73%.

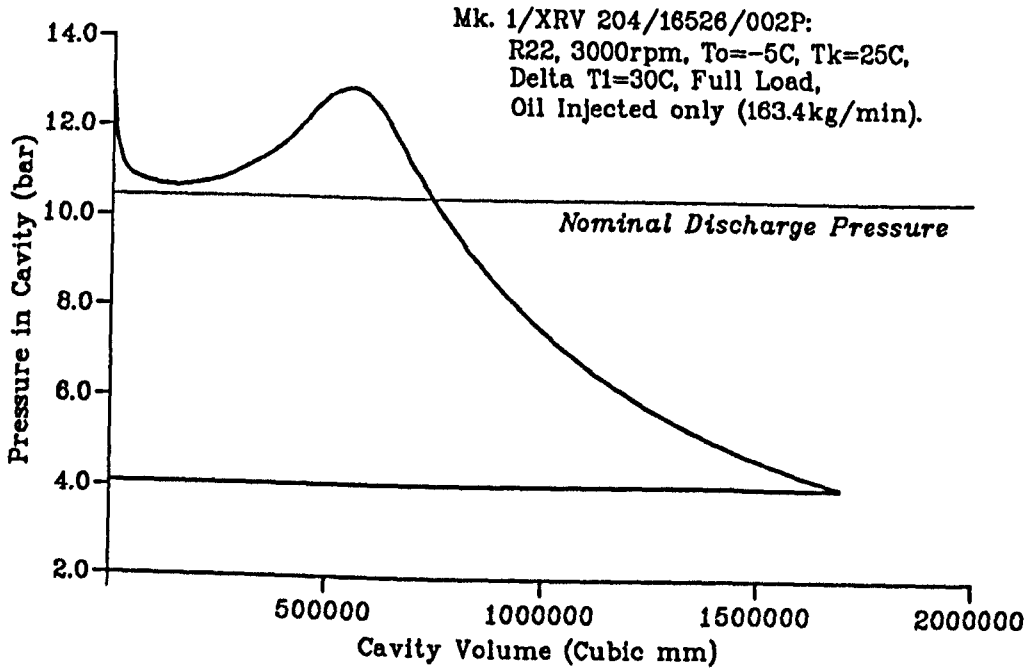

Fig. 4.6 p-V diagram

4.6.4 Analysis of Simulation Results

From prediction results many diagrams describing the behaviour of the compressor can be plotted. The analysis of these diagrams is very helpful towards understanding the behaviour of the compressor, and from the analysis many useful results can be obtained, which may be used to the optimise the design of a compressor.

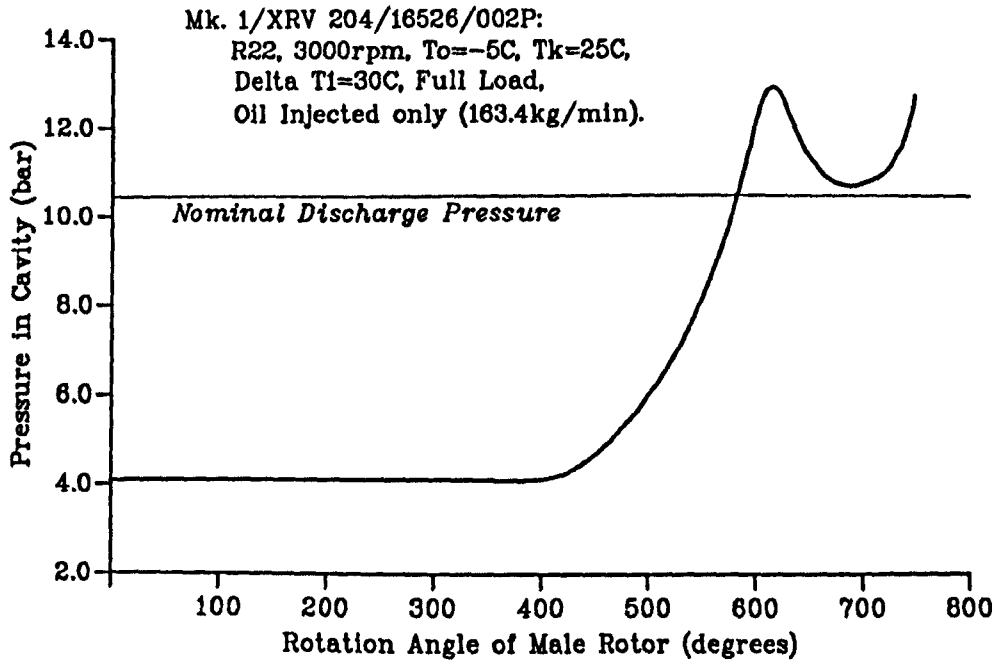

Fig. 4.7 Pressure in the cavity vs the rotational angle of the male rotor

Fig. 4.6 shows the p-V diagram of the compressor, which is the most important diagram the working process simulation program can obtain. The area enclosed by the pressure curve is the indicated work of the compressor from which its indicated power can be calculated easily. A p-V diagram can also show if the discharge port of a compressor is designed optimally for a specific working condition. For example Fig. 4.6 shows that the vapour in the cavity is over-compressed before the discharge process begins, that is the pressure in the cavity is higher than the nominal discharge pressure at the end of the compression process, which results in an increased power consumption. For the specific running condition the discharge port of the compressor is not designed properly, or in other words, the given machine is not suitable for running under the specific running condition. In order to reduce the power consumed and increase the indicated efficiency, the volume ratio for the discharge port design should be reduced if the machine is to run under the specific running condition for a prolonged period. Fig. 4.7 shows the relationship between the pressure in the cavity and the rotational angle of the male rotor, which is the information needed if a force analysis is to be done

for compressor.

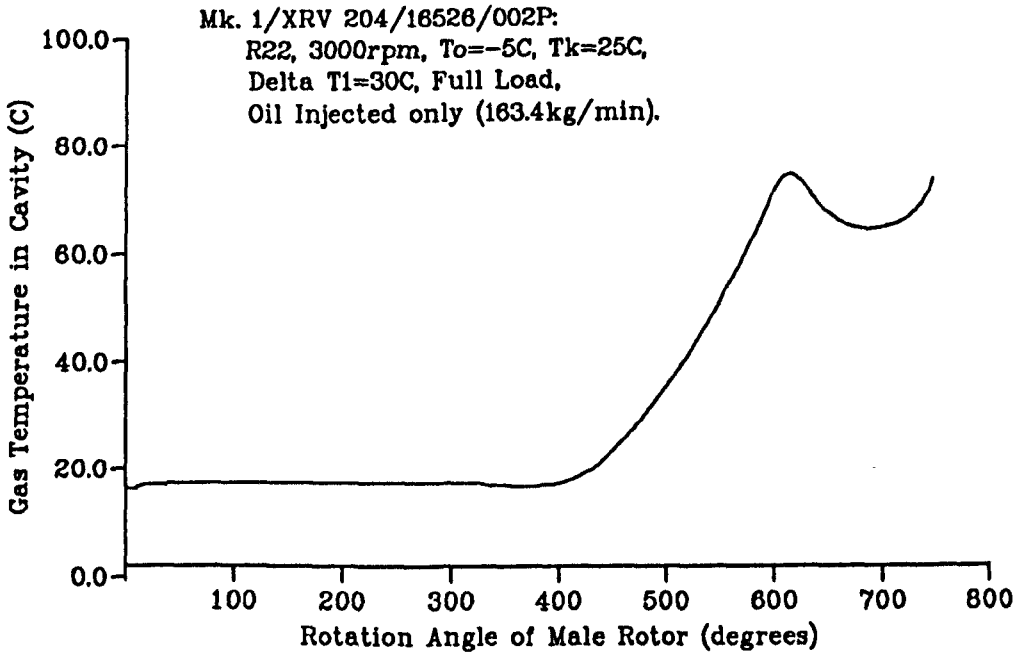

Fig. 4.8 Gas temperature in the cavity vs the rotational angle of the male rotor

Fig. 4.8 shows the relationship between the gas temperature in the cavity and the rotational angle of the male rotor. Fig. 4.9 shows the relationship between the gas mass in the cavity and the rotational angle of the male rotor.

Mach No through the suction and discharge ports is shown in Fig. 4.10. Mach No through the suction port is much lower than through the discharge port. From the beginning of the discharge process, the Mach No increases rapidly and during this period only, the radial discharge port which is designed according to the volume ratio of 2.6, is on duty. Following this period, the axial discharge port becomes effective and the Mach No through the discharge port reduces until its lowest value is reached. After that it begins to increase again, which is due to the discharge pocket volume effect. Generally Mach No through the discharge port is high, and this means that the performance of the compressor is very sensitive to discharge port design.

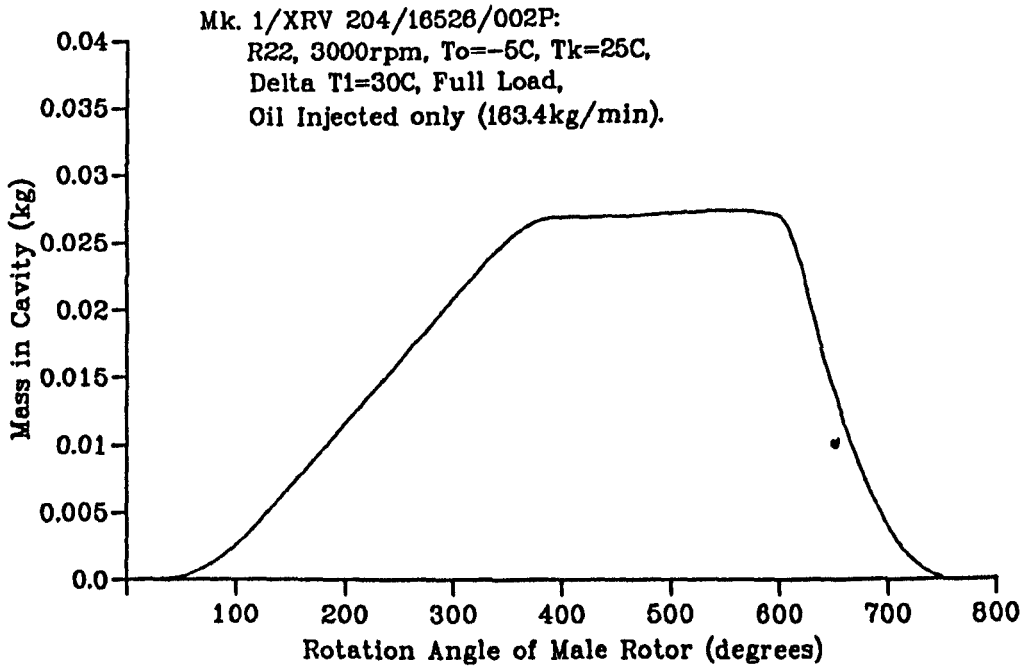

Fig. 4.9 Gas mass in the cavity vs the rotational angle of the male rotor

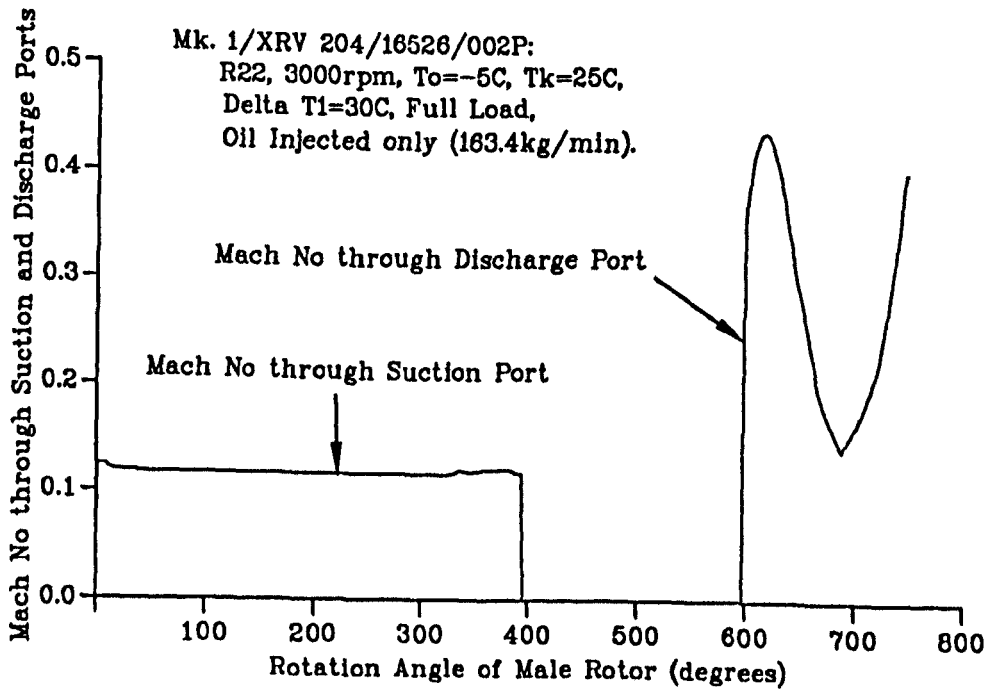

Fig. 4.10 Mach No through the suction and discharge ports vs the rotational angle of the male rotor

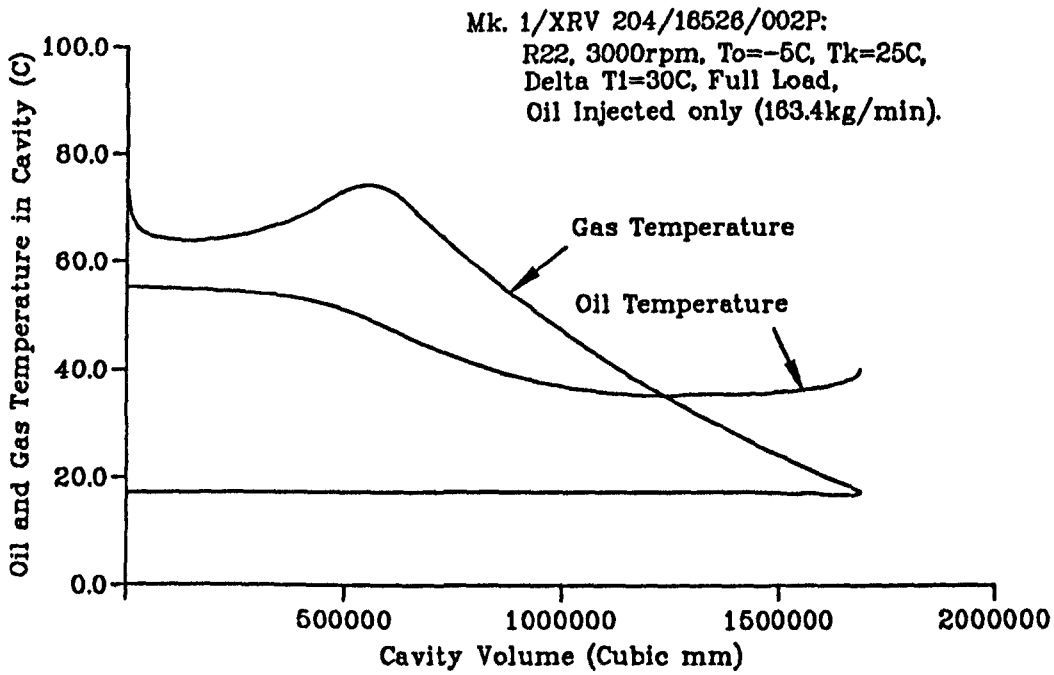

Fig. 4.11 Oil and gas temperatures in the cavity vs cavity volume

Fig. 4.11 shows the relationship between the oil temperature in the cavity and the cavity volume. The oil temperature here is the average temperature of all the oil droplets in the cavity. The gas temperature in the cavity is also presented in the same diagram. As the oil temperature is higher than the gas temperature in the cavity at the beginning of the compression process, the oil gives up heat to the compressed gas and the oil temperature decreases. As the compression process continues, the temperature of the compressed gas gets higher and higher. Once the temperature of the compressed gas is higher than the oil temperature, the oil begins to absorb heat from the compressed gas and its temperature begins to increase.

4.7 SIMULATION AND TEST RESULTS COMPARED

In order to confirm the mathematical model and the working process simulation program, the performance predicted by the working process simulation program is compared with results from compressor tests. The comparison is done

for compressors of different sizes (nominal rotor diameter from 163 mm to 510 mm) with various running conditions (various rotational speeds, full and partial loading, liquid refrigerant injection and oil draining only or oil drained and injected) and different profiles (SRM A and D standards), and part of the comparison results are presented here. The agreement between the predicted and measured results is good and the maximum prediction variation is about $\pm 5\%$. All the measured data is from (9), and the system diagram for the measurement rig is shown in Appendix F.

4.7.1 Simulation and Test Performances for Various Speeds

Figs. 12 to 15 show the simulation and test performances for a fully loaded compressor with a male rotor rotational speed from 1500 rev/min to 4000 rev/min. In every figure, Fig. (a) is used to show the volumetric efficiency and total efficiencies, Fig. (b) to show the calculated and measured input torques of the compressor, and Fig. (c) to show the percentage variations of the calculated results compared with the measured results. The specification of the simulated twin screw compressor is as follows:

- Refrigeration twin screw compressor — WRV204/165 35 made by Howden Compressors Ltd.
- Rotor lobe profile—SRM A standard.
- Male and female rotor diameters (equal): $204mm$.
- Male rotor wrap angle: 300°.
- Length/diameter ratio: 1.65.
- Volume ratio for the axial discharge port: 3.6.
- Volume ratio for the radial discharge port on the slide valve: 3.50.

The running conditions of the simulated compressor are as follows:

- Refrigerant: $R22$.
- Speed of male (driven) rotor: 1500 - 4000 rev/min.
- Condensing temperature: $30°C$ (saturation pressure: 11.92 bar).

- Pressure ratio: 3 - 12.
- Suction superheat degrees: 15 - 20°C.
- Oil drained only.
- Oil temperature: 45°C.
- Oil pressure: Condensing pressure + 1.96 *bar*.
- No liquid refrigerant injected.
- The superfeed is not on duty.
- The compressor is on full load.

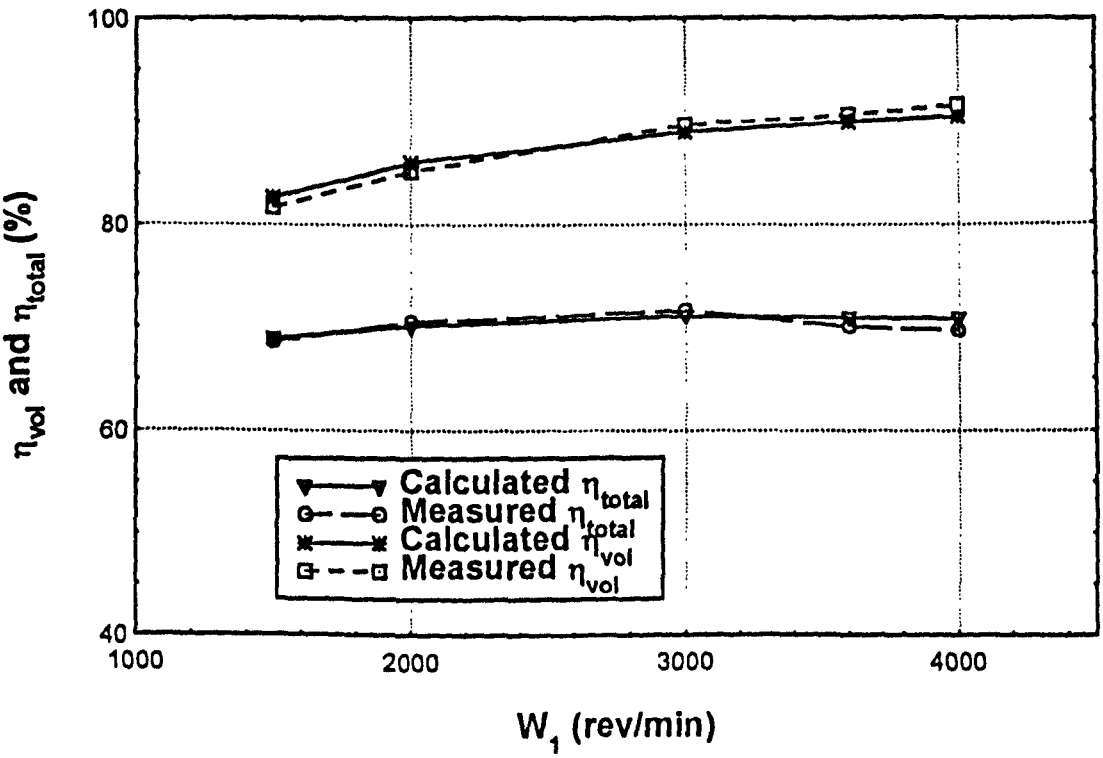

Fig. 4.12 (a) Measured and calculated η_{vol} and η_{total} vs W_1 ($p_2/p_1 = 3.0$)

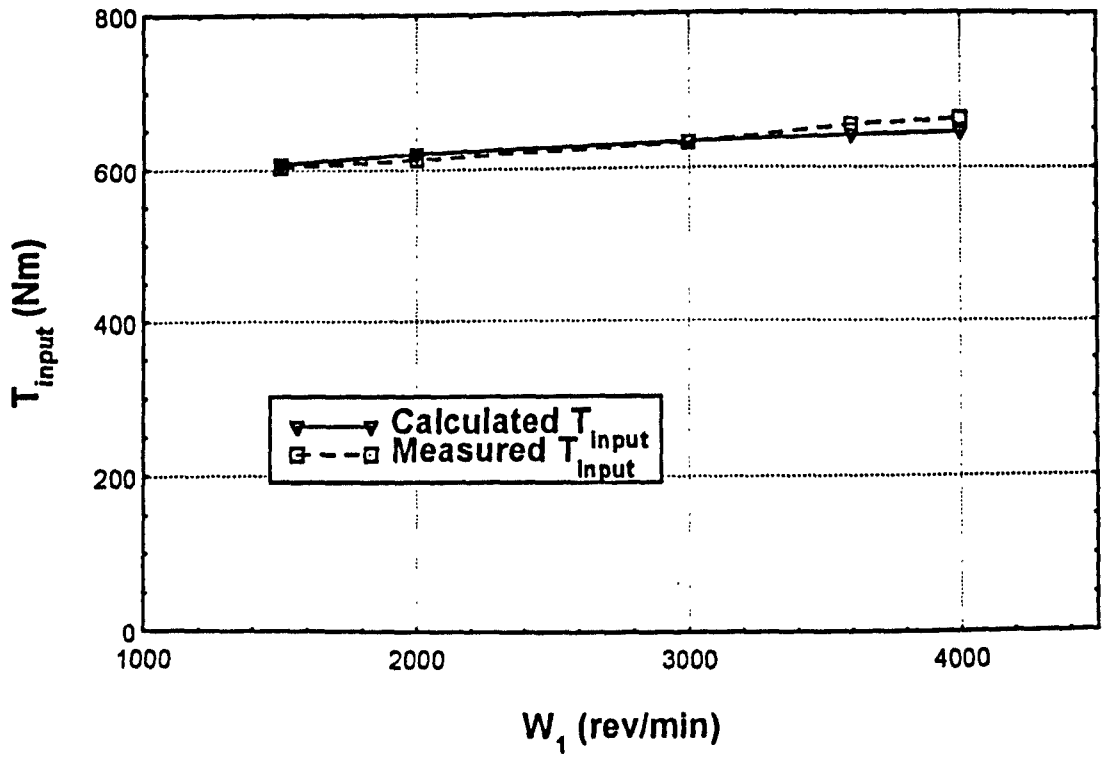

Fig. 4.12 (b) Measured and calculated T_{input} vs W_1 ($p_2/p_1 = 3.0$)

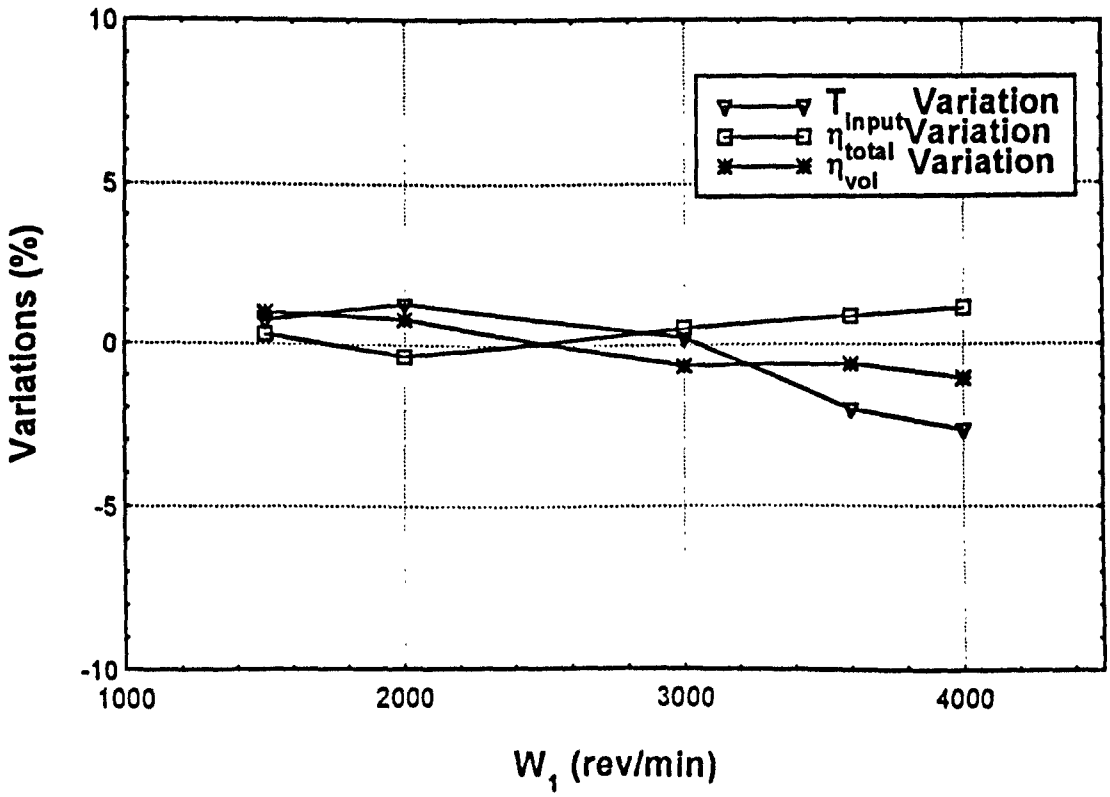

Fig. 4.12 (c) Percentage variations of η_{vol}, η_{total} and T_{input} vs W_1 ($p_2/p_1 = 3.0$)

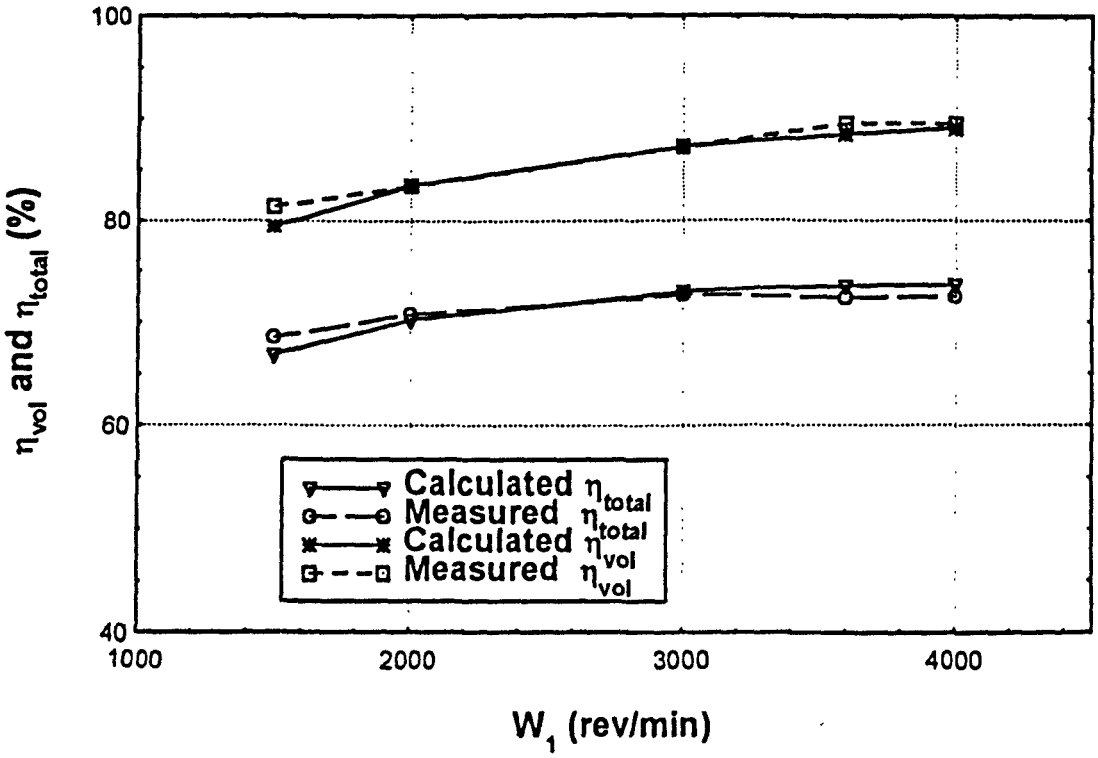

Fig. 4.13 (a) Measured and calculated η_{vol} and η_{total} vs W_1 ($p_2/p_1 = 5.0$)

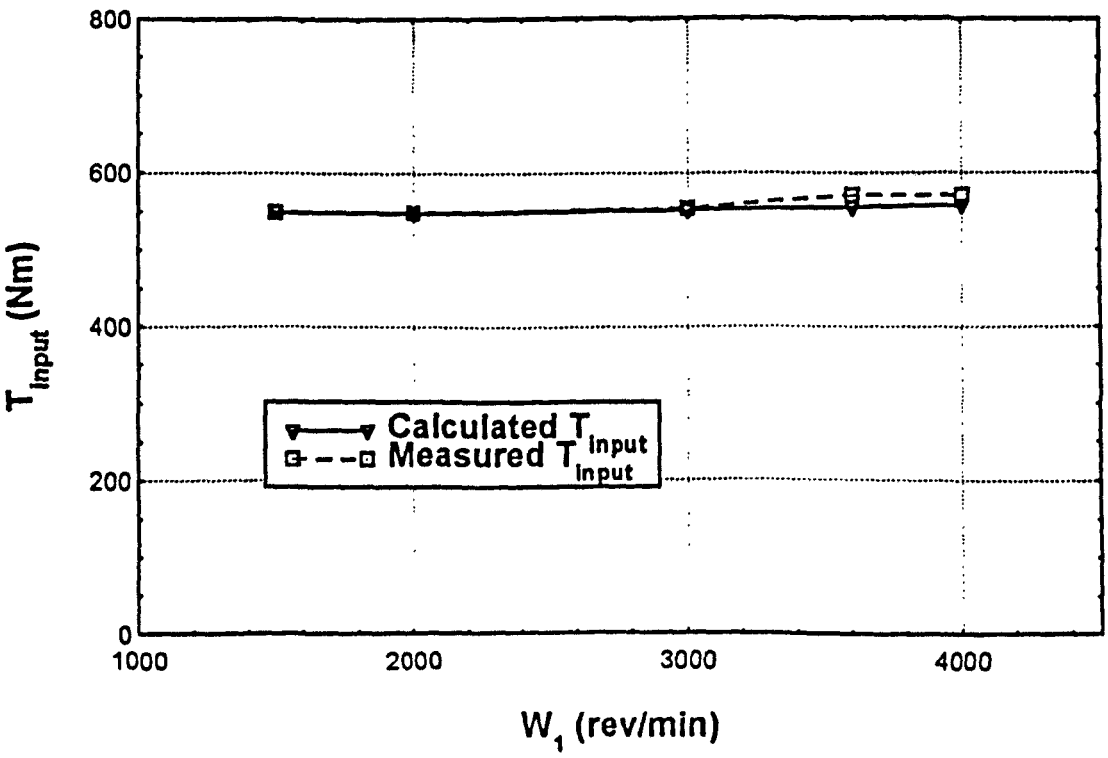

Fig. 4.13 (b) Measured and calculated T_{input} vs W_1 ($p_2/p_1 = 5.0$)

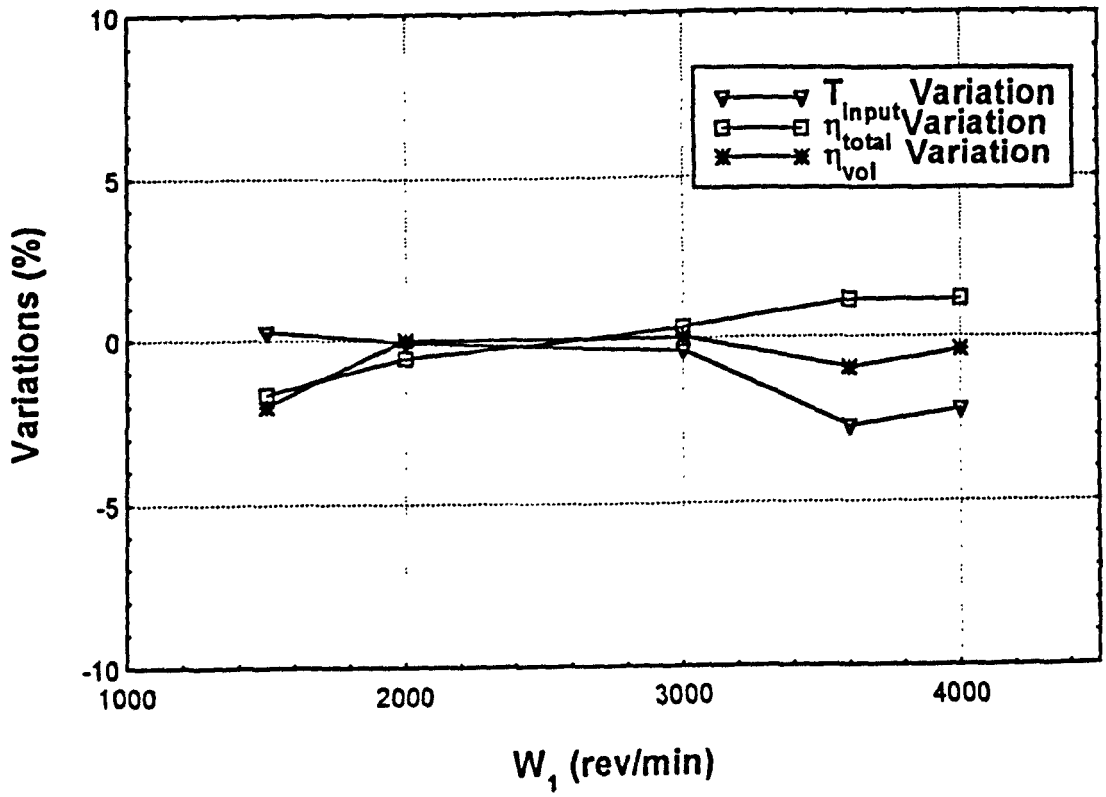

Fig. 4.13 (c) Percentage variations of η_{vol}, η_{total} and T_{input} vs W_1 ($p_2/p_1 = 5.0$)

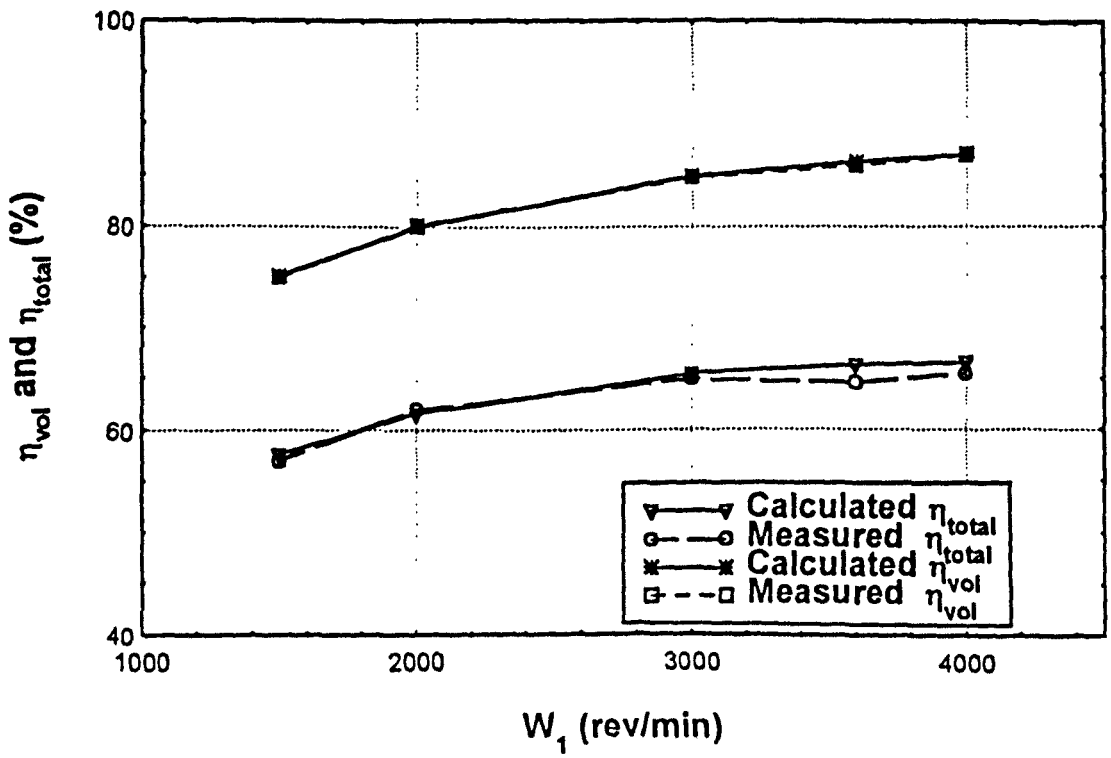

Fig. 4.14 (a) Measured and calculated η_{vol} and η_{total} vs W_1 ($p_2/p_1 = 8.0$)

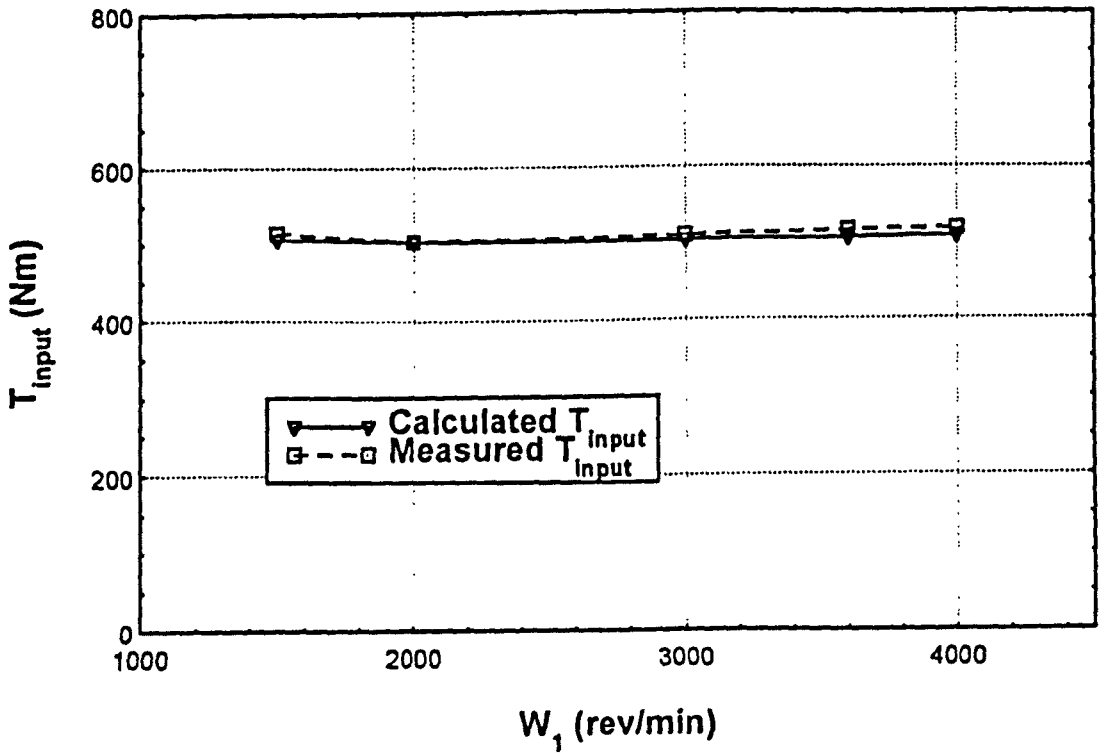

Fig. 4.14 (b) Measured and calculated T_{input} vs W_1 ($p_2/p_1 = 8.0$)

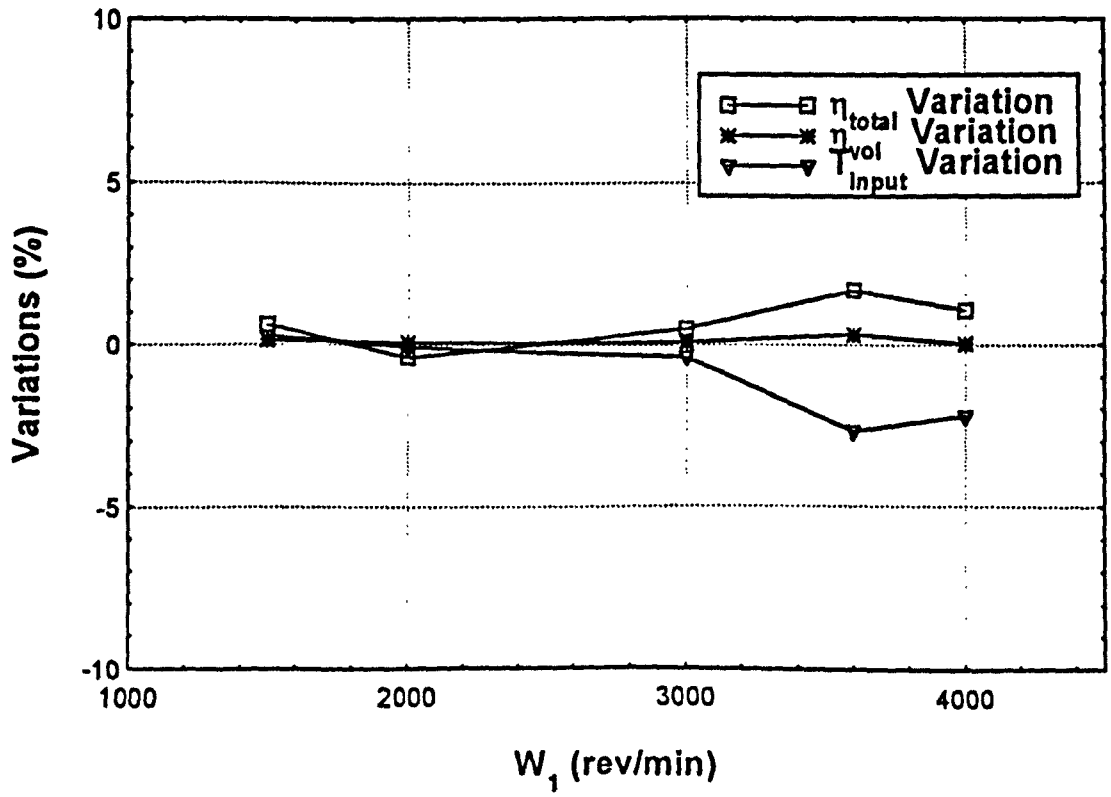

Fig. 4.14 (c) Percentage variations of η_{vol}, η_{total} and T_{input} vs W_1 ($p_2/p_1 = 8.0$)

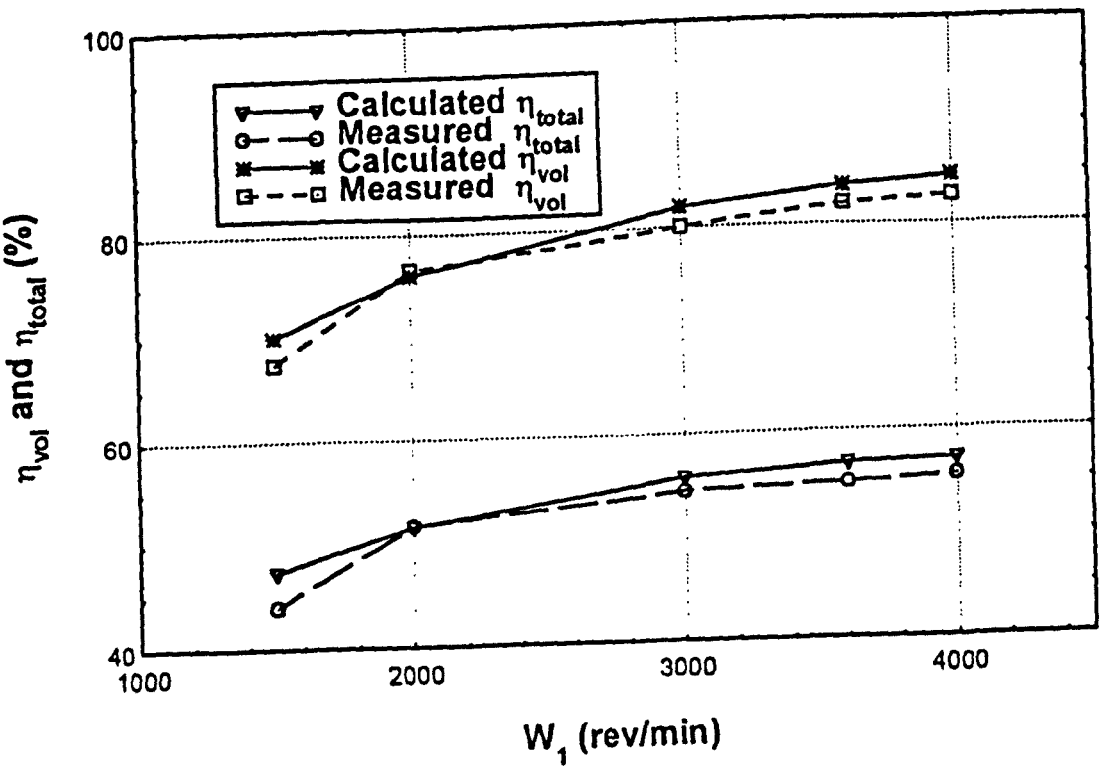

Fig. 4.15 (a) Measured and calculated η_{vol} and η_{total} vs W_1 ($p_2/p_1 = 12.0$)

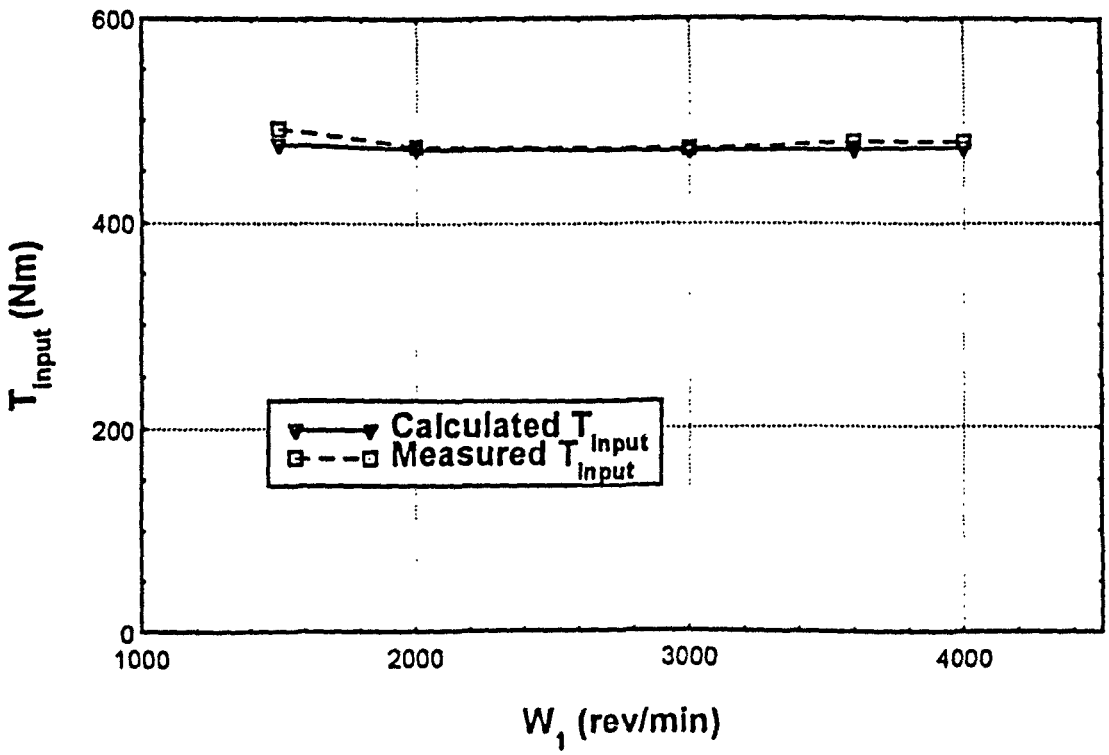

Fig. 4.15 (b) Measured and calculated T_{input} vs W_1 ($p_2/p_1 = 12.0$)

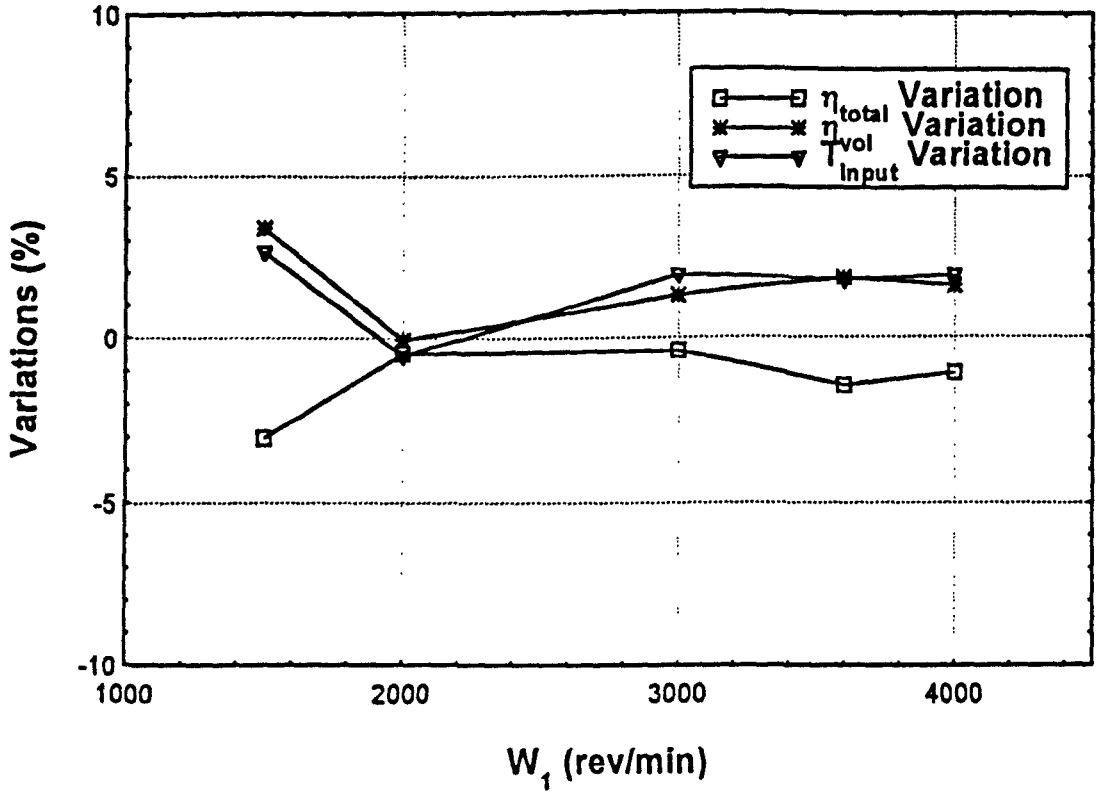

Fig. 4.15 (c) Percentage variations of η_{vol}, η_{total} and T_{input} vs W_1 ($p_2/p_1 = 12.0$)

4.7.2 Simulation and Test Performances for a Full Loaded Compressor

Part of the simulation and test performances for a fully loaded compressor with a different volume ratio for the radial discharge port is shown in Figs. 4.16 to 18. In every figure, Fig. (a) is used to show the volumetric efficiency and total efficiencies, Fig. (b) to show the calculated and measured input powers of the compressor, and Fig. (c) to show the percentage variations of the calculated results compared with the measured results. The calculated volumetric efficiency in Fig. (c) is compared with the average measured result. The specification of the simulated twin screw compressor is as follows:

- Refrigeration twin screw compressor — MK. 1/XRV 204/165 made by Howden Compressors Ltd.
- Rotor lobe profile—SRM D standard.
- Male and female rotor diameters (equal): 203.92mm.

- Male rotor wrap angle: 299.2°.
- Length/diameter ratio: 1.65.
- Volume ratio for the axial discharge port: 5.00.

The running conditions of the simulated compressor for Fig. 4.16 are as follows:

- Refrigerant: *R22*.
- Speed of male (driven) rotor: 3000 rev/min.
- Condensing temperature: 25°C (saturation pressure: 10.44 bar).
- Suction superheat degrees: 30°C.
- Oil drained and injected.
- Oil temperature: 39 - 42°C.
- Oil pressure: $p_1 + (3.4 \sim 5.4)$ bar.
- No liquid refrigerant injected.
- The superfeed is not on duty.
- The compressor is on full load.

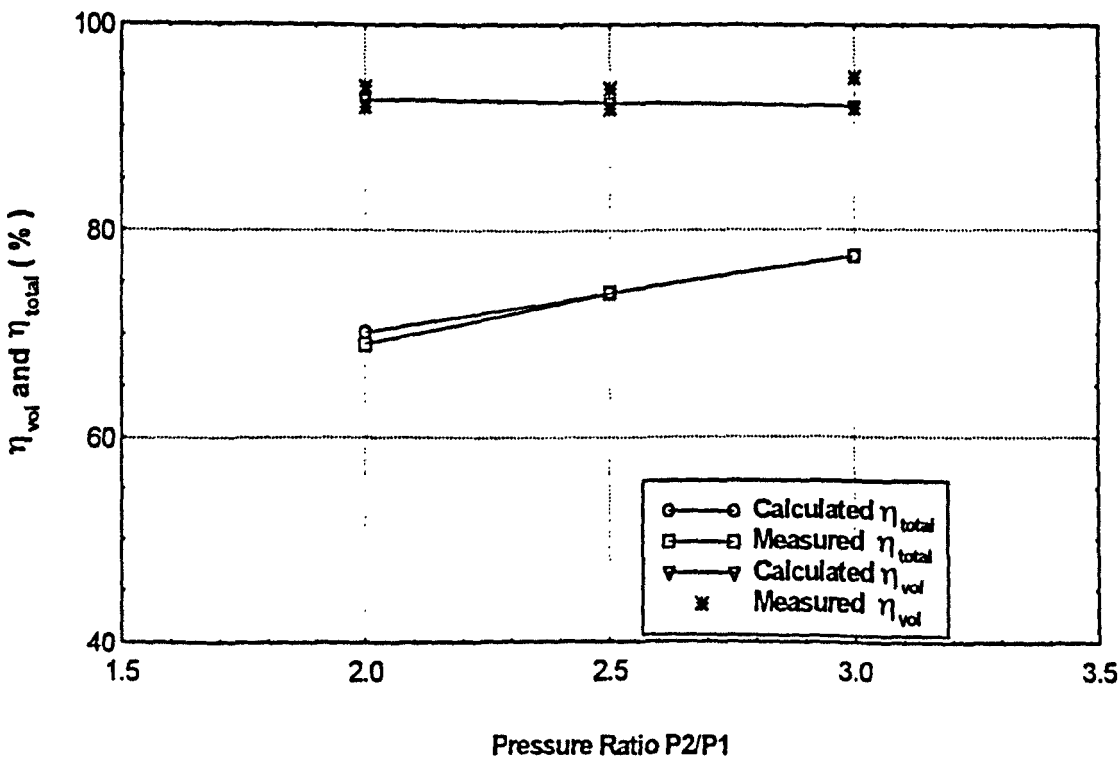

Fig. 4.16 (a) Measured and calculated η_{vol} and η_{total} vs p_2/p_1 ($V_{ir} = 2.6$)

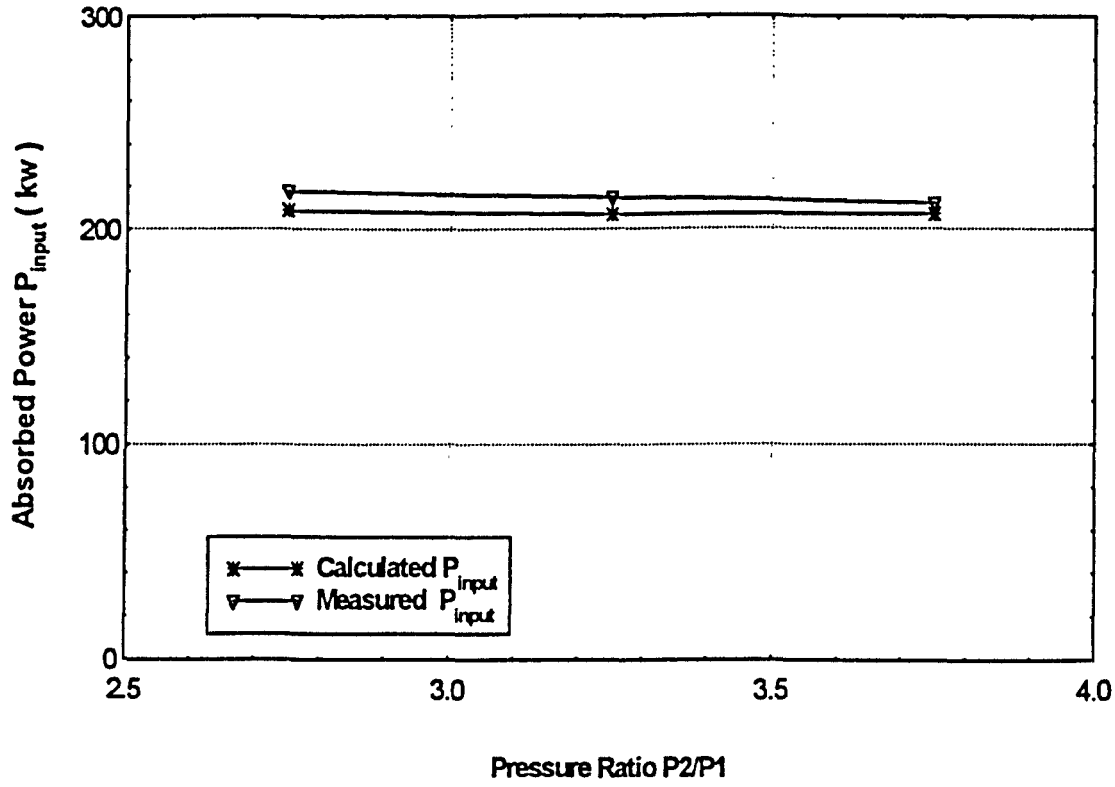

Fig. 4.16 (b) Measured and calculated P_{input} vs p_2/p_1 ($V_{ir} = 2.6$)

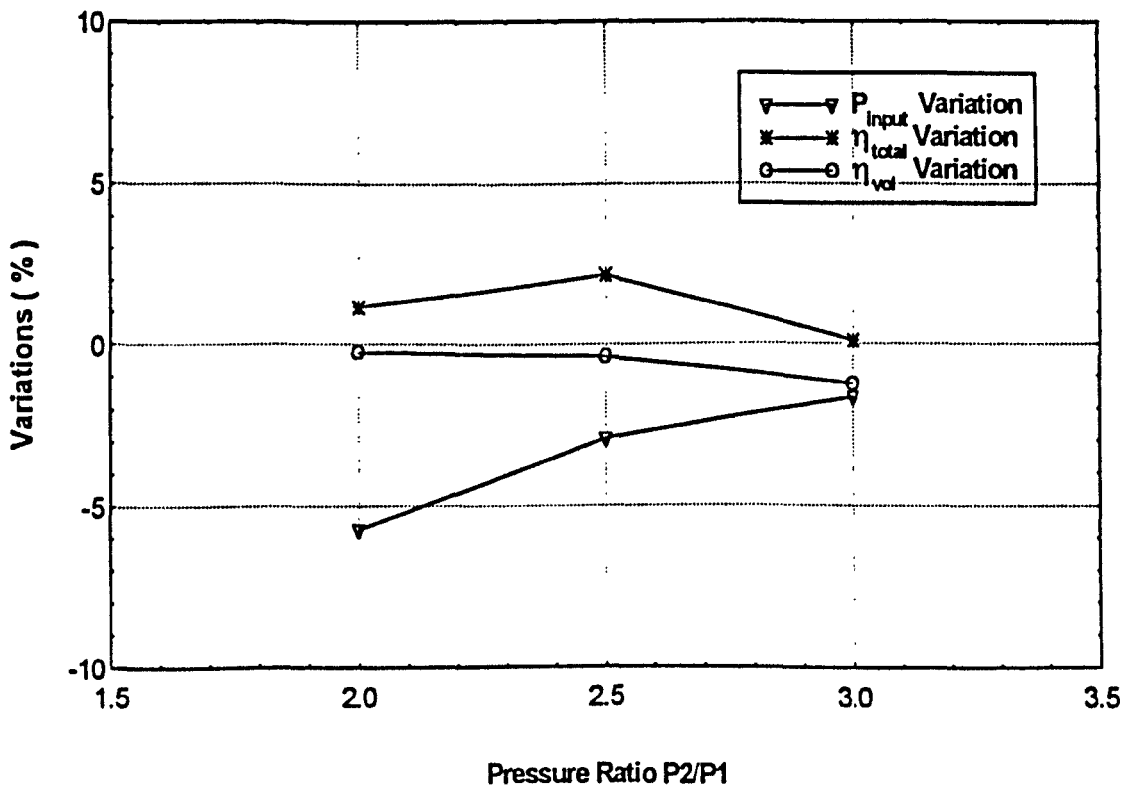

Fig. 4.16 (c) Percentage variations of η_{vol}, η_{total} and P_{input} vs p_2/p_1 ($V_{ir} = 2.6$)

The running conditions of the simulated compressor for Fig. 4.17 are as follows:

- Refrigerant: $R22$.
- Speed of male (driven) rotor: 3000 rev/min.
- Condensing temperature: 25°C (saturation pressure: 10.44 bar).
- Suction superheat degrees: 25 - 35°C.
- Oil drained and injected.
- Oil temperature: 37 - 41°C.
- Oil pressure: $p_1 + (7.5 \sim 8.7)$ bar.
- No liquid refrigerant injected.
- The superfeed is not on duty.
- The compressor is on full load.

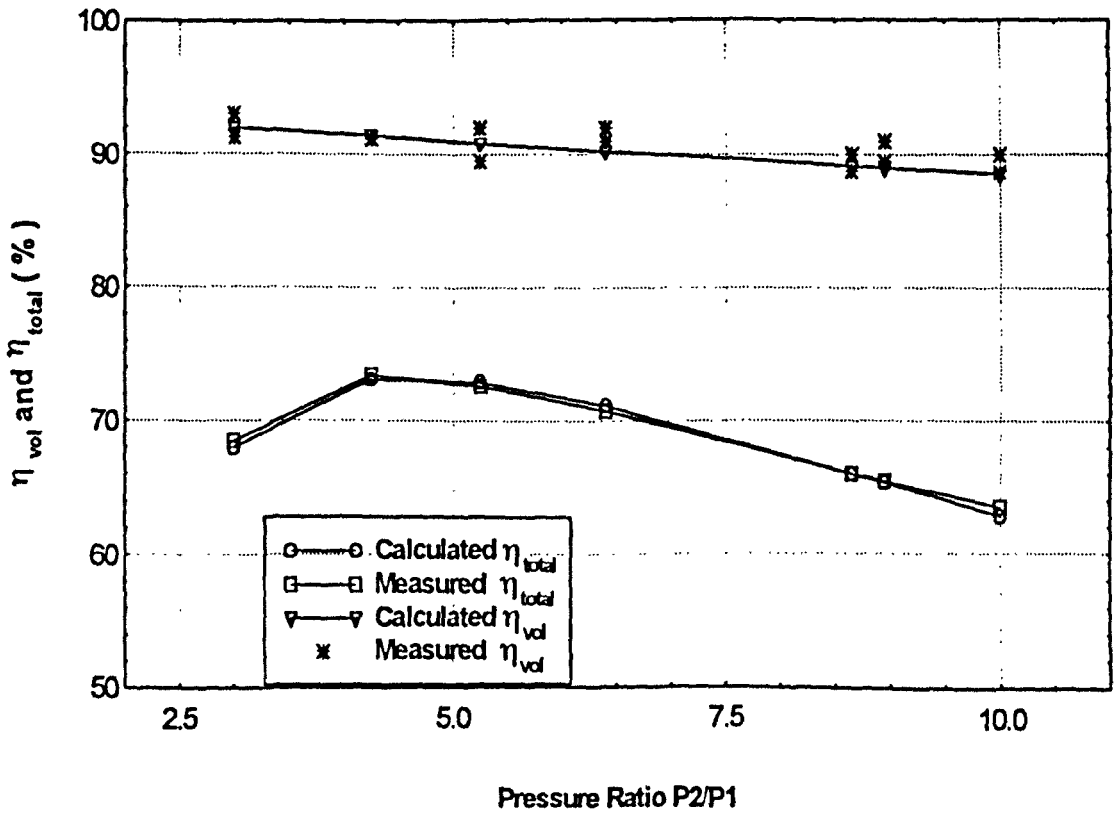

Fig. 4.17 (a) Measured and calculated η_{vol} and η_{total} vs p_2/p_1 ($V_{ir} = 3.6$)

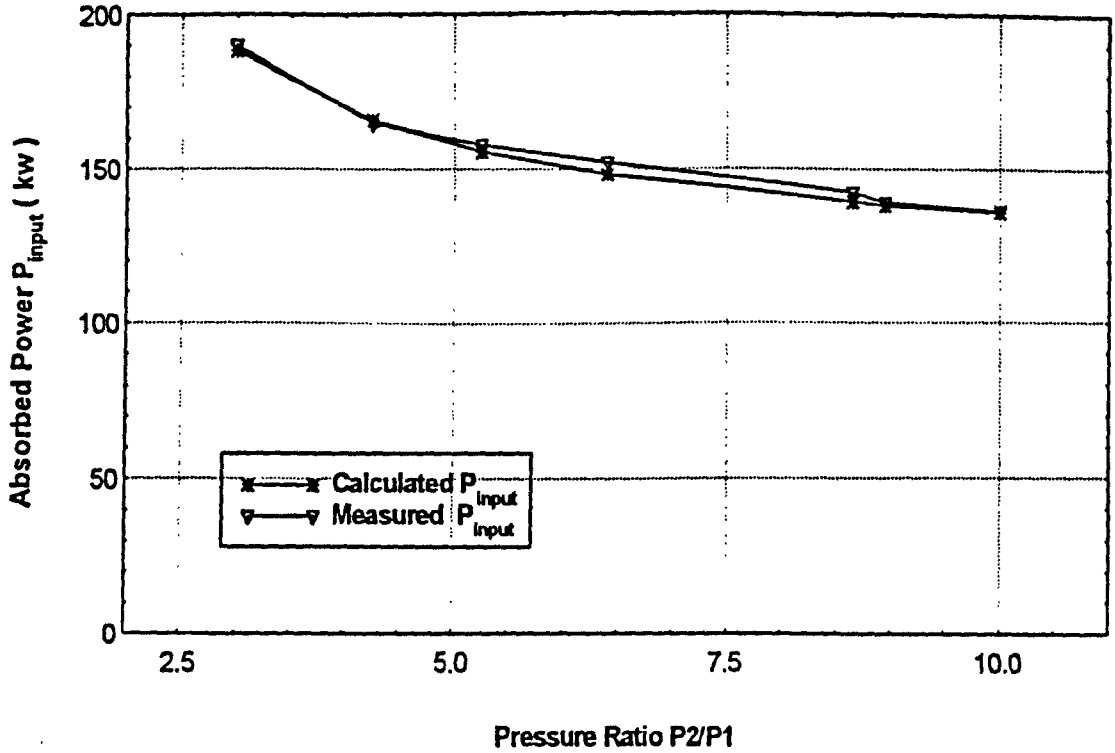

Fig. 4.17 (b) Measured and calculated P_{input} vs p_2/p_1 ($V_{ir} = 3.6$)

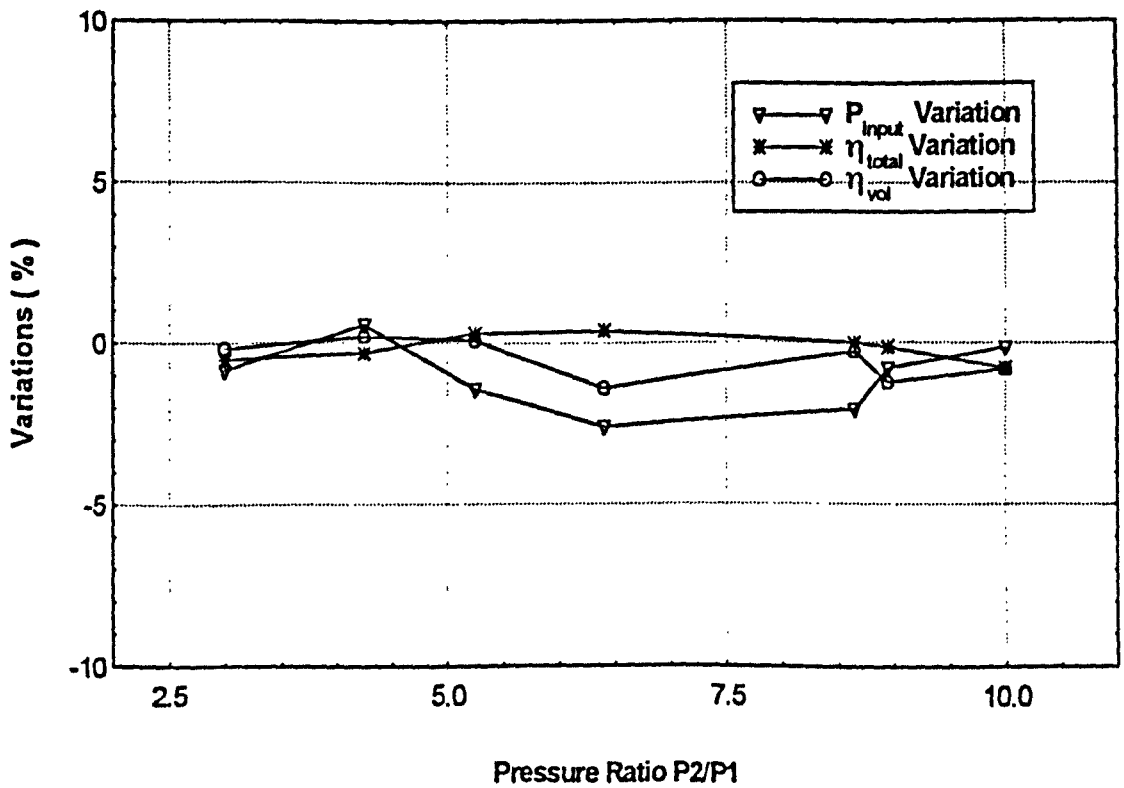

Fig. 4.17 (c) Percentage variations of η_{vol}, η_{total} and P_{input} vs p_2/p_1 ($V_{ir} = 3.6$)

The running conditions of the simulated compressor for Fig. 4.18 are as follows:

- Refrigerant: $R22$.
- Speed of male (driven) rotor: 3000 rev/min.
- Condensing temperature: 25°C (saturation_ pressure: 10.44 bar).
- Suction superheat degrees: 35 – 50°C.
- Oil drained and injected.
- Oil temperature: 42 – 46°C.
- Oil pressure: p_1+ (7.6 ~ 8.8) bar.
- No liquid refrigerant injected.
- The superfeed is not on duty.
- The compressor is on full load.

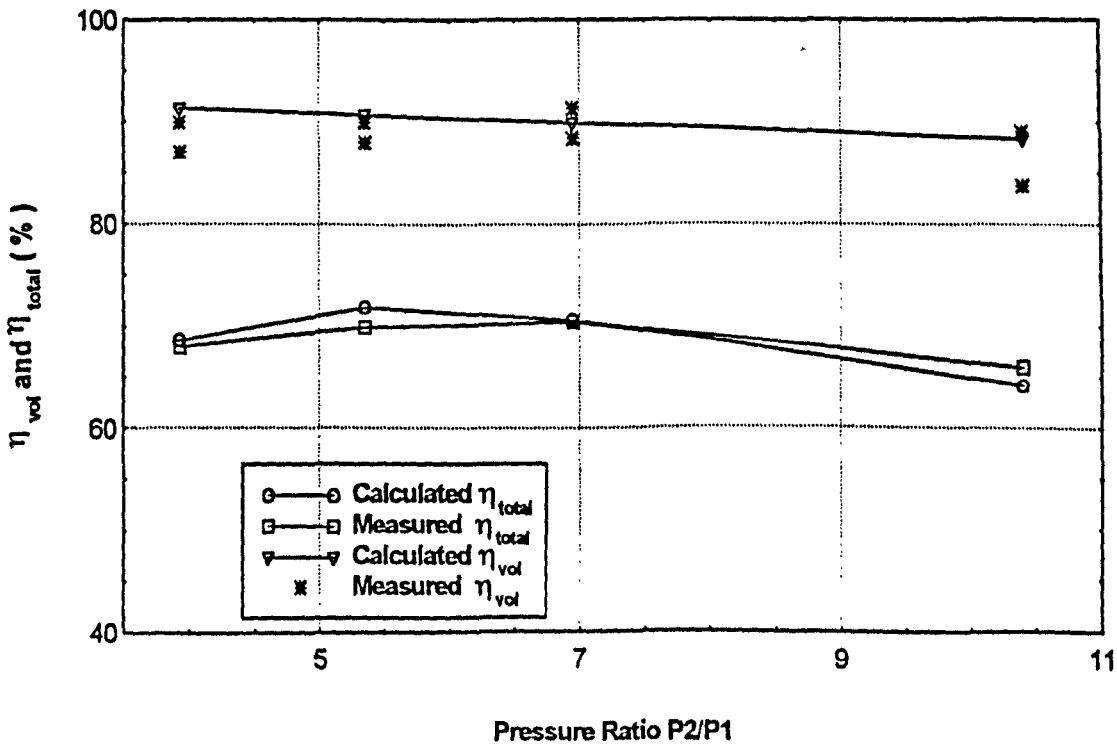

Fig. 4.18 (a) Measured and calculated η_{vol} and η_{total} vs p_2/p_1 (V_{ir} = 5.0)

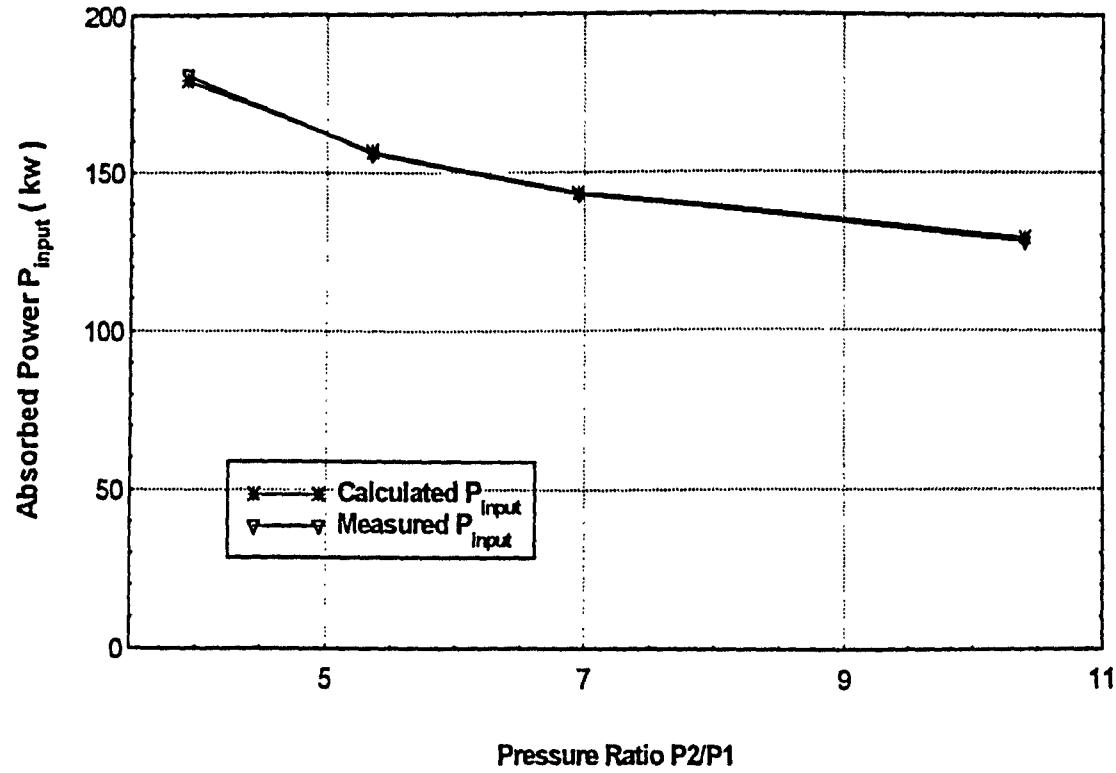

Fig. 4.18 (b) Measured and calculated P_{input} vs p_2/p_1 ($V_{ir} = 5.0$)

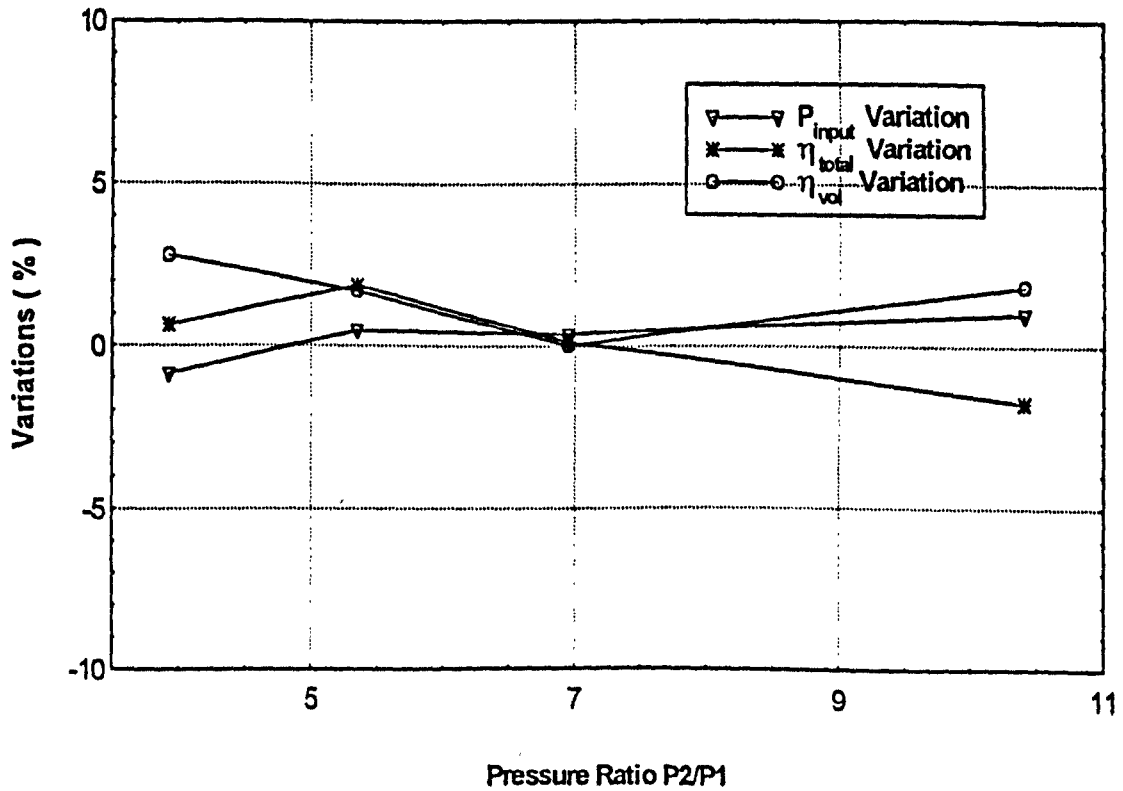

Fig. 4.18 (c) Percentage variations of η_{vol}, η_{total} and P_{input} vs p_2/p_1 ($V_{ir} = 5.0$)

4.7.3 Simulation and Test Performances for Partially Loaded Compressors

When a screw compressor is on a partial load condition due to its slide-valve by-pass port being opened partly, both the capacity and volumetric efficiency will be reduced. Part of the simulation and test performances for partially loaded compressors are shown in Fig. 4.19 to Fig. 4.26.

Fig. 4.19, 4.20, 4.21 and 4.22 show the simulation and test performances for compressor MK. 1/XRV 204/165 with volume ratio for radial discharge port of 2.6. The running conditions for Fig. 4.19 are:

- Refrigerant: $R22$.
- Speed of male (driven) rotor: $3000 rev/min$.
- Evaporating temperature: $-5°C$ (saturation pressure: 4.21 bar).
- Condensing temperature: $25°C$ (saturation pressure: 10.44 bar).
- Superheat degrees: $30°C$.
- Oil drained and injected.

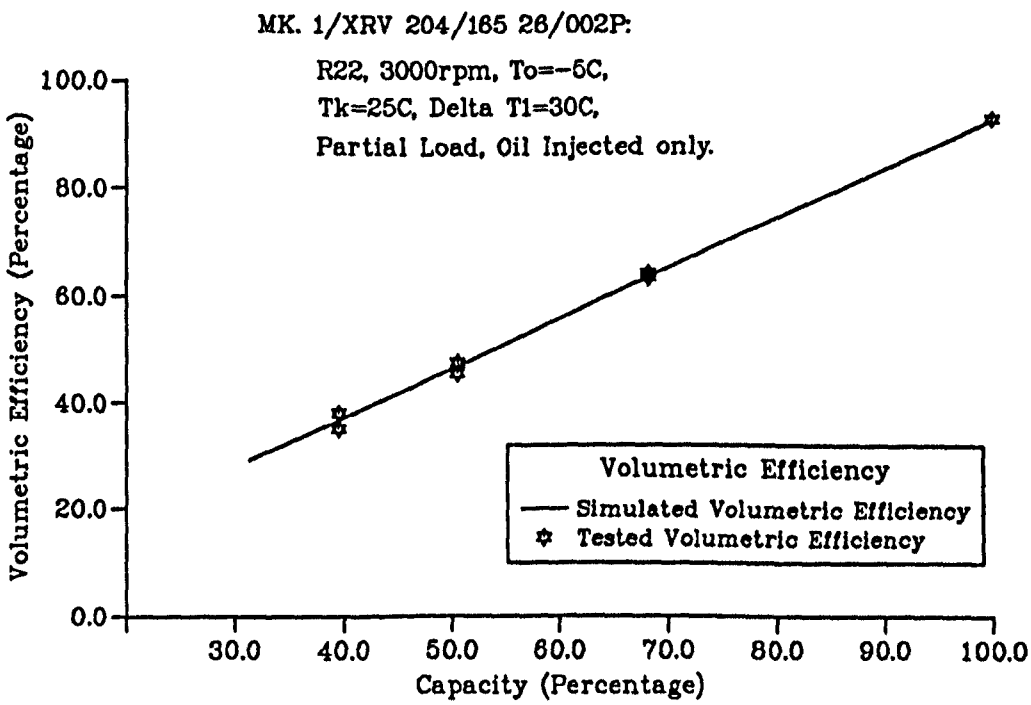

Fig. 4.19 Prediction and test volumetric efficiency vs capacity

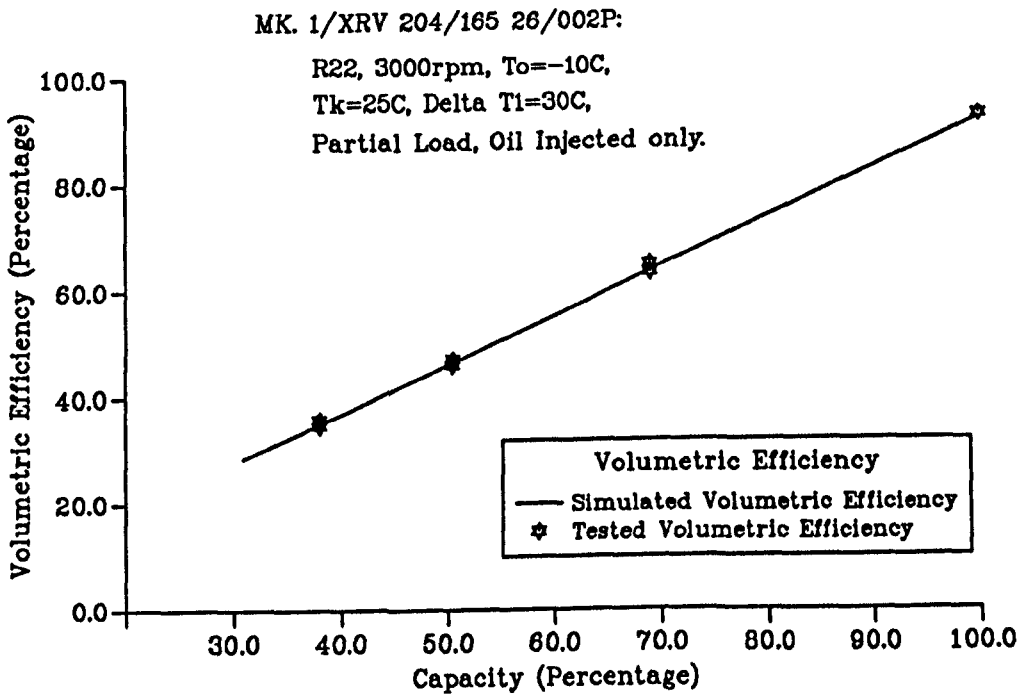

Fig. 4.20 Prediction and test volumetric efficiency vs capacity

The running conditions for Fig. 4.20 are the same as those for Fig. 4.19 except for the evaporating temperature which is $-10°C$ (saturation pressure: 3.54 *bar*). The running conditions for Fig. 4.21 are:

- Refrigerant: *R*22.
- Speed of male (driven) rotor: $3000 rev/min$.
- Evaporating temperature: $0°C$ (saturation pressure: 4.98 *bar*).
- Condensing temperature: $35°C$ (saturation pressure: 13.55 *bar*).
- Superheat degrees: $30°C$.
- Oil drained and injected.

The running conditions for Fig. 4.22 are the same as those for Fig. 4.21 except for the evaporating temperature which is $-10°C$ (saturation pressure: 3.54 *bar*).

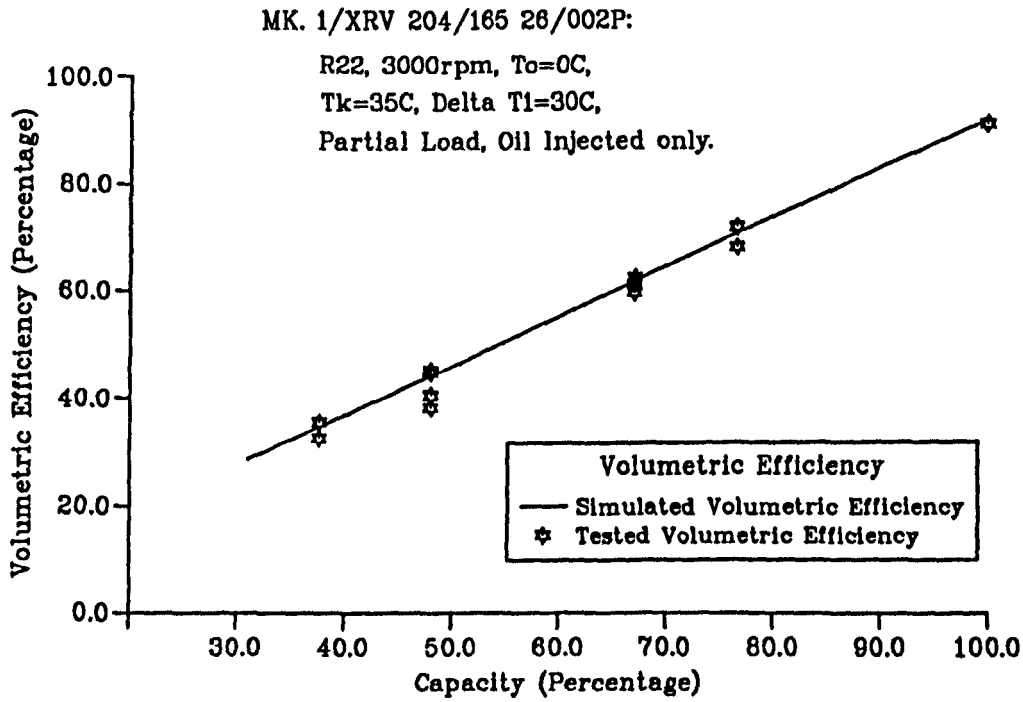

Fig. 4.21 Prediction and test volumetric efficiency vs capacity

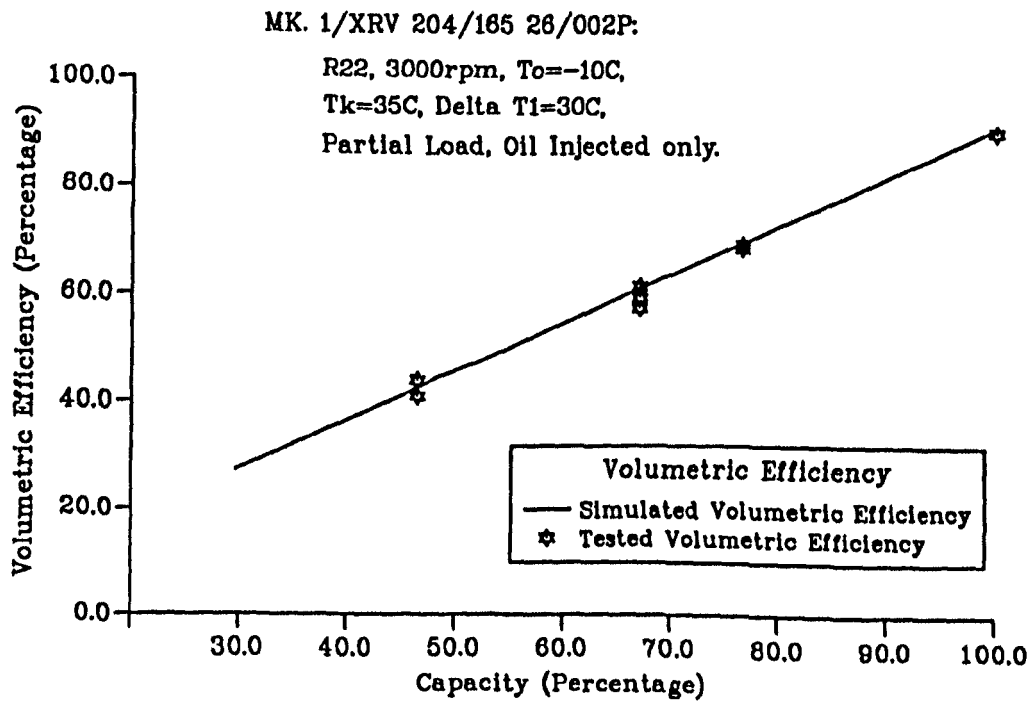

Fig. 4.22 Prediction and test volumetric efficiency vs capacity

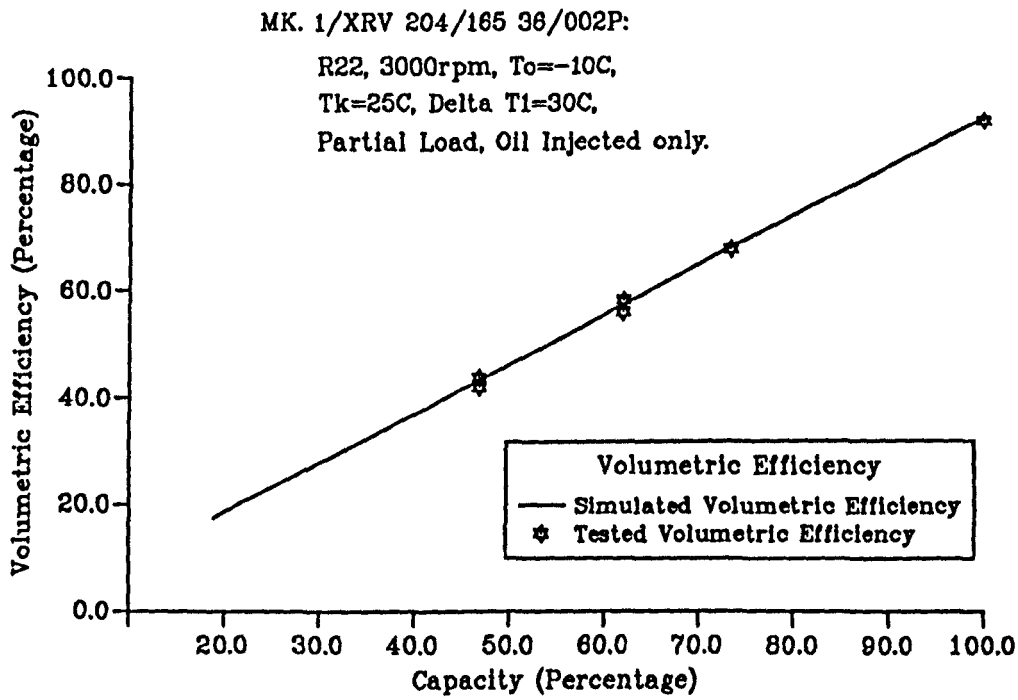

Fig. 4.23 Prediction and test volumetric efficiency vs capacity

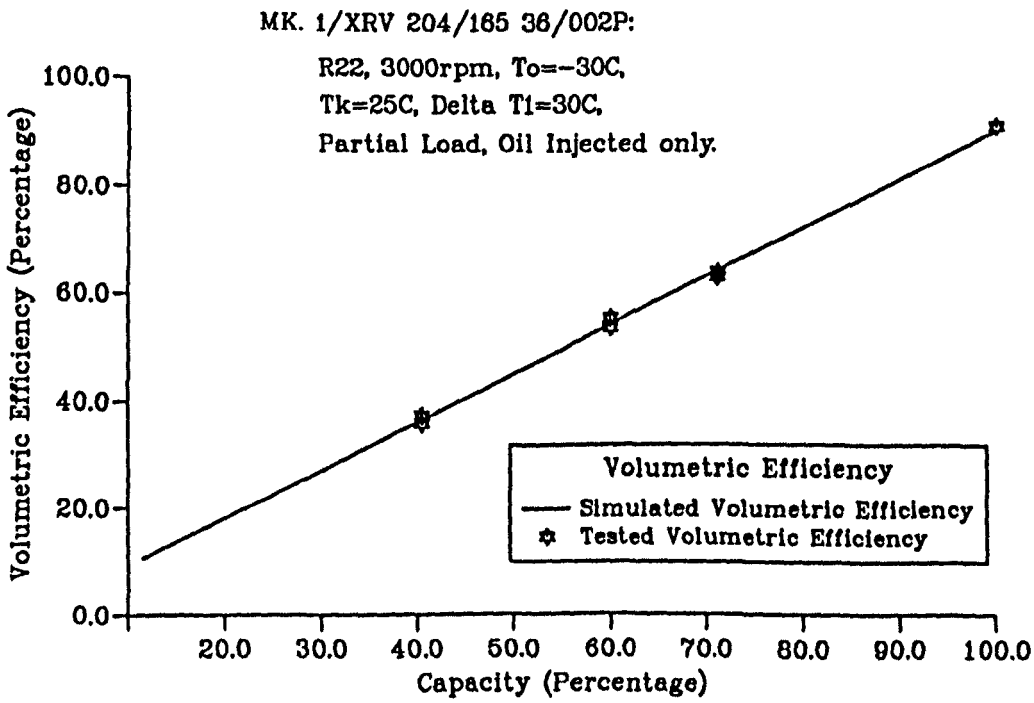

Fig. 4.24 Prediction and test volumetric efficiency vs capacity

Fig. 4.23, 4.24, 4.25 and 4.26 show the simulation and test performances for compressor MK. 1/XRV 204/165 with volume ratio for radial discharge port of 3.6. The running conditions for Fig. 4.23 are:

- Refrigerant: *R*22.
- Speed of male (driven) rotor: $3000 rev/min$.
- Evaporating temperature: $-10°C$ (saturation pressure: 3.54 *bar*).
- Condensing temperature: $25°C$ (saturation pressure: 10.44 *bar*).
- Superheat degrees: $30°C$.
- Oil drained and injected.

The running conditions for Fig. 4.24 are the same as those for Fig. 4.23 except for the evaporating temperature which is $-30°C$ (saturation pressure: 1.63 *bar*).

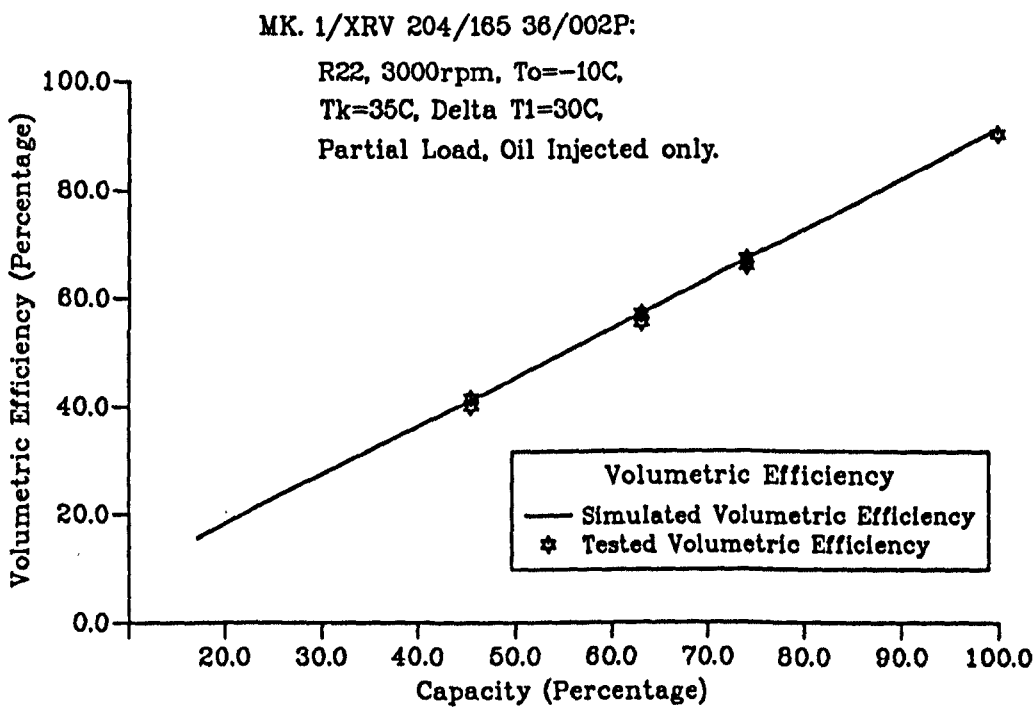

Fig. 4.25 Prediction and test volumetric efficiency vs capacity

The running conditions for Fig. 4.25 are:

- Refrigerant: *R*22.
- Speed of male (driven) rotor: $3000 rev/min$.
- Evaporating temperature: $-10°C$ (saturation pressure: 3.54 *bar*).

- Condensing temperature: 35°C (saturation pressure: 13.55 *bar*).
- Superheat degrees: 30°C.
- Oil drained and injected.

The running conditions for Fig. 4.26 are the same as those for Fig. 4.25 except for the evaporating temperature which is −30°C (saturation pressure: 1.63 *bar*).

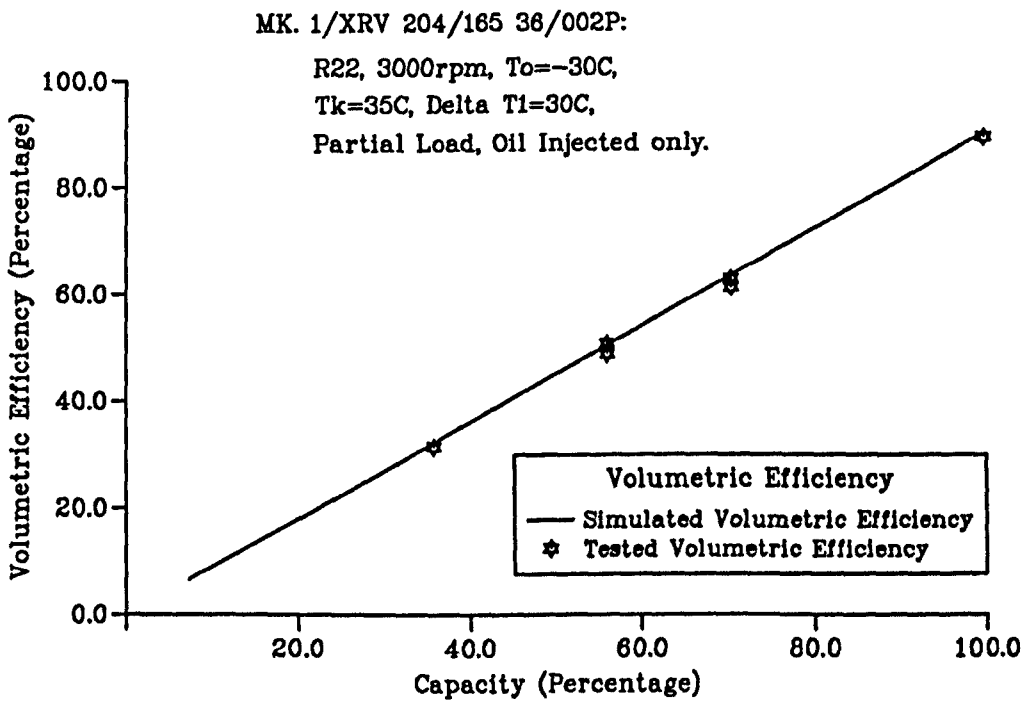

Fig. 4.26 Prediction and test volumetric efficiency vs capacity

From Fig. 4.19 to Fig. 4.26 it can be seen that the working process simulation program has a very high prediction accuracy also for the partial loading condition.

4.7.4 Simulation and Test Performances for Liquid Refrigerant Injection

Part of the simulation and test performances for compressor MK. 1/XRV 204/165 with liquid refrigerant injection and a different volume ratio for the radial discharge port is shown in Figs. 4.27 to 29. In every figure, Fig. (a) is used to show the volumetric efficiency and total efficiencies, Fig. (b) to show the

calculated and measured input powers of the compressor, and Fig. (c) to show the percentage variations of the calculated results compared with the measured results. The calculated volumetric efficiency in Fig. (c) is compared with the average measured result.

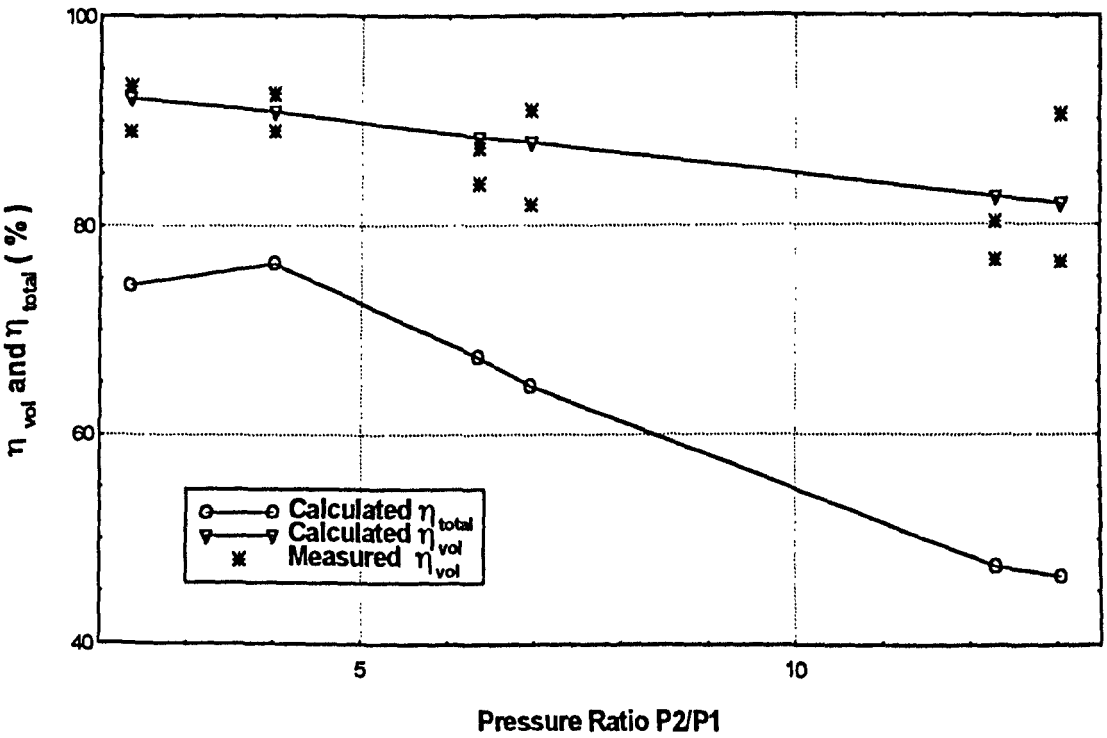

Fig. 4.27 (a) Measured and calculated η_{vol} and η_{total} vs p_2/p_1 ($V_{ir} = 2.6$)

The running conditions of the simulated compressor for Fig. 4.27 are as follows:

- Refrigerant: *R22*.
- Speed of male (driven) rotor: 3000 *rev/min*.
- Condensing temperature: 35°*C* (saturation pressure: 13.55 *bar*).
- Suction superheat degrees: 30°*C*.
- Oil drained and injected.
- Oil temperature: 62 - 68°*C*.
- Oil pressure: $p_1 + 9.7 \sim 11.2$ *bar*.
- Injected liquid refrigerant flow rate: 771.8 - 2156.5 *kg/hour*.
- Pressure at liquid refrigerant injection port: 3.05 - 6.45 *bar*.
- The superfeed is not on duty.

- The compressor is on full load.

There are no total efficiency measured results for the above operating conditions.

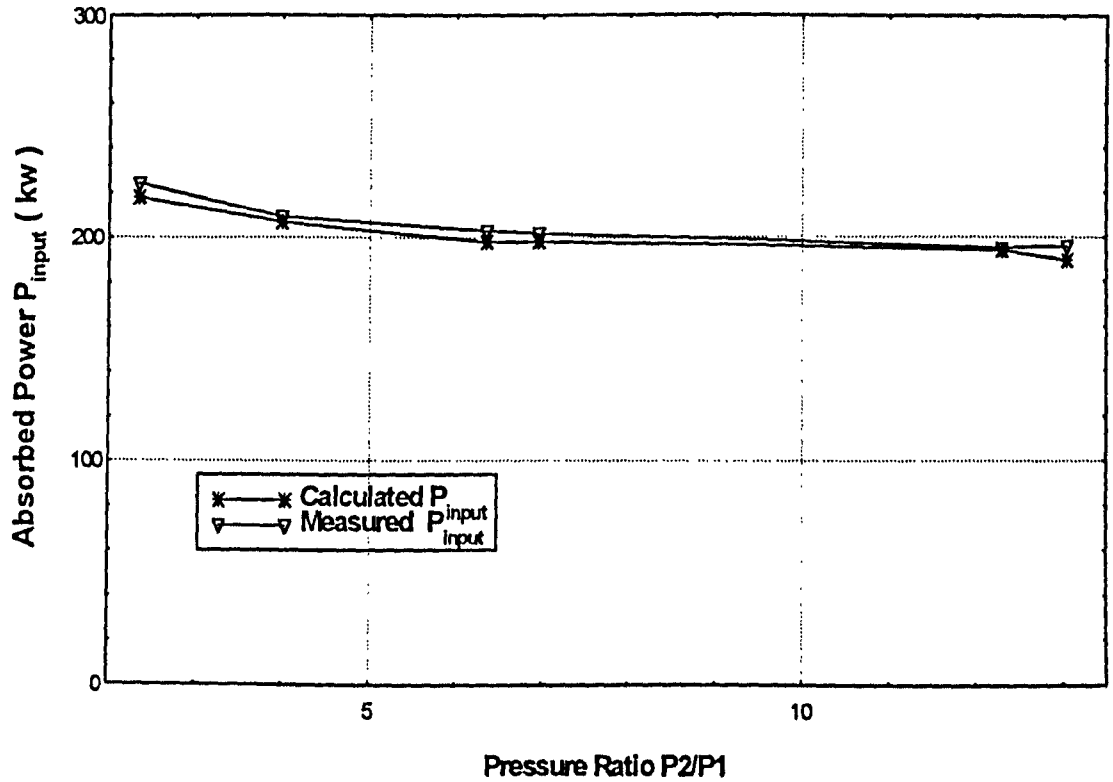

Fig. 4.27 (b) Measured and calculated P_{input} vs p_2/p_1 ($V_{ir} = 2.6$)

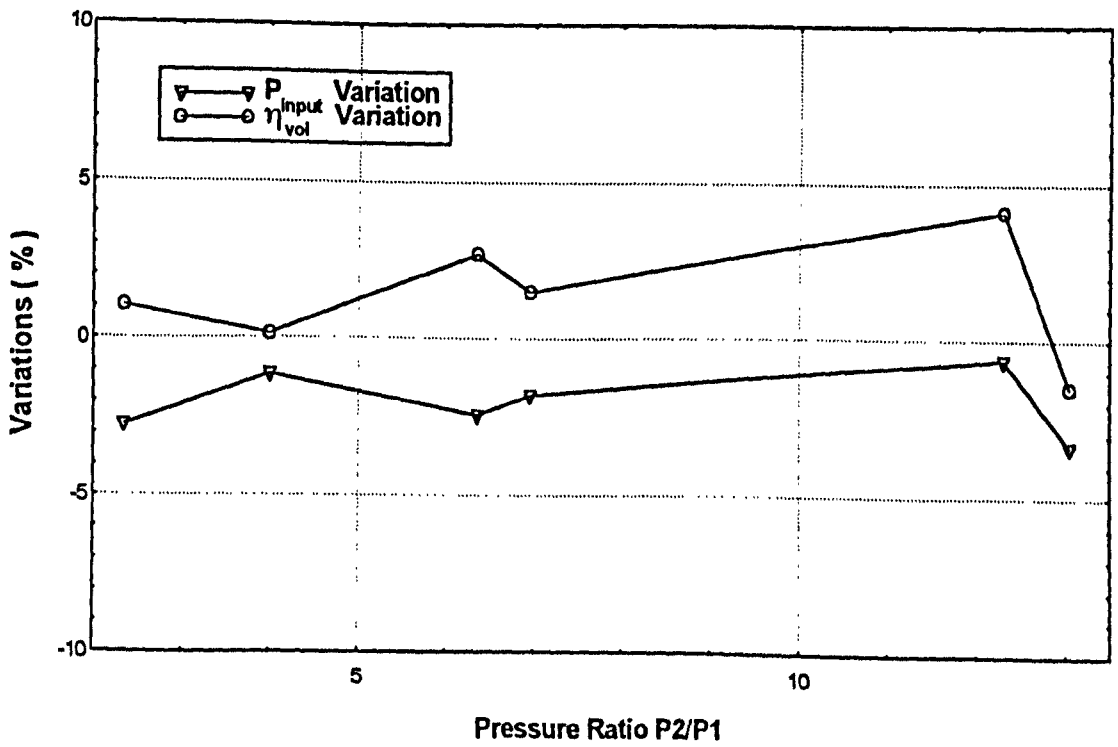

Fig. 4.27 (c) Percentage variations of η_{vol} and P_{input} vs p_2/p_1 ($V_{ir} = 2.6$)

The running conditions of the simulated compressor for Fig. 4.28 are as follows:

- Refrigerant: $R22$.
- Speed of male (driven) rotor: 3000 rev/min.
- Condensing temperature: 35°C (saturation pressure: 13.55 bar).
- Suction superheat degrees: 25 - 35°C.
- Oil drained and injected.
- Oil temperature: 71 - 72°C.
- Oil pressure: $p_1 + 9.6 \sim 11.3$ bar.
- Injected liquid refrigerant flow rate: 1559.5 - 2179.2 $kg/hour$.
- Pressure at liquid refrigerant injection port: 3.65 - 6.25 bar.
- The superfeed is not on duty.
- The compressor is on full load.

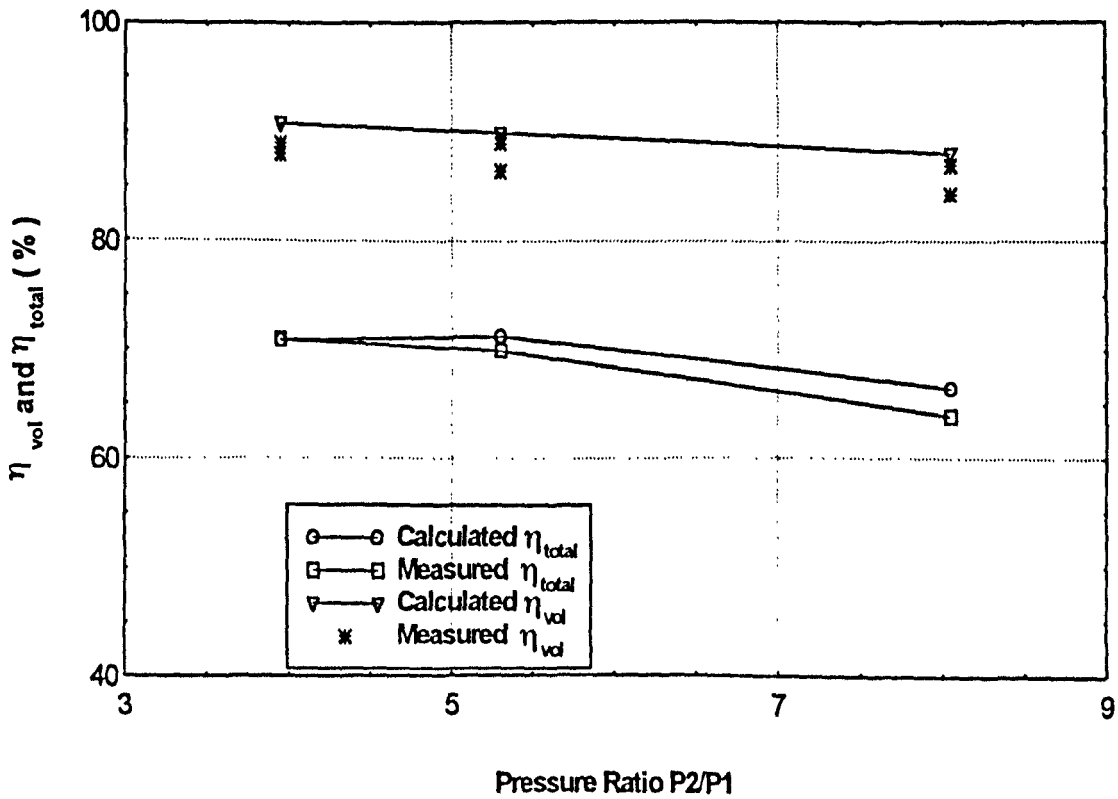

Fig. 4.28 (a) Measured and calculated η_{vol} and η_{total} vs p_2/p_1 ($V_{ir} = 3.6$)

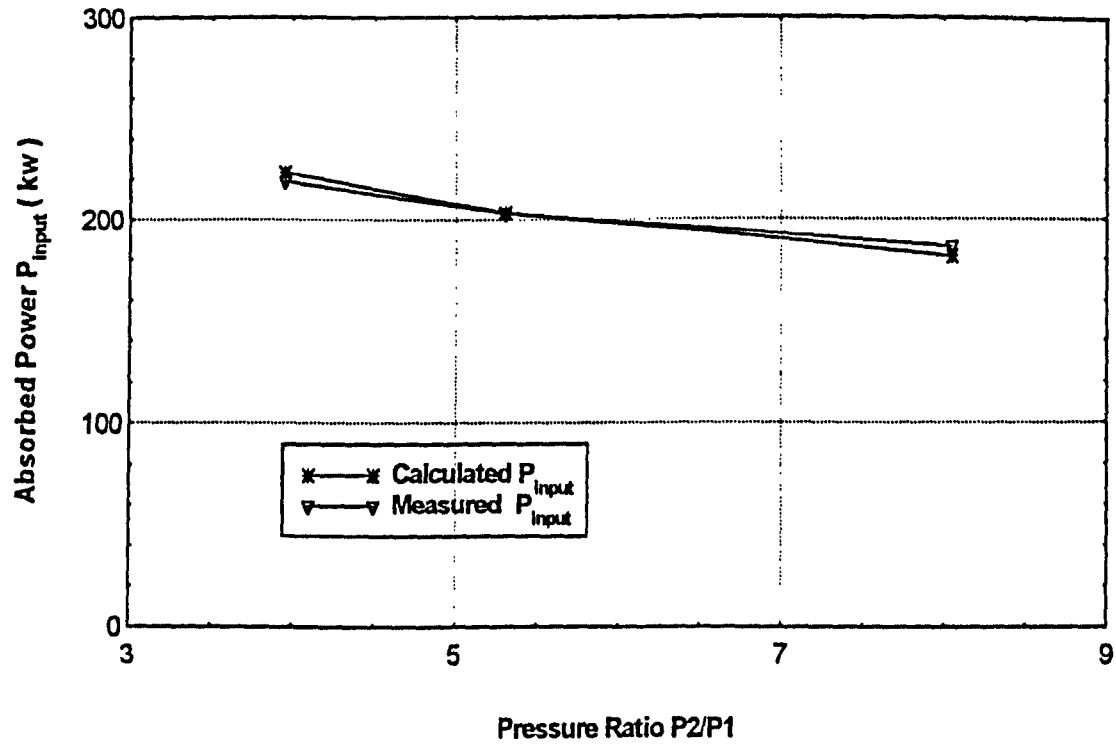

Fig. 4.28 (b) Measured and calculated P_{input} vs p_2/p_1 ($V_{ir} = 3.6$)

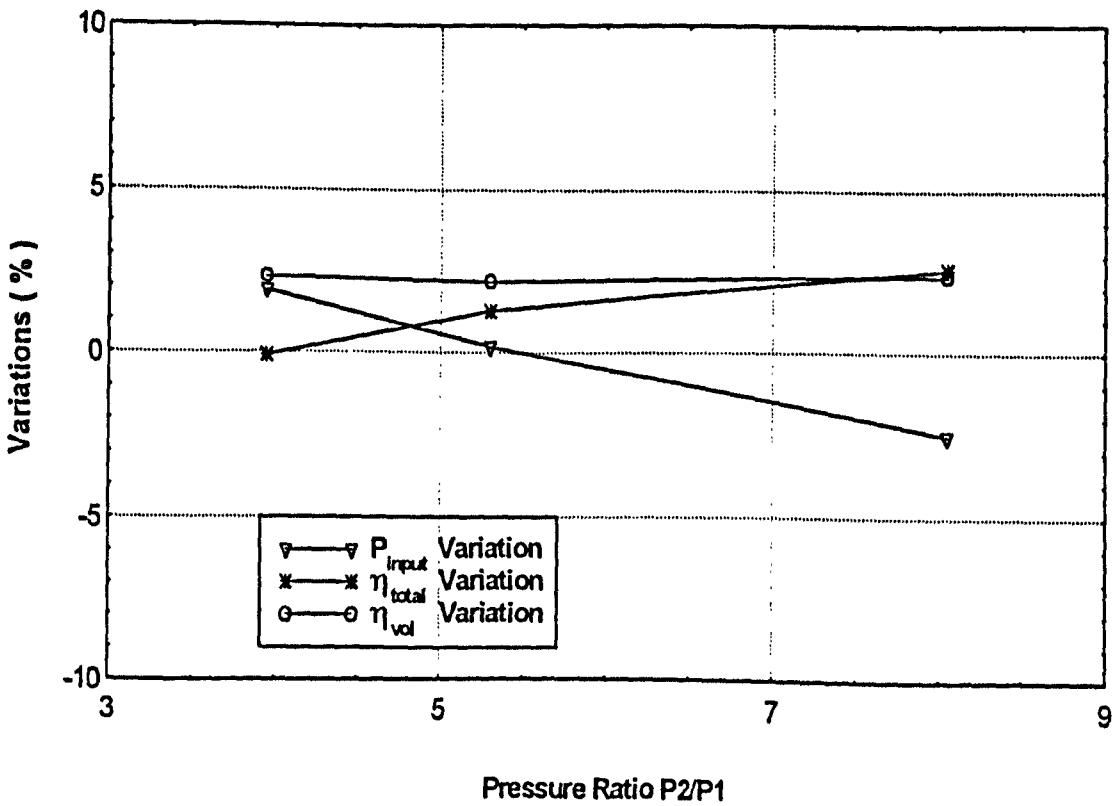

Fig. 4.28 (c) Percentage variations of η_{vol}, η_{total} and P_{input} vs p_2/p_1 ($V_{ir} = 3.6$)

The running conditions of the simulated compressor for Fig. 4.29 are as follows:

- Refrigerant: $R22$.
- Speed of male (driven) rotor: 3000 rev/min.
- Condensing temperature: 25°C (saturation pressure: 10.44 bar).
- Suction superheat degrees: 25 - 35°C.
- Oil drained and injected.
- Oil temperature: 70 - 72°C.
- Oil pressure: p_1+ 8.5 - 9.0 bar.
- Injected liquid refrigerant flow rate: 1543.6 - 1702.5 $kg/hour$.
- Pressure at liquid refrigerant injection port: 2.65 - 5.5 bar.
- The superfeed is not on duty.
- The compressor is on full load.

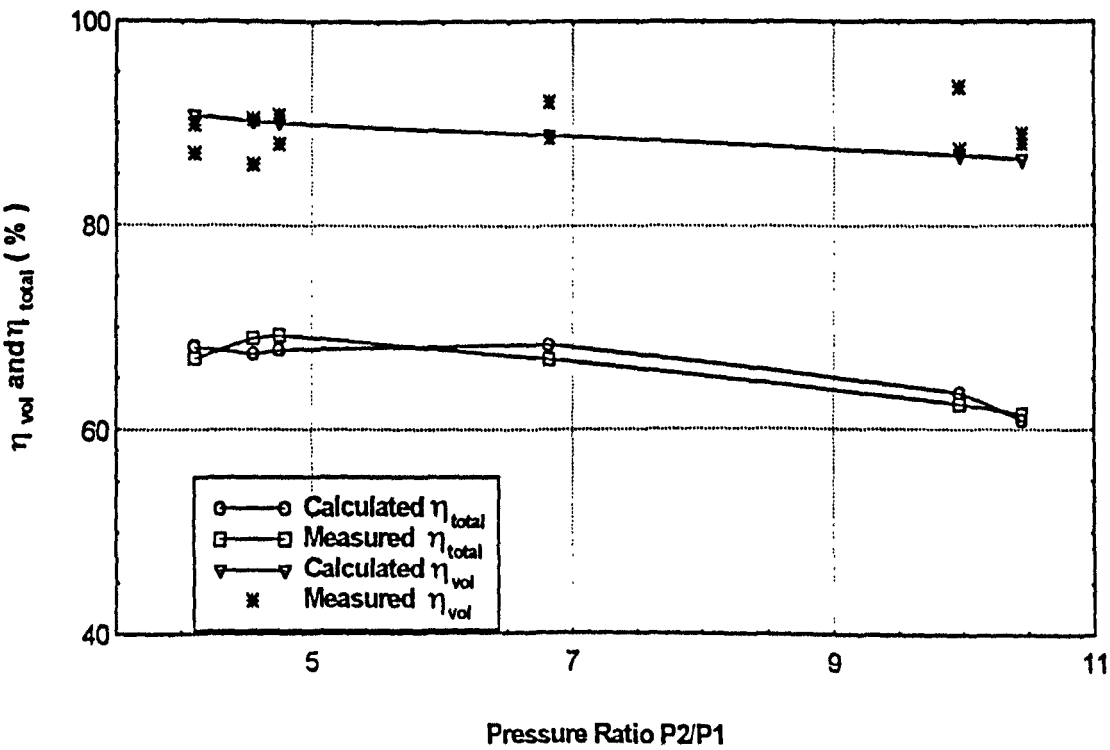

Fig. 4.29 (a) Measured and calculated η_{vol} and η_{total} vs p_2/p_1 (V_{ir} = 5.0)

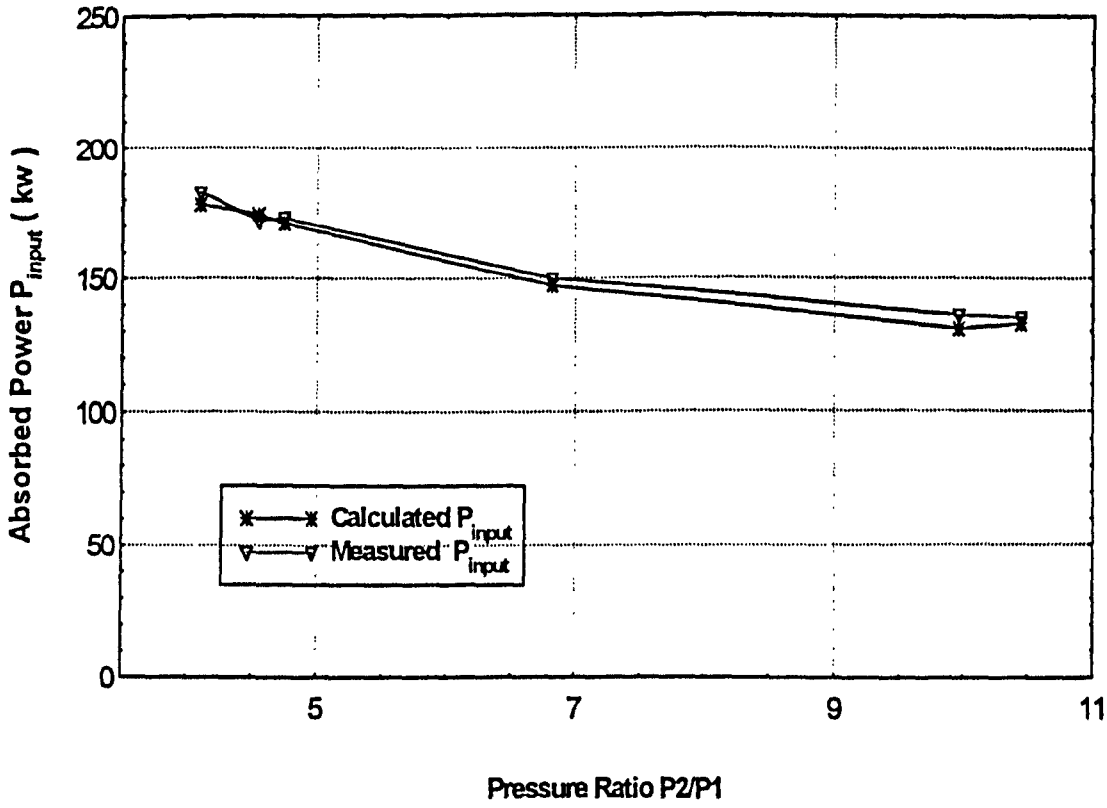

Fig. 4.29 (b) Measured and calculated P_{input} vs p_2/p_1 ($V_{ir} = 5.0$)

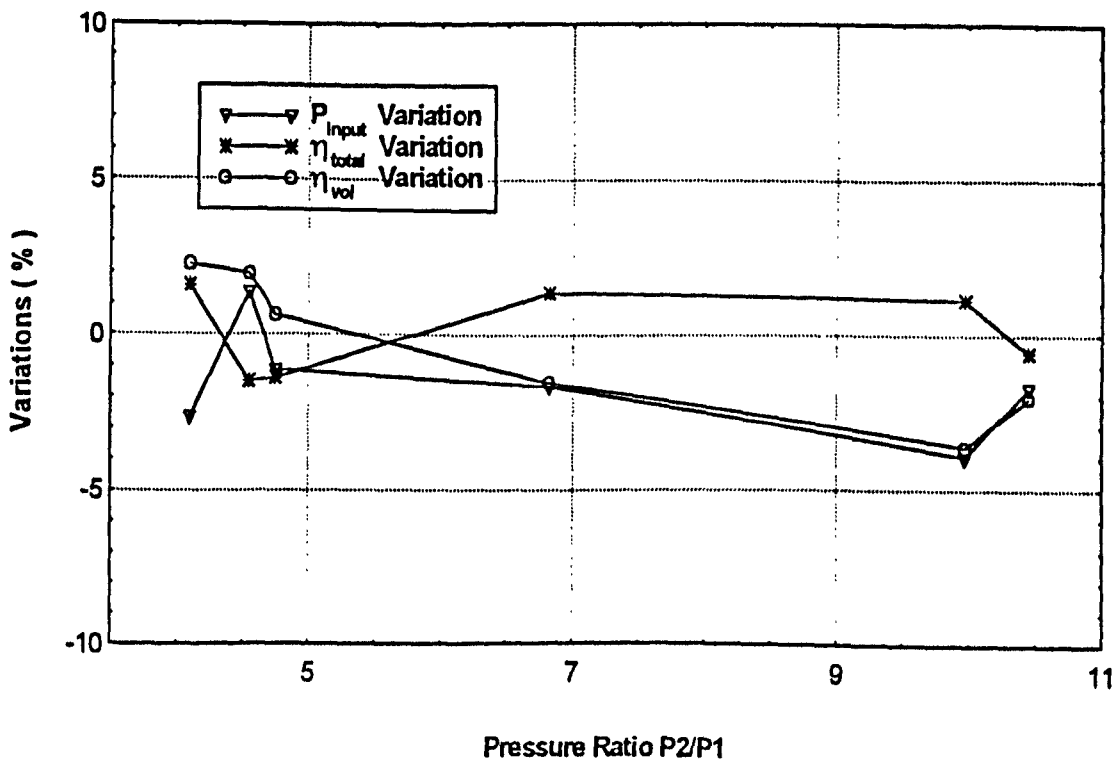

Fig. 4.29 (c) Percentage variations of η_{vol}, η_{total} and P_{input} vs p_2/p_1 ($V_{ir} = 5.0$)

4.7.5 p-V Diagrams for Different Working Conditions

A p-V diagram of a twin screw compressor is very important, and can give much information about the operation of the machine. For example, it can indicate if a compressor is designed properly for a certain working condition. Also from the p-V diagram, the indicated power, bearing forces and rotor torques due to gas pressure can be calculated. For different working conditions p-V diagrams must be different. Fig. 4.30 shows four p-V diagrams corresponding to the following four conditions of compressor MK. /XRV 204/165 with volume ratio for radial discharge port of 3.6, oil injection and draining being common to all:

- Oil injection and draining alone (total oil flow rate: 198.72 kg/min; oil pressure at injection port: 13 bar; oil temperature at injection port: 42°C).
- Liquid refrigerant injection (liquid refrigerant flow rate: 25.88 kg/min; liquid refrigerant pressure at injection port: 6.2 bar; total oil flow rate: 182.16 kg/min; oil pressure at injection port: 13bar; oil temperature at injection port: 65.5°C).
- Superfeed on duty (temperature in superfeed: 10°C; total oil flow rate: 198.72 kg/min; oil pressure at injection port: 13 bar; oil temperature at injection port: 42°C).
- Slide valve on duty (capacity: 71.8 $percentage$; total oil flow rate: 198.72 kg/min; oil pressure at injection port: 13 bar; oil temperature at injection port: 42°C).

The other operational conditions are common for the four p-V diagrams and as follows:

- Refrigerant: $R22$.
- Speed of male (driven) rotor: 3000rev/min.
- Evaporating temperature: $-10°C$ (saturation pressure: 3.54 bar).
- Condensing temperature: 35°C (saturation pressure: 13.55 bar).
- Superheat degrees: 30°C.

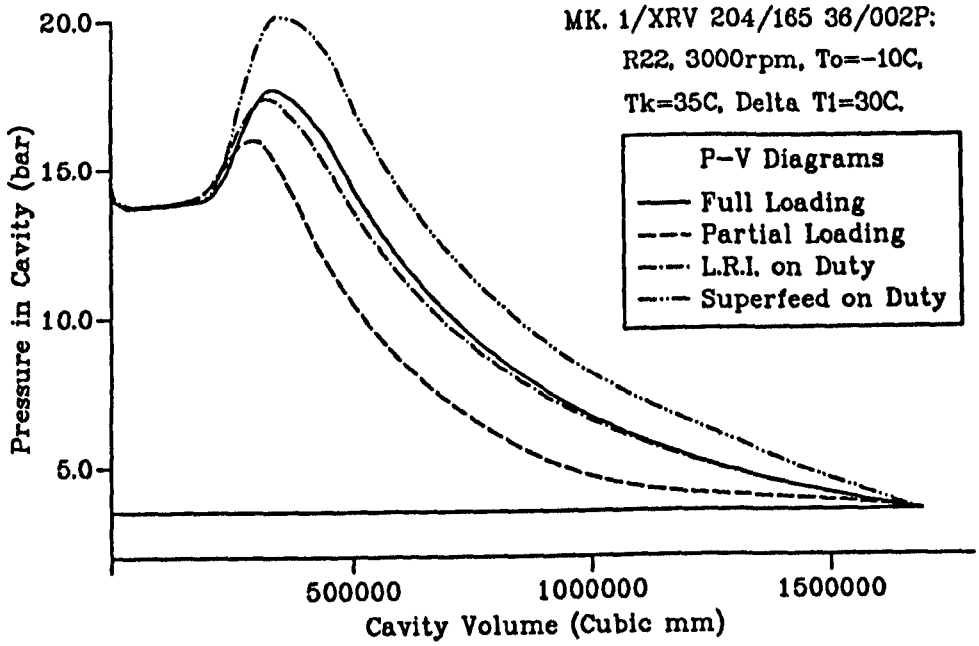

Fig. 4.30 p-V diagrams

4.8 REFERENCES

1 **Press, William H., Flannery, Brian P., Teukolsky, Saul A.** and **Vetterling, William T.** Numerical Recipes. The Art of Scientific Computing. *Cambridge University Press*, 1986.

2 **Singh, Pawan J.** and **Onuschak, Anthony D.** A Comprehensive, Computerized Method for Twin-Screw Rotor Profile Generation and Analysis. *Proceedings of International Compressor Engineering Conference at Purdue*. Purdue University, U.S.A., 1984.

3 **Afgan, N.H.** and **Schunder, E.U.** Heat Exchangers: Design and Theory Sourcebook. *Scripta Book Company*, 1974.

4 **Zhang, ZhiYou** Refrigeration Principles and Equipments. **Mechanical Industry Publisher**. Bejing, 1989.

5 **Fleming, J.S. You, C.X.** and **Tang, Y.** Rotor Tip Design in Oil Injected Helical Twin Screw Compressors with Respect to Viscous Friction Loss. Proceedings of the Institution of Mechanical Engineers, Developments in Industrial Compressors and Their Systems, European Conference, London, 1994, pp.115–122.

6 Data and Charts Supplied by Howden Compressors Ltd., 1993.

7 **Martin, F.A.** and **Garner, D.R.** Plain Journal Bearings under Steady Loads: Design Guidance for Safe Operation. *First European Tribology Congress*, LB371/73, I Mech E, London, 1973.

8 **Singh, Pawan J,** and **Patel, Ghanshyam C.** A Generalized Performance Computer Program for Oil Flooded Twin-Screw Compressors. *Proceedings of the International Compressor Engineering Conference at Purdue,* Purdue University, U.S.A., 1984, pp.544–553.

9 The Measured Data Books of Howden Compressors Ltd. from 1978 to 1994.

10 **Kanyshev, G.A. Vuzhva, A.A.** and **Sapronov, V.I.** Influence of Viscosity of Oil and ist Solubility with Refrigerant upon Characteristics of Screw Compressors. *Proceedings of IIR Congress*, Moscow, 1975, pp.949–956.

11 **Sjoholm, Lars I.** and **Short, Glenn D.** Twin-Screw Compressor Performance and Complex Ester Lubricants with HCFC-22. *Proceedings of the International Compressor Engineering Conference at Purdue,* Purdue University, U.S.A., 1990, pp.724–732.

12 **Sjoholm, Lars I.** and **Short, Glenn D.** Twin-Screw Compressor Performance and Suitable Lubricants with HFC-134a. *Proceedings of the International Compressor Engineering Conference at Purdue,* Purdue University, U.S.A., 1990, pp.733–740.

13 **Ignatiev, K.M. Tang, Yan Fleming, John S.** and **Tramschek, A.B.** Thermal Interaction in a Refrigeration Twin Screw Compressor during the

Compression Process. *Proceedings of the International Compressor Engineering Conference at Purdue,* Purdue University, U.S.A., 1994, accepted and to be published.

14 **Stošić, N. Milutinović, Lj. Hanjalić, K.** and **Kovačević** Invetigation of the Influence of Oil Injection Upon the Screw Compressor Working Process. *Int. J. Refrig.*, 1992, Vol 15, No 4, pp.206–220.

15 **Stockholm, J.-G.** Heat-Exchange in Liquid-Injected Screw-Compressors. *VDI BERICHTE NR. 640*, 1987, pp.121–135.

16 **Mugele, R.A.** and **Evans, H.D.** Droplet Size Distribution in Sprays. *Indutrial and Engineering Chemistry*, Vol. 43, No. 6, 1951, pp.1317–1324.

17 **Downing, R.C** Refrigerant Equations. *ASHRAE Transactions*, Vol. 80, Part II, 1974, P158.

18 Handbook of Air Conditioning (in Japanese). 1981.

19 **Haugland, K.** Pressure Indication of Twin Screw Compressor. *Proceedings of the International Compressor Engineering Conference at Purdue,* Purdue University, U.S.A., 1990, pp.450–456.

20 **Miyoshi, Kiyotada** Analysis of Screw Compressor Performance Based on Indicator Diagrams. *Proceedings of the International Compressor Engineering Conference at Purdue,* Purdue University, U.S.A., 1990, pp.450–456.

21 **Tang, Yan** and **Fleming, John S.** Simulation of the Working Process of a Modern Refrigeration Twin Screw Compressor. *Research Report 10*, Feb., 1994.

Chapter 5

CUTTER BLADE SHAPE DETERMINATION AND OPTIMISATION

Although helical screw compressors contain only two moving parts, the male and female rotors, their shapes must mesh to very fine clearances. The precision with which the rotors are manufactured influences the thermodynamic performance of the compressor and its manufacturing cost. Although the rotors can be manufactured by milling and hobbing, in this chapter only milling is considered as milling is the method used by Howden Compressors Ltd. and indeed by most manufacturers. The most effective method of producing rotors with a practical operational clearance is to cut the rotors with blades shaped in such a manner that the mating rotor pair has a prescribed clearance distribution. This approach is proposed in this chapter. Cutter blade geometry influences manufacturing costs as follows: (i) sharp points and tight curvatures require greater precision of blade geometry and more frequent regrinding, (ii) a small angle between flanks or between one flank and the line joining the rotor and cutter centres, means that at each regrind a greater quantity of material has to be removed to restore the blade geometry than would be the case for a larger angle, hence a shorter blade life. Different geometric schemes for determining blade shapes result in different patterns of clearance distribution along the contact line and have different effects on the thermodynamic performance of the compressor due to the different leakage mass flow rates which they permit. Indeed, the thermodynamic performance depends principally on the internal leakage rates in the compressor, in particular, the leakage across the contact line.

This chapter deals with different geometric schemes for determining cutter blade shapes and their different influences on the thermodynamic performance of the compressor, and on the manufacturing cost of the rotors. Two basic geo-

metric schemes are described and others are discussed, including the possibility of an optimised clearance distribution. A quantitative analysis of their different influences on the thermodynamic performance is made. Although cutter shapes depend principally on the profile to be produced, a preferred cutter orientation chosen for the milling operation may require a change of cutter shape, thus influencing manufacturing costs. The computer program described in this chapter calculates the cutter blade shapes needed to produce rotor profiles of *any* practical shape and as a consequence, is a *universal* program. The thermodynamic model of compressor behaviour developed by the author is used to predict the performance as influenced by the different clearance distributions resulting from the different geometrical schemes. A design technique for obtaining a clearance distribution optimised to give the best thermodynamic performance is discussed. Similarly, a technique for obtaining cutter blade shapes which reduce manufacturing costs is also discussed.

5.1 INTRODUCTION

Along the contact line between the male and female rotors a clearance should exist to allow for gas loading deflections and thermal distortions of the rotors, bearings and housing, and for manufacturing errors and oil film thickness. The manufacturing process of the rotors influences both the thermodynamic performance of the compressor and its manufacturing cost. Profiles requiring blades having strong curvature and/or sharp points have higher manufacturing costs and may also influence leakage due to an increase in the difficulty of maintaining tolerances.

This chapter describes different methods of providing inter-rotor clearance, and presents the process of determining cutter geometry according to a chosen geometric scheme so that a mating rotor pair when manufactured has a known clearance distribution along the contact line. The average clearance and the leakage area are calculated and used in the computerized thermodynamic model of the working process of the compressor to determine its volumetric and isentropic

efficiencies and leakage rates etc. The problem of determining optimum blade shapes is discussed with regard to the conflicting demands of cutter economics; ie number and frequency of regrinds; desirable machining angles; actual inter-rotor clearances as actually produced and the thermodynamic consequences which result from the leakages they permit.

Although rotors can be manufactured by milling and hobbing, in this chapter only milling is considered as milling is used by Howden Compressors Ltd. and indeed by most other manufacturers. There are two quite distinct geometrical schemes used for cutter blade calculation and inter-rotor clearance determination practically. In the first, called the equidistant lobe profile method, the zero clearance lobe profile in the end plane is replaced by an equidistant profile, and then the appropriate cutter shape needed to produce it is determined. In the second, the cutter shape needed to produce zero clearance lobes is determined and then replaced with an equidistant cutter blade to ensure a clearance when the rotors are cut. This is known as the equidistant helical surface method. These two geometrical schemes are still widely used, especially for profiles developed in the earlier period of compressor development. In new profiles, some manufacturers have introduced non-equidistant schemes, that is, the inter-rotor clearance is not equidistant in the end plane or normal to the helical surface. This new scheme enables the machine to obtain the minimum inter-rotor clearance during operation, at least in theory. Although the non-equidistant scheme has the same basic procedure used to calculate the cutter blades as the equidistant schemes, its key point is to decide the clearance distribution during the manufacturing stage. The author has given much thought to this scheme, which includes the development of a force analysis program and a rotor deflection program etc., but the work at the time of writing is not complete.

This chapter presents a *universal* cutter blade calculation program; ie one capable of calculating blade shapes to cut profiles of *any* practical shape and of course it provides them with a clearance distribution determined by one of the two equidistant schemes presented here or with a clearance distribution defined by a pre-calculated data file, which provides a choice for the non-equidistant scheme.

The program also calculates the real profile and real cutter blades, which are required by the modern Holroyd CNC (computer numerically controlled) machine tools and automatic cutter grinding machines. The average clearance for one lobe can also be calculated by the program, which then can be used as input for the working process simulation program.

Different geometric schemes for providing inter-rotor clearance are described in this chapter, but even more attention is paid to the quite different distributions of clearance along the contact line which result because leakage rates and thermodynamic performances are influenced. A quantitative analytical method is used.

Although much of work still needs to be done for the unequal modification of the profiles of the rotors, a design technique for obtaining an optimum clearance distribution is discussed in this chapter.

The geometric clearance schemes used to calculate cutter blade shapes do not significantly affect the macro geometry of the blade, only the clearance distribution along the contact line of a rotor pair, and as a consequence, the leakage across the contact line, the volumetric efficiency and the indicated isentropic efficiency. The cutter shapes are defined mainly by the profile used in the compressor, and when a profile is chosen (the choice of a profile is a separate topic, which also involves the thermodynamic performance of the compressor and the manufacturing cost of the rotors and needs the optimisation of many profile parameters) certain values of manufacturing parameters such as the offset angle and the angle between the cutter axis and the rotor axis, can require a change in cutter shape with a consequent increase in the manufacturing cost of the rotors. This chapter also discusses the optimisation of these manufacturing parameters.

5.2 CUTTER GEOMETRY AND DETERMINATION OF INTER-ROTOR CLEARANCE

In helical screw compressor design it is normal practice to begin the design by determining a workable lobe profile in the plane normal to the rotor axes,

that is in the rotor end plane (the lobe profile geometry) and then to choose a combination of wrap angle and screw pitch (rotor geometry) that will have the desired characteristics of pressure ratio and volumetric delivery. The complete design is a process in which rotor, bearing and housing deflections due to pressure loads and thermal gradients have to be taken into account.

For manufacture by milling and hobbing, there are in general four methods for producing clearances between rotors to accommodate tolerance build-up, gas force deflections, and the thermal distortions which occur during operation. They are as follows:

1. A zero clearance (perfect) lobe profile is produced in the first instance and then modified according to a chosen geometric scheme to produce a real profile with clearance. In the first scheme considered here which is commonly used by manufacturers, a real profile equidistant from the zero clearance profile in the end plane is proposed. The equidistant profile is constructed by stepping out the same distance along the normal to the tangent at each location point on the zero clearance lobe profile. A suitable cutter geometry is then determined for the equidistant lobe geometry and the given helix angle.

   It is of course possible to produce a *non*-equidistant lobe profile by stepping out *different* distances at each location point. This is in fact proposed as part of the process for producing a compressor having clearances optimized to suit running conditions as described in Section 5.5, the author believes that this method has been used in some new developed profiles.

2. Cutter blade geometry capable of manufacturing the zero clearance lobe profile is determined and then a real cutter blade geometry is created by modifying the zero clearance blade according to a chosen geometric scheme. In this scheme a real cutter blade equidistant from the zero clearance blade is created in the same manner as the equidistant lobe profile in method 1.

3. A reduced centre distance between cutter and rotor can be used to produce a pair of rotors with a working clearance between them.

4. On assembly, inter-rotor clearance can be created by increasing the centre distance between the rotors.

All the above methods have been used by the twin screw compressor manufacturers, and in the gear industry they have longer history. Examination of the influence of the different clearance scheme procedures on the compressor performance and manufacturing cost is unavoidable in a comprehensive compressor computer aided design study. Parts of the process will have been used by manufacturers while other parts may differ from their procedures. Since they publish so little it is impossible to tell. This chapter analyses the influence of clearance schemes quantitatively and proposes a procedure for obtaining the optimum clearance distribution.

In this chapter method 1 and method 2 are considered in detail with methods 3 and 4 being seen as possible ways of modifying methods 1 and 2 to suit special running conditions in practice. Only the milling cutter blades and the inter-rotor clearances they produce are discussed since milling is used by Howden Compressors Ltd. in common with most manufacturers of helical screw compressors. Deformations caused by the gas compression process and by thermal gradients are not examined quantitatively but are discussed in relation to the optimization of clearance distribution.

The calculation procedure of the cutter blades and real profile etc. for different inter-rotor clearance schemes are briefly explained as follows:

Zero Clearance Cutter Shapes The theory on which calculation of zero clearance cutter shapes is based can be found in many textbook on gears and also in many textbooks on industrial mathematics. For the convenience of the reader of this thesis, the mathematical procedure and equations used for the calculation of zero clearance cutter shapes are presented in Appendix G. Most equations in Appendix G are from (**1**), (**2**) and (**3**). They can also be found in (**4**) and (**5**) in Russian.

The Equidistant Lobe Profile Method The cutter calculation method described in Section G.1 is used to calculate a theoretical cutter blade because it is determined for rotors having zero clearance. If the clearance is obtained

by the equidistant profile method, the coordinates of the real profile should be calculated by the equations presented in Section G.2. The real cutter blade capable of cutting practical rotors is then calculated according to the calculated real profile by the equations presented in Section G.1.

The Equidistant Helical Surface Method If the clearance is obtained by the equidistant helical surface method, the real cutter blade can be calculated by the equations described in Section G.3. The last four equations in Section G.3 are developed by the author, and they are used to calculate the real profile in the end plane. The author thinks it likely that they have been developed and used in practice by manufacturers although they are not to be found in the published work.

The Non-Equidistant Clearance Distribution If the clearance is obtained by the non-equidistant clearance distribution scheme, the equations presented in Appendix G can also be used to calculate the real profile and cutter blades. If the data file gives data for clearance normal to the helical surface, the mathematical procedure and equations presented in Section G.3 can be used to calculate the real profile and cutter profile. If the data file gives data for clearance normal to the profile in the end plane, the data can be transferred to be normal to the helical surface quite easily, and then the real profile and cutter blades can be calculated.

The Average Clearance The average clearance normal to the helical surface is calculated by the following procedure: the leakage area per lobe along the contact line is calculated according to local clearance by a simple numerical procedure, and the leakage area per lobe is divided by the contact line length per lobe to yield the average clearance, which is used as an input to the working process simulation program.

5.3 COMPUTER PROGRAM FOR CUTTER SHAPE

In accordance with the foregoing brief explanation for the theory of cutter calculation and the equations presented in Appendix G, a computer program has

been developed, and its flow diagram is shown in Fig. 5.1. Before this program is run the profile generation program should be run first to get all the required data files (see Chapter 2).

The cutter calculation program reads the results of the data files generated by the profile generation program. In addition, the following the rotor and manufacturing parameters are needed for the cutter calculation and must be entered by the user in the places requested by the program (6):

1. The wrap angle of the male rotor.
2. The screw lead of the male rotor.
3. The centre distance between the rotor and its cutter.
4. The angle between the rotor and cutter axes.
5. The offset angle of the coordinates of the profile (see section 5.6).
6. The right-handed or left-handed male rotor.
7. The clearance scheme used.
8. The equidistant clearance or the non-equidistant clearance distribution data file.

Further research is required to determine the non-equidistant clearance distributions needed to accommodate the range of the thermal and pressure deformations which occur under load. The nature of the output from this research will determine the nature of the non-equidistant clearance distribution data file.

When the cutter calculation program run is complete, the following coordinates and geometrical characteristics are output as data files:

1. The real profiles of both the male and female lobes.
2. The zero clearance and real cutter blades for male and female.
3. The variation of the total clearance both normal to the profile and to the helical surface along the length of the contact line.

In addition to the above, the program gives outputs such as rotor parameters, manufacturing parameters and average clearance along the contact line etc. to a data file.

A display program has been developed to show the calculated results of the cutter calculation program. The diagrams such as the zero clearance and real lobe profiles, the zero clearance and real cutter blades, and the clearance distributions along the contact line etc. can be shown on the monitor by the program or hard copies can be produced.

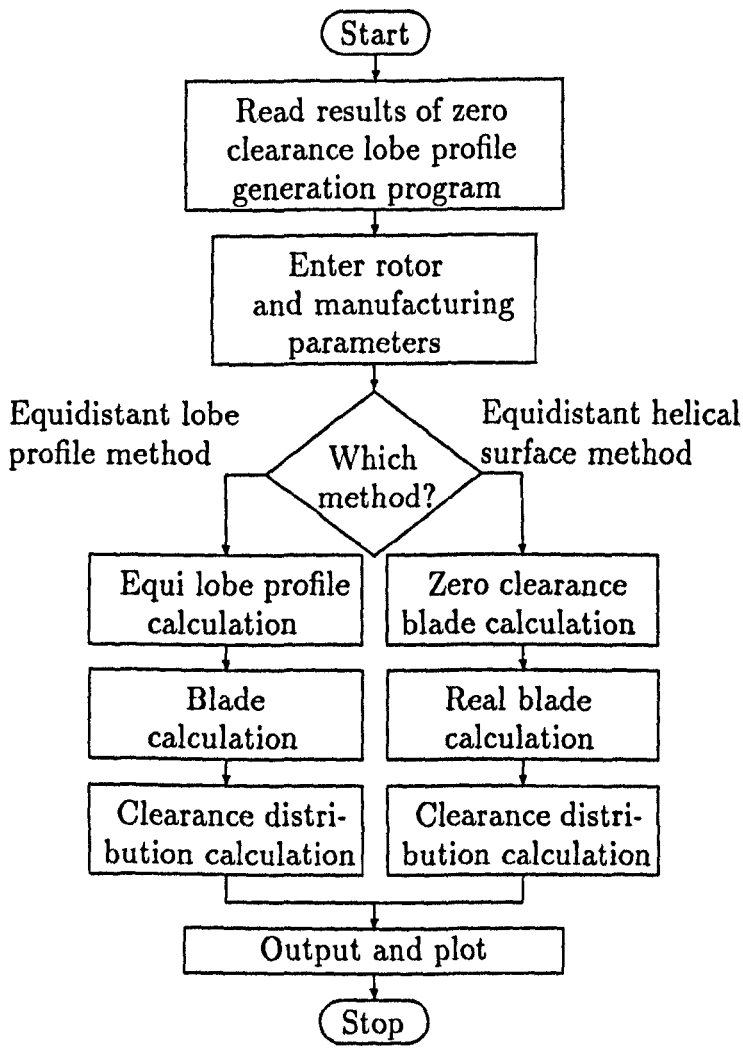

Fig. 5.1 The flow diagram of the cutter calculation program

5.4 A COMPARISON OF THE TWO SCHEMES OF EQUIDISTANT CLEARANCE DETERMINATION

5.4.1 The Equidistant Lobe Profile Method

The real lobe profile shown in Fig. 5.2 is the result calculated by the equidistant profile method. Fig. 5.3 shows the cutter blade shapes deriving from the equidistant profile method. Although the real lobe profile is equidistant from its zero clearance lobe profile, the real cutter blade shapes needed for the male and female rotors are not equidistant from their zero clearance shapes.

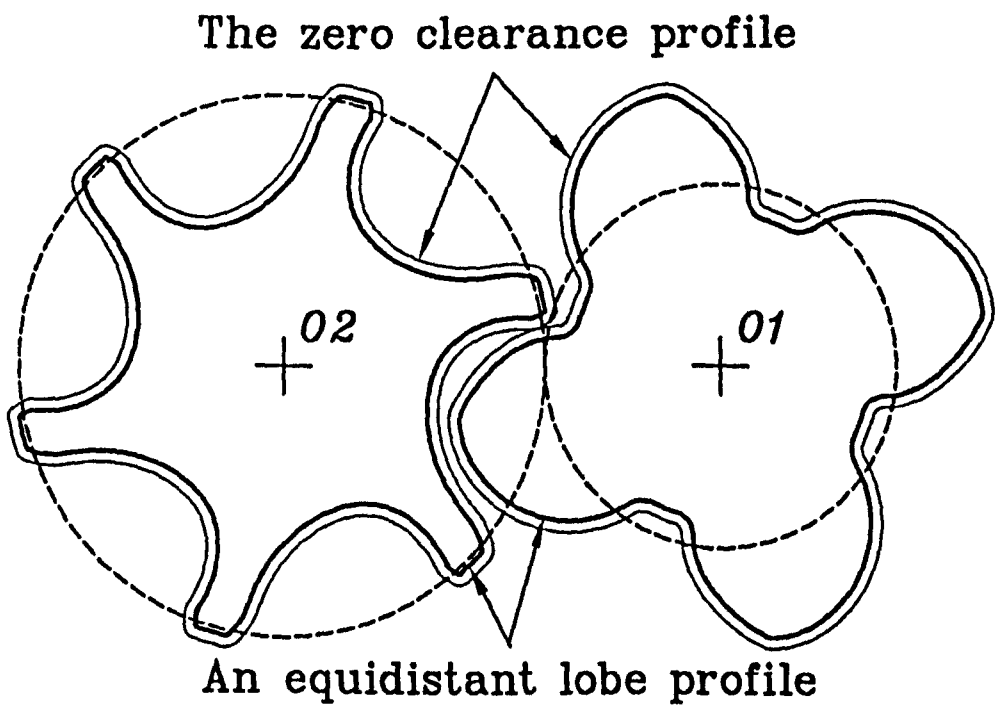

Fig. 5.2 A zero clearance lobe profile and its equidistant real profile

5.4.2 The Equidistant Helical Surface Method

The outcome of the equidistant helical surface method is illustrated in Fig. 5.4 and Fig. 5.5. As can be seen in Fig. 5.4 and Fig. 5.5, the real and the zero clearance cutter blades are equidistant because they have been set that way, but the real and the zero clearance lobe profiles are not equidistant.

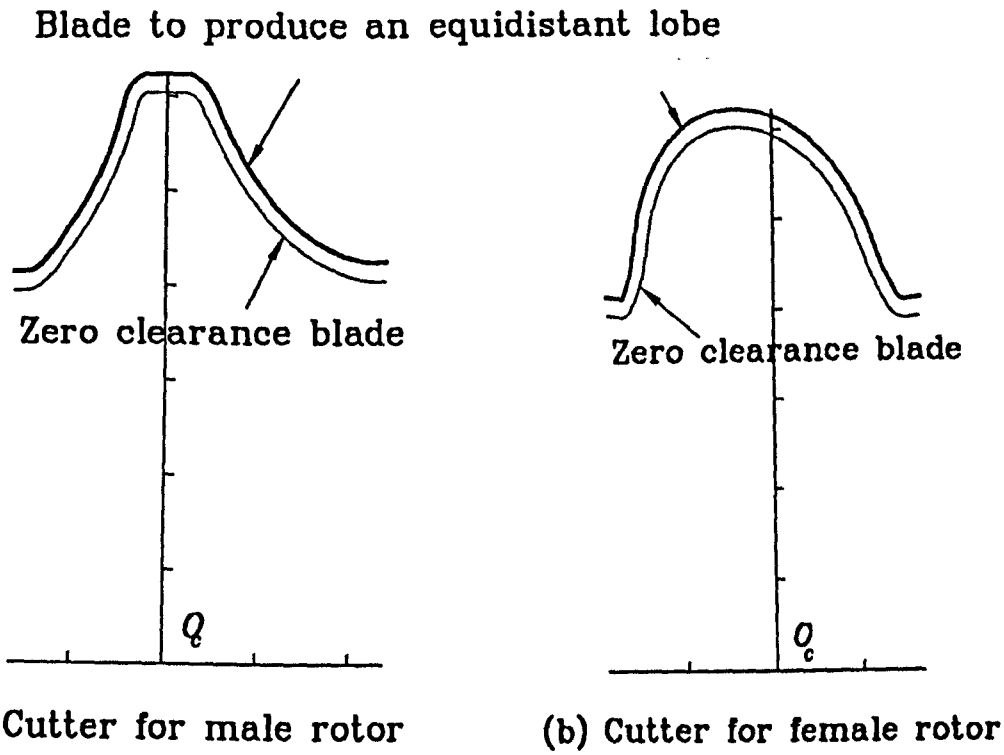

Fig. 5.3 The zero clearance and real cutter blades to produce equidistant lobes

5.4.3 Clearance Distributions of the Two Methods

In the following sections of this chapter, if no special definition is given, the inter-rotor clearance or compressor clearance means the clearance at the contact line normal to the local helical surfaces. The inter-rotor clearance distribution is an important factor in helical screw compressors. A design aim should be to ensure a uniform running clearance distribution, the value of which to be as small as is practically attainable.

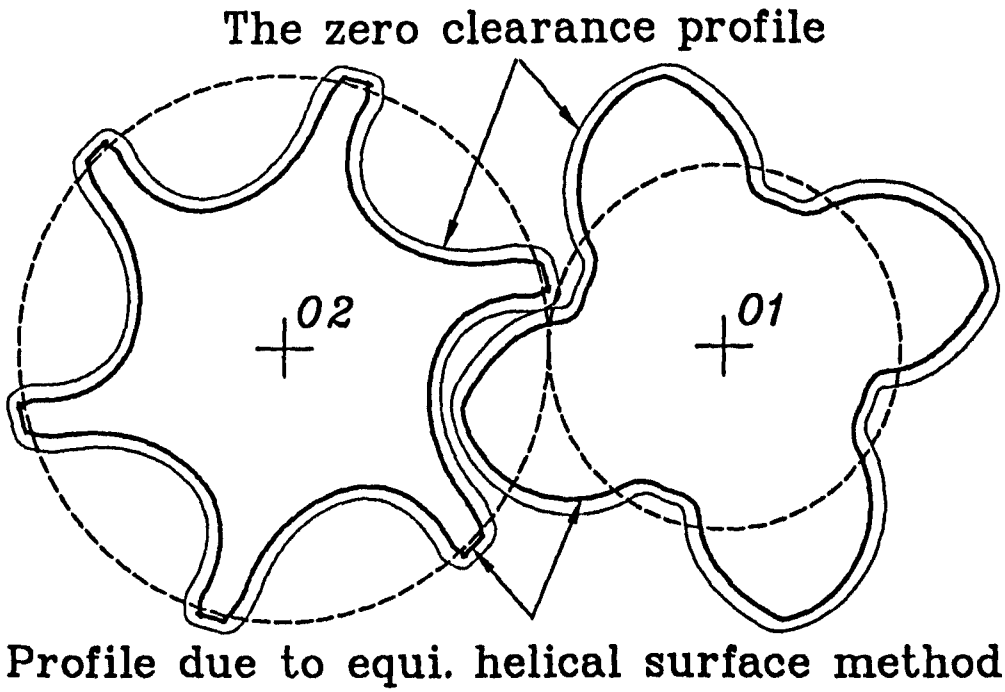

Fig. 5.4 The zero clearance and real lobe profiles deriving from the equidistant helical surface method

Fig. 5.6 shows a graph of the clearance distributions along the contact line obtained using the two clearance schemes subject to the condition that the minimum inter-rotor clearance is the same for both methods. For the equidistant lobe profile method, the maximum inter-rotor clearance, which equals the uniform distance between the real and the zero clearance end profiles, occurs at the tips and the roots of the rotors, while along the lobe flanks the clearance normal to the helical surface is less than the clearance normal to the end profile. For the equidistant helical surface method the situation is very different. For this case the minimum distance between the real and zero clearance end lobe profiles, which equals the (uniform) clearance normal to the helical surface, occurs at the tips and roots of the rotors. On the lobe flanks of the end profile the distance is larger than the (uniform) inter-rotor clearance normal to the helical surface.

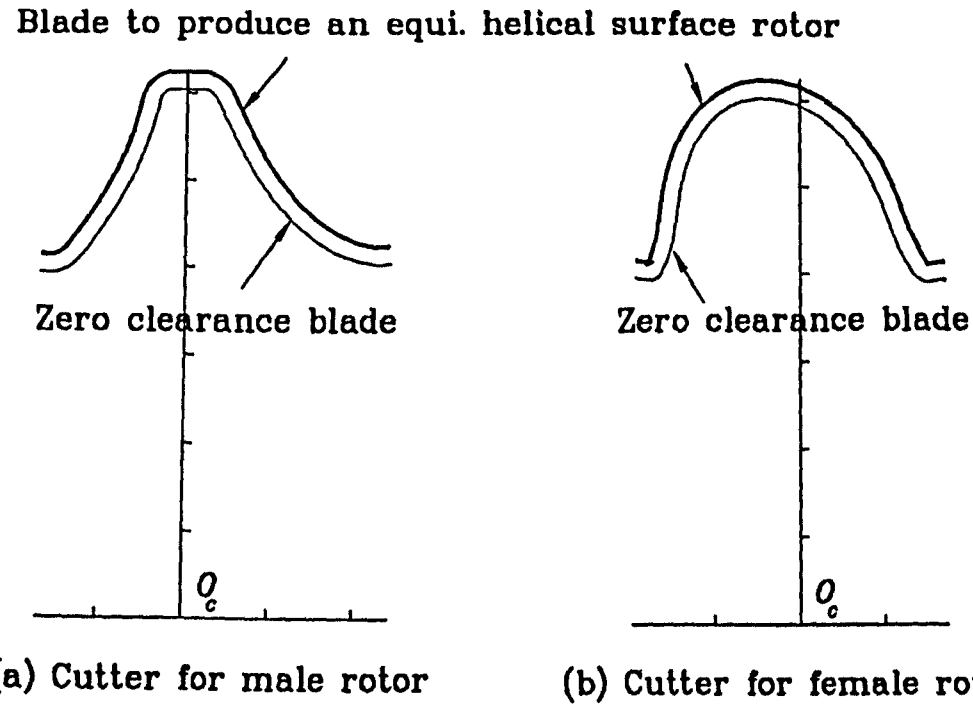

Fig. 5.5 The zero clearance and real cutter blades to produce an equidistant helical surface

The areas under the graphs of the inter-rotor clearances in Fig. 5.6 represent the leakage areas for gas leaking across the contact line. The equidistant helical surface method results in the same inter-rotor clearance everywhere on the contact line. In magnitude, it is equal to the minimum value resulting from the equidistant lobe profile method so that its leakage area per lobe is only 89 per cent of the equidistant lobe profile method; that is the average inter-rotor clearance of the equidistant lobe profile method is bigger than the equidistant helical surface method by twelve per cent for the following rotor specification:

- Lobe profile — SRM D standard.
- The minimum clearance normal to the helical surface for both methods is $13\mu m$, which is equivalent to $18\mu m$ in the plane of the profile.
- Male and female rotor diameters (equal): $201mm$.
- Male rotor wrap angle: 300°.
- Length/diameter ratio: 1.65.

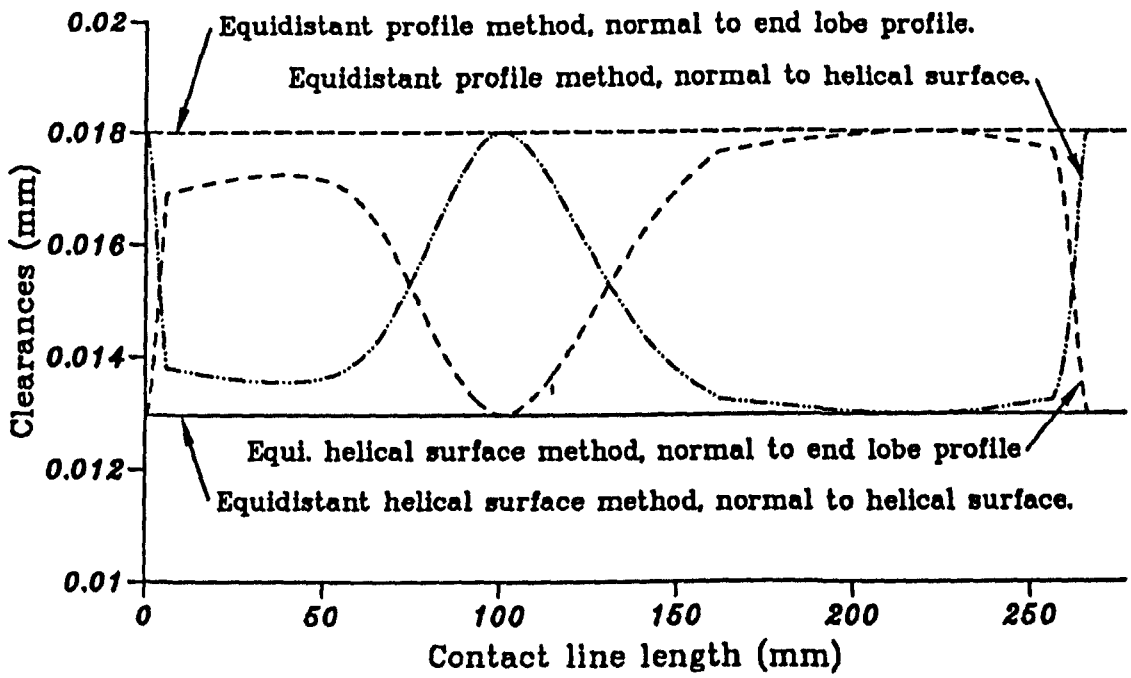

Fig. 5.6 The clearance distributions along the contact line

For refrigeration compressors, the temperature of the rotors is slightly higher than the normal atmospheric temperature, which results in a very small thermal expansion in the radial direction, and at the same time the rotor deflection caused by the cavity pressure always tends to separate the rotors, so that the clearances at the tips and the roots of the rotor lobes do not need to be larger than at their flanks. As a result, the inter-rotor clearance distribution obtained by the equidistant helical surface method is to be preferred over that of the equidistant lobe profile method.

5.4.4 Timing Gear Accuracy

Fig 5.7 shows a zero clearance lobe profile and its two real profiles calculated by the two methods used in this chapter. In this case both methods have been arranged to give the same average clearances, that is, they cause the same leakage across the contact line and result in the same compressor performance, but the real profile obtained by the equidistant helical surface method results in a larger

flank clearance than does the equidistant lobe profile method. This geometrical characteristic is very useful for an oil free helical screw compressor, which needs timing gears to transmit the torque between the rotors because gears of a lower accuracy can be used with no detrimental effect on the thermodynamic performance of the compressor.

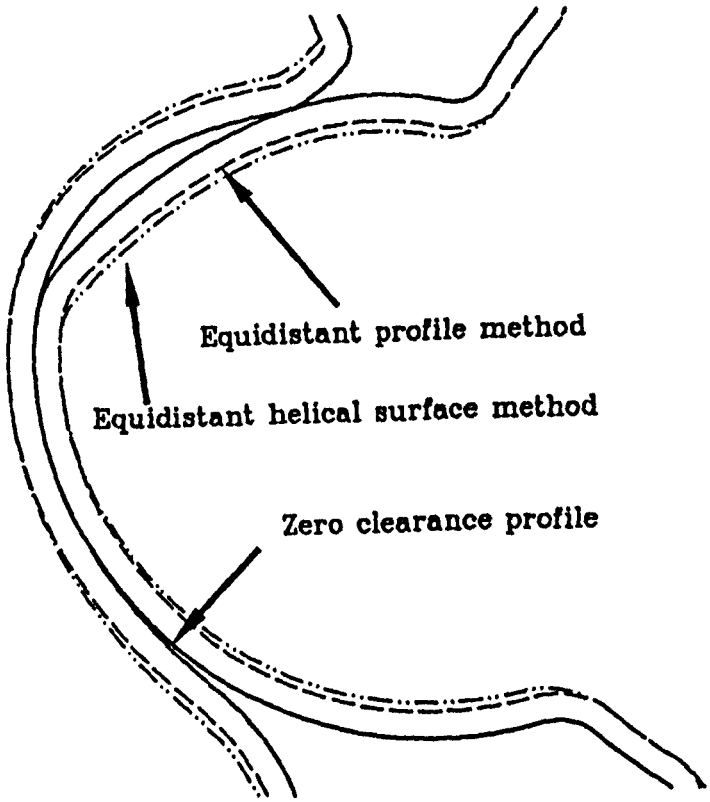

Fig. 5.7 A zero clearance profile and its two real profiles

5.4.5 Leakage Influence on Thermodynamic Performance

The leakage path across the contact line is the most important of all the leakage paths because it has a large leakage area combined with the short path length in the direction of flow and the largest pressure difference. As a consequence it has a large effect on the performance of the compressor. A leakage analysis (7) conducted by the author for a refrigeration helical screw compressor shows that the net leakage across the contact line is about 1.3 times the leakage across the tip sealing lines of the male and female rotors and about 5 times the leakage rate through the blow hole.

Fig. 5.8 shows the model's prediction of the effect of changing from an equidistant lobe profile clearance to an equidistant helical surface clearance when the *minimum* clearance is maintained at the same value, a sensible design criterion chosen to avoid physical contact. The volumetric and indicated efficiencies are both predicted to improve over the whole range of running conditions. This is as expected since the leakage area across the contact line is smaller for the equidistant helical surface method. And since the leakage is directly proportional to the pressure ratio, the efficiency gain should become greater with increasing pressure ratio. Although small, this is predicted, and can be seen in Fig. 5.8. The compressor specification for Fig. 5.8 is as follows:

- Lobe profile—SRM D standard.
- Clearance set by the equidistant profile method, approximately half backlash: $18\mu m$.
- Bore diameters (equal): $204mm$.
- Male rotor wrap angle: 300°.
- Length/diameter ratio: 1.65.

The running conditions are:

- Refrigerant: $R22$.
- Speed of male (driven) rotor: $3000rev/min$.
- Condensing temperature: $25°C$ (saturation pressure: 10.44 bar).
- Evaporating temperature: $-40 - 5°C$ (saturation pressure: 1.05 - 5.84 bar).
- Superheat degrees: $30°C$.
- Oil and liquid refrigerant injected.

In Fig. 5.8 a direct comparison of simulated volumetric efficiency with measured values is made and the agreement is seen to be reasonably good.

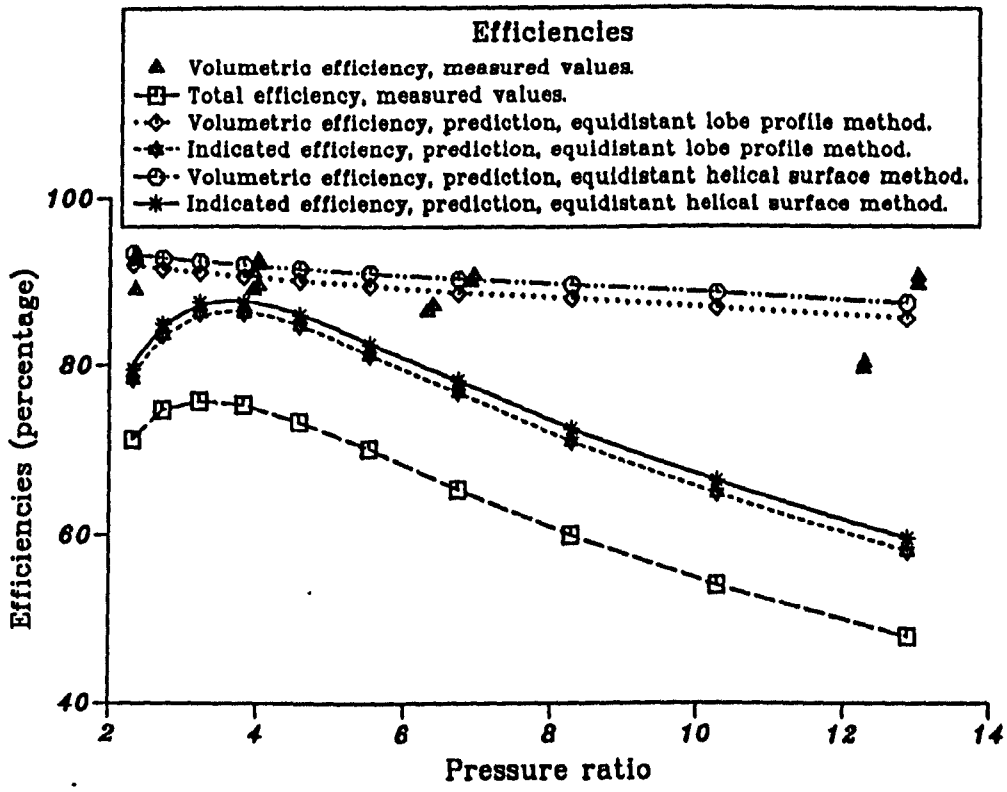

Fig. 5.8 Predicted and test results for a compressor with oil and liquid refrigerant injection—two clearance schemes compared

5.5 DETERMINATION OF OPTIMUM CLEARANCE DISTRIBUTION

The determination of practical optimized clearances is a complicated multi-stage process requiring the use of special purpose and general purpose modern software. Clearly, the first stage must be the establishment of the basic zero clearance geometry of the male and female lobes in a plane normal to the axes of rotation (i.e. the end profiles). At this stage optimization processes evolved by the author (8) should be used to achieve the optimum lobe profile geometry. At the conclusion of these processes the optimized zero clearance lobe profiles will have been established and consideration can now be given to the process of determining a practical working clearance distribution along the sealing line so that under operational conditions the smallest possible leakage *area* is combined

with lobe profiles which will not come into metal to metal contact with each other or with the housing.

First, the rotor and housing deflections caused by operational effects must be considered and evaluated so that they can be taken into account in the clearance determination procedure. When the compressor is operated (at its standard conditions say) gas forces, temperature rises and temperature gradients will occur which will cause deflections of the rotors and the housing. The zero clearance condition of the meshing lobes, appropriate to an unpressured compressor at rest and at ambient temperature will no longer hold; interference will occur at some places and gaps at others. Deflections are caused by the following effects:

1. *Temperature effects causing expansion*

   Operation causes temperature increases which cause expansion; greater for the rotors in the hot centre of the machine than for the cooler outer surface of the housing. In addition, a temperature gradient develops along the rotor axes of the machine, cold to hot, suction to discharge which causes an uneven expansion. In practice for some machines which work under relatively high discharge temperature, conical rotors are used by Howden Compressors Ltd. and perhaps by other manufactures to achieve small uniform tip clearances.

2. *Gas pressure effects causing rigid body separation of the rotors*

   The pressure of the gas being compressed in the cavities causes a force which tends to separate the rotors by an amount which depends on the bearing clearances and stiffnesses.

3. *Gas pressure effects causing bending of the rotors*

   The gas pressure effects of (2) also tend to cause the rotors to bend away from each other, increasing the gap between them, the effect being greatest approximately mid-way between the bearings according to the author's deflection program.

4. *Drive contact forces between lobes causing rigid body deflections and bending*

   These effects are similar to those caused by gas pressure in the cavities as described in (2) and (3).

The author is in the process of developing a force analysis program and a rotor deflection program, which can be used to calculate the deflections described in (3) and (4). This is proposed as suitable further work.

The separation effect described in (2) may be calculated without too much difficulty. A knowledge of the combined bearing stiffness derived from experiment or analysis permits the determination of the elastic deformation in the bearings. The bearing clearance should be added to this. The most important deflections are likely to be due to (1). Their determination is outside the scope of this thesis and will be the subject of a separate study by the author.

Besides the above factors which need to be taken into account to obtain a good cold clearance distribution, the factors related to rotor manufacture, such as the deflection of the rotor and its cutter during the manufacturing process, should also need to be taken into account, and again a special computer program has to be developed. Part of this work is described in (9), (10) and (11). Related to this research, the rotor profile measurement becomes very important. The coordinate measuring machine (CMM) is becoming more commonly used for this work, and is providing a more direct indication of an individual rotor. Holroyd have announced that they are working with a very interesting alternative to the CMM, in the form of an automatic profile inspection machine (PIM) that can measure the clearances between two rotors by means of light (12).

Once all the above effects on the basic zero clearance lobe profiles have been established, the basic profiles can be altered point by point over all the points describing one lobe in such a way that a zero clearance mating is re-established. In the ideal situation, at this stage a "zero clearance when operating" profile can established. The cutter blade calculation program should now be used to generate cutter shapes capable of manufacturing the "zero clearance when operating" profiles. The final stage is to choose equidistant blade shapes which allow for rotor manufacturing imperfections and oil film thickness etc. These blades may now be used to manufacture real practical rotors having an optimized clearance distribution under operating conditions.

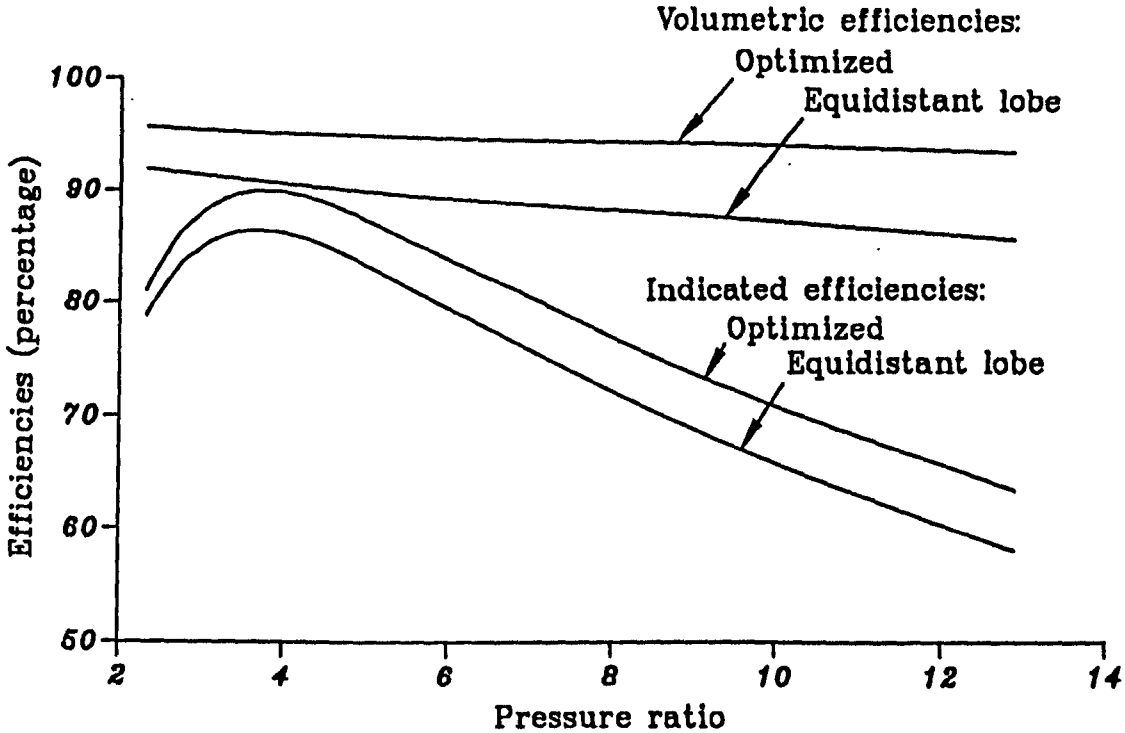

Fig. 5.9 Predicted results of a compressor with oil and liquid refrigerant injection—optimized and equidistant profile schemes compared

Since the predictive reliability of the thermo-fluid model appears to be good (see Chapter 4) it is reasonable to use it to compare the performance of a compressor having its inter-rotor clearance optimized in the sophisticated manner described here with the performance of the machine discussed in Section 5.4.5 in which a single inter-rotor clearance was chosen to accommodate all effects, manufacturing and operational, by the equidistant lobe profile method. The object of this exercise is to get an estimate of the performance of the 'best possible practically attainable design'. If an equidistant helical surface clearance of $5\mu m$ is attainable when operating, then the improvements in the volumetric and indicated efficiencies are quite dramatic as can be seen in Fig. 5.9. Since the gas forces and temperature gradients would not be constant over the range of operating pressure ratios indicated, the graphs would not be exactly the same as the shapes shown but they do give an indication of the improvements attainable, and they are significant.

5.6 THE OPTIMISATION OF CUTTER SHAPE

Cutter shapes have an important influence on the manufacturing cost of rotors. If a cutter has a interrupted blade or a sharp point, or the cutter edge has a rapid variation of its radius of curvature, or regions of unusually small radius of curvature, great exactness of the cutter shape is required to produce of a rotor having reasonable tolerances, which would require an increase in manufacturing cost to produce a compressor having a competitive thermodynamic performance. The interrupted blade, the sharp point and the fast variation of the radius of curvature also mean a lower number of rotors produced between resharpening operations of the cutter, restrictions on favourable cutting angles and cutting speeds, again resulting higher manufacturing costs. The angle between the two flanks of the cutter blade, especially the angle at the outer end of the blade where it is a minimum for the male rotor cutter, has an important influence on the manufacturing cost of rotors. If the minimum angle is large, the number of possible resharpening operations of the new blade before it is cut down to its minimum usable size will be large, as the amount of material to be ground away in each operation will be small. The tooling cost can thus be cut down drastically which means a more economical production of rotors.

Cutter shapes are defined mainly by the profile used. Some old profiles have sharp points and can result in interrupted cutter blades; they also have rapid variations of the radius of curvature on the edges. However, modern profiles, such as SRM D, require a cutter which has a shape where the edge follows a continuous curve without abrupt changes of the radius of its curvature. The modern profiles require their cutters to have a large angle between the two flanks of the blades, and permit a wider selection of the angles between the cutting tool and the workpiece during the manufacturing operation; which in turn means that the more favourable cutting angles can be chosen, so that the wear of the tool is reduced and simultaneously the possibility of increasing the cutting speed is opened up. In other words the modern profiles open up the possibility of manufacturing a more efficient compressor for a lower cost than is possible when

the older profiles are used.

Cutter shapes can be changed by changing profile parameters, but usually the optimisation of a cutter shape will not depend solely on the change of profile parameters, which are chosen in order to obtain the best thermodynamic performance for the compressor as in (8). Once the profile parameters are settled according to optimisation procedures to gain the best thermodynamic performance, the cutter shapes can then be calculated according to different clearance distribution schemes to determine the basic cutter shapes. Thereafter manufacturing parameters such the offset angle and the angle between the cutting tool and the workpiece, influence cutter shapes considerably; the angle between the two flanks of the cutter blades, and the angle between one of the flanks and the line connecting the rotor and cutter centres, are particularly influential (**13 & 14**).

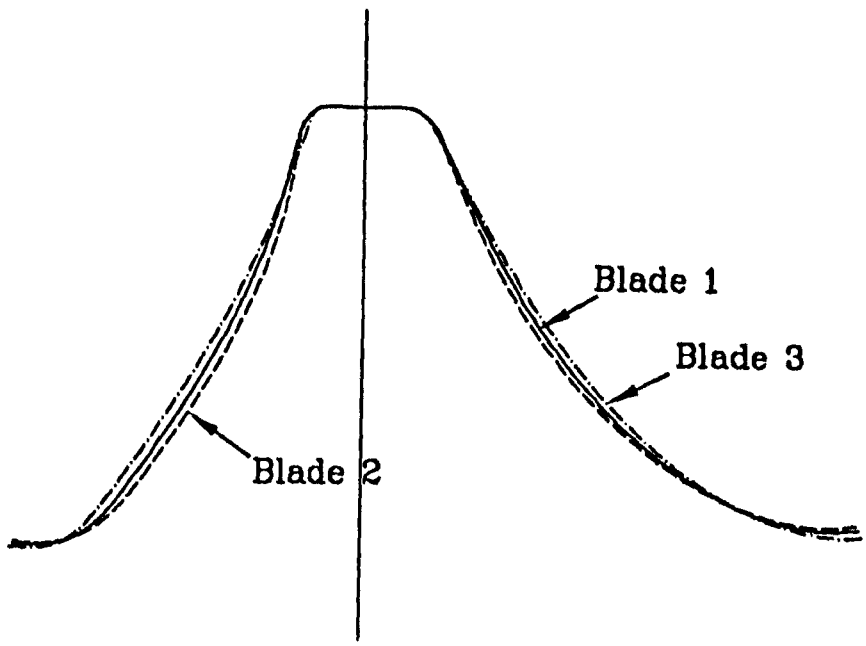

Fig. 5.10 The influence on cutter shape of the angle between the cutter and rotor axes

Fig. 5.10 shows the influence on the cutter shape of the angle between the cutter and rotor axes on the cutter shape. All the blades in Fig. 5.10 are used

to cut the same profile, and have the same profile parameters, the same rotor parameters and the same offset angle, which is $-36.72°$. Blade 1 is the cutter blade used to cut the male rotor of the compressor mentioned in section 5.4, and the angle between its cutter axis and the rotor axis is 45°. The angles between the cutter axis and the rotor axis of blades 2 and 3 are 47.5° and 41° respectively. The minimum angles between the two flanks of blade 1, 2 and 3 are 36°, 28° and 50° respectively. The smaller the angle between the cutter axis and the rotor axis, the larger the minimum angle between the two flanks of a cutter blade. The tooling costs of blade 3 are less than those of blades 1 and 2.

Fig. 5.11 shows the influence of the offset angle on the cutter shape. Blade 1 is the cutter blade used to cut the female rotor of the compressor mentioned in Section 5.4, and its offset angle is 7.5°. Blades 2 and 3 have the same angle between the cutter axis and the rotor axis as has blade 1, which is 45°, but different offset angles, which are 17.5° and $-2.5°$ respectively. The offset angle does not change the basic cutter shape, but changes the minimum angle between the primary flank and the line connecting the cutter and rotor centres, which has an important influence on the number of possible resharpening operations of the cutter for female rotors. For blade 3 the minimum angle between the primary flank and the connecting line is small, about 5°, which means that a large amount of material is ground away in each resharpening operation and the number of possible resharpening operations of the new blade before it is cut down to its minimum size will be small, but the minimum angle between the secondary flank and the connecting line is large and about 20°. The angles between the primary flank and the connecting line and between the secondary flank and the connecting line are too dissimilar for good design. A change of the offset angle can change this arrangement. Blade 1 has 7° and 18°, and blade 2 has 10° and 15° for the minimum angles between the primary flank and the connecting line and between the secondary flank and the connecting line respectively. For blade 2, the combination of the angles between the primary flank and the connecting line and between the secondary flank and the connecting line is much more reasonable than for blades 1 and 3.

It should be mentioned here that another important manufacturing parameter, namely the distance between the cutter and rotor centres, has no influence on the cutter shape in modern profiles. For old profiles, on which one or more sharp points exist, the distance is dependent on the angle between the cutter axis and the rotor axis (**2**, **4** and **5**).

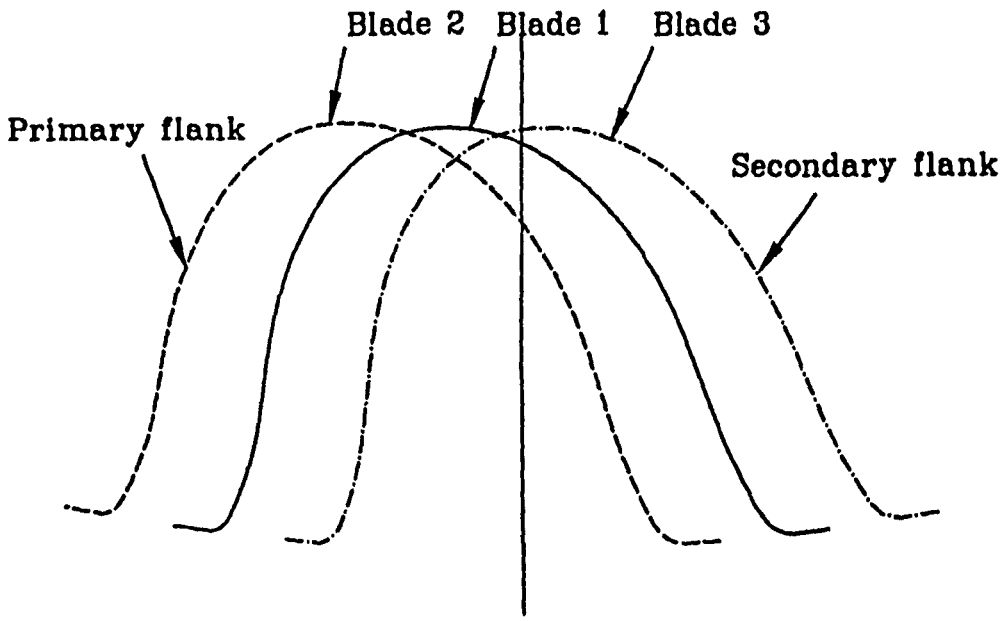

Fig. 5.11 The influence of offset angle on the cutter shape

In both methods, changing the offset angle and changing the angle between the cutter and the rotor axes, can be used to optimise the cutter shapes of both male and female rotors. Fig. 5.12 shows the cutter blades which are used to cut the improved SRM D-profile proposed in Chapter 6 (Fig. 6.4) by the author. Both methods are used to optimise the cutter shapes shown in Fig. 4.12. The minimum angles between the two flanks of the male and female rotor cutters are 52° and 46° respectively, and both cutter blades are good practical shapes. The main rotor parameters and the manufacturing parameters for the improved profile are as follows:

- The screw pitch of the male rotor: 1.985 *times the diameter of the male rotor tip circle.*

- The wrap angle of the male rotor: 299.2°.
- Angle between the axes of the male rotor and its cutter: 39°.
- Angle between the axes of the female rotor and its cutter: 37°.
- Offset angle of the male rotor: −25°.
- Offset angle of the female rotor: 20°.

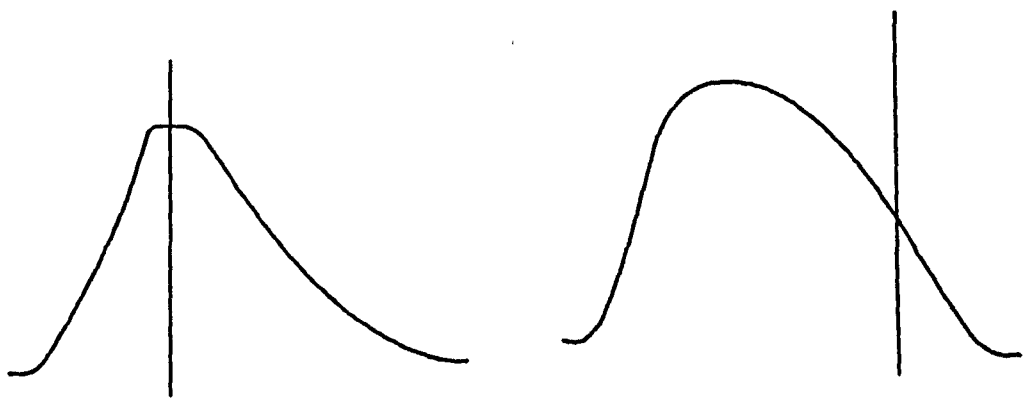

(a) Cutter blade of male rotor (b) Cutter blade of female rotor

Fig. 5.12 The cutter blades for the proposed improved profile

5.7 REFERENCES

1 **Buckingham, E.** Analytical Mechanics of Gears. *McGraw-Hill Book Company, Inc.*, 1949.

2 **Wu, Xu-Tang** Mating Theory of Gears (in Chinese). *Mechanical Industry Book Company*, Beijing, 1982.

3 **Nutbourne, A.W.** Differential Geometry Applied to Curve and Surface Design (Volume 1: Foundations). *Ellis Horwood Ltd.*, Chichester, 1988.

4 САКУН, И. А.: ВИНТОВЫЕ КОМПРЕССОРЫ. МАШГИЗ, 1960.

5 АМОСОВ, П. Е.: ВИНТОВЫЕ КОМПРЕССОРНЫЕ МАШИНЫ (СПРАВОЧНИК). МАШГИЗ, 1977.

6 **Tang, Yan** and **Fleming, John S.** Manufacture by Milling of the Rotors of Twin Screw Compressors: Cutter Blade Shape Determination to Combine Increased Thermodynamic Efficiency with Reduced Manufacturing Cost. *Research Report 9*, Dec., 1993.

7 **Fleming, John S. Tang, Yan Young, W.** and **Anderson, H.** Leakage Analysis of a Helical Screw Compressor. *Proceedings of I Mech E European Conference on Developments in Industrial Compressors and their Systems*, London, U.K., 1994, pp. 1–8.

8 **Tang, Yan** and **Fleming, John S.** Obtaining the Optimum Geometrical Parameters of a Refrigeration Helical Screw Compressor. *Proceedings of International Compressor Engineering Conference at Purdue*, Purdue University, U.S.A., 1992, pp. 221–227.

9 **Edstrom, Soren E.** A Modern Way to Good Screw Rotors. *Proceedings of International Compressor Engineering Conference at Purdue*, Purdue University, U.S.A., 1992, pp. 421–430.

10 **Bennewitz, Christer** Software Support for Screw Rotor Design, Manufacture and Quality Control. *Proceedings of International Compressor Engineering Conference at Purdue*, Purdue University, U.S.A., 1992, pp. 431–437.

11 **Edstrom, Soren E.** Quality Classes for Screw Compressor Rotors. *Proceedings of the Institute of Mechanical Engineers*, paper C390/019, London, 1989.

12 **Holmes, C.S.** and **Munro, R.G.** A Study of Screw Compressor Rotor Geometry with a New Mothod for Remote Measurement of Clearances. *VDI Berichte 859*, 1990.

13 **Fleming, John S. Tang, Yan. Young, W.** and **Anderson, H.** The Calculation of Cutter Blades of a Helical Screw compressor and Optimisation of Their Shapes. *I Mech E European Conference on Developments in Industrial Compressors and their Systems*, London, 1994, pp.17–25.

14 **Tang, Yan** and **Fleming, John S.** Clearance between the Rotors of Helical Screw Compressors: Their Determination, Optimisation and Thermodynamic Consequences. *Proc I Mech E Vol 208 Part E, Journal of Process Mechanical Engineering*, 1994.

Chapter 6

DISCUSSION OF THE USE OF THE PROGRAMS IN THE OPTIMISATION OF COMPRESSOR DESIGN

In this chapter the four principal computer programs developed by the author, ie the profile generation program, the geometrical characteristic calculation program, the working process simulation program and the cutter blade calculation program are used to optimise a twin screw compressor. Its internal and external leakages are analysed. A method for optimising the basic geometrical parameters of the rotor profile, the rotor geometrical parameters, the position of the discharge port and the slide valve definition parameters etc. is presented. The optimisation technique described in this chapter is very useful for the practical design of a twin screw compressor.

6.1 INTRODUCTION

Although many factors influence the performance of a twin screw compressor, they may be grouped into two categories as follows:

- The operating parameters such as rotational speed, refrigerant, suction pressure, condensing pressure, quantity of oil or liquid refrigerant injected etc.
- The geometrical parameters such as basic profile parameters, rotor parameters, discharge port position and slide valve definition parameters etc.

From the view point of designing a screw compressor for given running conditions (usually, evaporating temperature or suction pressure, condensing temperature or pressure, suction superheat degrees, refrigerant and capacity of a refrigeration system), the choice or decision of the basic geometrical parameters

of the rotor profile, the rotor geometrical parameters, the position of the discharge port, the slide valve definition parameters, and even the positions and sizes of the ports for oil injection, liquid refrigerant injection and superfeed etc. should be optimised. In this chapter, the optimisation techniques are discussed. The techniques concentrate on the profile and rotor geometrical parameters, the position of the discharge port, and the slide valve definition parameters.

Increasing the quantity of liquid refrigerant injected always results in a slight decrease of the COP (coefficient of performance) as calculated for the simple cycle in which only changes of state of the refrigerant are considered. But the injection of liquid refrigerant can in some cases eliminate the need for separate oil cooling. As a consequence, the effect on the thermodynamic efficiency of a real plant can be difficult to predict. If the discharge temperature is lower than that permitted, the quantity of liquid refrigerant injected should be as small as possible. This quantity can be predicted by the working process simulation program. Increases of rotational speed and quantity of oil injected always result in a decrease of leakage through all leakage paths with a consequent increase in the volumetric efficiency. On the other hand, an increase in the quantity of oil injected will result in an increase of the fluid-dynamic losses, fluid and mechanical friction losses etc., so as to increase the energy consumption. For the rotational speed and quantity of oil injected there exist optimum values, between which there is a relationship.

The performance of a twin screw compressor is influenced more by the internal gas leakages than by any other thermo-fluid aspect of its behaviour. Six separate leakage paths can be identified (see Chapter 4). Only the cusp blow holes have a constant geometry; every other path has a geometry (and a resistance to flow) which varies (periodically) in a manner unique to it. The pressure difference driving the gas along a leakage path also varies (periodically) and does so in a manner which is not the same for every leakage path. This is quite obviously a problem requiring insight in the thermo-fluid modeling process and the solution of a large number of simultaneous equations. Fortunately, the developed working process simulation program provides a powerful tool for the leakage analysis of the compressor. The leakage of each leakage path and the percentage by which it can

reduce the volumetric and indicated efficiencies can be calculated by the program (see Chapter 4). The resultant "leakage table" can be used in an optimised compressor design. This is presented in this chapter.

The following computer programs described in the previous chapters are used for the analysis in this chapter:

- Profile generation program (see Chapter 2).
- Geometrical characteristic calculation program (see Chapter 3).
- Cutter blade calculation program (see Chapter 5)
- Working process simulation program (see Chapter 4).

The cutter blade calculation program is only used to calculate the average clearance along the contact line, which is required by the working process simulation program.

Although the discussion in this chapter is concerned with a refrigeration twin screw compressor, the working fluid of which is *R*22, the optimisation technique described can be applied to a twin screw compressor compressing any working fluid, which could be pure or mixed refrigerants, air and other gases and gas mixtures.

6.2 LEAKAGE ANALYSIS OF A TWIN SCREW COMPRESSOR

The helical screw compressor is a positive displacement compressor, the working cavity of which is enclosed by the housing bores, housing end plates and the helical surfaces of the male and female rotors. As the result of the rotation of the rotors, the volume of the working cavity varies from zero to its maximum and from its maximum to zero periodically. As a consequence of this periodic variation, the compressor completes its suction, compression and discharge processes.

Due to the geometry of the mating parts and the need for clearances between them the compressor has several leakage paths as follows: across the contact line, across the rotor tips and end sealing lines, and through the cusp blow holes and the compression start blow hole. The summation of the leakages through all these paths has a greater influence than anything else on the performance of the

compressor. Leakages are of two kinds. The first is called external which is the leakage from the cavity to the suction chamber or to the cavity in suction process, and it reduces both the volumetric and indicated efficiencies. The second is called internal which is the leakage from a cavity to the following enclosed cavity, and it reduces the indicated efficiency, but has no direct influence on the volumetric efficiency.

Each leakage path has a different influence on the performance of the compressor. It is very important to know the leakage through each leakage path and the percentage by which it can reduce the efficiencies for the purpose of improving the rotor end profile and optimizing the compressor geometrical parameters. For example, reducing the blow hole area and the contact line length always results in increasing the performance, but very often for a given rotor profile the reduction of the blow hole area would result in an increase of the contact line length. If the influence of the contact line length on the efficiencies is (say) much smaller than that of the blow hole area, a improved profile may be generated, which has relatively large contact line length, from which other benefits can be obtained.

It is difficult to calculate the leakage of a given leakage path through the whole working process, as during the operation of a compressor the states of the working medium before and after the leakage path, the leakage area and the length of the path etc. vary periodically and continuously. Fortunately the working process simulation program developed by the author is capable of doing the quantitative leakage analysis (see Chapter 4). The program is specially designed in order to calculate the leakage rates leaking in to and leaking out of a chosen cavity volume and the net leakage rates through each leakage path. The percentage by which the leakage of each path reduces the volumetric and indicated efficiencies can also be calculated. Some of the leakage analysis results have been published by the author (1). These results can be used to improve the profile and to optimize the geometrical characteristics. The greatest attention should be paid to those leakage paths which have the greatest influence on performance. Some suggestions and all the leakage analysis results are presented in this section.

6.2.1 Influences of Leakage Paths on Compressor Performance

Fig. 6.1 shows the leakage analysis results for a twin screw compressor, the specification of which is as follows:

- Lobe profile: SRM D standard.
- Lobe combination: $4 + 6$
- Bore diameters (equal): $204mm$.
- Male rotor wrap angle: 300°.
- Length/diameter ratio: 1.65.
- Volume ratio for axial discharge port: 5.0.
- Volume ratio for radial discharge port: 3.6.

Its running conditions are:

- Refrigerant: $R22$.
- Speed of male (driven) rotor: 3000 rev/min.
- Condensing temperature: $25°C$ (saturation pressure: 10.44 bar).
- Evaporating temperature: $-20°C$ (saturation pressure: 2.45 bar).
- Superheat degrees: $30°C$.
- Superfeed and liquid refrigerant injection not on duty.
- Oil drained and injected.

Fig. 6.1 (a) shows the leaking outflow rates from the considered cavity through the different leakage paths. The working fluid can leak out to the following cavity or to suction pressure (suction chamber). Fig. 6.1 (b) shows the leaking inflow rates through the same leakage paths. The working fluid can leak into the considered cavity from the leading cavity or from the discharge chamber. The net leaking outflow rates from the considered cavity through the different paths are shown in Fig. 6.1 (c). The measured and predicted efficiencies for the specified compressor and running conditions are listed in Table 6.1.

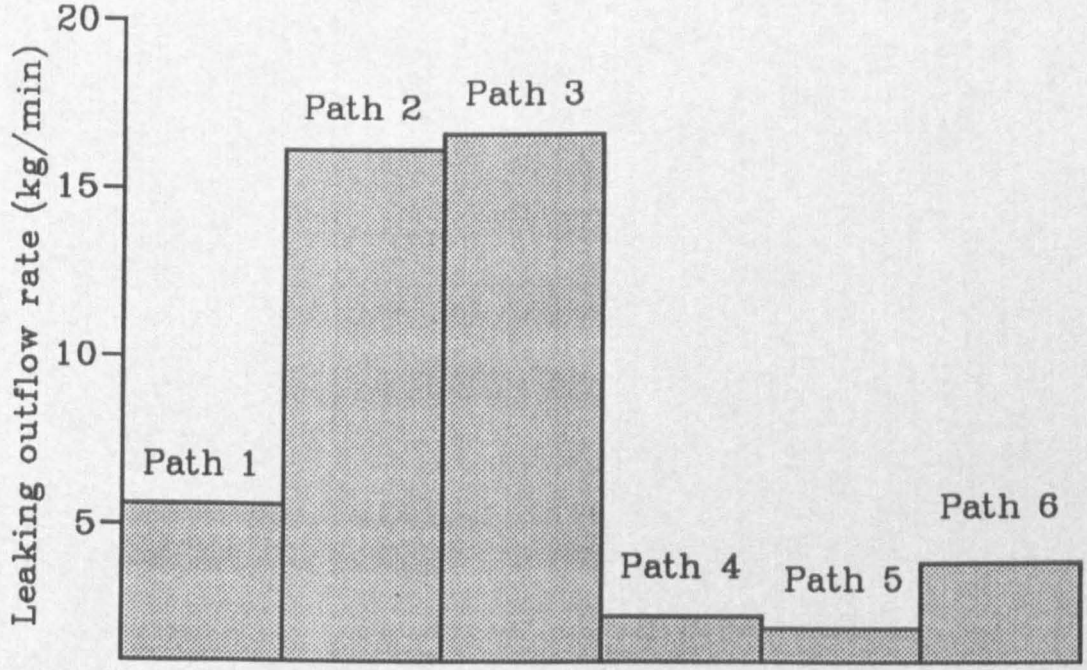
Leaking outflow rate (kg/min)
20
15
10
5
Path 1
Path 2
Path 3
Path 4
Path 5
Path 6

(a)

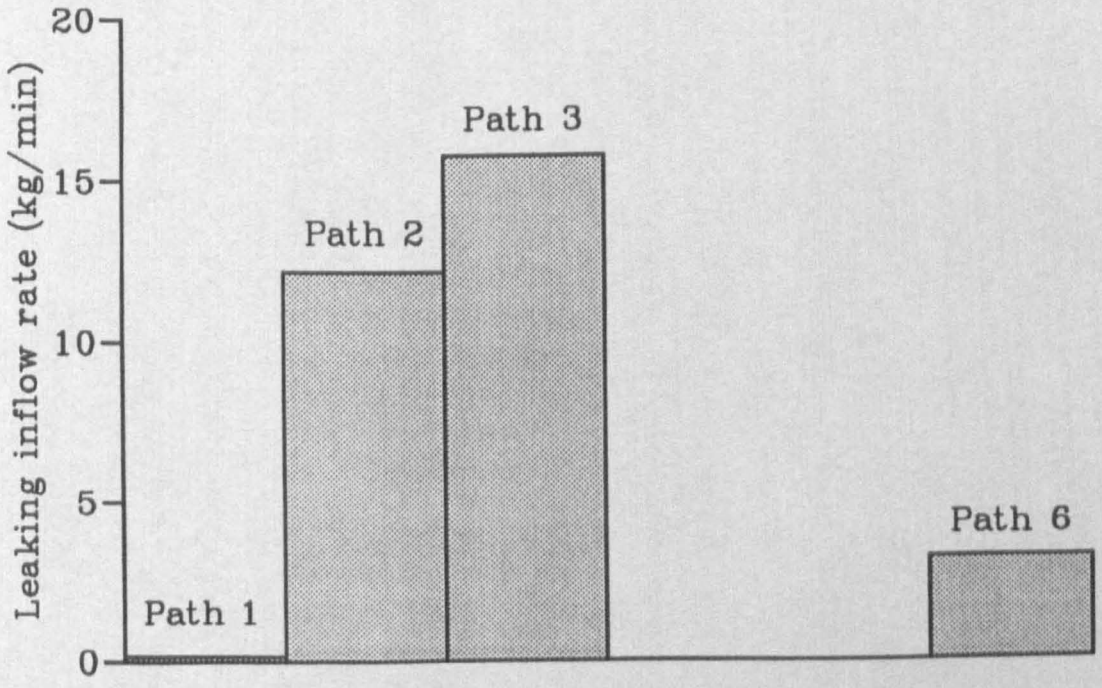
Leaking inflow rate (kg/min)
20
15
10
5
0
Path 1
Path 2
Path 3
Path 6

(b)

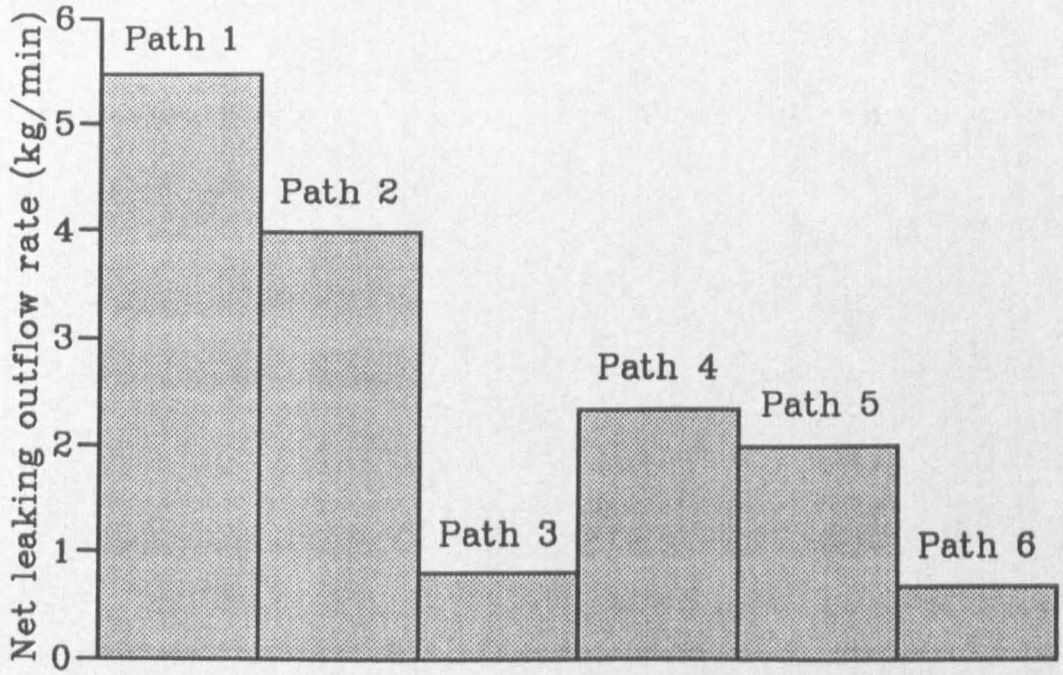

(c)

Fig. 6.1 The leakage flow rate through each leakage path (Running conditions: Speed of male (driven) rotor: $3000 rev/min$; Condensing temperature: $25°C$ (saturation pressure: $10.44\ bar$); Evaporating temperature: $-20°C$ (saturation pressure: $2.45\ bar$); Superheat degrees: $30°C$)

Table 6.1 The measured and simulated efficiencies

Simulated volumetric efficiency (%)	Measured volumetric efficiency (%)	Simulated indicated efficiency (%)	Simulated total efficiency (%)	Measured total efficiency (%)
91.44	91.30	82.54	73.19	73.5

As shown in Fig. 6.1, the cusp blow hole (Path 3) has the maximum leaking out and leaking in flow rates, but the net leaking outflow rate is quite small. The leakage rates across the male and female tip sealing lines (Path 2) are similar to those through the blow holes, but the net leaking outflow rate is much bigger. The leaking outflow rate across the contact line (Path 1) is much smaller than through Path 3 or Path 2, but since the leaking inflow is very small, Path 1 has

the maximum net leaking outflow rate. The situation is similar for the leakage through the compression start blow hole (Path 4) and the rotor end clearance at the suction pressure end (Path 5), which have zero leaking inflow rates and as a result have large net leaking outflow rates. The leakage through the rotor end clearance at the discharge pressure end (Path 6) is small compared with most of the others.

For different running conditions, the leakage table is similar. Fig. 6.2 shows the net leaking outflow rates through every leakage path for the same machine but the different running conditions. The evaporating temperature for Fig. 6.2 (a) is $-10°C$ (saturation pressure: 3.54 *bar*), and for Fig. 6.2 (b) is $-30°C$ (saturation pressure: 1.63 *bar*). The other running conditions are the same as for Fig. 6.1. For the evaporating temperature $-10°C$ (saturation pressure: 3.54 *bar*), the predicted and measured volumetric efficiencies are 93.08 percent and 93 percent respectively. For the evaporating temperature $-30°C$ (saturation pressure: 1.63 *bar*), the predicted and measured volumetric efficiencies are 91.16 percent and 91 percent. Both Figs. 6.2 (a) and (b) are for the same condensing temperature, ie the same discharge pressure, but different evaporating temperatures, ie different suction pressures. Although the presure ratio for Fig. 6.2 (b) is large, the theoretical mass capacity of the compressor for Fig. 6.2 (b) is less than for Fig. 6.2 (a) due to a larger suction specific volume caused by the lower suction pressure, and thus Fig. 6.2 (b) has also a smaller net leaking outflow rate for every leakage path except Path 6. However the running conditions for Fig. 6.2 (b) still have a volumetric efficiency which is about 2 percent lower than for Fig. 6.2 (a), due to the larger pressure ratio. The situation here is different from that pertaining to an air compressor in which the theoretical mass capacity is virtually constant due to virtually constant suction conditions. Furthermore, an air compressor operates at a higher pressure ratio which results in a higher net leakage flow rate and a lower volumetric efficiency.

Fig. 6.3 shows the influence of each leakage path on both volumetric and isentropic indicated efficiencies for the same machine and running conditions as for Fig. 6.1. Worthy of note is the very different influence on the two efficiencies a

particular leakage path can have. The cusp blow hole (Path 3), which has a small

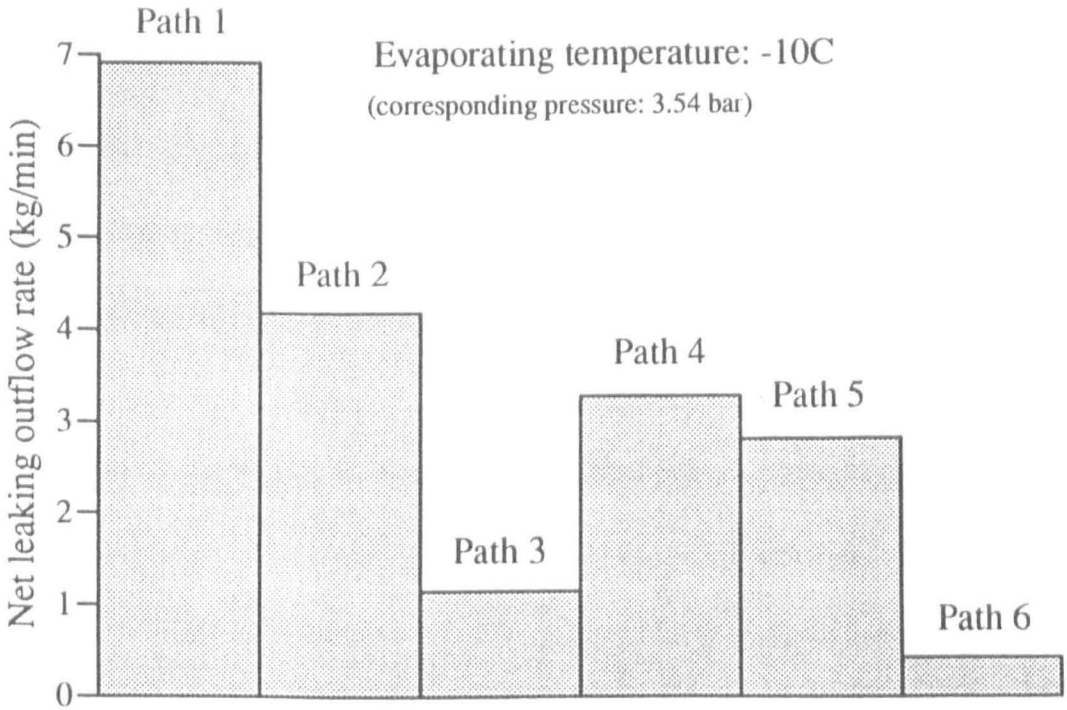

(a)

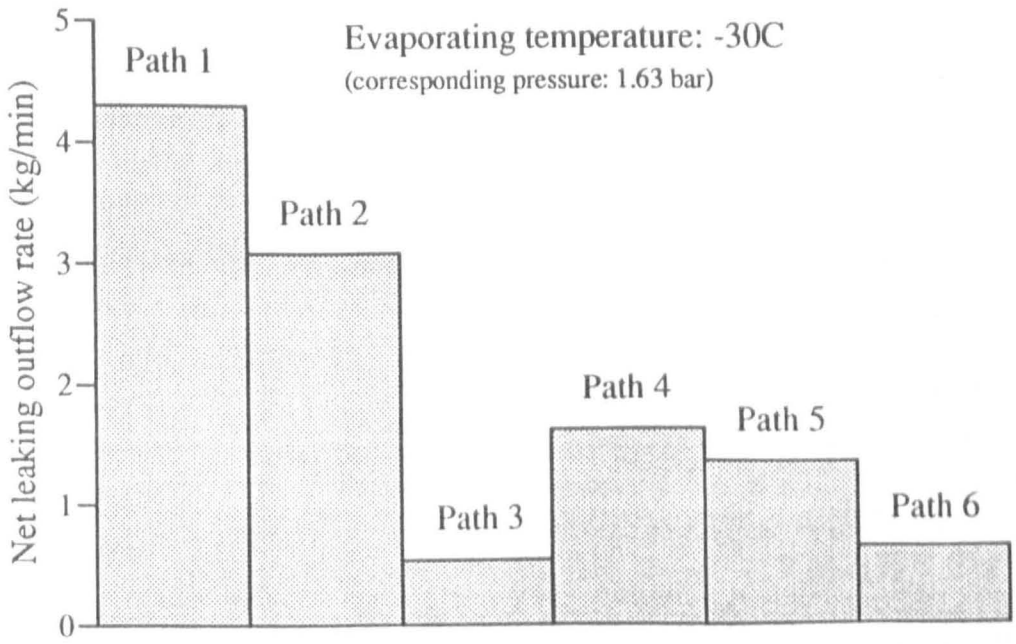

(b)

Fig. 6.2 Leakage tables for different running conditions

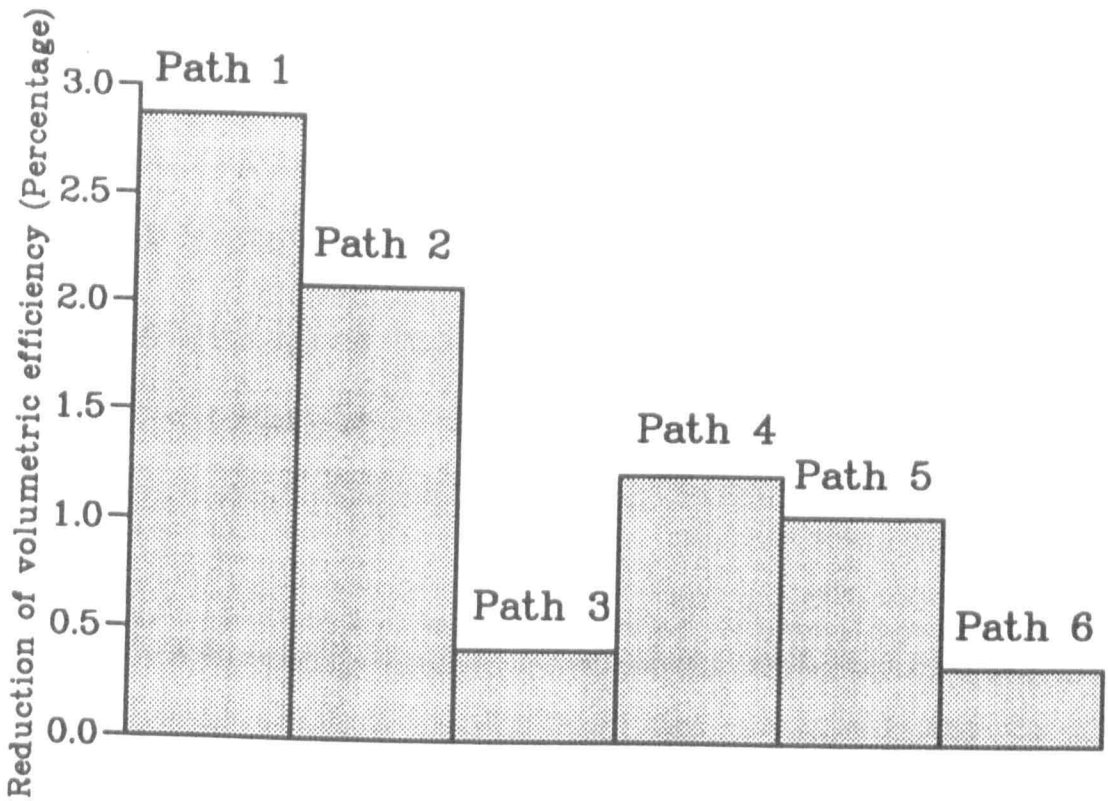

(a)

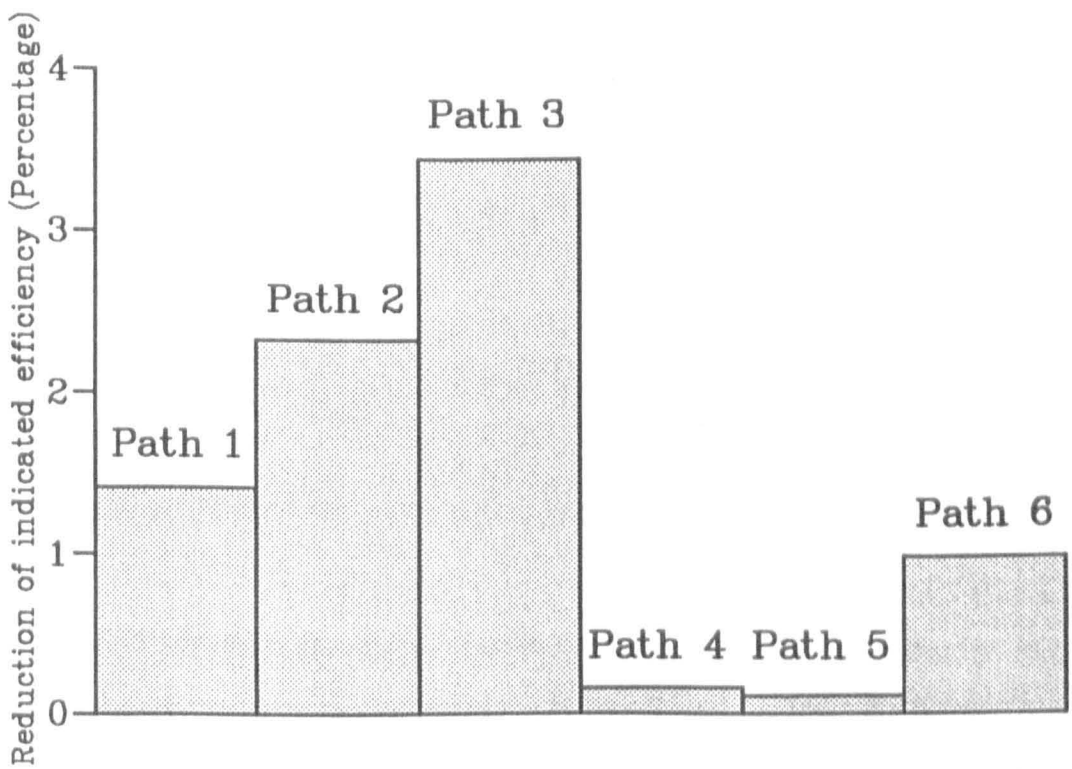

(b)

Fig. 6.3 Reduced volumetric and isentropic indicated efficiencies: leakage along each path compared with zero leakage

net leaking outflow rate, has a small effect on the volumetric efficiency, but a big effect on the isentropic indicated efficiency, which it reduces by 3.44 percent. Although the contact line (Path 1) has the most important influence of the six on the volumetric efficiency which it reduces by 2.87 percent, its influence on the isentropic indicated efficiency is less important, coming in order of importance after the cusp blow hole (Path 3) and the rotor tip sealing lines (Path 2). The leakages through the compression start blow hole (Path 4) and the rotor end clearance at the suction pressure end (Path 5) have a considerable influence on the volumetric efficiency, but have no significant influence on the isentropic indicated efficiency as the leakages take place at the very beginning of the compression process when the pressure in the cavity is very low. The leakage through the rotor end clearance at the discharge pressure end (Path 6) has an unimportant influence on both the volumetric efficiency and the isentropic indicated efficiency.

6.2.2 Application of Leakage Analysis Results

Each leakage path has its own unique influence on the volumetric and isentropic indicated efficiencies. A big reduction in volumetric efficiency is not necessarily accompanied by a big reduction in isentropic indicated efficiency. From the point of view of saving energy it is more important to obtain a high isentropic indicated efficiency than to obtain a high volumetric efficiency. The higher the isentropic indicated efficiency, the more energy saved. The user of the compressor can save operational expenses. Obtaining a higher volumetric efficiency means that a slightly smaller machine can be used for the same capacity, and the manufacturer can save some manufacturing cost.

To improve the performance of a compressor by reducing the leakages through the different leakage paths, optimising the geometric parameters of a profile must be the most valuable method, as Path 3 (the cusp blow hole), Path 1 (the contact line) and Path 4 (the compression start blow hole) depend strongly on the parameters chosen. Path 3 and Path 1 have a particularly strong influence on the isentropic indicated efficiency. With regard to reducing the leakages through

Path 2 (the rotor tip sealing line), Path 5 (the rotor end clearance at the suction pressure end) and Path 6 (the rotor end clearance at the discharge pressure end), the compressor designers should give consideration to an analysis of the thermal and dynamic distortions of the rotors and housing so as to choose optimal clearances for Paths 2, 5 and 6. The control of manufacturing quality is critical to this endeavour.

A method used to optimise the parameters of a profile has been presented by author (**2**) as has a procedure to obtain the optimum clearance distribution between the rotors (**3** and **4**). It has been used to reduce the leakage through Path 1, which has a considerable influence on both volumetric and isentropic indicated efficiencies. The leakage analysis results show that the cusp blow hole has the most important influence on the isentropic indicated efficiency, so that the improvement of a profile should concentrate on reducing the cusp blow hole area, although its influence on the volumetric efficiency is very small. Usually the reduction of the cusp blow hole area will result in a little longer contact line length, but the total leakage area across the contact line can be reduced by the method described in (**3** and **4**). Reducing the cusp blow hole area may result in increasing the compression start blow hole area, with a consequent slight net reduction in volumetric efficiency, but with no significant influence on the isentropic indicated efficiency.

Making use of the above ideas and the optimisation method presented in (**2**), an improved D-profile shown in Fig. 6.4 has been developed for a lobe combination of 5/7. and it is just an example used to show how the profile parameters and rotor parameter etc. influence the leakage pattern and thus the volumetric and isentropic indicated efficiencies. Through the example given here the author wishes to suggest that the designers of twin screw compressors do a similar leakage analysis and follow a similar optimisation procedure to design a good quality compressor. Fig. 6.5 shows for this compressor the reduced volumetric and isentropic indicated efficiencies due to the effects of the the different leakage paths. The proposed machine has the same theoretical capacity as the existing machine described in the last section. Both machines have the same wrap angle of the

male rotor, the ratio of rotor length to diameter and equal bore diameters, but the rotor diameter of the proposed machine is required to be $8mm$ bigger. The predicted results in Fig. 6.5 are for the same running conditions as in Fig. 6.3, and the clearances of the different parts of the machines are exactly same except for the clearance between the two rotors, which is redefined according to the procedure presented in Chapter 5, that is, both machines have the same minimum clearance between the rotors. The cutter blades for a proposed machine are calculated by the equidistant helical surface method (see Chapter 5).

Compared with the existing machine, the isentropic indicated efficiency has improved by 6.98 percent, but the volumetric efficiency has decreased by 0.45 percent. This is mainly due to the fact that the improved profile produces a bigger leakage through the compression start blow hole, which reduces the volumetric efficiency by 2.28 percent, a greater reduction than for the existing machine, but

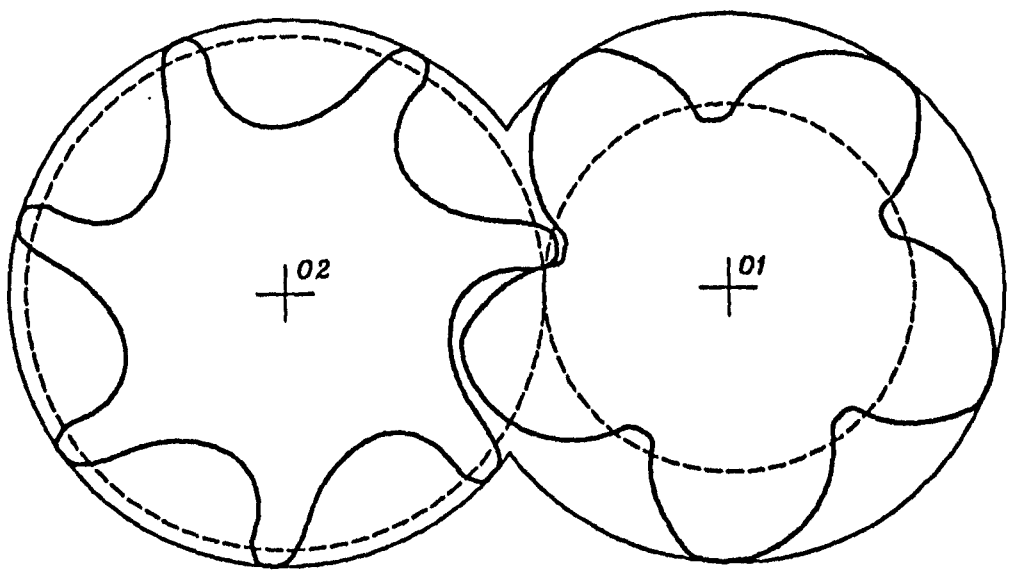

Fig. 6.4 A proposed improved profile

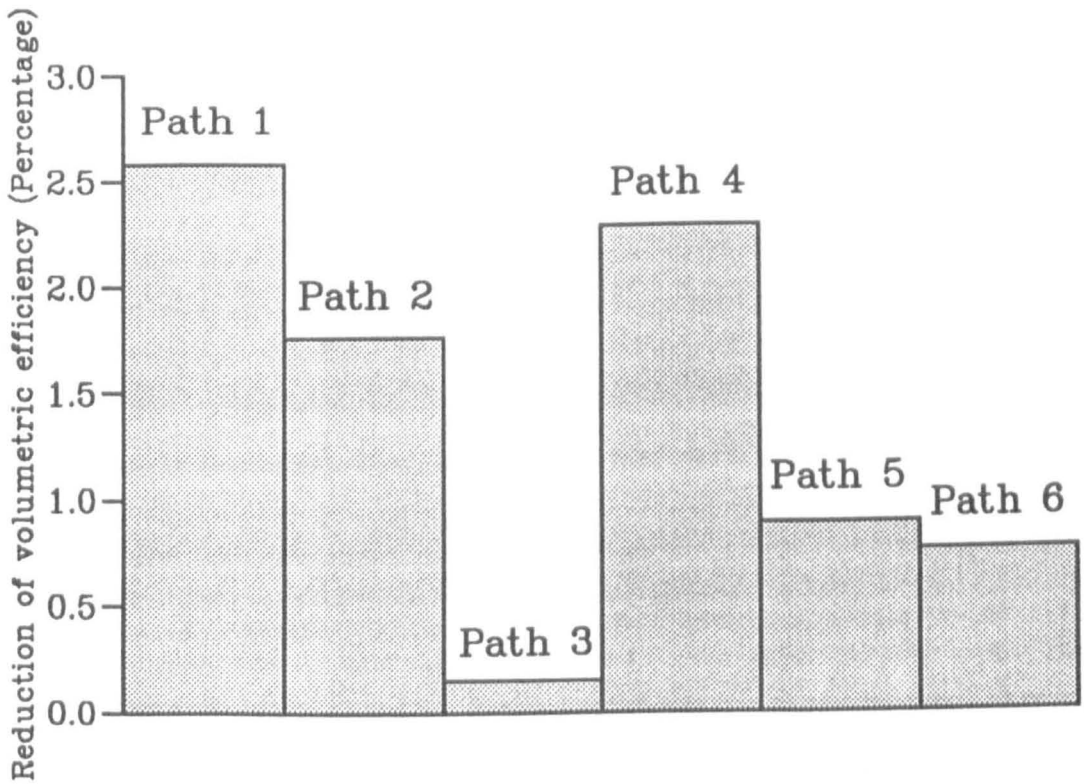

(a)

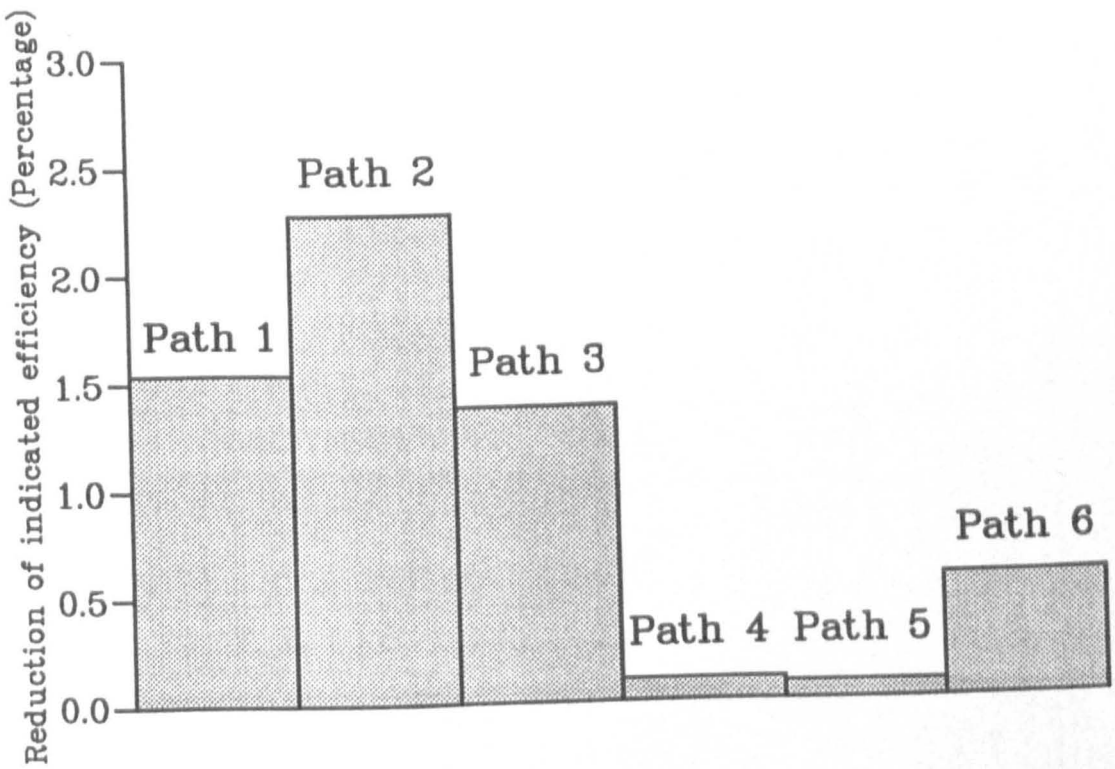

(b)

Fig. 6.5 Reduced volumetric and isentropic indicated efficiencies: for a new proposed compressor having a 5/7 lobe combination (Running conditions: as for Fig. 6.1)

the leakage through the compression start blow hole does not make a significant difference to the isentropic indicated efficiency. The change in the leakage pattern does improve the isentropic indicated efficiency, but a 6.98 percent improvement is not only due to the change in the leakage pattern, but also due to the other factors such as the reduction of discharge resistance. 2.46 percent improvement of the indicated efficiency is obtained by changing the leakage pattern, especially changing the leaking outflow and leaking inflow rates through the cusp blow hole (Path 3). Comparing Fig. 6.5 (b) with Fig. 6.3 (b) shows that the reduced indicated efficiency due to the cusp blow hole in the proposed machine has become the third in importance after the tip sealing lines (Path 2) and the contact line (Path 1). In addition, the distribution of reduced volumetric efficiencies has been changed.

6.3 OPTIMISATION OF GEOMETRICAL PARAMETERS OF A PROFILE

The purpose of the procedure for the optimisation of the geometrical parameters of a profile is to combine the smallest blow hole area and with the shortest contact line length per lobe. For a given wrap angle and screw pitch, the blow hole area and contact line length per lobe are totally decided by the end profiles of the male and female rotors. The purposes of optimising the geometrical parameters of a profile are to obtain small leakage areas and a better performance. The following two considerations should be kept in mind:

- The profiles should be streamlined.
- The cutter blades of the rotors should have ideal shapes (see Chapter 5).

In this section some of the problems of optimization of profile geometrical parameters are discussed.

6.3.1 The Blow Hole Constant and the Contact Line Constant

It is obvious that the end profile shapes of the rotors of a helical screw compressor have a great effect on the compressor's performance and reliability. A good

profile will result in the compressor having small fluid-dynamic loses, good performance, high reliability and make the machining cost of its rotors low. A profile influences the performance mainly through two important geometrical characteristics, that is, blow hole area and contact line length per lobe, which provide the two most important leakage paths from an enclosed cavity volume to the following cavity volume or to the cavity in suction process. Increased leakage results in decreases in both the volumetric and total efficiencies.

So that large and small compressors and compressors having different profiles may be compared on a rational basis, two relative values, relative blow hole area and relative contact line length per lobe, have been introduced by the author (**2**).

The blow hole is a small triangular-shaped area formed by the housing cusp and the male and female rotor tips. Different definitions are used in the literature for the blow hole area. As mentioned in Chapter 3, the definition of Singh and Onuschak (**5**) is used to calculate the "throat" blow hole area normal to the streamlines in the leakage flow which is constrained by the tip geometry to be along the helix of the female rotor. To produce a blow hole area which is a function of profile geometry alone, that is, is independent of the helix angle and the length of the rotor, the throat area is projected into the plane which contains the cusp line and the female rotor axis. The cavity cross-sectional area in the end plane is projected at the helix angle onto the plane containing the two cusps. The relative blow hole area A_r is the dimensionless ratio as follows:

$$A_r = \frac{A_b / \sin \beta_{ftip}}{(A_{01} + A_{02}) / \tan \beta_{pitch}} \tag{71}$$

The relative contact line length per lobe is defined as the meshing line length, which is the projection of the contact line length per lobe on the end plane of the rotors, divided by the distance between the centers of the male and female rotors:

$$l_r = \frac{l_c}{A} \tag{72}$$

These relative values are dimensionless constants which depend only on the profile or the parameters that define the profile and are independent of compressor size, wrap angles and lengths of rotors, so they can be called blow hole constant

and contact line constant respectively. Since for a given profile the blow hole and contact line constants are determined uniquely, they can be used as a basis for comparing different profiles. The optimization of a profile consists of determining the basic parameters which define the profile, so as to produce the smallest blow hole and contact line constants consistent with a streamlined shape and good practical cutter blade shapes. For the standard SRM D-profile with the lobe combination of 4+6, the blow hole and contact line constants are 7.31×10^{-3} and 1.29 respectively. For the proposed improved profile shown in Fig. 6.4, the blow hole and contact line constants are 5.00×10^{-3} and 1.01 respectively, and both are reduced by 31.6 percent and 21.7 percent. This results in the considerable performance improvement (see Section 6.2.2). The optimum cutter blade shapes for the proposed improved profile are presented in Chapter 5.

6.3.2 A Method of Reducing the Blow Hole Area

Certain basic parameters define the shape of a profile. For the SRM D-profile one distance, three diameters, four radii and four angles are required. If these basic parameters are changed, the shape of profile changes, as do the blow hole and contact line constants.

A common method used to reduce the blow hole area, is to reduce its height. But a larger height of blow hole reduces the relative sliding coefficient between the rotors and with it, the wear. A large height also contributes to increasing the maximum cavity volume and as a consequence, to the production of a smaller compressor. As an exercise, the author (2) used another method to reduce the blow hole constant. This consisted of changing the shapes of two curved sides of the blow hole area. Tip profile parameters can be selected to make the curvilinear triangle narrower and sharper, so that the blow hole constant will be reduced considerably.

Fig. 6.6 shows a comparison of two blow holes in the $Y - Z$ plane. These blow holes have the same height and the same bottom width. From the original profile choice to the improved profile, the blow hole constant is reduced by thirty

two per cent, from 7.53×10^{-3} to 5.14×10^{-3} , and the contact line constant remains unchanged. Due to the reduction of blow hole constant the indicated efficiency and volumetric efficiency are increased by 0.933 per cent and 0.313 per cent respectively for the compressor, the center distance of which is $160mm$ and which operates under the following condition: refrigerant, $R22$; rotational speed, $3000rpm$; evaporating temperature, $-10°$ (corresponding pressure: 3.54 bar); condensing temperature,25° (corresponding pressure: 10.44 bar); suction superheat, 30°. The blow hole area has a much greater influence on the indicated efficiency than on the volumetric efficiency, which is also the conclusion drawn from the leakage analysis.

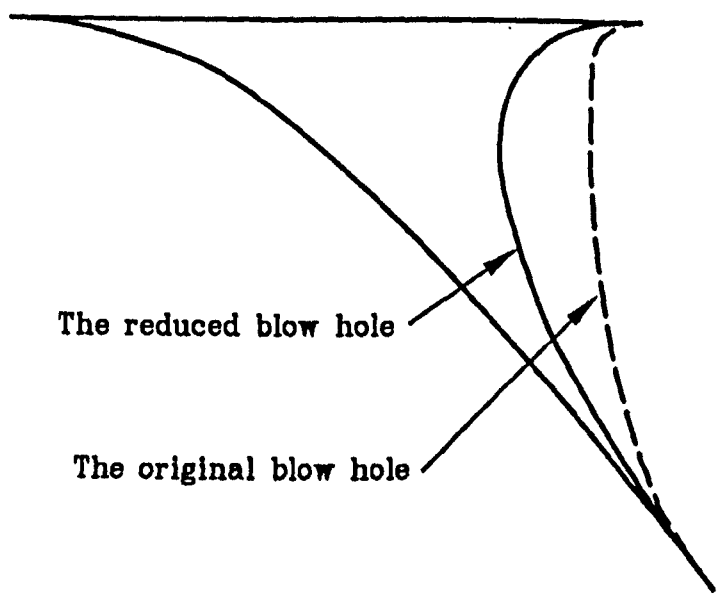

Fig. 6.6 Blow hole area reduction

It should be mentioned that in order to reduce the blow hole constant the other basic parameters can be optimized besides those which define the curved sides of the blow hole. For example, for the above original profile if the other basic parameters are optimized, the blow hole constant will be reduced to 4.26×10^{-3} and the contact line constant will be reduced from 1.31 to 1.20, and the indicated and volumetric efficiencies will be increased by 1.16 per cent and 0.21 per cent respectively.

6.4 DETERMINATION OF THE DISCHARGE PORT POSITION

The discharge port position of a helical screw compressor is determined according to the built-in volume ratio, which is the ratio between the real maximum cavity volume and the discharge cavity volume at the instant at which it connects to the discharge chamber of the compressor. For a given compressor the built-in volume ratio is fixed by the basic geometry. Corresponding to the built-in volume ratio there exists a so-called built-in pressure ratio or internal pressure ratio, which is the ratio between the pressure in the discharge cavity volume and the pressure in the suction chamber. For a given compressor the internal pressure ratio is not determined by its operating conditions. The operating condition decides an external pressure ratio or nominal pressure ratio, which is the ratio between the pressure in the discharge chamber and the pressure in the suction chamber. The internal and external pressure ratios may be equal or not, as determined by the operating conditions.

Theoretically, in order to get the highest indicated efficiency the internal pressure p_i in the discharge cavity volume should be equal to the nominal discharge pressure p_2 in the discharge chamber. That is, it appears at first sight that to eliminate wasteful energy consumption the internal pressure ratio should be equal to the external pressure ratio, but for a real working process the highest indicated efficiency is not obtained when p_i equals p_2. Fig. 6.7 shows the relationships between the indicated and total efficiencies and the ratio of p_2 to p_i. In Fig. 6.7 the highest efficiencies do not occur at the position where p_2/p_i equals one, but where the ratio equals about 1.25. When p_2/p_i is less than one the efficiencies decreases rapidly along with the reduction of the ratio, but when p_2/p_i is larger than one high efficiencies can be obtained over a range of values of the ratio. The prediction and measurement results in Fig. 6.7 are obtained for the following compressor:

- Lobe profile: SRM D standard.
- Lobe combination: $4 + 6$
- Bore diameters (equal): $204mm$.

- Male rotor wrap angle: 300°.
- Length/diameter ratio: 1.65.
- Volume ratio for axial discharge port: 5.0.
- Volume ratio for radial discharge port: 2.6.

Its running conditions are:

- Refrigerant: *R*22.
- Speed of male (driven) rotor: $3000 rev/min$.
- Condensing temperature: $25°C$ (saturation pressure: 10.44 *bar*).
- Evaporating temperature: $-10°C$ (saturation pressure: 3.54 *bar*).
- Superheat degrees: $30°C$.
- Superfeed and liquid refrigerant injection not on duty.
- Oil drained and injected.

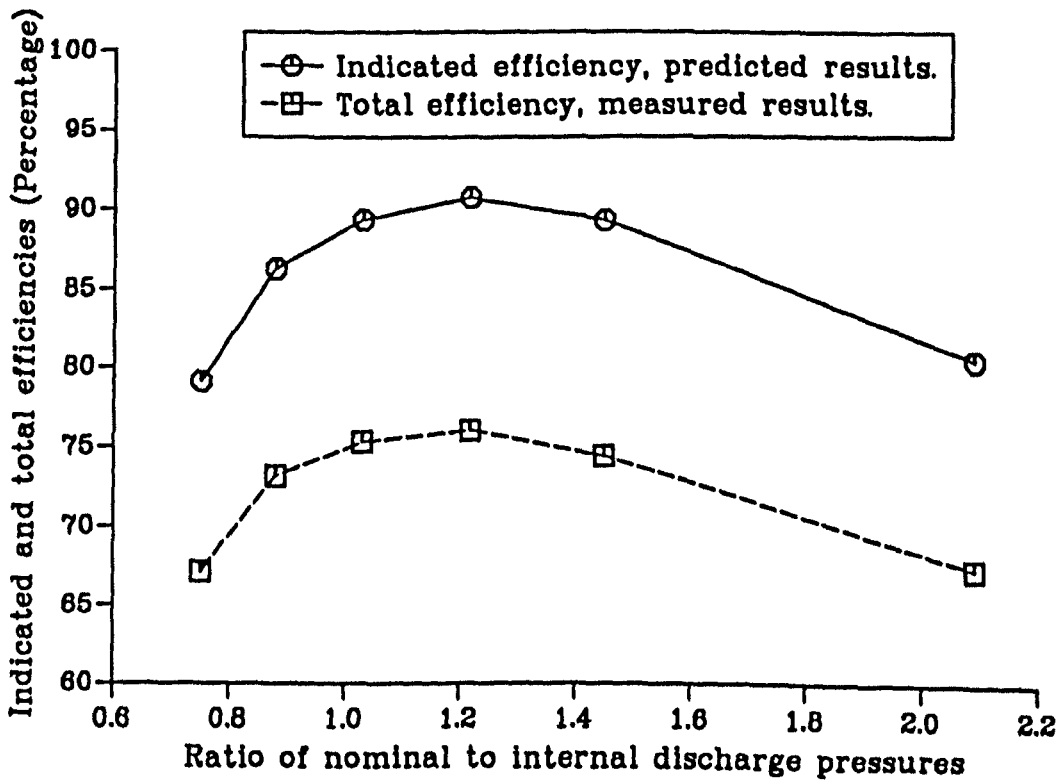

Fig. 6.7 The total and indicated efficiencies vs p_d/p_i

The four p-V diagrams in Fig. 6.8 explain why the above phenomenon happens. All four diagrams have the same nominal pressure ratios, but different

internal pressure ratios. For the diagram B p_i is less than p_2. After the cavity volume connects to the discharge chamber the refrigerant vapour will flow back into the cavity volume, but since the discharge port area is small at the beginning the back-flow rate is small. At this stage the cavity volume is reducing quickly, so the pressure in it quickly becomes larger than the nominal discharge pressure, and the discharge process begins. When normal forward flow begins the discharge port area is large so that the discharge process has a small flow resistance. This is why the diagram B encloses the smallest area, that is, the smallest indicated work, in the four diagrams, even smaller than the diagram C for $p_i = p_2$, which begins its discharge process immediately after the cavity volume connects to the discharge chamber and, as a consequence, meets a larger flow loss since both the discharge port area is very small in the beginning and the cavity volume continues to reduce rapidly, which results in a larger energy consumption than for $p_i < p_2$. If p_i is larger than p_2 more energy consumption is needed (the digram D in Fig. 6.8). The diagram A shows that if p_i is much less than p_2 the energy consumption is also increased.

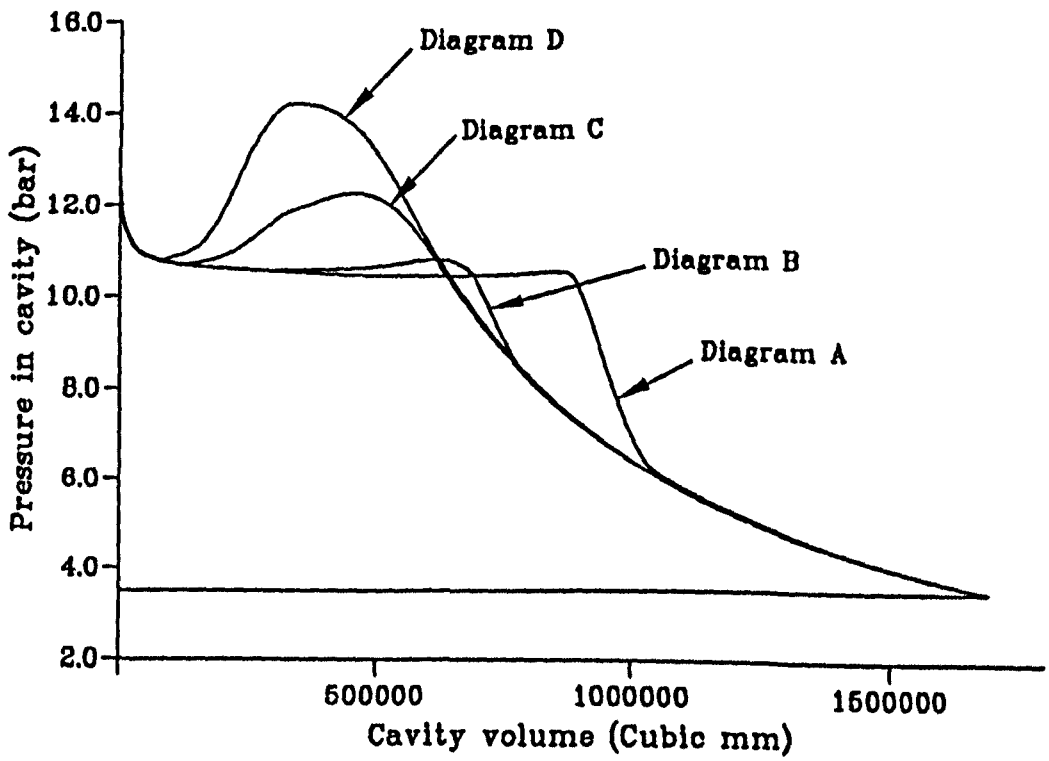

Fig. 6.8 p-V diagrams for different p_2/p_i ratios

If a compressor operates under an unchanged condition the optimum position of the discharge port can be determined by the computer programs very easily so that the highest indicated or total efficiency is obtained. Since a refrigeration screw compressor frequently operates under a range of conditions it is difficult to determine the optimum position of the discharge port. In the absence of detailed knowledge of the pattern of running conditions over a typical cycle, it is reasonable to design or choose a compressor according to the minimum nominal pressure ratio of the various conditions under which the compressor will operate.

6.5 ROTOR PARAMETERS AND COMPRESSOR PERFORMANCE

Besides the basic parameters defining a profile and the discharge port position which influence the performance of a refrigeration twin screw compressor, the rotor definition parameters, such as the wrap angle and the length/diameter ratio, have a great influence on the performance of the compressor (6).

After the profile is chosen, in order to define the geometry of a pair of rotors completely the wrap angle of the male rotor and the length/diameter ratio of rotors must be decided. These two parameters, especially the wrap angle, influence the performance, size and thus the manufacturing cost of the compressor considerably. For the given running conditions, the designer of the compressor should optimise these two parameters so as to design a compressor which has the best performance and a reasonable size. In this section, the design is restricted to male and female rotors which have equal diameters.

The specifications of the compressor used for the analysis in this section are as follows:

- Rotor lobe profile—SRM D standard.
- Male and female rotor diameters (equal): $204mm$.

The running conditions are:

- Refrigerant: $R22$.
- Speed of male (driven) rotor: $3000rev/min$.

- Condensing temperature: 25°C (saturation pressure: 10.44 bar).
- Evaporating temperature: −10°C (saturation pressure: 3.54 bar).
- Superheat degrees: 30°C.
- Superfeed and liquid refrigerant injection not on duty.
- Oil drained and injected.

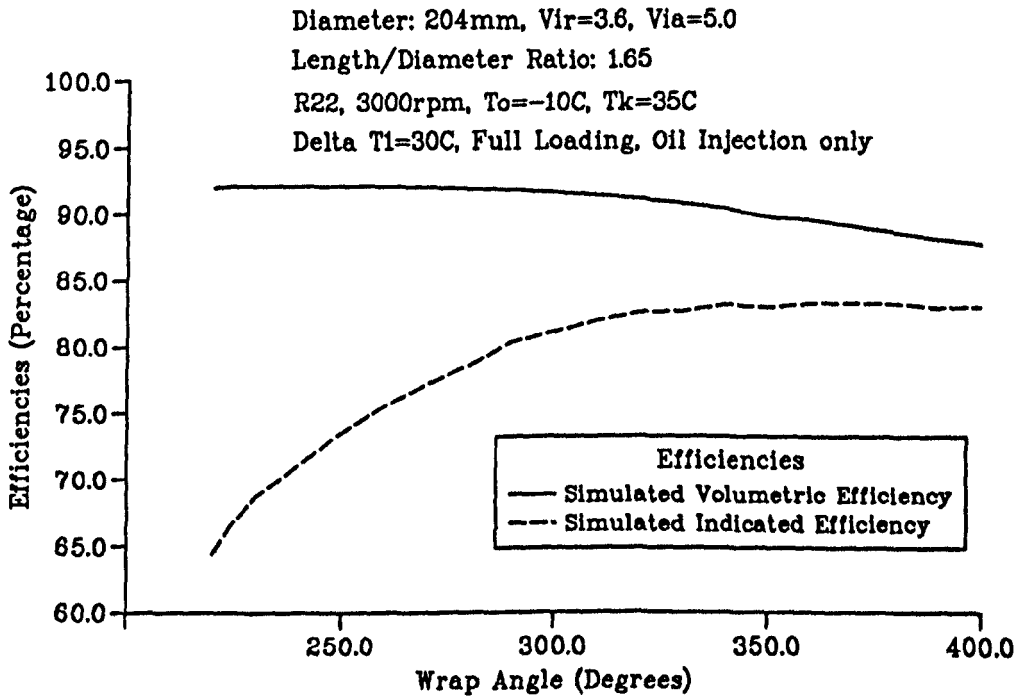

Fig. 6.9 Efficiencies vs the wrap angle of the male rotor

Table 6.2 The measured and simulated efficiencies

Simulated volumetric efficiency (%)	Measured volumetric efficiency (%)	Simulated indicated efficiency (%)	Simulated total efficiency (%)	Measured total efficiency (%)
91.6	91.0–91.8	81.0	73.1	72.5

Fig. 6.9 shows the relationship between the indicated and volumetric efficiencies and the wrap angle of the male rotor for the specified compressor and running conditions. For the range of wrap angles in Fig. 6.9, the length/diameter ratio remains constant, at 1.65. The measured and simulated efficiencies for the machine which has a wrap angle of 300° are listed in Table 6.2. It can be seen from Fig. 6.9 that the larger the wrap angle, the higher the indicated efficiency,

but the lower the volumetric efficiency. These features are explained as follows: when the wrap angle increases, the sealing lines of the cavity increase much faster than its volume which results in greater relative leakage; the discharge port area also increases much faster than the cavity volume which results in a considerable reduction of discharge resistance. As a consequence, the volumetric efficiency decrease is accompanied by an indicated efficiency increase.

The highest volumetric efficiency, 92.1 percent, can be obtained when the wrap angle equals about 240°. The highest indicated efficiency, 83.3 percent, can be obtained when the wrap angle is about 380°. It is a pity that the wrap angles corresponding to the highest volumetric and indicated efficiencies do not coincide together. In general a compromise wrap angle should be chosen between the wrap angles corresponding to the highest volumetric and indicated efficiencies to make sure that the compressor has relatively high values of both efficiencies. When the wrap angle is being chosen, the relationship between the wrap angle and the overlap constant of the compressor must be considered (see Fig. 6.10). If a wrap angle larger than the optimum is chosen, the compressor will have an increased size for the given real capacity due to both the low volumetric efficiency and small overlap constant. This means an increase in manufacturing cost. For the compressor specified in this section, a wrap angle about 300° is a suitable choice.

The influence of the length/diameter ratio of rotors on the compressor performance is not as great as that of the wrap angle (see Fig. 6.11). Both the volumetric and indicated efficiencies increase slowly as the length/diameter ratio increases. This is due to the relatively reduced sealing line length for the cavity. From the point of view of improving the compressor performance, a large length/diameter ratio should be chosen, but from the point of view of reducing the dynamic distortion of rotors, a small one should be chosen. If the object is to obtain the smallest bearing forces, an optimum length/diameter ratio must exist. This is beyond the scope of this section, and the author will publish on this topic elsewhere.

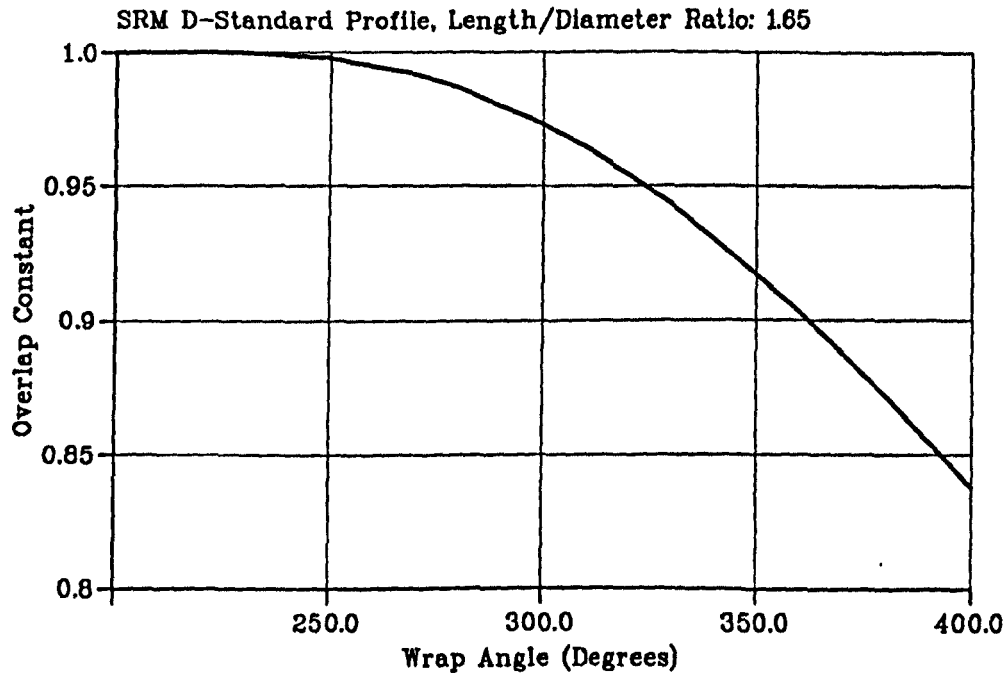

Fig. 6.10 The overlap constant vs the wrap angle of the male rotor

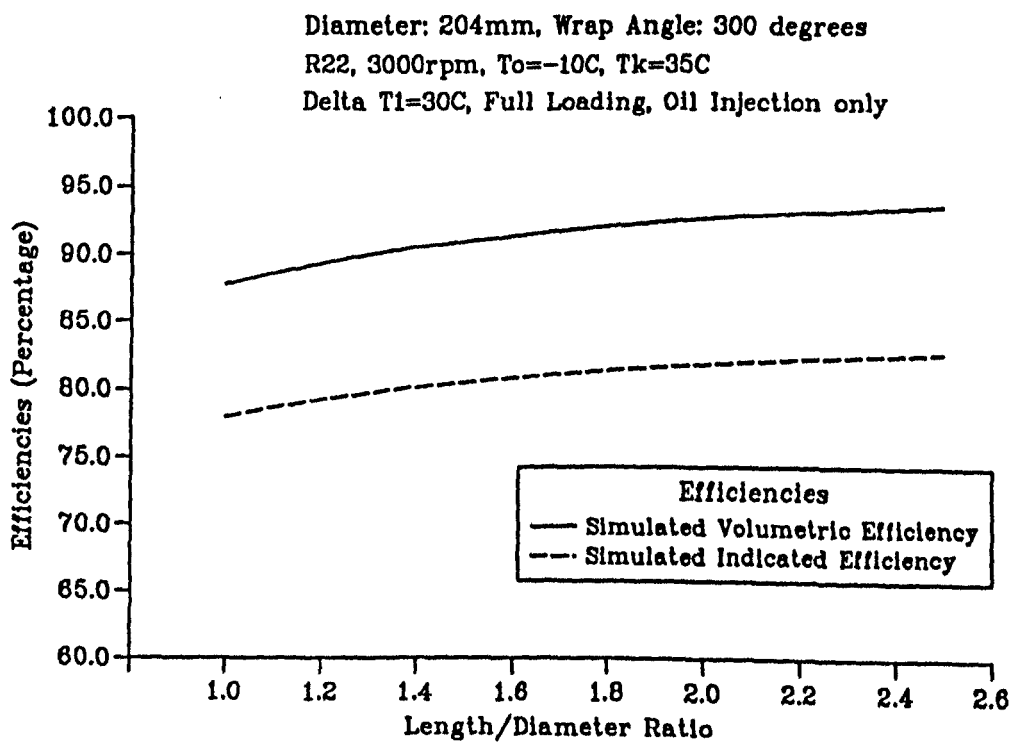

Fig. 6.11 Efficiencies vs the length/diameter ratio of rotors

6.6 OPTIMISATION OF SLIDE VALVE DEFINITION PARAMETERS

Capacity control is needed to enable a refrigeration twin screw compressor to meet the wide range of load demands which are a feature of modern refrigeration plants. The most common method makes use of a slide valve which allows a measured quantity of the compressed cavity volume to "blow out" back to suction. However, when a compressor is at its full load condition, the slide valve reduces the discharge port area of the compressor, and increases the gas flow resistance through the discharge port so that the indicated efficiency decreases considerably. When at a partial loading condition, the adjusting characteristics of a slide valve, that is, the relationship between the indicated efficiency and the various capacities of the compressor, is defined by the slide stop. If a slide valve has a good adjusting characteristic, the compressor can obtain a high indicated efficiency over a wide range of load. The slide stop is the most important parameter for a slide valve and must be optimised.

The specifications of the compressor used for the analysis in this section are as follows:

- Rotor lobe profile—SRM D standard.
- Male and female rotor diameters (equal): $204mm$.

The running conditions are:

- Refrigerant: $R22$.
- Speed of male (driven) rotor: $3000rev/min$.
- Condensing temperature: $25°C$ (saturation pressure: 10.44 bar).
- Evaporating temperature: $-10°C$ (saturation pressure: 3.54 bar).
- Superheat degrees: $30°C$.
- Superfeed and liquid refrigerant injection not on duty.
- Oil drained and injected.

6.6.1 With and without Slide Valve

In a refrigeration compressor the slide valve is applied to adjust capacity. The volume ratio for the definition of the axial discharge port is much higher than that for the radial discharge port. Usually the volume ratio for the radial discharge port can be chosen optimumly according the running conditions of the compressor (see Section 6.4).

A slide valve can make a twin screw compressor run with a high indicated efficiency during partial loading of the compressor, but at the full load condition, it reduces the compressor indicated efficiency. Fig. 6.12 shows the relationship between the indicated efficiency and the volume ratio of the radial discharge port for the specified compressor and running conditions. For the compressor with a slide valve, the volume ratio of the axial discharge port is 5.0, and for the compressor without a slive valve the volume ratio of the axial discharge port has the same value as the radial discharge port. The tested and simulated performance for the compressor with a slide valve is listed in Table 6.3.

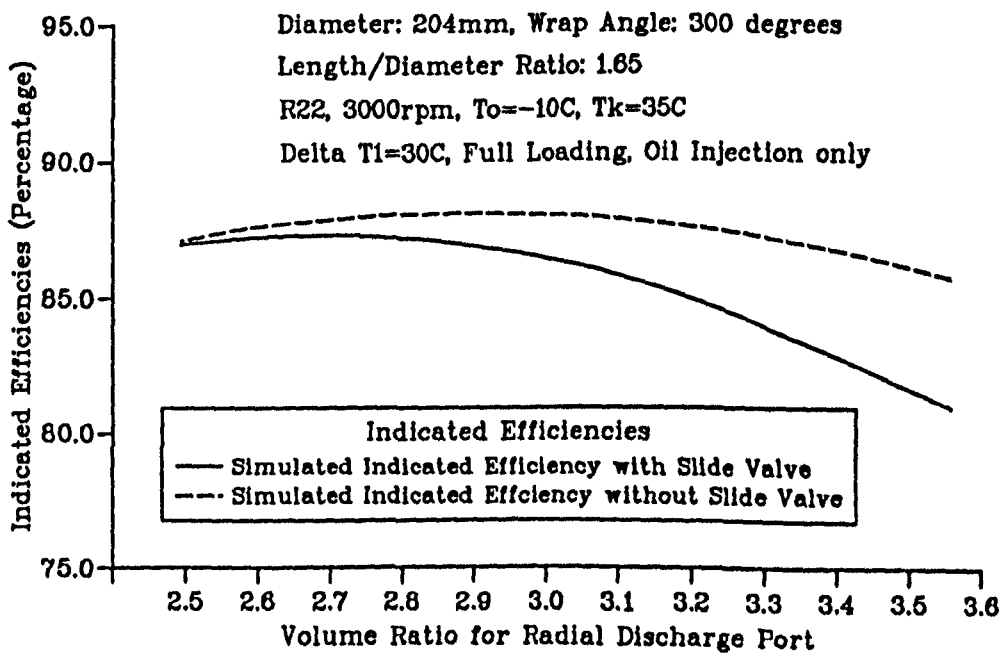

Fig. 6.12 Indicated efficiency vs volume ratio of radial discharge port

Table 6.3 The measured and simulated efficiencies

Volume ratio	Simulated volumetric efficiency	Measured volumetric efficiency	Simulated indicated efficiency	Simulated total efficiency	Measured total efficiency
2.6	91.4%	89.0–92.2%	87.2%	77.0%	75.0%
3.6	91.6%	91.0–91.8%	81.0%	73.1%	72.4%

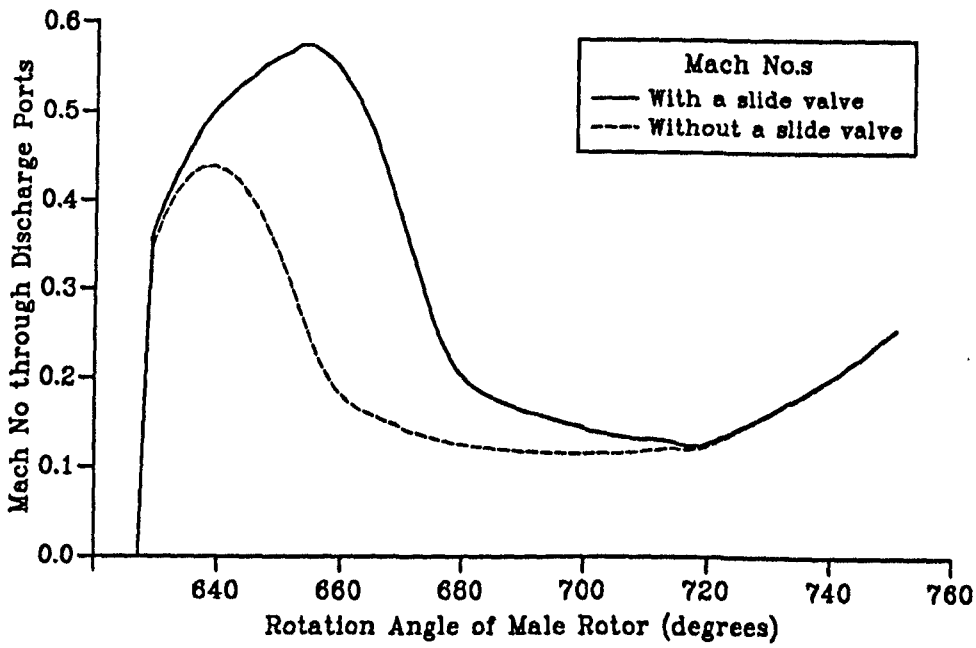

Fig. 6.13 Discharge Mach Nos vs rotation angle of the male rotor

Over a wide range of volume ratio for the radial discharge port, the indicated efficiency for the compressor without a slide valve is higher or much higher than that for the compressor with a slide valve. The highest indicated efficiency for the compressor with a slide valve, 87.3 percent, is obtained when the volume ratio equals 2.75. However, the highest indicated efficiency for the compressor without a slide valve, 88.1 percent, appears when the volume ratio is equal to 2.9. For the specified running conditions, the indicated efficiency of the compressor without a slide valve is 4.76 percent points higher than that of the compressor with a slide valve (volume ratio for radial discharge port is 3.6). This is due to the following

compressor reduces the discharge port area and increases the resistance to gas flow through the discharge port, thus increasing the indicated power considerably. Fig. 6.13 shows the relationship between the Mach numbers of gas flow through the discharge ports and the rotation angle of the male rotor for the compressors with and without slide valves. Fig. 6.14 shows the p-V diagrams. The larger the discharge Mach number, the larger is the indicated power and the lower the indicated efficiency.

It is quite common for two or more twin screw compressors to be used in one refrigeration plant. In order to reduce the total energy consumption of the compressors, the author suggests that in such a situation some of the compressors should be without slide valves. They should have the same volume ratios for the radial and axial discharge ports, and always run under the full loading conditions. The numbers can be decided according to the minimum refrigeration capacity of the plant in a complete loading cycle of one year say.

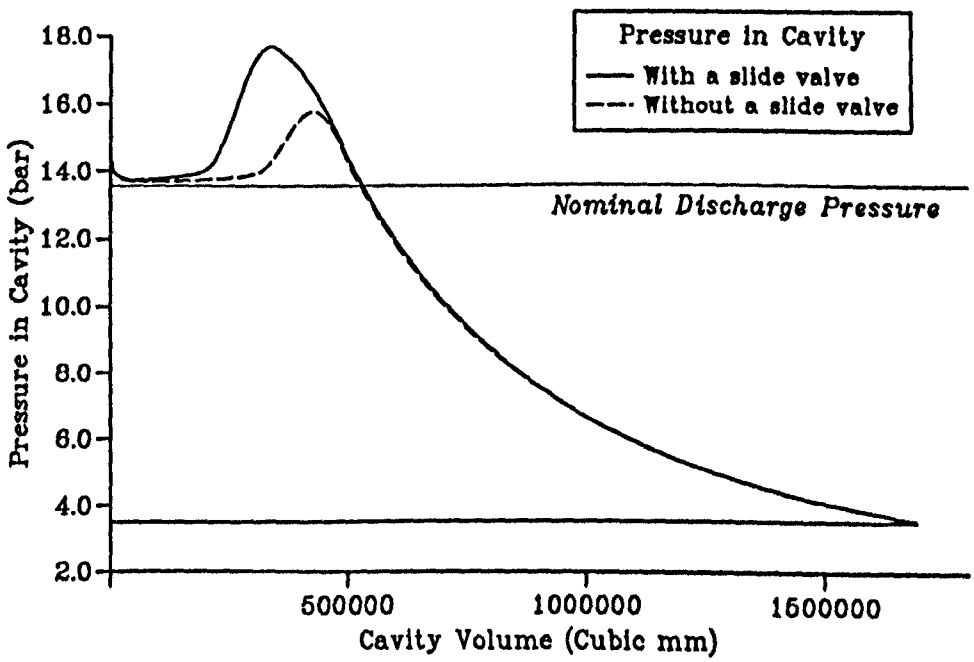

Fig. 6.14 p-V diagrams

6.6.2 Slide Stop and Adjusting Characteristics of a Slide Valve

The most important geometrical parameter describing a slide valve is the slide stop (L_{stop} in Fig. 6.15). After the volume ratios for the axial and radial discharge ports are chosen, a slide stop must be chosen which limits the adjusting characteristics of the slide valve. An important adjusting characteristic is the relationship between the indicated efficiency of the compressor and its partial loading capacity. A good adjusting characteristic should be to have over a wide range of partial loading capacity a high indicated efficiency. Fig. 6.16 shows a choice of three adjusting characteristics for the specified compressor and running conditions. The compressor has 3.6 and 5.0 as its volume ratios for the radial and axial discharge ports respectively. As shown in Fig. 6.16, different slide stops result in different adjusting characteristics. When the slide stop equals $111mm$ in length, the adjusting characteristic is at its best (solid line in Fig. 6.16).

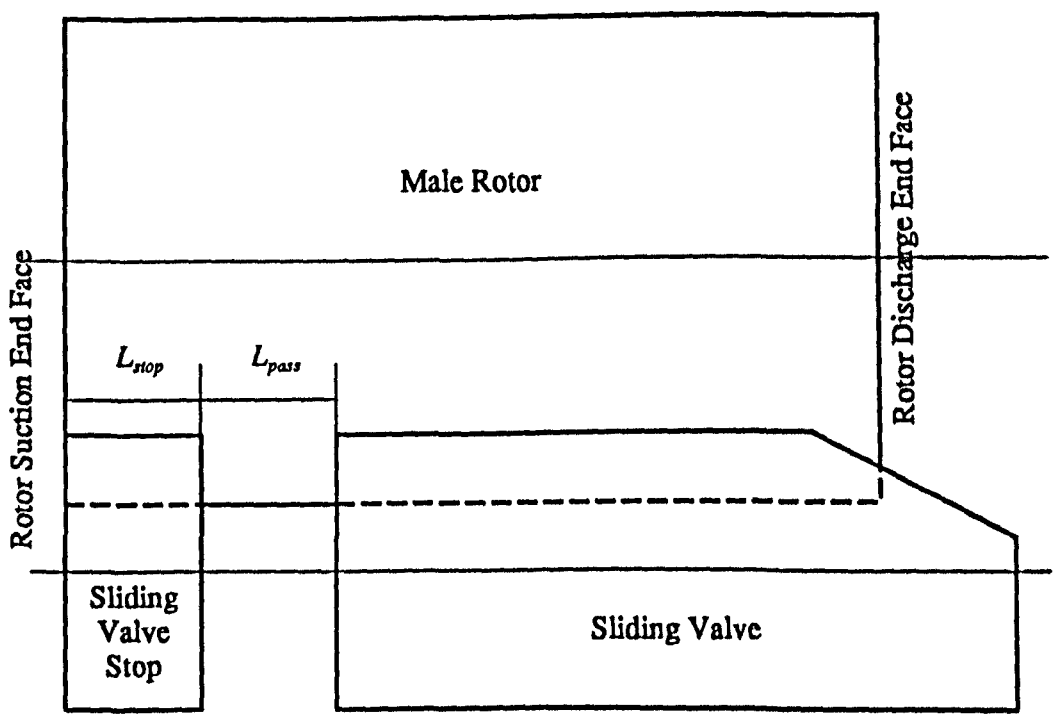

Fig. 6.15 Stop and position parameters of a slide valve

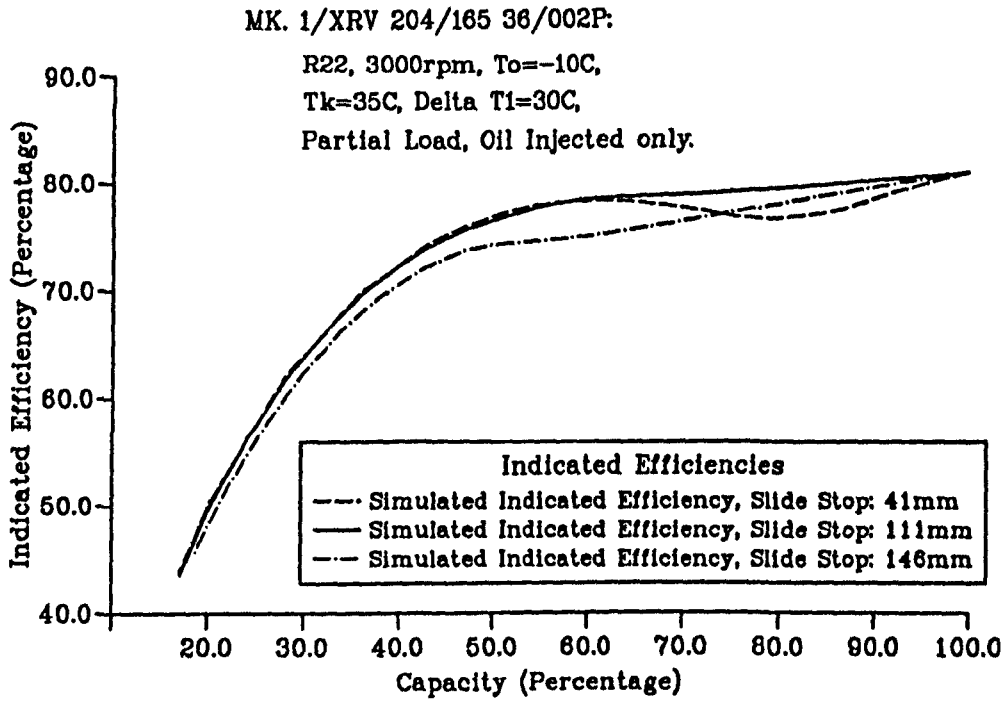

Fig. 6.16 Adjusting characteristics of different slide stops

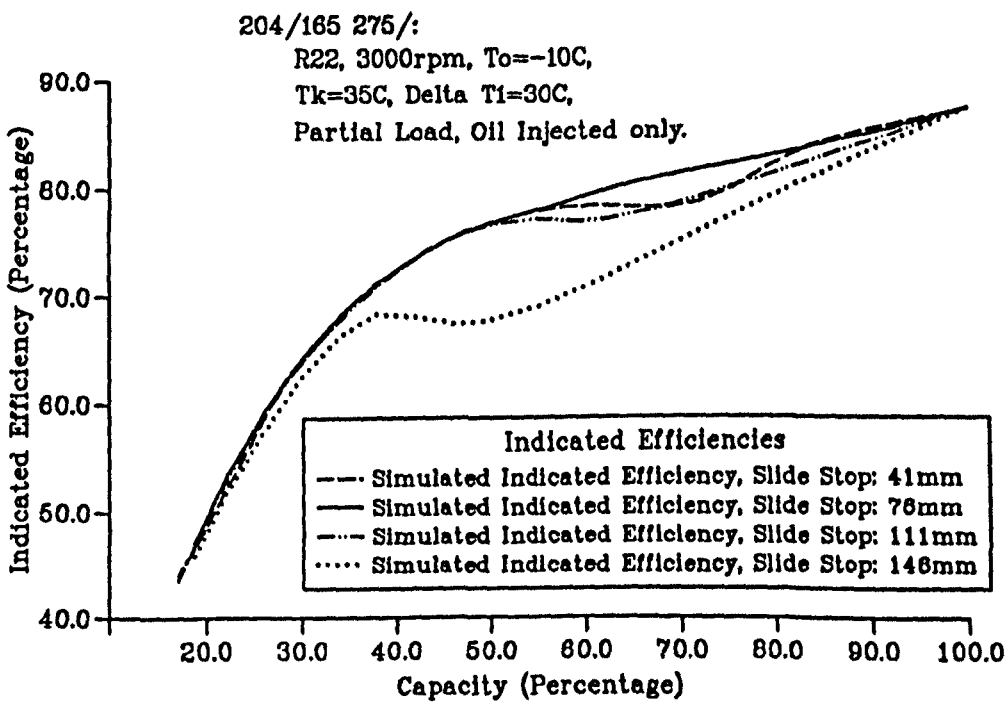

Fig. 6.17 Adjusting characteristics of different slide stops

As mentioned in Section 6.6.1, for the specified running conditions the compressor with a slide valve has its highest indicated efficiency when the volume

ratio of the radial discharge port equals 2.75. Fig. 6.17 shows the adjusting characteristics of the compressor, the volume ratio of the radial discharge port of which is 2.75. When the slide stop equals $76mm$, the slide valve obtains its best adjusting characteristic (solid line in Fig. 6.17). For the two volume ratios, the two optimumally adjusted characteristics are different, and their comparison is shown in Fig. 6.18. Over a wide range of partial loading capacity, the compressor with 2.75 as the volume ratio for its radial discharge port has a considerably higher indicated efficiency. This means that when a designer designs a twin screw compressor, he or she should decide the optimum volume ratio for the given running conditions and for full load, and then choose a suitable slide stop to ensure that the slide valve has the optimum adjusting characteristics.

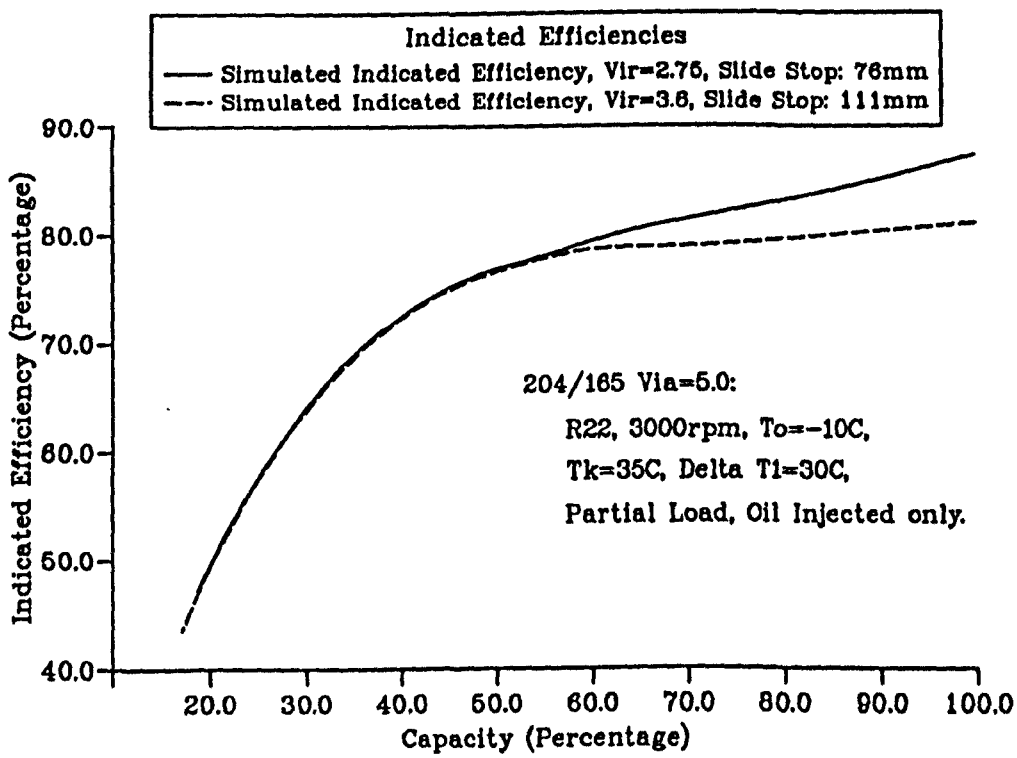

Fig. 6.18 Adjusting characteristics of different volume ratios

6.7 REFERENCES

1 Fleming, John S. Tang, Yan Young, W. and Anderson, H. Leakage Analysis of a Helical Screw Compressor. *Proceedings of I Mech E European*

Conference on Developments in Industrial Compressors and their Systems, London, U.K., 1994, pp. 1–8.

2 **Tang, Yan** and **Fleming, John S.** Obtaining the Optimum Geometrical Parameters of a Refrigeration Helical Screw Compressor. *Proceedings of International Compressor Engineering Conference at Purdue*, Purdue University, U.S.A., 1992, pp. 221–227.

3 **Fleming, John S. Tang, Yan Young, W.** and **Anderson, H.** The Calculation of Cutter Blades of a Helical Screw Compressor and Optimisation of Their Shapes.*Proceedings of I Mech E European Conference on Developments in Industrial Compressors and their Systems*, London, U.K., 1994, pp. 17–25.

4 **Tang, Yan** and **Fleming, John S.** Clearances between the Rotors of Helical Screw Compressors: Their Determination, Optimisation and Thermodynamic Consequences. *Proc I Mech E Vol 208 Part E, Journal of Process Mechanical Engineering*, 1994.

5 **Singh, Pawan J.** and **Onuschak, Anthony D.** A Comprehensive, Computerized Method for Twin-Screw Rotor Profile Generation and Analysis. *Proceedings of International Compressor Engineering Conference at Purdue*, Purdue University, U.S.A., 1984.

6 **Fleming, John S. Tang, Yan** and **Anderson, H.** Optimisation Techniques Applied to the Design of a Refrigeration Twin Screw Compressor. *Proceedings of International Compressor Engineering Conference at Purdue*, Purdue University, U.S.A., 1994, accepted and to be published.

Chapter 7

CONCLUSIONS

1. The SRM D-profile is a profile *system* and has become very successful. The equations and formulas used to calculate all the derived parameters of the profile from the given basic geometrical parameters are developed and presented in the thesis. All the parametric equations describing all the segments of the profile are developed and presented also. The first derivatives of the profile are required in order to calculate the cutter blade shapes of the male and female rotors. The equations describing the first derivatives of each segment of the profile are developed and presented. The author believes they are of practical value to designers and are not published elsewhere. The common method used for the profile mathematical analysis, which is from other literature, is presented in Appendix A for the convenience of the reader.

2. A computer program used to generate various profiles under the definition of the symmetrical circular, the SRM A- and the SRM D-profiles has been developed. It outputs all the profile parameters and data files required by a compressor designer and by the other programs developed by the author. The basic geometrical parameters input to the program should be physically reasonable, otherwise an error will appear. The program can detect some errors and modify them automatically, but not all. The profile generation program is the basis of computer aided design of twin screw compressors. For other profiles, separate but similar profile generation programs require to be developed. These new developed generation programs should have the same output data files as the existing profile generation program. A program used to display the profile generated by the generation program

has been developed. Many diagrams of the profile can be drawn to any desired scale by a plotter, or can be shown on the monitor. A few other support programs have also been developed.

3. In order to test the mathematical analysis for the profiles and the profile generation program, some standard profiles generated by the program are compared with profiles used in practice. They are identical. For a standard SRM D-profile, the coordinates of some key points generated by the program are presented and compared with those from the data files for the profiles used in practice. They are also identical.

4. The definitions of all the geometrical relationships and parameters, which are used for the working process simulation and the geometric design of a helical screw compressor, are presented.

5. A *universal* geometrical characteristic calculation program is developed by the author, which can be used for the analysis of the geometrical characteristics of a helical screw compressor. *All* the useful geometrical relationships and parameters of a helical screw compressor can be calculated and output to different data files in a few minutes on a personal computer. The geometrical relationships include those which are required in a thermodynamic model for simulating the working processes of the compressor. For the convenience of the compressor designer all the geometrical parameters are also calculated and output to a data file. A program used to display the calculated results of the geometrical characteristics calculation program has also been developed. The program can plot many useful plots, some of which can form the starting point for the design of a machine in practice.

6. A mathematical model for the working process of a refrigeration twin screw compressor is presented. In the model, which is based on real gas laws, the influence of factors such as the oil draining from end casings, the oil injection through the holes on the main casing or the slide valve, liquid refrigerant injection, liquid refrigerant dissolved in the oil, vapour charge from the

superfeed, leakage through every leakage path in the compressor, friction losses in the end casings and main casing, different refrigerants and partial loading etc., are considered simultaneously and separately. Modification coefficients are introduced in the model which are required to be determined from measured data derived from compressor performance tests.

7. A *universal* working process simulation program based on the mathematical model has been developed by the author. *All* the useful running parameters, efficiencies, leakage rate through every leakage path, gas state in a cavity and state of injected oil in the same cavity etc. can be calculated and output to different data files on a personal computer. The efficiencies predicted by the program include the volumetric efficiency, the isentropic indicated efficiency, the isentropic total efficiency and the mechanical efficiency. All the leakage paths are considered in the working process simulation program. The leaking outflow rate, leaking inflow rate and net leaking outflow rate through every leakage path are calculated. Consequently, the simulation results are very useful for the leakage analysis of a refrigeration twin screw compressor. The parameters input to the working process simulation program should be physically reasonable, otherwise an error will appear. The program can not detect errors resulting from unreasonable input data. If the vapour in the cavity is compressed into the two-phase region, the program will not continue the simulation for the compression process. An error message and some suggestions to solve the problem will appear on the monitor and the program stops. A program used to display the simulated results of the working process simulation program has also been developed. The program can plot many useful plots, by which the behaviour of the compressor is described.

8. In order to show how to simulate the working process of a refrigeration twin screw compressor by using the working process simulation program, an example is given in Chapter 4. The simulation results are explained, analysed and compared with the test results. In order to confirm the mathematical

model and the working process simulation program, the performance predicted by simulation is compared with the results from compressor tests. Comparisons have been made for various running conditions and different compressors which have nominal diameters of 163 *mm* to 510 *mm* and the standard A- and D-profiles, all running on refrigerant R22. The results are shown to be very good. The maximum variation for the volumetric efficiency, the total efficiency and the input power or the input torque is about $\pm$ 5 percent.

9. Procedures for calculating the cutter blade shapes of the male and female rotors of a helical screw compressor and for setting the inter-rotor clearance distribution are presented in this thesis. The basic theory and most equations are from other published literature on gear theory and engineering mathematics etc. They are listed in Appendix G for the convenience of the reader. The equations used to calculate the real profile for the equidistant helical surface method are developed by the author and are also presented in Appendix G. The author believes that they are used by practicing engineers. Of the two commonly used geometrical schemes for determining inter rotor clearances, namely the equidistant lobe profile method and the equidistant helical surface method, the latter is the superior for both oil injected and dry machines, and in dry machines it has the added advantage that it permits the use of less accurate and therefore cheaper timing gears. The optimum scheme to obtain the clearance between the rotors is a *non-equidistant* modification on the zero clearance profile chosen to accommodate operational distortions of the rotors. It is described and discussed in the thesis.

10. A *universal* cutter calculation program is developed by the author. *All* the useful manufacturing parameters, such as the cutter blade coordinates, the real profile coordinates, the clearance distributions along the contact line and its average value etc. can be calculated and output to different data files on a personal computer. The user can choose different inter-rotor clear-

ance schemes, ie the equidistant lobe profile, the equidistant helical surface, and the non-equidistant clearance distribution (the data file describing the clearance distribution is required), for his or her cutter blade and real profile calculation. A program used to display the calculated results of the cutter calculation program is also developed. The program can plot many useful plots.

11. By using the existing programs, the influence of different inter-rotor clearance schemes on the compressor performance has been analysed quantitatively. If the non-equidistant clearance scheme can be applied successfully, the performance of the compressor could be improved considerably.

12. The shapes of cutter blades have an important influence on the manufacturing costs of rotors. Some manufacturing parameters, such as the offset angle and the angle between the cutter axis and rotor axis, can be used to optimise the cutter shapes so as to reduce the manufacturing cost of the rotors, especially the tooling cost.

13. By using the existing computer programs, the leakage analysis for an existing profile and an existing compressor has been completed, and the leakage patterns for different running conditions have been obtained. The leakage paths have very different influences on the volumetric and isentropic indicated efficiencies. A path, apparently very important to volumetric efficiency such as cusp blow hole, in fact has very little influence on volumetric efficiency, but has a very considerable influence on isentropic indicated efficiency. An example is presented in the thesis, which makes use of the leakage analysis results to propose an improved SRM D-profile. The profile gains a higher isentropic indicated efficiency, but at the cost of a slightly reduced volumetric efficiency. The change in the leakage pattern achieves a considerable improvement in isentropic indicated efficiency.

14. Two dimensionless constants, the blow hole constant and contact line constant, which are functions of profile geometry and are independent of compressor size, wrap angles and lengths of rotors, make possible a rational

comparison of blow hole areas and contact line lengths of compressors with different profiles. In addition, they can be used as parameters to be optimized in an optimisation scheme.

15. A very efficient method, which is used to reduce the blow hole area, is to change the shapes of its two curved sides, and to make it as sharp and narrow as possible. This method is useful for the optimisation of a profile or the generation of a new profile.

16. For a real working process the highest indicated or total efficiency always is obtained when the internal discharge pressure is less than the nominal discharge pressure. A discharge port position should be chosen to make the internal pressure ratio less than the external.

17. Of the two parameters which define rotor geometry, the wrap angle and length/diameter ratio, the wrap angle has a greater influence on the performance and size of the compressor and thus its manufacturing cost. The choice of the wrap angle is based on the following three factors: reasonable indicated and volumetric efficiencies and compressor size.

18. A slide valve ensures that the compressor obtains a relatively high indicated efficiency on the partial loading condition, but for full load it reduces the compressor performance considerably. In order to reduce the energy consumption of the compressor, the author suggests that in the situation in which two or more twin screw compressors are applied in one refrigeration plant one or more of the compressors should be without a slide valve. They should have the same volume ratios for the radial and axial discharge ports, and always run under the full load conditions. The compressor numbers, with and without slide valves, can be decided according to the minimum refrigeration capacity of the plant in a complete load cycle of (say) one year.

19. If the running conditions and the volume ratios are fixed, a careful choice of the slide stop can result in a good optimum adjusting characteristic of the slide valve. When designing a twin screw compressor with a slide valve,

the optimum volume ratio on the full loading condition can be decided first, and then a suitable slide stop should be chosen to ensure that the slide valve has the optimum adjusting characteristics.

Chapter 8

SUGGESTIONS FOR FURTHER WORK

1. Although some optimisation procedures and many optimisation results for the design of twin screw compressors are presented in the thesis, making use of the developed computer programs, the following optimisation analyses are suggested, preferably to be done in the near future:
   (a) The influence of the suction port close position on the compressor performance, and its optimisation.
   (b) The influence of the oil draining port positions and flow rates, the oil injection port position and flow rate on the compressor performance, and their optimisation.
   (c) The influence of the liquid refrigerant injection port position and flow rate on the compressor performance and the COP of the refrigeration system, and their optimisation.
   (d) The influence of the superfeed port position, the gas flow rate from the superfeed and the gas state in the superfeed on the compressor performance and the COP of the refrigeration system, and their optimisation.
   (e) The influence of the male rotor rotational speed on the suction port position, discharge port position and compressor performance, and its optimisation.
   (f) The influence of the liquid refrigerant dissolved in oil on the compressor performance.
2. In the existing mathematical model for the compressor working processes, the heat transfer between the compressed gas and the rotors or the housing is treated as negligible. The author suggests that the mathematical model be modified to take this heat transfer into account in order to improve the

prediction accuracy of the model further especially for the gas compressors which could have much higher discharge temperature than a refrigeration compressor.

3. In the existing mathematical model the friction power generated in the main casing is not treated as heating the oil or the compressed gas directly, but the oil delivery temperature is modified according to the friction power. A suitable model to describe the heating process to the oil and the compressed gas due to the friction power in the main casing needs to be developed. The author suggests that such a model be developed and used in the simulation program.

4. In the existing mathematical model, the suction and discharge pressures of the compressor are assumed to be constant. The author suggests that a program used to simulate the gas behaviour in the suction line and chamber be developed, and a program used to simulate the gas and oil behaviour in the discharge chamber and line be developed. The new programs can be included in the existing simulation program as subroutines, or they can be separate programs. The output of the new programs then will be read by the compressor working process simulation program, and the influence of the periodical variations of the gas pressure and temperature at the suction and discharge ports on the compressor performance will be taken into account. As a result, the p-V diagram simulated could be a little different and more accurate, which could improve the accuracy of the force analysis program when completed. In addition, the simulation program for the discharge chamber and line could be a help towards obtaining a more accurate heat transfer coefficient between the gas and oil, particularly if experiments are arranged to complement the simulation.

5. The existing working process simulation program can not be used for refrigerant in the two-phase region due to the limitations of the state equation used, but in practice the refrigerant at the suction port could be in the two-phase region, and if too much oil or liquid refrigerant is injected into the

compressor the refrigerant vapour in the cavity could be compressed into the two-phase region. The author suggests that the mathematical model be modified further so that the behaviour of the refrigerant in the two-phase region can be simulated.

6. Refrigeration twin screw compressors run on partial loading conditions very often. In the existing program, the heating effect on the suction gas due to the re-cycling of oil together with the by-pass gas is treated as negligible. In order to improve the prediction accuracy for the partial loading, the author suggests that a model used to simulate this heating effect be added into the working process simulation program.

7. So far four refrigerants, that is, R12, R22, R134a and R717, are considered in the working process simulation program, but the structure of the main program and the property calculation subroutines make it possible to extend the use of the program to other working fluids including various gases, mixtures of gases and other pure and binary refrigerants if the required property equations or the required property calculation subroutines are known. This belongs to the author's further research work.

8. In the working process simulation program many modification coefficients are introduced to make idealised behaviour more realistic. Each coefficient has its own influence on the results predicted by the program. A sensitivity analysis of the modification coefficients is capable of determining their relative importance. For the most important coefficients further possible experiments with the model should be arranged to obtain the most appropriate values. The construction of test rigs to determine leakage coefficients path by path would be instructive, beginning with dry gas.

9. The author described an optimum inter-rotor clearance scheme for the cutter blade and real profile calculation. The process of optimizing clearance distribution requires the development of accurate methods of calculating the following: distortions in the casing, rotors and bearings due to thermal

gradients, and gas pressure forces, and deviations from nominal rotor geometry caused by cutter-rotor forces during the milling process. Although the author has nearly completed two programs aimed at achieving these ends, ie the force analysis program and the rotor deflection program, much more research work remains to be done in the future, which includes the verification of the two programs and the development of new programs, particularly the thermal distortion program.

10. Making use of curve fit techniques, a universal profile generation program can be developed, which can be used to generate various existing profiles and new profiles. Such a program can be used to analyse the advantages and disadvantages of the existing profiles, and based on the results of this analysis a new profile could be developed. This belongs to the author's further research work.

11. The author believes that the research work presented in this thesis is basic to the process of the computer aided design of twin screw compressors. The above list of suggestions for further work could not include all the possible further research work. As the market for the twin screw compressor is expanding year by year, and the number produced is increasing, many researchers can find interesting projects in the area. The author is very glad to have had the opportunity to have worked in the field, which he has found to be very interesting. The work presented in this thesis may not be perfect, but at least the author has done his best.

Appendix A

BASIC EQUATIONS FOR PROFILE ANALYSIS

The coordinate systems shown as Fig. A.1, which is used to describe profiles in this thesis, must be established first. $O_1X_1Y_1$ and $O_2X_2Y_2$ are two static coordinate systems, origins O_1 and O_2 coinciding with the centres of the male and female rotors respectively. Planes X_1Y_1 and X_2Y_2 are normal to the axes of rotation of the rotors which pass through O_1 and O_2. $o_1x_1y_1$ and $o_2x_2y_2$ are two rotating coordinate systems which rotate with the male and female rotors.

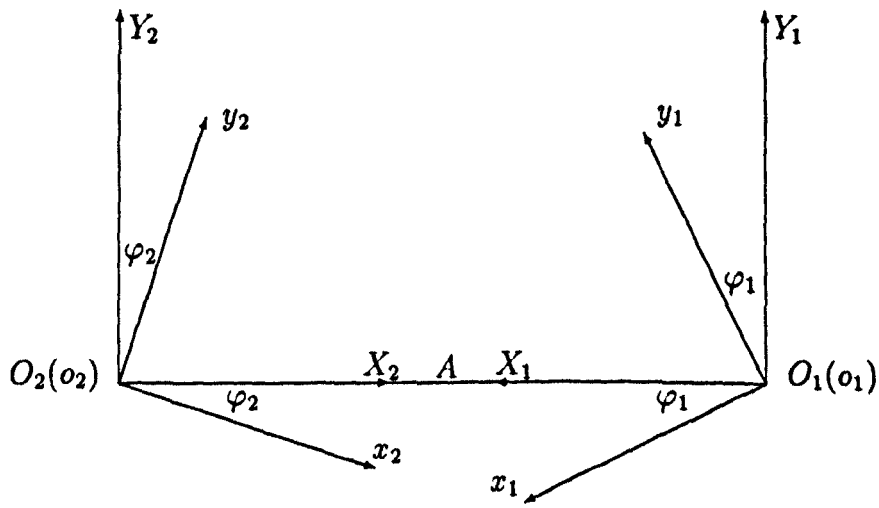

Fig. A.1 Coordinate systems for profile analysis

Their origins o_1 and o_2 coincide with the centres of the male and female rotors respectively. At the start position $o_1x_1y_1$ coincides with $O_1X_1Y_1$, and $o_2x_2y_2$ coincides with $O_2X_2Y_2$. After a time interval the male rotor, that is, $o_1x_1y_1$, rotates around the centre $O_1(o_1)$ by the angle φ_1 anticlockwise, and the female rotor, that is, $o_2x_2y_2$, rotates around the centre $O_2(o_2)$ by the angle φ_2 clockwise. The transmission ratio i from the male rotor to the female rotor, which is constant

with time, is given by the following equations:

$$i = \frac{\varphi_2}{\varphi_1} = \frac{z_1}{z_2} = \frac{r_M}{r_F} = \frac{\omega_2}{\omega_1} \tag{73}$$

The following two equation systems are the transform equations of the coordinates between the two rotational coordinate systems:

$$\begin{cases} x_1 &= -x_2 \cos k\varphi_1 - y_2 \sin k\varphi_1 + A\cos\varphi_1 \\ y_1 &= -x_2 \sin k\varphi_1 + y_2 \cos k\varphi_1 + A\sin\varphi_1 \end{cases} \tag{74}$$

$$\begin{cases} x_2 &= -x_1 \cos k\varphi_1 - y_1 \sin k\varphi_1 + A\cos i\varphi_1 \\ y_2 &= -x_1 \sin k\varphi_1 + y_1 \cos k\varphi_1 + A\sin i\varphi_1 \end{cases} \tag{75}$$

The generation of the envelope to a set of curves, that is, a rotor profile in this case, requires a mathematical method which gives the mating rotor profile equations. A given segment of the female rotor profile may be described by the following parametric equations:

$$\begin{cases} x_2 &= x_2(t) \\ y_2 &= y_2(t) \end{cases} \tag{76}$$

When substituted into equation 74 a set of curves is obtained in the system $o_1x_1y_1$ described by the following equations:

$$\begin{cases} x_1 &= x_1(t,\varphi_1) \\ y_1 &= y_1(t,\varphi_1) \end{cases} \tag{77}$$

This set of curves generates an envelope which is the mating segment on the male rotor profile. Between the envelop and any curve of the set there exists a contact point, at which both the envelop and the curve have a common tangent. The slope of the tangent at any point in the envelop can be obtained by differentiation of equations 77:

$$\frac{dy_1}{dx_1} = \frac{\left(\frac{\partial y_1}{\partial t} + \frac{\partial y_1}{\partial \varphi_1}\frac{\partial \varphi_1}{\partial t}\right)dt}{\left(\frac{\partial x_1}{\partial t} + \frac{\partial x_1}{\partial \varphi_1}\frac{\partial \varphi_1}{\partial t}\right)dt} \tag{78}$$

The slope of the tangent at any point in any curve of the set for which φ_1 equals a constant can also be obtained by the differentiation of equation 77:

$$\frac{dy_1}{dx_1} = \frac{\left(\frac{\partial y_1}{\partial t}\right)dt}{\left(\frac{\partial x_1}{\partial t}\right)dt} \tag{79}$$

The above two slopes are equal at the contact point where the envelop and any curve of the set have the common tangent. Equating the right hand sides of equations 78 and 79, gives the following equation:

$$\frac{\partial x_1}{\partial t}\frac{\partial y_1}{\partial \varphi_1} - \frac{\partial x_1}{\partial \varphi_1}\frac{\partial y_1}{\partial t} = 0 \tag{80}$$

or

$$\begin{vmatrix} \frac{\partial x_1}{\partial t} & \frac{\partial x_1}{\partial \varphi_1} \\ \frac{\partial y_1}{\partial t} & \frac{\partial y_1}{\partial \varphi_1} \end{vmatrix} = 0 \tag{81}$$

This equation is called the envelop condition equation or the conjugate condition equation. It is an equation of the implicit function which describes the relationship between the parameter t and the rotation angle of the male rotor φ_1, so that it can be represented simply by the following equation:

$$f(t, \varphi_1) = 0 \tag{82}$$

The simultaneous equations 77 and 82 define the mating segment of the male rotor for a chosen segment of the female rotor:

$$\begin{cases} x_1 = x_1(t, \varphi_1) \\ y_1 = y_1(t, \varphi_1) \\ f(t, \varphi_1) = 0 \end{cases} \tag{83}$$

A given segment in the profile of the male rotor, is represented by the following equations:

$$\begin{cases} x_1 = x_1(t) \\ y_1 = y_1(t) \end{cases} \tag{84}$$

Substituting these equation into equation 75, gives a set of curves in the coordinate system $o_2x_2y_2$ as follows:

$$\begin{cases} x_2 = x_2(t, \varphi_1) \\ y_2 = y_2(t, \varphi_1) \end{cases} \tag{85}$$

By the same method the following envelop condition equations are obtained:

$$\begin{vmatrix} \frac{\partial x_2}{\partial t} & \frac{\partial x_2}{\partial \varphi_1} \\ \frac{\partial y_2}{\partial t} & \frac{\partial y_2}{\partial \varphi_1} \end{vmatrix} = 0 \tag{86}$$

The simultaneous equations 85 and 86 define the mating segment in the profile of the female rotor for a chosen segment in the profile of the male rotor:

$$\begin{cases} x_2 &= x_2(t,\varphi_1) \\ y_2 &= y_2(t,\varphi_1) \\ f(t,\varphi_1) &= 0 \end{cases} \tag{87}$$

Besides equations 74, 75, 81 and 86, which are the most important and widely used equations in the mathematical analysis of profiles, the following equations are often used:

- At the contact point of the profiles of the male and the female rotors, that is for a chosen rotation angle of the male rotor, the derivatives of the profiles have the following relationships:

$$\begin{cases} \frac{dx_1}{dt} &= -\frac{dx_2}{dt}\cos k\varphi_1 - \frac{dy_2}{dt}\sin k\varphi_1 \\ \frac{dy_1}{dt} &= -\frac{dx_2}{dt}\sin k\varphi_1 + \frac{dy_2}{dt}\cos k\varphi_1 \end{cases} \tag{88}$$

$$\begin{cases} \frac{dx_2}{dt} &= -\frac{dx_1}{dt}\cos k\varphi_1 - \frac{dy_1}{dt}\sin k\varphi_1 \\ \frac{dy_2}{dt} &= -\frac{dx_1}{dt}\sin k\varphi_1 + \frac{dy_1}{dt}\cos k\varphi_1 \end{cases} \tag{89}$$

- The transform equations of the coordinates from the rotational systems to the static systems are as follows:

$$\begin{cases} X_1 &= x_1\cos\varphi_1 + y_1\sin\varphi_1 \\ Y_1 &= -x_1\sin\varphi_1 + y_1\cos\varphi_1 \end{cases} \tag{90}$$

$$\begin{cases} X_2 &= x_2\cos i\varphi_1 + y_2\sin i\varphi_1 \\ Y_2 &= -x_2\sin i\varphi_1 + y_2\cos i\varphi_1 \end{cases} \tag{91}$$

- The transform equations of the coordinates from the static systems to the rotational systems are as follows:

$$\begin{cases} x_1 &= X_1\cos\varphi_1 - Y_1\sin\varphi_1 \\ y_1 &= X_1\sin\varphi_1 + Y_1\cos\varphi_1 \end{cases} \tag{92}$$

$$\begin{cases} x_2 &= X_2\cos i\varphi_1 - Y_2\sin i\varphi_1 \\ y_2 &= X_2\sin i\varphi_1 + Y_2\cos i\varphi_1 \end{cases} \tag{93}$$

- The transform equations of the coordinates between the two static systems are as follows:

$$\begin{cases} X_1 = A - X_2 \\ Y_1 = Y_2 \end{cases} \tag{94}$$

$$\begin{cases} X_2 = A - X_1 \\ Y_2 = Y_1 \end{cases} \tag{95}$$

It should be mentioned that the locus of the contact point between the profiles of the male and the female rotors in the static coordinate system is called the meshing line, which is the projection of the contact line between the rotors in the cross-sectional plane. The meshing line is an enclosed line usually. If there exists an interruption in the meshing line, there exists an interruption in the contact line between the rotors so that the cavity volume of a helical screw compressor is not sealed and the profile is not usable. The meshing line lengths are different for different profiles, and the longer the meshing line length, the longer the contact line length. The meshing line is an important factor in the evaluation of a profile. The equations of the meshing line are obtained by substituting equation 84 into equation 90 or by substituting equation 76 into equation 91 which are simultaneous with the envelop condition equation. The following two equation systems show the equations of the meshing line in the two static coordinate systems respectively:

$$\begin{cases} X_1 = X_1(t, \varphi_1) \\ Y_1 = Y_1(t, \varphi_1) \\ f(t, \varphi_1) = 0 \end{cases} \tag{96}$$

$$\begin{cases} X_2 = X_2(t, \varphi_1) \\ Y_2 = Y_2(t, \varphi_1) \\ f(t, \varphi_1) = 0 \end{cases} \tag{97}$$

Appendix B

PARAMETER EQUATIONS OF THE SRM D-PROFILE

The basic design, common for all D-profiles, is shown in Fig. B.1 (a) and (b).

The Circular Arc A_MB_M and the Circular Arc A_FB_F

The crest portion A_MB_M of the male rotor follows a convex circular arc having its centre P on the pitch circle of the male rotor and having r as its radius. Its parametric equations and the parameter limits are as follows:

$$\begin{cases} x_1 = r_M + r\cos t \\ y_1 = -r\sin t \end{cases} \quad -\beta_1 \le t \le \beta_2 \tag{98}$$

where,

r is the radius of the circular arc A_MB_M, $[mm]$.

β_1 is the start angle of the arc, $[rad]$.

β_2 is the end angle of the arc, $[rad]$.

The bottom segment A_FB_F of the female rotor is a concave circular arc having its centre P on the pitch circle of the female rotor and having r as its radius. It has the same shape as the crest segment A_MB_M of the male rotor. They only mesh when the male rotation angle equals zero at which instant the meshing line and the contact line have the same shape as the segment. The parametric equations of the arc A_FB_F are represented in the coordinate system $o_2x_2y_2$ as follows:

$$\begin{cases} x_2 = r_M - r\cos t \\ y_2 = -r\sin t \end{cases} \quad -\beta_1 \le t \le \beta_2 \tag{99}$$

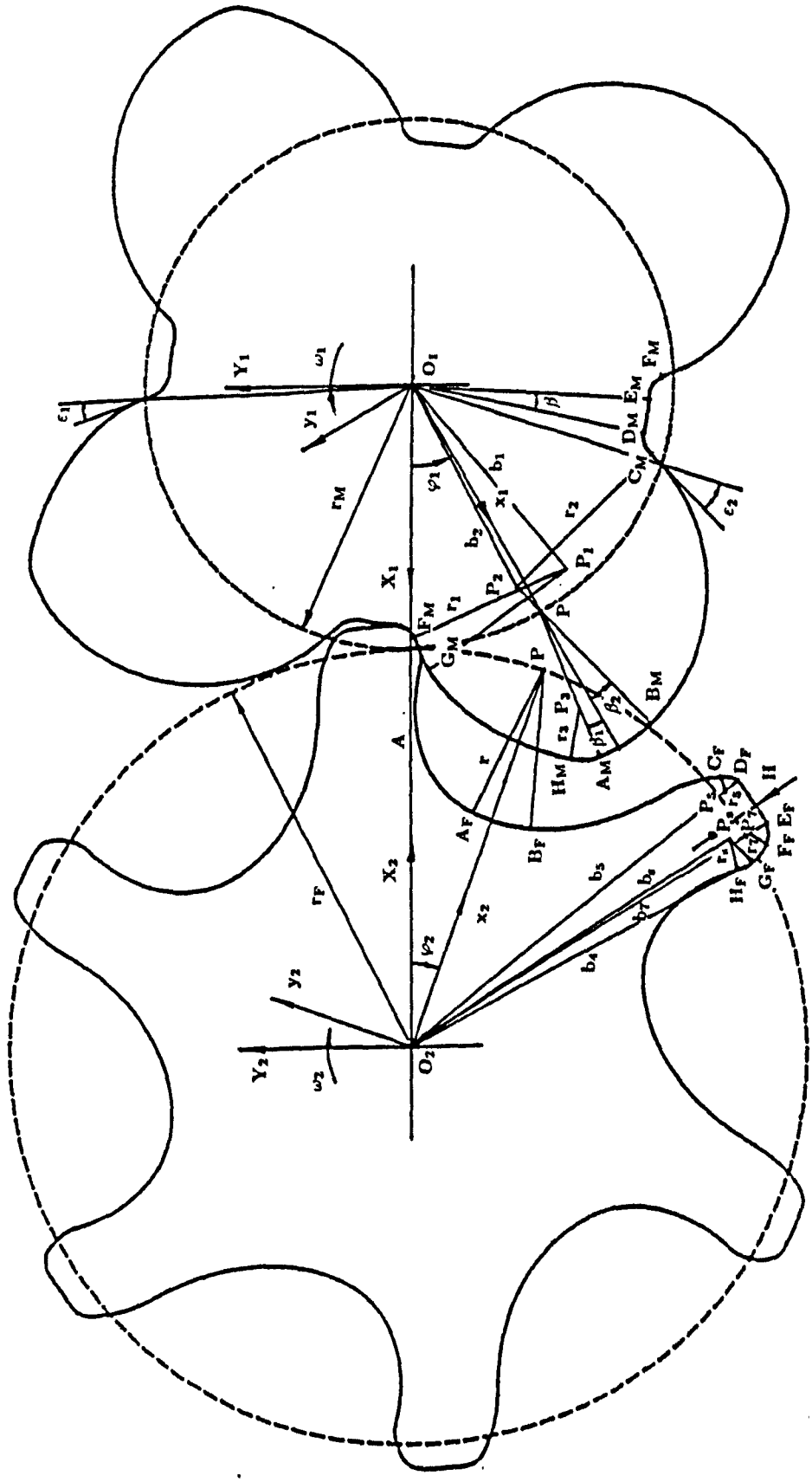

Fig. B.1 (a) SRM D-profile and its symbols

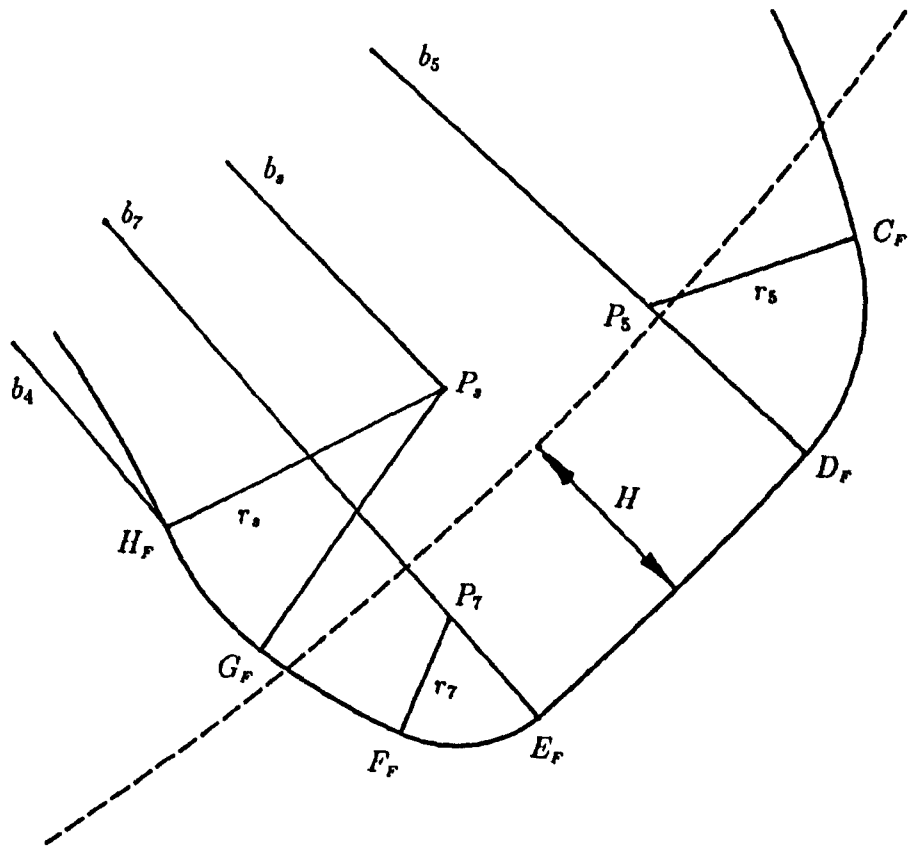

Fig. B.1 (b) Female rotor lobe tip detail

The Circular Arc $B_M C_M$ and the Convex-Concave Curve $B_F C_F$

The secondary flank $B_M C_M$ of the male rotor follows a circular arc having a radius r_2 and centre P_2 lying on an arc of radius b_2 and centre o_1 of the male rotor. It extends from the point C_M inside the pitch circle of the male rotor to the crest portion $A_M B_M$, and has a smooth connection with the crest portion at the point B_M. The arc intersects with the pitch circle and has in this intersecting point a tangent which forms an angle ε_2 with the radial line passing through the same point. Making use of the cosine law the following relationships can be obtained:

$$b_2 = \sqrt{r_2^2 + r_M^2 - 2 r_2 r_M \sin \varepsilon_2} \tag{100}$$

and

$$b_2 = \sqrt{(r_2 - r)^2 + r_M^2 - 2(r_2 - r) r_M \cos \beta_2} \tag{101}$$

Equating the right hand sides of 100 and 101 leads to the following formula, which defines the radius r_2 of the circular arc $B_M C_M$:

$$r_2 = \frac{r + 2rr_M \cos\beta_2}{2r - 2r_M \sin\varepsilon_2 + 2r_M \cos\beta_2} \tag{102}$$

The angle $\angle P_2 O_1 P$ is represented by β_3, which according to the cosine law is given by the following formula:

$$\beta_3 = \arccos\left[\frac{r_M^2 + b_2^2 - (r_2 - r)^2}{2r_M b_2}\right] \tag{103}$$

where r and r_M are known, r_2 is calculated by equation 102, and b_2 is calculated by equation 100 or 101. The coordinates of the centre P_2 are described as follows:

$$\begin{cases} x_1 &= b_2 \cos\beta_3 \\ y_1 &= b_2 \sin\beta_3 \end{cases} \tag{104}$$

The following equations are the parametric equations of the circular arc $B_M C_M$:

$$\begin{cases} x_1 &= b_2 \cos\beta_3 + r_2 \cos t \\ y_1 &= b_2 \sin\beta_3 - r_2 \sin t \end{cases} \quad \beta_2 \le t \le t_c \tag{105}$$

The parameter t_c will be determined according to the basic parameters chosen for the SRM D-profile.

The secondary flank $B_F C_F$ of the female rotor groove follows a convex-concave curve having a point of inflection generated by the mating, secondary flank $B_M C_M$ of the male rotor. Substituting equation 105 into equation 75, gives the following set of curves in the female rotor coordinate system $o_2 x_2 y_2$:

$$\begin{cases} x_2 &= -x_1 \cos k\varphi_1 - y_1 \sin k\varphi_1 + A\cos i\varphi_1 \\ &= -(b_2 \cos\beta_3 + r_2 \cos t)\cos k\varphi_1 - (b_2 \sin\beta_3 - r_2 \sin t)\sin k\varphi_1 \\ &\quad + A\cos i\varphi_1 \\ &= -b_2 \cos(k\varphi_1 - \beta_3) - r_2 \cos(k\varphi_1 + t) + A\cos i\varphi_1 \\ y_2 &= -x_1 \sin k\varphi_1 + y_1 \cos k\varphi_1 + A\sin i\varphi_1 \\ &= -(b_2 \cos\beta_3 + r_2 \cos t)\sin k\varphi_1 + (b_2 \sin\beta_3 - r_2 \sin t)\cos k\varphi_1 \\ &\quad + A\sin i\varphi_1 \\ &= -b_2 \sin(k\varphi_1 - \beta_3) - r_2 \sin(k\varphi_1 + t) + A\sin i\varphi_1 \end{cases} \tag{106}$$

From the above equations the following partial derivatives can be obtained:

$$\begin{cases} \frac{\partial x_2}{\partial t} &= r_2 \sin(k\varphi_1 + t) \\ \frac{\partial x_2}{\partial \varphi_1} &= b_2 k \sin(k\varphi_1 - \beta_3) + r_2 k \sin(k\varphi_1 + t) - Ai \sin i\varphi_1 \\ \frac{\partial y_2}{\partial t} &= -r_2 \cos(k\varphi_1 + t) \\ \frac{\partial y_2}{\partial \varphi_1} &= -b_2 k \cos(k\varphi_1 - \beta_3) - r_2 k \cos(k\varphi_1 + t) + Ai \cos i\varphi_1 \end{cases} \tag{107}$$

Substituting the above partial derivatives into equation 86, that is, the envelop condition equation, and developing it, the following envelop condition equation for the convex-concave curve $B_F C_F$ is obtained:

$$\frac{Ai}{k} \sin(\varphi_1 + t) - b_2 \sin(t + \beta_3) = 0 \tag{108}$$

Since $\frac{Ai}{k} = r_M$ in the above formula, it can be rewritten as follows:

$$r_M \sin(\varphi_1 + t) - b_2 \sin(t + \beta_3) = 0 \tag{109}$$

or

$$\varphi_1 = \arcsin\left[\frac{b_2}{r_M} \sin(t + \beta_3)\right] - t \tag{110}$$

The following simultaneous equations of equations 106 and 110 define the mating secondary flank $B_F C_F$ of the female rotor groove generated by the secondary flank $B_M C_M$ of the male rotor lobe:

$$\begin{cases} x_2 &= -b_2 \cos(k\varphi_1 - \beta_3) - r_2 \cos(k\varphi_1 + t) + A \cos i\varphi_1 \\ y_2 &= -b_2 \sin(k\varphi_1 - \beta_3) - r_2 \sin(k\varphi_1 + t) + A \sin i\varphi_1 \quad \beta_2 \le t \le t_c \\ \varphi_1 &= \arcsin\left[\frac{b_2}{r_M} \sin(t + \beta_3)\right] - t \end{cases} \tag{111}$$

The Circular Arc $C_F D_F$ and the Concave Curve $C_M D_M$

The convex circular arc $C_F D_F$ is used to connect the secondary flank $B_F C_F$ smoothly with the crest portion $D_F E_F$ of the female rotor grooves. Its centre is P_5 and its radius is r_5.

From the equations of the circular arc $B_M C_M$, that is, equations 105, the following derivatives at point C_M can be obtained:

$$\begin{cases} \frac{dx_1}{dt} &= -r_2 \sin t_c \\ \frac{dy_1}{dt} &= -r_2 \cos t_c \end{cases} \tag{112}$$

Substituting the above equations into equation 89, and noticing that the male rotor rotational angle φ_1 corresponding to parameter t_C is given by the envelop condition equation 110, the following derivatives of the point C_F on the female rotor grooves which mates with C_M on the male lobe are obtained:

$$\begin{cases} \frac{dx_2}{dt} &= -\frac{dx_1}{dt}\cos k\varphi_1 - \frac{dy_1}{dt}\sin k\varphi_1 \\ &= r_2 \sin t_C \cos k\varphi_1 + r_2 \cos t_C \sin k\varphi_1 \\ &= r_2 \sin(t_C + k\varphi_1) \\ \frac{dy_2}{dt} &= -\frac{dx_1}{dt}\sin k\varphi_1 + \frac{dy_1}{dt}\cos k\varphi_1 \\ &= r_2 \sin t_C \sin k\varphi_1 - r_2 \cos t_C \cos k\varphi_1 \\ &= -r_2 \cos(t_C + k\varphi_1) \\ \varphi_1 &= \arcsin\left[\frac{b_2}{r_M}\sin(t_C + \beta_3)\right] - t_C \end{cases} \tag{113}$$

From the above equations, the slope of point C_F is obtained:

$$\begin{cases} \frac{dy_2}{dx_2} &= -\cot(t_C + k\varphi_1) \\ \varphi_1 &= \arcsin\left[\frac{b_2}{r_M}\sin(t_C + \beta_3)\right] - t_C \end{cases} \tag{114}$$

β_{13}, the angle between the tangent at point C_F and the coordinate axis x_2, is calculated by the following formula:

$$\begin{cases} \beta_{13} &= \arctan\left(\frac{dy_2}{dx_2}\right) \\ &= \arctan[-\cot(t_C + k\varphi_1)] \\ \varphi_1 &= \arcsin\left[\frac{b_2}{r_M}\sin(t_C + \beta_3)\right] - t_C \end{cases} \tag{115}$$

b_{10} is the distance between the point C_F and the female rotor centre o_2, and β_{14} is the angle between the coordinate axis x_2 and the connecting line of the point and the centre. They can be calculated easily by the following two formulas respectively:

$$b_{10} = \sqrt{x_{2C}^2 + y_{2C}^2} \tag{116}$$

$$\beta_{14} = \arctan\left(\frac{y_{2C}}{x_{2C}}\right) \tag{117}$$

where x_{2C} and y_{2C} are the coordinates of the point C_F in the coordinate system $o_2x_2y_2$. b_5 is the distance between the centre P_5 of the circular arc C_FD_F and the centre o_2 of the female rotor. Obviously, b_5 can be calculated by the following simple equation:

$$b_5 = r_{2tip} - r_5 \tag{118}$$

where r_{2tip} is the radius of the tip circle of the female rotor. According to the cosine law, the following relationship exists:

$$b_5^2 = b_{10}^2 + r_5^2 - 2b_{10}r_5 \cos\left(\frac{\pi}{2} - \mid \beta_{13} - \beta_{14} \mid\right) \tag{119}$$

Substituting equation 118 into the above equation and developing it, the following formula used to calculate the radius r_5 is obtained:

$$r_5 = \frac{-r_{2tip}^2 + b_{10}^2}{2b_{10}\cos\left(\frac{\pi}{2} - \mid \beta_{13} - \beta_{14} \mid\right) - 2r_{2tip}} \tag{120}$$

It should be mentioned here that the parameter t_C is a function of the radius r_5. In practice the above equation is used to determine the parameter t_C from the chosen basic parameter r_5.

$\angle C_F o_2 D_F$ is represented by β_4, and according to the cosine law and the sine law the following calculation formulas for β_4 can be obtained respectively:

$$\beta_4 = \arccos\frac{b_{10}^2 + b_5^2 - r_5^2}{2b_{10}b_5} \tag{121}$$

$$\beta_4 = \arcsin\frac{r_5 \sin(\frac{\pi}{2} - \mid \beta_{13} - \beta_{14} \mid)}{b_5} \tag{122}$$

$\angle C_F P_5 D_F$ is represented by β_{16}. The angle between the coordinate axis x_2 and the line connecting P_5 to o_2 is represented by β_{15}. β_5 is used to represent the angle between the coordinate axis x_1 and the line connecting point D_M to the centre o_1. They can be calculated by the following simple formulas:

$$\beta_{16} = \beta_4 + (\frac{\pi}{2} - \mid \beta_{13} - \beta_{14} \mid) \tag{123}$$

$$\beta_{15} = \beta_{14} + \beta_4 \tag{124}$$

$$\beta_5 = \frac{\beta_{15}}{i} \tag{125}$$

The parametric equations of the circular arc $C_F D_F$ are as follows:

$$\begin{cases} x_2 = b_5 \cos\beta_{15} + r_5 \cos t \\ y_2 = -b_5 \sin\beta_{15} + r_5 \sin t \end{cases} \quad -\beta_{15} \le t \le \beta_{16} - \beta_{15} \tag{126}$$

The concave curve $C_M D_M$ is used to connect the secondary flank $B_M C_M$ smoothly to the bottom portion $D_M E_M$ of the male rotor, and is generated by

the circular arc $C_F D_F$ on the female rotor. Substituting equation 126 into equation 74, the following equations of a set of curves in the female rotor coordinate system $o_1 x_1 y_1$ are obtained:

$$\begin{cases} x_1 = -x_2 \cos k\varphi_1 - y_2 \sin k\varphi_1 + A\cos\varphi_1 \\ \quad = -(b_5 \cos\beta_{15} + r_5 \cos t)\cos k\varphi_1 - (-b_5 \sin\beta_{15} + r_5 \sin t)\sin k\varphi_1 \\ \quad\quad +A\cos\varphi_1 \\ \quad = -b_5 \cos(k\varphi_1 + \beta_{15}) - r_5 \cos(k\varphi_1 - t) + A\cos\varphi_1 \\ y_1 = -x_2 \sin k\varphi_1 + y_2 \cos k\varphi_1 + A\sin\varphi_1 \\ \quad = -(b_5 \cos\beta_{15} + r_5 \cos t)\sin k\varphi_1 + (-b_5 \sin\beta_{15} + r_5 \sin t)\cos k\varphi_1 \\ \quad\quad +A\sin\varphi_1 \\ \quad = -b_5 \sin(k\varphi_1 + \beta_{15}) - r_5 \sin(k\varphi_1 - t) + A\sin\varphi_1 \end{cases} \tag{127}$$

From the above equations the following partial derivatives can be obtained:

$$\begin{cases} \frac{\partial x_1}{\partial t} = -r_5 \sin(k\varphi_1 - t) \\ \frac{\partial x_1}{\partial \varphi_1} = b_5 k \sin(k\varphi_1 + \beta_{15}) + r_5 k \sin(k\varphi_1 - t) - A\sin\varphi_1 \\ \frac{\partial y_1}{\partial t} = r_5 \cos(k\varphi_1 - t) \\ \frac{\partial y_1}{\partial \varphi_1} = -b_5 k \cos(k\varphi_1 + \beta_{15}) - r_5 k \cos(k\varphi_1 - t) + A\cos\varphi_1 \end{cases} \tag{128}$$

Substituting the above partial derivatives into equation 81, that is, the envelop condition equation, and developing it, the following envelop condition equation for the concave curve $C_M D_M$ is obtained:

$$\varphi_1 = \frac{1}{i}\left\{\arcsin\left[-\frac{b_5}{r_F}\sin(t + \beta_{15})\right] + t\right\} \tag{129}$$

The following simultaneous equations of equations 127 and 129 define the mating curve $C_M D_M$ on the male rotor lobe generated by the circular arc $C_F D_F$ on the female rotor groove:

$$\begin{cases} x_1 = -b_5 \cos(k\varphi_1 + \beta_{15}) - r_5 \cos(k\varphi_1 - t) + A\cos\varphi_1 \\ y_1 = -b_5 \sin(k\varphi_1 + \beta_{15}) - r_5 \sin(k\varphi_1 - t) + A\sin\varphi_1 \quad \beta_{14} \le t \le \beta_{14} + \beta_{16} \\ \varphi_1 = \frac{1}{i}\left\{\arcsin\left[-\frac{b_5}{r_F}\sin(t + \beta_{15})\right] + t\right\} \end{cases} \tag{130}$$

The Circular Arc $A_M H_M$ and the Concave Curve $A_F H_F$

One curve $A_M H_M$ comprising a small part of the male rotor primary flank follows a circular arc having a radius r_3. Its centre P_3 is disposed on a radius b_3 from the centre o_1 of the male rotor. $A_M H_M$ extends from the point H_M where it has a tangent common with that of the other flank portion $H_M G_M$, to the point A_M where it connects smoothly with the crest portion $A_M B_M$. Using the cosine law, the following formula can be obtained to calculate the distance b_3:

$$b_3 = \sqrt{(r - r_3)^2 + r_M^2 - 2(r - r_3) r_M \cos(\pi - \beta_1)} \tag{131}$$

so that the coordinates of the centre P_3 can be presented as follows:

$$\begin{cases} x_1 = b_3 \cos\beta_6 \\ y_1 = b_3 \sin\beta_6 \end{cases} \tag{132}$$

where β_6 is $\angle P o_1 P_3$, which can be calculated from the following equation derived from the sine law:

$$\beta_6 = \arcsin\left(\frac{r - r_3}{b_3} \sin\beta_1\right) \tag{133}$$

The equations of the circular arc $A_M H_M$ are as follows:

$$\begin{cases} x_1 = b_3 \cos\beta_6 + r_3 \cos t \\ y_1 = b_3 \sin\beta_6 + r_3 \sin t \end{cases} \quad \beta_1 \le t \le t_H \tag{134}$$

The parameter t_H will be determined from the chosen basic parameters of the SRM D-profile.

One concave curve $A_F H_F$ comprising a large part of the female rotor groove primary flank follows a curve generated by the portion $A_M H_M$ of the mating primary flank of the male rotor, which extends from the bottom portion $A_F B_F$ to the portion $H_F G_F$ and has smooth connections with these two portions at points A_F and H_F respectively. Substituting equation 133 into equation 75, the following equations of a set of curves in the female rotor coordinate system $o_2 x_2 y_2$

are obtained:

$$\begin{cases} x_2 &= -x_1\cos k\varphi_1 - y_1\sin k\varphi_1 + A\cos i\varphi_1 \\ &= -(b_3\cos\beta_6 + r_3\cos t)\cos k\varphi_1 - (b_3\sin\beta_6 + r_3\sin t)\sin k\varphi_1 \\ &\quad +A\cos i\varphi_1 \\ &= -b_3\cos(k\varphi_1 - \beta_6) - r_3\cos(k\varphi_1 - t) + A\cos i\varphi_1 \\ y_2 &= -x_1\sin k\varphi_1 + y_1\cos k\varphi_1 + A\sin i\varphi_1 \\ &= -(b_3\cos\beta_6 + r_3\cos t)\sin k\varphi_1 + (b_3\sin\beta_6 + r_3\sin t)\cos k\varphi_1 \\ &\quad +A\sin i\varphi_1 \\ &= -b_3\sin(k\varphi_1 - \beta_6) - r_3\sin(k\varphi_1 - t) + A\sin i\varphi_1 \end{cases} \tag{135}$$

From the above equations the following partial derivatives can be obtained:

$$\begin{cases} \frac{\partial x_2}{\partial t} &= -r_3\sin(k\varphi_1 - t) \\ \frac{\partial x_2}{\partial \varphi_1} &= b_3k\sin(k\varphi_1 - \beta_6) + r_3k\sin(k\varphi_1 - t) - Ai\sin i\varphi_1 \\ \frac{\partial y_2}{\partial t} &= r_3\cos(k\varphi_1 - t) \\ \frac{\partial y_2}{\partial \varphi_1} &= -b_3k\cos(k\varphi_1 - \beta_6) - r_3k\cos(k\varphi_1 - t) + Ai\cos i\varphi_1 \end{cases} \tag{136}$$

Substituting the above partial derivatives into equation 86, that is, the envelop condition equation, and developing it, the following envelop condition equation for the concave curve A_FH_F is obtained:

$$\varphi_1 = \arcsin\left[\frac{b_3}{r_M}\sin(\beta_6 - t)\right] + t \tag{137}$$

The following simultaneous equations of equations 135 and 137 define the mating primary flank A_FH_F of the female rotor groove generated by the circular arc B_MC_M on the male rotor lobe:

$$\begin{cases} x_2 &= -b_3\cos(k\varphi_1 - \beta_6) - r_3\cos(k\varphi_1 - t) + A\cos i\varphi_1 \\ y_2 &= -b_3\sin(k\varphi_1 - \beta_6) - r_3\sin(k\varphi_1 - t) + A\sin i\varphi_1 \quad \beta_1 \le t \le t_H \\ \varphi_1 &= \arcsin\left[\frac{b_3}{r_M}\sin(\beta_6 - t)\right] + t \end{cases} \tag{138}$$

The Circular Arc G_FH_F and the Convex Curve G_MH_M

The primary flank section G_FH_F of the female rotor follows a circular arc having a radius r_s and a centre P_s, disposed on a distance b_s from the centre o_2 of the

female rotor. It has smooth connections with the two other flank portions $A_F H_F$ and $F_F G_F$ at the points G_F and H_F respectively, and the point H_F is disposed on a distance b_4 from the centre o_2 of the female rotor. It should be mentioned that the section $G_F H_F$ can be decreased down to zero length whereby, however, the section will be replaced by an obtuse corner. If $\angle H_F o_2 P$ is represented by β_7, according to equation 138 β_7 and b_4 can be calculated by the following equations:

$$\beta_7 = \arctan \frac{y_{2H}}{x_{2H}} \tag{139}$$

and

$$b_4 = \sqrt{y_{2H}^2 + x_{2H}^2} \tag{140}$$

Also according to equation 138 the slope at the point H_F, at which the circular arc $G_F H_F$ has the same slope, can be calculated by the following equations:

$$\begin{cases} \frac{dy_2}{dx_2} &= -\cot(k\varphi_1 - t_H) \\ \varphi_1 &= \arcsin\left[\frac{b_3}{r_M}\sin(\beta_6 - t_H)\right] + t_H \end{cases} \tag{141}$$

The angle between the tangent line of the point H_F and the coordinate axis x_2 is represented by β_8, and can be calculated easily by the following formula:

$$\beta_8 = \arctan \frac{dy_2}{dx_2} \tag{142}$$

According to the cosine law the distance b_s between the centre P_s of the circular arc $G_F H_F$ and the centre o_2 of the female rotor can be calculated by the following formula:

$$b_s = \sqrt{b_4^2 + r_s^2 - 2b_4 r_s \cos(\frac{\pi}{2} + \beta_7 - \beta_8)} \tag{143}$$

and if β_9 is used to represent $\angle P_s o_2 H_F$, it is calculated by the following formula:

$$\beta_9 = \arccos \frac{b_s^2 + b_4^2 - r_s^2}{2b_s b_4} \tag{144}$$

The coordinates of the centre P_s are as follows:

$$\begin{cases} x_2 &= b_s \cos(\beta_9 + \beta_7) \\ y_2 &= b_s \sin(\beta_9 + \beta_7) \end{cases} \tag{145}$$

The parametric equations of the circular arc $G_F H_F$ are as follows:

$$\begin{cases} x_2 &= b_s \cos(\beta_9 + \beta_7) + r_s \cos t \\ y_2 &= b_s \sin(\beta_9 + \beta_7) + r_s \sin t \end{cases} \quad -\frac{\pi}{2} + \beta_8 \le t \le t_G \tag{146}$$

where the parameter t_G will be determined from the chosen basic parameters of the SRM D-profile.

The portion $G_M H_M$ of the male rotor primary flank follows a generally epitrochoidal curve, generated by the section $G_F H_F$ of the mating primary flank of the female rotor groove, and extends from the point G_M, where it has a tangent common to that of the other primary flank portion $G_M F_M$, to the point H_M, where it has smooth connection with the circular arc $A_M H_M$. Substituting equation 146 into equation 74, the following equations of a set of curves in the male rotor coordinate system $o_1 x_1 y_1$ are obtained:

$$\begin{cases} x_1 = -x_2 \cos k\varphi_1 - y_2 \sin k\varphi_1 + A\cos\varphi_1 \\ \quad = -(b_s \cos(\beta_9+\beta_7) + r_s \cos t)\cos k\varphi_1 - (b_s \sin(\beta_9+\beta_7) + r_s \sin t)\sin k\varphi_1 \\ \quad\quad +A\cos\varphi_1 \\ \quad = -b_s \cos(k\varphi_1 - \beta_9 - \beta_7) - r_s \cos(k\varphi_1 - t) + A\cos\varphi_1 \\ y_1 = -x_2 \sin k\varphi_1 + y_2 \cos k\varphi_1 + A\sin\varphi_1 \\ \quad = -(b_s \cos(\beta_9+\beta_7) + r_s \cos t)\sin k\varphi_1 + (b_s \sin(\beta_9+\beta_7) + r_s \sin t)\cos k\varphi_1 \\ \quad\quad +A\sin\varphi_1 \\ \quad = -b_s \sin(k\varphi_1 - \beta_9 - \beta_7) - r_s \sin(k\varphi_1 - t) + A\sin\varphi_1 \end{cases} \tag{147}$$

From the above equations the following partial derivatives can be obtained:

$$\begin{cases} \dfrac{\partial x_1}{\partial t} = -r_s \sin(k\varphi_1 - t) \\ \dfrac{\partial x_1}{\partial \varphi_1} = b_s k \sin(k\varphi_1 - \beta_9 - \beta_7) + r_s k \sin(k\varphi_1 - t) - A\sin\varphi_1 \\ \dfrac{\partial y_1}{\partial t} = r_s \cos(k\varphi_1 - t) \\ \dfrac{\partial y_1}{\partial \varphi_1} = -b_s k \cos(k\varphi_1 - \beta_9 - \beta_7) - r_s k \cos(k\varphi_1 - t) + A\cos\varphi_1 \end{cases} \tag{148}$$

Substituting the above partial derivatives into equation 81, that is, the envelop condition equation, and developing it, the following envelop condition equation for the convex curve $G_M H_M$ is obtained:

$$\varphi_1 = \frac{1}{i}\left\{\arcsin\left[\frac{b_s}{r_F}\sin(\beta_9+\beta_7-t)\right] + t\right\} \tag{149}$$

The following simultaneous equations of equations 147 and 149 define the mating curve $G_M H_M$ on the male rotor lobe generated by the circular arc $G_F H_F$ on the

female rotor groove:

$$\begin{cases} x_1 = -b_s\cos(k\varphi_1-\beta_9-\beta_7)-r_s\cos(k\varphi_1-t) \\ \qquad +A\cos\varphi_1 \\ y_1 = -b_s\sin(k\varphi_1-\beta_9-\beta_7)-r_s\sin(k\varphi_1-t) \\ \qquad +A\sin\varphi_1 \\ \varphi_1 = \frac{1}{i}\left\{\arcsin\left[\frac{b_s}{r_F}\sin(\beta_9+\beta_7-t)\right]+t\right\} \end{cases} \quad -\frac{\pi}{2}+\beta_8 \le t \le t_G \qquad (150)$$

The Circular Arc F_MG_M and the Convex Curve F_FG_F

The portion F_MG_M of the primary flank of a male rotor groove follows a circular arc having a radius r_1 and its centre P_1 disposed on a distance b_1 from the centre o_1 of the male rotor and extends from the point F_M inside the pitch circle, where it has a smooth connection with the transition concave curve E_MF_M, to the point G_M outside the pitch circle, where it has a tangent common to that of the portion G_MH_M. The circular arc F_MG_M intersects with the pitch circle of the male rotor and at the intersecting point has a tangent which forms an angle ε_1 with the radial line which goes through the same point. As the curvature radius of the generally epitrochoidal curve defining the flank portion G_MH_M increases continuously from the outer point H_M to the inner point G_M where it has a functional maximum equal to the radius r_1, the radius r_1 is the curvature radius of point G_M on the convex curve G_MH_M, which can be calculated by the following formula:

$$r_1 = \left.\frac{\left[\left(\frac{dx_1}{dt}\right)^2+\left(\frac{dy_1}{dt}\right)^2\right]^{\frac{3}{2}}}{\left|\frac{dx_1}{dt}\frac{d^2y_1}{dt^2}-\frac{d^2x_1}{dt^2}\frac{dy_1}{dt}\right|}\right|_{t=t_G} \qquad (151)$$

The derivatives in the above formula can be obtained from equation 150, and the

results are as follows:

$$
\begin{cases}
\frac{dx_1}{dt} = b_s k \sin(k\varphi_1 - \beta_9 - \beta_7)\frac{d\varphi_1}{dt} + r_s k \sin(k\varphi_1 - t)\frac{d\varphi_1}{dt} \\
\qquad -r_s \sin(k\varphi_1 - t) - A \sin\varphi_1 \frac{d\varphi_1}{dt} \\
\frac{d^2x_1}{dt^2} = b_s k^2 \cos(k\varphi_1 - \beta_9 - \beta_7)\left(\frac{d\varphi_1}{dt}\right)^2 \\
\qquad +b_s k \sin(k\varphi_1 - \beta_9 - \beta_7)\frac{d^2\varphi_1}{dt^2} \\
\qquad +r_s k^2 \cos(k\varphi_1 - t)\left(\frac{d\varphi_1}{dt}\right)^2 - r_s k \cos(k\varphi_1 - t)\frac{d\varphi_1}{dt} \\
\qquad +r_s k \sin(k\varphi_1 - t)\frac{d^2\varphi_1}{dt^2} - r_s k \cos(k\varphi_1 - t)\frac{d\varphi_1}{dt} \\
\qquad +r_s \cos(k\varphi_1 - t) - A\cos\varphi_1\left(\frac{d\varphi_1}{dt}\right)^2 - A\sin\varphi_1\frac{d^2\varphi_1}{dt^2} \\
\frac{dy_1}{dt} = -b_s k \cos(k\varphi_1 - \beta_9 - \beta_7)\frac{d\varphi_1}{dt} - r_s k \cos(k\varphi_1 - t)\frac{d\varphi_1}{dt} \\
\qquad +r_s \cos(k\varphi_1 - t) + A\cos\varphi_1\frac{d\varphi_1}{dt} \\
\frac{d^2y_1}{dt^2} = b_s k^2 \sin(k\varphi_1 - \beta_9 - \beta_7)\left(\frac{d\varphi_1}{dt}\right)^2 \\
\qquad -b_s k \cos(k\varphi_1 - \beta_9 - \beta_7)\frac{d^2\varphi_1}{dt^2} \\
\qquad +r_s k^2 \sin(k\varphi_1 - t)\left(\frac{d\varphi_1}{dt}\right)^2 - r_s k \sin(k\varphi_1 - t)\frac{d\varphi_1}{dt} \\
\qquad -r_s k \cos(k\varphi_1 - t)\frac{d^2\varphi_1}{dt^2} - r_s k \sin(k\varphi_1 - t)\frac{d\varphi_1}{dt} \\
\qquad +r_s \sin(k\varphi_1 - t) - A\sin\varphi_1\left(\frac{d\varphi_1}{dt}\right)^2 + A\cos\varphi_1\frac{d^2\varphi_1}{dt^2}
\end{cases}
\tag{152}
$$

In the above equations, the first and second derivatives $\frac{d\varphi_1}{dt}$ and $\frac{d^2\varphi_1}{dt^2}$ can be obtained from the envelop condition equation 149. Equation 149 can be rewritten as follows:

$$b_s \sin(\beta_9 + \beta_7 - t) - r_F \sin(i\varphi_1 - t) = 0 \tag{153}$$

From the following first derivative of the above equation with respect to t:

$$\frac{d}{dt}\left[b_s \sin(\beta_9 + \beta_7 - t) - r_F \sin(i\varphi_1 - t)\right] = 0 \tag{154}$$

the following first derivative of φ_1 with respect to t can be obtained:

$$\frac{d\varphi_1}{dt} = \frac{-b_s \cos(\beta_9 + \beta_7 - t) + r_F \cos(i\varphi_1 - t)}{r_F \cos(i\varphi_1 - t)} \tag{155}$$

and from the following second derivative of equation 153 with respect to t:

$$\frac{d^2}{dt^2}\left[b_s \sin(\beta_9 + \beta_7 - t) - r_F \sin(i\varphi_1 - t)\right] = 0 \tag{156}$$

the following second derivative of φ_1 with respect to t can also be obtained:

$$\begin{aligned}\frac{d^2\varphi_1}{dt^2} &= \frac{1}{r_F i\cos(i\varphi_1 - t)}[-b_s\sin(\beta_9+\beta_7-t) \\ &\quad + r_F i^2\sin(i\varphi_1-t)\left(\frac{d\varphi_1}{dt}\right)^2 - 2r_F i\sin(i\varphi_1-t)\frac{d\varphi_1}{dt} \\ &\quad + r_F\sin(i\varphi_1-t)]\end{aligned} \tag{157}$$

The coordinates of the centre P_1 of the circular arc F_MG_M can be calculated by the following equations:

$$\begin{cases} x_{1p_1} = x_1|_{t=t_G} - \left.\dfrac{\dfrac{dy_1}{dt}\left[\left(\dfrac{dx_1}{dt}\right)^2+\left(\dfrac{dy_1}{dt}\right)^2\right]}{\dfrac{dx_1}{dt}\dfrac{d^2y_1}{dt^2}-\dfrac{d^2x_1}{dt^2}\dfrac{dy_1}{dt}}\right|_{t=t_G} \\ y_{1p_1} = y_1|_{t=t_G} + \left.\dfrac{\dfrac{dx_1}{dt}\left[\left(\dfrac{dx_1}{dt}\right)^2+\left(\dfrac{dy_1}{dt}\right)^2\right]}{\dfrac{dx_1}{dt}\dfrac{d^2y_1}{dt^2}-\dfrac{d^2x_1}{dt^2}\dfrac{dy_1}{dt}}\right|_{t=t_G} \end{cases} \tag{158}$$

The distance b_1 between the two centres p_1 and o_1 is calculated by the following equation:

$$b_1 = \sqrt{x_{1p_1}^2 + y_{1p_1}^2} \tag{159}$$

$\angle P_1o_1P$ is represented by β_{10}, and it can be calculated by the following formula:

$$\beta_{10} = \arctan\frac{y_{1p_1}}{x_{1p_1}} \tag{160}$$

According to the cosine law the angle ε_1 can be calculated by the following formula:

$$\varepsilon_1 = \frac{\pi}{2} - \arccos\left(\frac{r_1^2 + r_M^2 - b_1^2}{2r_1r_M}\right) \tag{161}$$

The equations of the circular arc F_MG_M are as follows:

$$\begin{cases} x_1 = b_1\cos\beta_{10} + r_1\cos t \\ y_1 = b_1\sin\beta_{10} + r_1\sin t \end{cases} \quad \frac{\pi}{2}+\beta_{10} \le t \le t_F \tag{162}$$

Where the parameter t_F will be determined from the chosen basic parameters of the SRM D-profile.

The primary flank portion F_FG_F of the female rotor follows a convex curve generated by the primary flank portion F_MG_M of the mating male rotor. It has smooth connections with the circular arcs G_FH_F and E_FF_F at the points G_F

and F_F respectively. Substituting equation 162 into equation 75, the following equations of a set of curves in the female rotor coordinate system $o_2x_2y_2$ are obtained:

$$\begin{cases} x_2 = -x_1\cos k\varphi_1 - y_1\sin k\varphi_1 + A\cos i\varphi_1 \\ \quad = -(b_1\cos\beta_{10} + r_1\cos t)\cos k\varphi_1 - (b_1\sin\beta_{10} + r_1\sin t)\sin k\varphi_1 \\ \quad\quad +A\cos i\varphi_1 \\ \quad = -b_1\cos(k\varphi_1 - \beta_{10}) - r_1\cos(k\varphi_1 - t) + A\cos i\varphi_1 \\ y_2 = -x_1\sin k\varphi_1 + y_1\cos k\varphi_1 + A\sin i\varphi_1 \\ \quad = -(b_1\cos\beta_{10} + r_1\cos t)\sin k\varphi_1 + (b_1\sin\beta_{10} + r_1\sin t)\cos k\varphi_1 \\ \quad\quad +A\sin i\varphi_1 \\ \quad = -b_1\sin(k\varphi_1 - \beta_{10}) - r_1\sin(k\varphi_1 - t) + A\sin i\varphi_1 \end{cases} \tag{163}$$

From the above equations the following partial derivatives can be obtained:

$$\begin{cases} \frac{\partial x_2}{\partial t} = -r_1\sin(k\varphi_1 - t) \\ \frac{\partial x_2}{\partial \varphi_1} = b_1k\sin(k\varphi_1 - \beta_{10}) + r_1k\sin(k\varphi_1 - t) - Ai\sin i\varphi_1 \\ \frac{\partial y_2}{\partial t} = r_1\cos(k\varphi_1 - t) \\ \frac{\partial y_2}{\partial \varphi_1} = -b_1k\cos(k\varphi_1 - \beta_{10}) - r_1k\cos(k\varphi_1 - t) + Ai\cos i\varphi_1 \end{cases} \tag{164}$$

Substituting the above partial derivatives into equation 86, that is, the envelop condition equation, and developing it, the following envelop condition equation for the convex curve F_FG_F is obtained:

$$r_M\sin(\varphi_1 - t) + b_1\sin(t - \beta_{10}) = 0 \tag{165}$$

or

$$\varphi_1 = \arcsin\left[-\frac{b_1}{r_M}\sin(t - \beta_{10})\right] + t \tag{166}$$

The following simultaneous equations of equations 164 and 166 define the mating primary flank F_FG_F of the female rotor groove generated by the primary flank F_MG_M of the male rotor lobe:

$$\begin{cases} x_2 = -b_1\cos(k\varphi_1 - \beta_{10}) - r_1\cos(k\varphi_1 - t) \\ \quad\quad +A\cos i\varphi_1 \\ y_2 = -b_1\sin(k\varphi_1 - \beta_{10}) - r_1\sin(k\varphi_1 - t) \quad \frac{\pi}{2} + \beta_{10} \le t \le t_F \\ \quad\quad +A\sin i\varphi_1 \\ \varphi_1 = \arcsin\left[-\frac{b_1}{r_M}\sin(t - \beta_{10})\right] + t \end{cases} \tag{167}$$

The Circular Arc E_FF_F and the Concave Curve E_MF_M

The convex circular arc E_FF_F is used to make a smooth connection between the primary flank F_FG_F and the crest portion D_FE_F of the female rotor grooves. Its centre is P_7 and its radius r_7.

From the equations of the circular arc F_MG_M, that is equation 162, the following derivatives at point F_M can be obtained:

$$\begin{cases} \frac{dx_1}{dt} &= -r_1 \sin t_F \\ \frac{dy_1}{dt} &= r_1 \cos t_F \end{cases} \tag{168}$$

Substituting the above equations into equation 89, and noticing that for the given parameter t_F the male rotor rotational angle φ_1 is given by the envelop condition equation 166, the following derivatives of the corresponding point F_F on the female rotor grooves are obtained:

$$\begin{cases} \frac{dx_2}{dt} &= -\frac{dx_1}{dt}\cos k\varphi_1 - \frac{dy_1}{dt}\sin k\varphi_1 \\ &= r_1 \sin t_F \cos k\varphi_1 - r_1 \cos t_F \sin k\varphi_1 \\ &= r_1 \sin(t_F - k\varphi_1) \\ \frac{dy_2}{dt} &= -\frac{dx_1}{dt}\sin k\varphi_1 + \frac{dy_1}{dt}\cos k\varphi_1 \\ &= r_1 \sin t_F \sin k\varphi_1 + r_1 \cos t_F \cos k\varphi_1 \\ &= r_1 \cos(t_F - k\varphi_1) \\ \varphi_1 &= \arcsin\left[-\frac{b_1}{r_M}\sin(t_F - \beta_{10})\right] + t_F \end{cases} \tag{169}$$

β_{20} is the angle between the tangent to the profile at point F_F and the coordinate axis x_2, which is calculated by the following formula:

$$\begin{cases} \beta_{20} &= \arctan\left(\frac{dy_2}{dx_2}\right) \\ &= \arctan\left[-\cot(t_F - k\varphi_1)\right] \\ \varphi_1 &= \arcsin\left[-\frac{b_1}{r_M}\sin(t_F - \beta_{10})\right] - t_F \end{cases} \tag{170}$$

b_{11} is the distance between the point F_F and the female rotor centre o_2, and β_{12} is the angle between the coordinate axis x_2 and the line connecting F_F to the centre. They can be calculated easily by the following two formulas respectively:

$$b_{11} = \sqrt{x_{2F}^2 + y_{2F}^2} \tag{171}$$

$$\beta_{12} = \arctan\left(\frac{y_{2F}}{x_{2F}}\right) \tag{172}$$

where x_{2F} and y_{2F} are the coordinates of the point F_F in the coordinate system $o_2x_2y_2$. b_7 is the distance between the centre P_7 of the circular arc E_FF_F and the centre o_2 of the female rotor. Obviously, b_7 can be calculated by the following simple equation:

$$b_7 = r_{2tip} - r_7 \tag{173}$$

where r_{2tip} is the radius of the tip circle of the female rotor. According to the cosine law, the following relationship exists:

$$b_7^2 = b_{11}^2 + r_7^2 - 2b_{11}r_7\cos(\frac{\pi}{2} - \beta_{20} + \beta_{12}) \tag{174}$$

Substituting equation 173 into the above equation and developing it, the following formula used to calculate the radius r_7 is obtained:

$$r_7 = \frac{-r_{2tip}^2 + b_{11}^2}{2b_{11}\cos(\frac{\pi}{2} - \beta_{20} + \beta_{12}) - 2r_{2tip}} \tag{175}$$

$\angle E_Fo_2F_F$ is represented by β_{18}, and acording to the sine law the following formula for β_{18} can be obtained:

$$\beta_{18} = \arcsin\frac{r_7\sin(\frac{\pi}{2} - \beta_{20} + \beta_{12})}{b_7} \tag{176}$$

β_{19} represents $\angle E_FP_7F_F$. β_{17} represents the angle between the coordinate axis x_2 and the line connecting o_2 to the centre P_7. β_{11} represents the angle between the coordinate axis x_1 and the line connecting o_1 to the point E_M. β_{19}, β_{17} and β_{11} may be calculated as follows:

$$\beta_{19} = \beta_{18} + (\frac{\pi}{2} - \beta_{20} + \beta_{12}) \tag{177}$$

$$\beta_{17} = \beta_{12} + \beta_{18} \tag{178}$$

$$\beta_{11} = \frac{\beta_{17}}{i} \tag{179}$$

The parametric equations of the circular arc E_FF_F are as follows:

$$\begin{cases} x_2 = b_7\cos\beta_{17} + r_7\cos t \\ y_2 = b_7\sin\beta_{17} + r_7\sin t \end{cases} \quad \beta_{17} - \beta_{19} \le t \le \beta_{17} \tag{180}$$

The concave curve $E_M F_M$ is used to make a smooth connection between the primary flank $F_M G_M$ and the bottom portion $D_M E_M$ of the male rotor, and is generated by the circular arc $E_F F_F$ on the female rotor. Substituting equation 180 into equation 74, the following equations of a set of curves in the male rotor coordinate system $o_1 x_1 y_1$ are obtained:

$$\begin{cases} x_1 = -x_2 \cos k\varphi_1 - y_2 \sin k\varphi_1 + A\cos\varphi_1 \\ \quad = -(b_7 \cos\beta_{17} + r_7 \cos t)\cos k\varphi_1 - (b_7 \sin\beta_{17} + r_7 \sin t)\sin k\varphi_1 \\ \quad\quad +A\cos\varphi_1 \\ \quad = -b_7 \cos(k\varphi_1 - \beta_{17}) - r_7 \cos(k\varphi_1 - t) + A\cos\varphi_1 \\ y_1 = -x_2 \sin k\varphi_1 + y_2 \cos k\varphi_1 + A\sin\varphi_1 \\ \quad = -(b_7 \cos\beta_{17} + r_7 \cos t)\sin k\varphi_1 + (b_7 \sin\beta_{17} + r_7 \sin t)\cos k\varphi_1 \\ \quad\quad +A\sin\varphi_1 \\ \quad = -b_7 \sin(k\varphi_1 - \beta_{17}) - r_7 \sin(k\varphi_1 - t) + A\sin\varphi_1 \end{cases} \tag{181}$$

From the above equations the following partial derivatives can be obtained:

$$\begin{cases} \dfrac{\partial x_1}{\partial t} = -r_7 \sin(k\varphi_1 - t) \\ \dfrac{\partial x_1}{\partial \varphi_1} = b_7 k \sin(k\varphi_1 - \beta_{17}) + r_7 k \sin(k\varphi_1 - t) - A\sin\varphi_1 \\ \dfrac{\partial y_1}{\partial t} = r_7 \cos(k\varphi_1 - t) \\ \dfrac{\partial y_1}{\partial \varphi_1} = -b_7 k \cos(k\varphi_1 - \beta_{17}) - r_7 k \cos(k\varphi_1 - t) + A\cos\varphi_1 \end{cases} \tag{182}$$

Substituting the above partial derivatives into equation 81, that is, the envelop condition equation, and developing it, the following envelop condition equation for the concave curve $E_M F_M$ is obtained:

$$\varphi_1 = \frac{1}{i}\left\{\arcsin\left[\frac{b_7}{r_F}\sin(\beta_{17} - t)\right] + t\right\} \tag{183}$$

The following simultaneous equations of equations 181 and 183 define the mating concave curve $E_M F_M$ on the male rotor lobe generated by the circular arc $E_F F_F$ on the female rotor:

$$\begin{cases} x_1 = -b_7 \cos(k\varphi_1 - \beta_{17}) - r_7 \cos(k\varphi_1 - t) \\ \quad\quad +A\cos\varphi_1 \\ y_1 = -b_7 \sin(k\varphi_1 - \beta_{17}) - r_7 \sin(k\varphi_1 - t) \quad \beta_{17} - \beta_{19} \le t \le \beta_{17} \\ \quad\quad +A\sin\varphi_1 \\ \varphi_1 = \frac{1}{i}\left\{\arcsin\left[\frac{b_7}{r_F}\sin(\beta_{17} - t)\right] + t\right\} \end{cases} \tag{184}$$

The Circular Arcs D_FE_F and D_ME_M

The crest portion D_FE_F of the female rotor land follows a circular arc having its centre at the centre o_2 of the female rotor and radius $r_F + H$, where H is the addendum of the female rotor or the dedendum of the male rotor. Its equations are as follows:

$$\begin{cases} x_2 = (r_F + H)\cos t \\ y_2 = (r_F + H)\sin t \end{cases} \quad i\beta_{11} \le t \le \frac{2\pi}{z_2} - i\beta_5 \tag{185}$$

The bottom portion D_ME_M of the male rotor groove follows a circular arc having its centre at the centre o_1 of the male rotor and radius $r_M - H$. Its equations are as follows:

$$\begin{cases} x_1 = (r_M - H)\cos t \\ y_1 = (r_M - H)\sin t \end{cases} \quad \beta_{11} \le t \le \frac{2\pi}{z_1} - \beta_5 \tag{186}$$

Appendix C

THE FIRST DERIVATIVES OF THE SRM D-PROFILE PARAMETRIC EQUATIONS

The first derivatives of x_1, y_1, x_2 and y_2 of the SRM D-profile with respect to the parameter t are required for the cutter blade calculations of the male and female rotors. The SRM D-profile parameter equations are listed in Appendix B.

The Circular Arc A_MB_M and the Circular Arc A_FB_F

From equation 98, the first derivatives of the circular arc A_MB_M are as follows:

$$\begin{cases} \frac{dx_1}{dt} = -r\sin t \\ \frac{dy_1}{dt} = -r\cos t \end{cases} -\beta_1 \le t \le \beta_2 \tag{187}$$

From equation 99, the first derivatives of the circular arc A_FB_F are as follows:

$$\begin{cases} \frac{dx_2}{dt} = r\sin t \\ \frac{dy_2}{dt} = -r\cos t \end{cases} -\beta_1 \le t \le \beta_2 \tag{188}$$

The Circular Arc B_MC_M and the Convex-Concave Curve B_FC_F

From equation 105, the first derivatives of the circular arc B_MC_M are as follows:

$$\begin{cases} \frac{dx_1}{dt} = -r_2\sin t \\ \frac{dy_1}{dt} = -r_2\cos t \end{cases} \beta_2 \le t \le t_c \tag{189}$$

For any given rotational angle of the male rotor, the first derivatives of the convex-concave curve B_FC_F can be calculated by the following equations, which

are obtained by substituting the above equations into equation 89 and are simultaneous with the envelop condition equation 110:

$$\begin{cases} \dfrac{dx_2}{dt} &= -\dfrac{dx_1}{dt}\cos k\varphi_1 - \dfrac{dy_1}{dt}\sin k\varphi_1 \\ &= r_2 \sin t \cos k\varphi_1 + r_2 \cos t \sin k\varphi_1 \\ &= r_2 \sin(k\varphi_1 + t) \\ \dfrac{dy_2}{dt} &= -\dfrac{dx_1}{dt}\sin k\varphi_1 + \dfrac{dy_1}{dt}\cos k\varphi_1 \qquad \beta_2 \le t \le t_c \\ &= r_2 \sin t \sin k\varphi_1 - r_2 \cos t \cos k\varphi_1 \\ &= -r_2 \cos(k\varphi_1 + t) \\ \varphi_1 &= \arcsin\left[\frac{b_2}{r_M}\sin(t+\beta_3)\right] - t \end{cases} \tag{190}$$

The Circular Arc $C_F D_F$ and the Concave Curve $C_M D_M$

From equation 126, the first derivatives of the circular arc $C_F D_F$ are as follows:

$$\begin{cases} \dfrac{dx_2}{dt} &= -r_5 \sin t \\ \dfrac{dy_2}{dt} &= r_5 \cos t \end{cases} \quad -\beta_{15} \le t \le \beta_{16} - \beta_{15} \tag{191}$$

For any given rotational angle of the male rotor, the first derivatives of the concave curve $C_M D_M$ can be calculated by the following equations, which are obtained by substituting the above equations into equation 88 and are simultaneous with the envelop condition equation 129:

$$\begin{cases} \dfrac{dx_1}{dt} &= -\dfrac{dx_2}{dt}\cos k\varphi_1 - \dfrac{dy_2}{dt}\sin k\varphi_1 \\ &= r_5 \sin t \cos k\varphi_1 - r_5 \cos t \sin k\varphi_1 \\ &= -r_5 \sin(k\varphi_1 - t) \\ \dfrac{dy_1}{dt} &= -\dfrac{dx_2}{dt}\sin k\varphi_1 + \dfrac{dy_2}{dt}\cos k\varphi_1 \qquad -\beta_{15} \le t \le \beta_{16} - \beta_{15} \\ &= r_5 \sin t \sin k\varphi_1 + r_5 \cos t \cos k\varphi_1 \\ &= r_5 \cos(k\varphi_1 - t) \\ \varphi_1 &= \frac{1}{i}\left\{\arcsin\left[-\frac{b_5}{r_F}\sin(t+\beta_{15})\right] + t\right\} \end{cases} \tag{192}$$

The Circular Arc $A_M H_M$ and the Concave Curve $A_F H_F$

From equation 134, the first derivatives of the circular arc $A_M H_M$ are as follows:

$$\begin{cases} \frac{dx_1}{dt} = -r_3 \sin t \\ \frac{dy_1}{dt} = r_3 \cos t \end{cases} \quad \beta_1 \le t \le t_H \tag{193}$$

For any given rotational angle of the male rotor, the first derivatives of the concave curve $A_F H_F$ can be calculated by the following equations, which are obtained by substituting the above equations into equation 89 and are simultaneous with the envelop condition equation 137:

$$\begin{cases} \frac{dx_2}{dt} = -\frac{dx_1}{dt}\cos k\varphi_1 - \frac{dy_1}{dt}\sin k\varphi_1 \\ \quad = r_3 \sin t \cos k\varphi_1 - r_3 \cos t \sin k\varphi_1 \\ \quad = -r_3 \sin(k\varphi_1 - t) \\ \frac{dy_2}{dt} = -\frac{dx_1}{dt}\sin k\varphi_1 + \frac{dy_1}{dt}\cos k\varphi_1 \\ \quad = r_3 \sin t \sin k\varphi_1 + r_3 \cos t \cos k\varphi_1 \\ \quad = r_3 \cos(k\varphi_1 - t) \\ \varphi_1 = \arcsin\left[\frac{b_3}{r_M}\sin(\beta_6 - t)\right] + t \end{cases} \quad \beta_1 \le t \le t_H \tag{194}$$

The Circular Arc $G_F H_F$ and the Convex Curve $G_M H_M$

From equation 146, the first derivatives of the circular arc $G_F H_F$ are as follows:

$$\begin{cases} \frac{dx_2}{dt} = -r_s \sin t \\ \frac{dy_2}{dt} = r_s \cos t \end{cases} \quad -\frac{\pi}{2} + \beta_8 \le t \le t_G \tag{195}$$

For any given rotational angle of the male rotor, the first derivatives of the convex curve $G_M H_M$ can be calculated by the following equations, which are obtained by substituting the above equations into equation 88 and are simultaneous

with the envelop condition equation 149:

$$\begin{cases} \frac{dx_1}{dt} &= -\frac{dx_2}{dt}\cos k\varphi_1 - \frac{dy_2}{dt}\sin k\varphi_1 \\ &= r_s \sin t \cos k\varphi_1 - r_s \cos t \sin k\varphi_1 \\ &= -r_s \sin(k\varphi_1 - t) \\ \frac{dy_1}{dt} &= -\frac{dx_2}{dt}\sin k\varphi_1 + \frac{dy_2}{dt}\cos k\varphi_1 \qquad -\frac{\pi}{2} + \beta_8 \le t \le t_G \\ &= r_s \sin t \sin k\varphi_1 + r_s \cos t \cos k\varphi_1 \\ &= r_s \cos(k\varphi_1 - t) \\ \varphi_1 &= \frac{1}{i}\left\{\arcsin\left[\frac{b_s}{r_F}\sin(\beta_9 + \beta_7 - t)\right] + t\right\} \end{cases} \tag{196}$$

The Circular Arc F_MG_M and the Convex Curve F_FG_F

From equation 162, the first derivatives of the circular arc F_MG_M are as follows:

$$\begin{cases} \frac{dx_1}{dt} &= -r_1 \sin t \\ \frac{dy_1}{dt} &= r_1 \cos t \end{cases} \qquad \frac{\pi}{2} + \beta_{10} \le t \le t_F \tag{197}$$

For any given rotational angle of the male rotor, the first derivatives of the convex curve F_FG_F can be calculated by the following equations, which are obtained by substituting the above equations into equation 89 and are simultaneous with the envelop condition equation 166:

$$\begin{cases} \frac{dx_2}{dt} &= -\frac{dx_1}{dt}\cos k\varphi_1 - \frac{dy_1}{dt}\sin k\varphi_1 \\ &= r_1 \sin t \cos k\varphi_1 - r_1 \cos t \sin k\varphi_1 \\ &= -r_1 \sin(k\varphi_1 - t) \\ \frac{dy_2}{dt} &= -\frac{dx_1}{dt}\sin k\varphi_1 + \frac{dy_1}{dt}\cos k\varphi_1 \qquad \frac{\pi}{2} + \beta_{10} \le t \le t_F \\ &= r_1 \sin t \sin k\varphi_1 + r_1 \cos t \cos k\varphi_1 \\ &= r_1 \cos(k\varphi_1 - t) \\ \varphi_1 &= \arcsin\left[-\frac{b_1}{r_M}\sin(t - \beta_{10})\right] + t \end{cases} \tag{198}$$

The Circular Arc E_FF_F and the Concave Curve E_MF_M

From equation 180, the first derivatives of the circular arc $E_F F_F$ are as follows:

$$\begin{cases} \frac{dx_2}{dt} = -r_7 \sin t \\ \frac{dy_2}{dt} = r_7 \cos t \end{cases} \quad \beta_{17} - \beta_{19} \le t \le \beta_{17} \tag{199}$$

For any given rotational angle of the male rotor, the first derivatives of the convex curve $E_M F_M$ can be calculated by the following equations, which are obtained by substituting the above equations into equation 88 and are simultaneous with the envelop condition equation 183:

$$\begin{cases} \frac{dx_1}{dt} = -\frac{dx_2}{dt}\cos k\varphi_1 - \frac{dy_2}{dt}\sin k\varphi_1 \\ \quad = r_7 \sin t \cos k\varphi_1 - r_7 \cos t \sin k\varphi_1 \\ \quad = -r_7 \sin(k\varphi_1 - t) \\ \frac{dy_1}{dt} = -\frac{dx_2}{dt}\sin k\varphi_1 + \frac{dy_2}{dt}\cos k\varphi_1 \\ \quad = r_7 \sin t \sin k\varphi_1 + r_7 \cos t \cos k\varphi_1 \\ \quad = r_7 \cos(k\varphi_1 - t) \\ \varphi_1 = \frac{1}{i}\left\{\arcsin\left[\frac{b_r}{r_F}\sin(\beta_{17} - t)\right] + t\right\} \end{cases} \quad \beta_{17} - \beta_{19} \le t \le \beta_{17} \tag{200}$$

The Circular Arcs $D_F E_F$ and $D_M E_M$

From equation 185, the first derivatives of the circular arc $D_F E_F$ are as follows:

$$\begin{cases} \frac{dx_2}{dt} = -(r_F + H)\sin t \\ \frac{dy_2}{dt} = (r_F + H)\cos t \end{cases} \quad i\beta_{11} \le t \le \frac{2\pi}{z_2} - i\beta_5 \tag{201}$$

According to equation 186, the first derivatives of the circular arc $D_M E_M$ are as follows:

$$\begin{cases} \frac{dx_1}{dt} = -(r_M - H)\sin t \\ \frac{dy_1}{dt} = (r_M - H)\cos t \end{cases} \quad \beta_{11} \le t \le \frac{2\pi}{z_1} - \beta_5 \tag{202}$$

Appendix D

KEY POINT COORDINATES OF A SRM D-PROFILE

In order to test the profile generation program, the coordinates of the profile generated by the program are compared with the coordinates of a practically used profile. The specifications of the profile are as follows:

- Profile: SRM D-standard.
- The centre distance between the male and female rotors: $100mm$.
- The number of lobes of the male rotor: 4.
- The number of grooves of the female rotor: 6.

The coordinates of the key points (see Appendix B) of the profile calculated by the author are as follows (the values in brackets are the coordinates of the practically used profile):

Male Rotor

Point D_M: $x_1 = 23.947776(23.9478)mm$; $y_1 = -27.246645(-27.2466)mm$.

Point C_M: $x_1 = 27.648228(27.6482)mm$; $y_1 = -26.391914(-26.3919)mm$.

Point B_M: $x_1 = 62.916590(62.9166)mm$; $y_1 = -6.1404820(-6.1405)mm$.

Point A_M: $x_1 = 63.494110(63.4941)mm$; $y_1 = 3.3018820(3.3019)mm$.

Point H_M: $x_1 = 61.497200(61.4972)mm$; $y_1 = 7.4314830(7.4315)mm$.

Point G_M: $x_1 = 38.409040(38.4090)mm$; $y_1 = 18.813450(18.8135)mm$.

Point F_M: $x_1 = 3.7140400(33.7140)mm$; $y_1 = 18.167278(18.1673)mm$.

Point E_M: $x_1 = 30.730742(30.7307)mm$; $y_1 = 19.274263(19.2743)mm$.

Female Rotor

Point D_F: $x_2 = 53.77023(53.7702)mm$; $y_2 = -34.19997(-34.2000)mm$.

Point C_F: $x_2 = 54.01574(54.0157)mm$; $y_2 = -30.352985(-30.3530)mm$.

Point B_F: $x_2 = 37.08341(37.0834)mm$; $y_2 = -6.140482(-6.1405)mm$.

Point A_F: $x_2 = 36.50589(36.5059)mm$; $y_2 = 3.301882(3.3019)mm$.

Point H_F: $x_2 = 53.99694(53.9969)mm$; $y_2 = 17.681078(17.6811)mm$.

Point G_F: $x_2 = 55.59201(55.5920)mm$; $y_2 = 18.12576(18.1258)mm$.

Point F_F: $x_2 = 58.79014(58.7901)mm$; $y_2 = 20.586666(20.5867)mm$.

Point E_F: $x_2 = 59.33264(59.3326)mm$; $y_2 = 23.248912(23.2489)mm$.

The results generated by the profile generation program are identical with the coordinates of the practically used profile.

Appendix E

Thermodynamic Property Equations of the Refrigerants Considered in the Mathematical Model

E.1 Thermodynamic Property Equations of R12 and R22

Martin-Hou equations are used to calculate the thermodynamic properties of R12 and R22 in the mathematical model.

Liquid Density of R12 and R22

$$d_L = A_L + B_L\left(1-\frac{T}{T_c}\right)^{\frac{1}{3}} + C_L\left(1-\frac{T}{T_c}\right)^{\frac{2}{3}} + D_L\left(1-\frac{T}{T_c}\right) + E_L\left(1-\frac{T}{T_c}\right)^{\frac{4}{3}} + F_L\left(1-\frac{T}{T_c}\right)^{\frac{1}{2}} + G_L\left(1-\frac{T}{T_c}\right)^{2} \tag{203}$$

where,

d_L Liquid density of refrigerants, $[lb/ft^3]$.

T Liquid temperature, $[F + 459.67$ (459.69, 459.6, 459.7 in some cases)].

T_c Critical temperature of refrigerants, $[R]$.

The constants in the liquid density equation for R12 and R22 are listed in Table E.1.

Table E.1 Constants for Liquid Density Equation

Refrigerant	A_L	B_L	C_L	D_L	E_L
12	34.84	53.341187	0	18.69137	0
22	32.76	54.634409	36.74892	-22.2925657	20.4732886

F_L	G_L	T_c	Add to F
21.98396	-3.150994	693.3	459.7
0	0	664.50	459.69

Vapour Pressure of R12 and R22

$$\log_{10} P = A + \frac{B}{T} + C \log_{10} T + DT + E\left(\frac{F-T}{T}\right)\log_{10}(F-T) \qquad (204)$$

where,

P Vapour pressure, $[lbf/in^2]$.

T Evaporating or condensing temperature, $[F + 459.67$ (459.69, 459.6, 459.7 in some cases)].

The constants in the vapour pressure equation for R12 and R22 are listed in Table E.2.

Table E.2 Constants for Vapour Pressure Equation

Refrigerant	A	B	C	D
12	39.88381727	-3436.632228	-12.47152228	4.73044244×10^{-3}
22	29.35754453	-3845.193152	-7.86103122	2.1909390×10^{-3}

E	F	Add to F
0	459.7	0
686.1	459.69	0.445746703

State Equation of R12 and R22

$$P = \frac{RT}{V-b} + \frac{A_2 + B_2T + C_2e^{-KT/T_c}}{(V-b)^2} + \frac{A_3 + B_3T + C_3e^{-KT/T_c}}{(V-b)^3}$$

$$+\frac{A_4 + B_4T + C_4e^{-KT/T_c}}{(V-b)^4} + \frac{A_5 + B_5T + C_5e^{-KT/T_c}}{(V-b)^5} \qquad (205)$$

$$+\frac{A_6 + B_6T + C_6e^{-KT/T_c}}{e^{aV}(1 + C'e^{aV})}$$

where,

P Pressure, $[lbf/in^2]$.

V Specific volume, $[ft^3/lb]$.

T Temperature, $[F + 459.67$ (459.69, 459.6, 459.7 in some cases)].

The constants in the state equation for R12 and R22 are listed in Table E.3.

Table E.3 Constants for Equation of State

Refrigerant	R	b	A_2	B_2
12	0.088734	0.0065093886	-3.40972713	1.59434848×10^{-3}
22	0.124098	0.002	-4.353547	2.407252×10^{-3}

C_2	A_3	B_3	C_3	A_4
-56.7627671	0.06023945	-1.879618×10^{-5}	1.31139908	-5.4873701×10^{-4}
-44.066868	-0.017464	7.62789×10^{-5}	1.483763	2.310142×10^{-3}

B_4	C_4	A_5	B_5	C_5
0	0	0	3.468834×10^{-9}	-2.54390678×10^{-5}
-3.605723×10^{-6}	0	-3.724044×10^{-5}	5.355465×10^{-8}	-1.845051×10^{-4}

A_6	B_6	C_6	K	a	C'	T_c	Add to F
0	0	0	5.475	0	0	693.3	459.7
1.363387×10^{10}	-1.672612×10^{5}	0	4.2	548.2	0	664.50	459.69

Latent Heat of Vaporization of R12 and R22

$$\Delta H_{lat} = JT(V_g - V_f)\left\{P\ln 10\left[\frac{-B}{T^2} + \frac{C}{T\ln 10} + D - E\left(\frac{\log_{10} e}{T} + \frac{F\log_{10}(F-T)}{T^2}\right)\right]\right\} \quad (206)$$

where,

ΔH_{lat} Latent heat of vaporization, $[Btu/lb]$.

$J = 0.185053$

V_g Specific volume of saturated vapour, $[ft^3/lb]$.

V_f Specific volume of saturated liquid, $[ft^3/lb]$.

T Evaporating or condensing temperature, $[R]$.

The constants in the latent heat equation of vaporization for R12 and R22 are listed in Table E.2.

Vapour Enthalpy of R12 and R22

$$\begin{aligned} H = {} & a'T + \frac{b'T^2}{2} + \frac{cT^3}{3} + \frac{dT^4}{4} - \frac{f}{T} + JPV + J\left\{\frac{A_2}{V-b}\right. \\ & + \frac{A_3}{2(V-b)^2} + \frac{A_4}{3(V-b)^3} + \frac{A_5}{4(V-b)^4} \\ & \left. + \frac{A_6}{a}\left[\frac{1}{e^{aV}} - C'\ln 10 \log_{10}\left(1 + \frac{1}{C'e^{aV}}\right)\right]\right\} \\ & + Je^{-KT/T_c}\left(1 + \frac{KT}{T_c}\right)\left[\frac{C_2}{(V-b)} + \frac{C_3}{2(V-b)^2} + \frac{C_4}{3(V-b)^3}\right. \\ & \left. + \frac{C_5}{4(V-b)^4} + \frac{C_6}{ae^{aV}} - \frac{C_6C'\ln 10}{a}\log_{10}\left(1 + \frac{1}{C'e^{aV}}\right)\right] + X \end{aligned} \tag{207}$$

where,

H Enthalpy of vapour, $[Btu/lb]$.

T Temperature of vapour, $[R]$.

P Pressure of vapour, $[lbf/in^2]$.

V Specific volume of vapour, $[ft^3/lb]$.

$J = 0.185053$

$X = \Delta H$ (latent heat at reference temperature) $-H$ (vapour enthalpy at reference temperature). For R12 and R22 the enthalpy of the liquid is assumed to be zero at $-40F$, and constant X is listed in Table E.4.

Constants a, b', c, d and f in the vapour enthalpy equation for R12 and R22 are listed in Table E.5, and the other constants in the equation are the constants from the equation of state, shown as in Table E.3.

Table E.4 Constant X for the Enthalpy Equation

Refrigerant	R12	R22
X	39.556551	62.4009

Table E.5 Constants for the Enthalpy Equation

Refrigerant	a'	b'	c	d	f
12	8.0945 $\times 10^{-3}$	3.32662 $\times 10^{-4}$	-2.413896 $\times 10^{-7}$	6.72363 $\times 10^{-11}$	0
22	0.02812836	2.255408 $\times 10^{-4}$	-6.509607 $\times 10^{-8}$	0	257.341

Vapour Entropy of R12 and R22

$$
\begin{aligned}
S \;=\; & a' \ln 10 \log_{10} T + b'T + \frac{cT^2}{2} + \frac{dT^3}{3} - \frac{f}{2T^2} + JR \ln 10 \log_{10}(V-b) \\
& - J\left\{ \frac{B_2}{V-b} + \frac{B_3}{2(V-b)^2} + \frac{B_4}{3(V-b)^3} + \frac{B_5}{4(V-b)^4} \right. \\
& \left. + \frac{B_6}{a}\left[\frac{1}{e^{aV}} - C' \ln 10 \log_{10}\left(1 + \frac{1}{C'e^{aV}}\right)\right]\right\} \\
& + \frac{JKe^{-KT/T_c}}{T_c}\left[\frac{C_2}{(V-b)} + \frac{C_3}{2(V-b)^2} + \frac{C_4}{3(V-b)^3} + \frac{C_5}{4(V-b)^4} \right. \\
& \left. + \frac{C_6}{ae^{aV}} - \frac{C_6 C' \ln 10}{a} \log_{10}\left(1 + \frac{1}{C'e^{aV}}\right)\right] + Y
\end{aligned}
\tag{208}
$$

where,

S Entropy of vapour, $[Btu/(lb \cdot R)]$.

T Temperature of vapour, $[R]$.

V Specific volume of vapour, $[ft^3/lb]$.

$J = 0.185053$

$Y = \Delta H$ (latent heat at reference temperature) $/T$ (reference temperature) $-S$ (vapour entropy at reference temperature). For R12 and R22 the entropy of the liquid is assumed to be zero at $-40F$, and constant Y is listed in Table E.6.

Constants a, b', c, d and f in the vapour entropy equation for R12 and R22 are listed in Table E.5, and the other constants in the equation are the constants from the equation of state, shown as in Table E.3.

Table E.6 Constant Y for the Entropy Equation

Refrigerant	R12	R22
Y	-0.016537936	-0.0453335

E.2 Thermodynamic Property Equations of R134a

Liquid Density of R134a

$$d_L = A + B\left(1 - \frac{T}{T_c}\right)^{1/3} + C\left(1 - \frac{T}{T_c}\right)^{2/3} + D\left(1 - \frac{T}{T_c}\right) + E\left(1 - \frac{T}{T_c}\right)^{4/3} \tag{209}$$

where,

d_L Liquid density of refrigerants, $[lb/ft^3]$.

T Liquid temperature, $[(F + 459.67)R]$.

T_c Critical temperature, $[672.64R]$.

$A = 30.9393$

$B = 20.55309362$

$C = 283.33564937$

$D = -526.61770852$

$E = 343.08761757$

Vapour Pressure of R134a

$$\log_{10} P = A + \frac{B}{T} + C \log_{10} T + DT \tag{210}$$

where,

P Vapour pressure, $[lbf/in^2]$.

T Evaporating or condensing temperature, $[(F + 459.67)R]$.

$A = 8.9771785$

$B = -2365.917278$

$C = -0.90741718$

$D = -0.0002026107$

State Equation of R134a

$$P = \frac{RT}{V-\beta} - \frac{\alpha}{V(V+\beta)T^{0.5}} \tag{211}$$

where,

P Pressure, $[lbf/in^2]$.

V Specific volume, $[ft^3/lb]$.

T Temperature, $[R]$.

$R = 0.105178$

$\alpha = 97.03357241$

$\beta = 0.01065681052$

Latent Heat of Vaporization of R134a

$$\Delta H_{lat} = JT(V_g - V_f)P \ln 10 \left(\frac{-B}{T^2} + \frac{C}{T \ln 10} + D\right) \tag{212}$$

where,

ΔH_{lat} Latent heat of vaporization, $[Btu/lb]$.

$J = 0.185053$

V_g Specific volume of saturated vapour, $[ft^3/lb]$.

V_f Specific volume of saturated liquid, $[ft^3/lb]$.

T Evaporating or condensing temperature, $[R]$.

$B = -2365.917278$

$C = -0.90741718$

$D = -0.0002026107$

Vapour Enthalpy of R134a

$$H = aT + \frac{bT^2}{2} + \frac{cT^3}{3} + \frac{dT^4}{4} - \frac{f}{T} + JPV - \frac{3J\alpha}{2\beta T^{0.5}} \ln \frac{(V+\beta)}{V} + X \tag{213}$$

where,

H Enthalpy of vapour, $[Btu/lb]$.

T Temperature of vapour, $[R]$.

P Pressure of vapour, $[lbf/in^2]$.

V Specific volume of vapour, $[ft^3/lb]$.

$J = 0.185053$

$X = 60.21174$

$\alpha = 97.03357241$

$\beta = 0.01065681052$

$a = -0.016373$

$b = 4.3403 \times 10^{-4}$

$c = -1.76325 \times 10^{-7}$

$d = 2.53592 \times 10^{-11}$

Vapour Entropy of R134a

$$S = a\ln T + bT + \frac{cT^2}{2} + \frac{dT^3}{3} - + JR\ln(V-\beta) - \frac{J\alpha}{2\beta T^{3/2}} \ln\frac{(V+\beta)}{V} + Y \tag{214}$$

where,

S Entropy of vapour, $[Btu/(lb \cdot R)]$.

T Temperature of vapour, $[R]$.

V Specific volume of vapour, $[ft^3/lb]$.

$Y = 0.12455$

$R = 0.105178$

Other constants See the constants for enthalpy of the vapour.

E.3 Thermodynamic Property Equations of R717 (ammonia)

State Equation of Vapour and Liquid of Ammonia

$$P = 0.1RT\rho\left[1 + \sum_{i=1}^{9}\sum_{j=1}^{6} iA_{ij}\rho^{i}(\tau - \tau_c)^{j-1}\right] \tag{215}$$

where,

P Pressure of vapour or liquid, $[kgf/cm^2]$.

ρ Density of vapour or liquid, $[g/cm^3]$.

T Temperature of vapour or liquid, $[K]$.

$\tau = \frac{500}{T}$

$\tau_c = \frac{500}{405.4} = 1.2333498$

$R = 49.7835\ kgf \cdot m/kg \cdot K.$

The constants in the state equation of vapour and liquid for ammonia are listed in Table E.7.

Vapour Pressure of Ammonia

$$\ln\left(\frac{P}{P_c}\right) = \frac{T_c}{T}\left[-7.296510\left(1 - \frac{T}{T_c}\right) + 1.618053\left(1 - \frac{T}{T_c}\right)^{3/2} - 1.956546\left(1 - \frac{T}{T_c}\right)^{5/2} - 2.114118\left(1 - \frac{T}{T_c}\right)^{5}\right] \tag{216}$$

where,

P Vapour pressure, $[kgf/cm^2]$.

T Evaporating or condensing temperature, $[K]$.

$P_c = 115.567\ kgf/cm^2.$

$T_c = 405.4\ K.$

Table E.7 Constants for Equation of State

i	j	A_{ij}	i	j	A_{ij}
1	1	-6.453 022 304 053	5	4	21 348.946 614 397 509
1	2	-13.719 926 770 503	5	5	0
1	3	-8.100 620 315 713	5	6	0
1	4	-4.880 096 421 085			
1	5	-12.028 775 626 818	6	1	247.341 745 995 422
1	6	6.806 345 929 616	6	2	299.983 915 547 501
			6	3	4 509.080 578 789 798
2	1	8.080 094 367 688	6	4	-37 980.849 881 791 548
2	2	14.356 920 005 615	6	5	0
2	3	-45.052 976 699 428	6	6	0
2	4	-166.188 998 570 498			
2	5	37.908 950 229 818	7	1	-306.557 885 430 971
2	6	-40.730 208 333 732	7	2	24.116 551 098 552
			7	3	-9 323.356 799 989 199
3	1	1.032 994 880 724	7	4	42 724.098 530 588 371
3	2	55.843 955 809 332	7	5	0
3	3	492.016 650 817 652	7	6	0
3	4	1 737.835 999 472 605			
3	5	-30.874 915 263 766	8	1	161.791 003 337 459
3	6	71.483 530 416 272	8	2	-507.478 070 464 266
			8	3	8 139.470 397 409 345
4	1	-8.948 264 632 008	8	4	-27 458.710 626 558 130
4	2	-169.777 744 139 056	8	5	0
4	3	-1 236.532 371 671 939	8	6	0
4	4	-7 812.161 168 316 763			
4	5	1.779 548 269 140	9	1	-27.821 688 793 683
4	6	-38.974 610 958 503	9	2	298.812 917 313 344
			9	3	-2 772.597 352 058 112

5	1	-66.922 858 820 152	9	4	7 668.928 677 924 520
5	2	-1.753 943 775 320	9	5	0
5	3	208.553 371 335 492	9	6	0

Latent Heat of Vaporization of Ammonia

$$\Delta H_{lat} = -\frac{P}{42.693}\left(\frac{1}{\rho''}-\frac{1}{\rho'}\right)\left[\ln\left(\frac{P}{P_c}\right) - 7.296510 + 2.427080\left(1-\frac{T}{T_c}\right)^{1/2} - 4.891365\left(1-\frac{T}{T_c}\right)^{3/2} - 10.57059\left(1-\frac{T}{T_c}\right)^{4}\right] \quad (217)$$

where,

ΔH_{lat} Latent heat of vaporization, $[kcal/kg]$.

P Vapour presure, $[kgf/cm^2]$.

T Evaporating or condensing temperature, $[K]$.

ρ'' Density of saturated vapour, $[g/cm^3]$.

ρ' Density of saturated liquid, $[g/cm^3]$.

$P_c = 115.567\ kgf/cm^2$.

$T_c = 405.4\ K$.

Vapour Enthalpy of Ammonia

$$H = \frac{RT}{426.93}\left\{\sum_{i=1}^{9}\sum_{j=1}^{6}[(i+j-1)\tau - i\tau_c]\,A_{ij}\rho^i(\tau-\tau_c)^{j-2} - a_1 - \sum_{k=2}^{11}(k-3)a_kT^{k-3}\right\} + X \quad (218)$$

where,

H Enthalpy of vapour, $[kcal/kg]$.

T Temperature of vapour, $[K]$.

ρ Density of vapour, $[g/cm^3]$.

$\tau = \frac{500}{T}$

$\tau_c = \frac{500}{405.4} = 1.2333498$

$R = 49.7835\ kgf \cdot m/kg \cdot K.$

$X = 282.1824191\ kcal/kg.$

Constant A_{ij} in the enthalpy equation of vapour for ammonia is listed in Table E.7, and constant a_k is listed in Table E.8.

Table E.8 Constants for Enthalpy Equation of Vapour

k	1	2	3	4
a_k	-3.872 727	0.644 637 24	3.223 875 9	-0.002 137 692 5

5	6	7
$0.868\ 908\ 33 \times 10^{-5}$	$-0.240\ 851\ 49 \times 10^{-7}$	$0.368\ 931\ 75 \times 10^{-10}$

8	9	10
$-0.350\ 346\ 64 \times 10^{-13}$	$0.205\ 630\ 3 \times 10^{-16}$	$-0.685\ 342\ 0 \times 10^{-20}$

11
$0.993\ 924\ 3 \times 10^{-24}$

Vapour Entropy of Ammonia

$$S = -\frac{R}{426.93}\left\{\ln\rho + \sum_{i=1}^{9}\sum_{j=1}^{6}[(2-j)\tau - \tau_c]\,A_{ij}\rho^i(\tau-\tau_c)^{j-2}\right. \tag{219}$$

$$\left. + a_1(\ln T + 1) + \sum_{k=2}^{11}(k-2)a_k a_k T^{k-3} + \ln(4.8180T)\right\} + Y$$

where,

S Entropy of vapour, $[kcal/kg \cdot K]$.

T Temperature of vapour, $[K]$.

ρ Density of vapour, $[g/cm^3]$.

$\tau = \frac{500}{T}$

$\tau_c = \frac{500}{405.4} = 1.2333498$

$R = 49.7835\ kgf \cdot m/kg \cdot K.$

$Y = -0.36055466\ kcal/kg \cdot K.$

Constants A_{ij} and a_k in the entropy equation of vapour for ammonia are listed in Table E.7 and Table E.8 respectively.

Appendix F

System Diagram of Measurement Rig

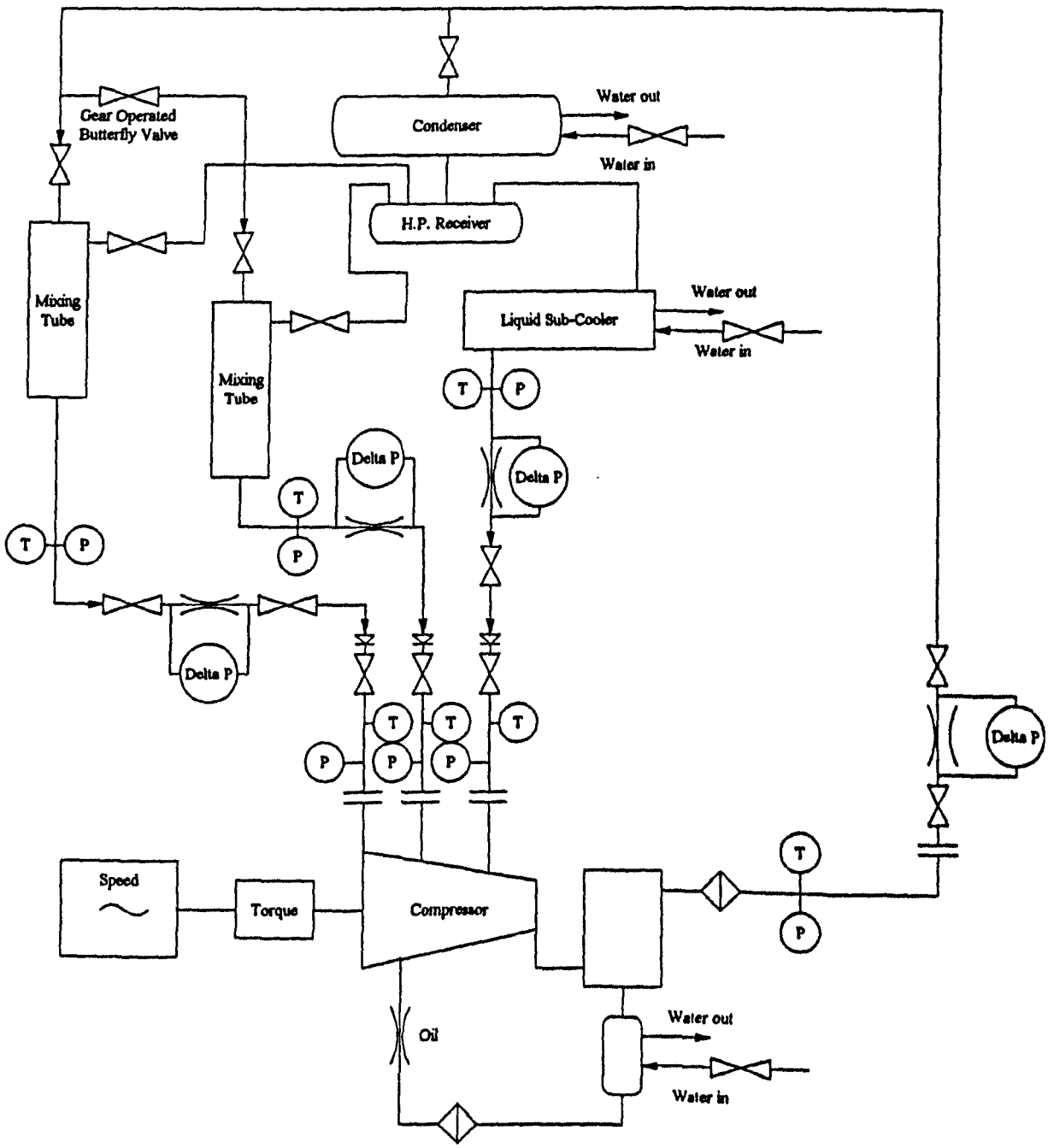

Appendix G

CALCULATION OF CUTTER GEOMETRY

G.1 The Zero Clearance Cutter Blades

In order to calculate the cutter blade of a screw rotor, the coordinate systems shown in Fig. G.1 should be established. The coordinate system $OXYZ$ is a rotor coordinate system, with its axis Z coinciding with the axis of the rotor, and the coordinate system $O_cX_cY_cZ_c$ is a cutter coordinate system, with its axis Z_c coinciding with the axis of rotation of the cutter.

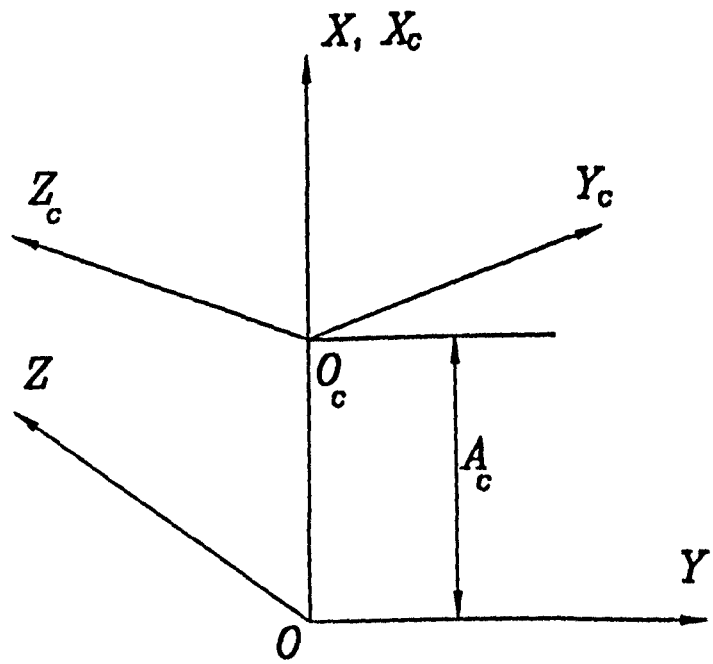

Fig. G.1 Coordinate systems of a rotor and its cutter

The parametric equations of a zero clearance lobe profile are as follows:

$$\begin{cases} X_p = X_p(t) \\ Y_p = Y_p(t) \end{cases} \tag{220}$$

where,

X_p, Y_p Coordinates of the rotor profile, $[m]$.

t Profile parameter of the helical surface (defined in [6]), $[rad$ or $m]$.

and its screw surface may similarly be described by the following equations:

$$\begin{cases} X = X_p(t)\cos\tau \mp Y_p(t)\sin\tau \\ Y = \pm X_p(t)\sin\tau + Y_p(t)\cos\tau \\ Z = p\tau \end{cases} \tag{221}$$

where,

X, Y, Z Coordinates of the helical surface, $[m]$.

τ Helical line parameter of the helical surface, $[rad]$.

$\pm$ **or** $\mp$ Upper and under symbols are used for the right-handed and the left-handed rotors respectively in this chapter.

T Screw pitch of the rotor, $[m]$.

p Screw pitch per radian of the rotor, $p = \frac{T}{2\pi}$, $[m/rad]$.

The equations to transform the coordinates and corresponding unit vectors from coordinates $OXYZ$ to coordinates $O_cX_cY_cZ_c$ are as follows respectively:

$$\begin{cases} X_c = X - A_c \\ Y_c = Y\cos\psi \pm Z\sin\psi \\ Z_c = \mp Y\sin\psi + Z\cos\psi \end{cases} \tag{222}$$

where,

X_c, Y_c, Z_c Coordinates of the cutter blade, $[m]$.

A_c Distance between the centres of the rotor and its cutter, $[m]$.

ψ Angle between the rotor and cutter axes, $[rad]$.

$$\begin{cases} \mathrm{i}_c = \mathrm{i} \\ \mathrm{j}_c = \cos\psi\cdot\mathrm{j} \pm \sin\psi\cdot\mathrm{k} \\ \mathrm{k}_c = \mp\sin\psi\cdot\mathrm{j} + \cos\psi\cdot\mathrm{k} \end{cases} \tag{223}$$

where,

$\mathbf{i}, \mathbf{j}, \mathbf{k}$ Unit vectors in the directions of the coordinates X, Y and Z respectively.

$\mathbf{i}_c, \mathbf{j}_c, \mathbf{k}_c$ Unit vectors in the directions of the coordinates X_c, Y_c and Z_c respectively.

In the cutter coordinate system $O_cX_cY_cZ_c$ the cutter rotary surface vectorial equation is as follows:

$$\rho = X_c \cdot \mathbf{i}_c + Y_c \cdot \mathbf{j}_c + Z_c \cdot \mathbf{k}_c \tag{224}$$

where ρ is a vector from O_c to any point on the cutter rotary surface, and X_c, Y_c and Z_c in the above equation can be represented as follows:

$$\begin{cases} X_c = R_c \cos\alpha \\ Y_c = R_c \sin\alpha \\ Z_c = \mp Y \sin\psi + Z \cos\psi \end{cases} \tag{225}$$

where,

α Rotational parameter of the cutter blade, $[rad]$.

R_c Rotary radius of any point on the cutter blade, $[m]$.

The tangent vectorial equation at any point on a circle of the cutter rotary surface is as follows:

$$\frac{\partial \rho}{\partial \alpha} = \frac{\partial X_c}{\partial \alpha} \cdot \mathbf{i}_c + \frac{\partial Y_c}{\partial \alpha} \cdot \mathbf{j}_c + \frac{\partial Z_c}{\partial \alpha} \cdot \mathbf{k}_c \tag{226}$$

Substituting equation 225 into the above equation and developing it, the following equation can be obtained:

$$\frac{\partial \rho}{\partial \alpha} = -Y_c \cdot \mathbf{i}_c + X_c \cdot \mathbf{j}_c \tag{227}$$

Substituting equations 222 and 223 into the above equation and developing it, the following resultant tangent vectorial equation represented in the coordinate system $OXYZ$ is obtained:

$$\frac{\partial \rho}{\partial \alpha} = -(Y\cos\psi \pm Z\sin\psi) \cdot \mathbf{i} + (X - A_c)\cos\psi \cdot \mathbf{j} \pm (X - A_c)\sin\psi \cdot \mathbf{k} \tag{228}$$

From following rotor helical surface vectorial equation:

$$\mathbf{r} = X \cdot \mathbf{i} + Y \cdot \mathbf{j} + Z \cdot \mathbf{k} \tag{229}$$

where $\mathbf{r}$ is a vector from O to any point on the rotor helical surface, the following two tangent vectors can be obtained:

$$\frac{\partial \mathbf{r}}{\partial \tau} = \frac{\partial X}{\partial \tau} \cdot \mathbf{i} + \frac{\partial Y}{\partial \tau} \cdot \mathbf{j} + \frac{\partial Z}{\partial \tau} \cdot \mathbf{k} \tag{230}$$

$$\frac{\partial \mathbf{r}}{\partial t} = \frac{\partial X}{\partial t} \cdot \mathbf{i} + \frac{\partial Y}{\partial t} \cdot \mathbf{j} + \frac{\partial Z}{\partial t} \cdot \mathbf{k} \tag{231}$$

Substituting equation 221 into the above two equations and developing them, the following two corresponding equations are obtained:

$$\frac{\partial \mathbf{r}}{\partial \tau} = \mp Y \cdot \mathbf{i} \pm X \cdot \mathbf{j} + p \cdot \mathbf{k} \tag{232}$$

$$\frac{\partial \mathbf{r}}{\partial t} = \frac{\partial X}{\partial t} \cdot \mathbf{i} + \frac{\partial Y}{\partial t} \cdot \mathbf{j} \tag{233}$$

At any contact point between a rotor and its cutter a common tangent plane must exist, that is, at any contact point the profile tangent vector $\frac{\partial \mathbf{r}}{\partial t}$, the helical line tangent vector $\frac{\partial \mathbf{r}}{\partial \tau}$ and the cutter circle tangent vector $\frac{\partial \rho}{\partial \alpha}$ should be in the same plane, that is, their vectorial mixture product should equal zero:

$$\frac{\partial \mathbf{r}}{\partial t} \times \frac{\partial \mathbf{r}}{\partial \tau} \cdot \frac{\partial \rho}{\partial \alpha} = 0 \tag{234}$$

The above equation is the contact condition equation between a helical rotor and its cutter. It can be represented as follows:

$$\begin{vmatrix} \mp Y & \pm X & p \\ \dfrac{\partial X}{\partial t} & \dfrac{\partial Y}{\partial t} & 0 \\ -(Y\cos\psi \pm Z\sin\psi) & (X - A_c)\cos\psi & \pm(X - A_c)\sin\psi \end{vmatrix} = 0 \tag{235}$$

Developing the above equation it may be restated as follows:

$$\left(X\frac{\partial X}{\partial t} + Y\frac{\partial Y}{\partial t}\right)(A_c + p\cot\psi - X) \pm p\left(p\tau\frac{\partial Y}{\partial t} \mp A_c\cot\psi\frac{\partial X}{\partial t}\right) = 0 \tag{236}$$

where partial derivatives $\frac{\partial X}{\partial t}$ and $\frac{\partial Y}{\partial t}$ are calculated by the following equations:

$$\begin{cases} \dfrac{\partial X}{\partial t} = \dfrac{dX_p}{dt}\cos\tau \mp \dfrac{dY_p}{dt}\sin\tau \\ \dfrac{\partial Y}{\partial t} = \pm\dfrac{dX_p}{dt}\sin\tau + \dfrac{dY_p}{dt}\cos\tau \end{cases} \tag{237}$$

For any given parameter t of a profile, a corresponding τ is calculated from equation 236. On substituting t and τ into equation 221, coordinates X, Y

and Z of a contact point between the helical surface and its cutter are obtained. These coordinates on the helical surface are transformed to the coordinate system $O_cX_cY_cZ_c$ to yield the corresponding coordinates of the same contact point on the cutter rotary surface. Changing the parameter t results in a series of contact points. The contact line between the rotor and its cutter is formed by all the contact points, from which the cutter blade is defined by the following equations:

$$\begin{cases} R_c &= \sqrt{X_c^2 + Y_c^2} \\ Z_c &= \mp Y \sin\psi + Z\cos\psi \end{cases} \tag{238}$$

It is worth mentioning that the same theory with equation 238 removed can be used to calculate the shape of a hob as the shape of a hob is the enveloped surface of a helical surface which is defined by equations 222 and 236.

G.2 The Equidistant Lobe Profile Method

The cutter calculation method described above is used to calculate a theoretical cutter blade because it is determined for rotors having zero clearance. If the clearance is obtained by the equidistant profile method, the coordinates of the real profile should be calculated by the following equations:

$$\begin{cases} X_{p.equi} &= X_p - \delta \dfrac{\dfrac{dY_p}{dt}}{\sqrt{\left(\dfrac{dX_p}{dt}\right)^2 + \left(\dfrac{dY_p}{dt}\right)^2}} \\ Y_{p.equi} &= Y_p + \delta \dfrac{\dfrac{dX_p}{dt}}{\sqrt{\left(\dfrac{dX_p}{dt}\right)^2 + \left(\dfrac{dY_p}{dt}\right)^2}} \end{cases} \tag{239}$$

where,

δ Clearance, ie gap between rotors normal to the rotor end profiles or the helical surface in this chapter, $[m]$.

equi Equidistant profile or equidistant helical surface in this chapter.

When the above equations are used to calculate the coordinates of the real profile, it should be noted that the normal vector of the zero clearance lobe profile is always directed out of the screw surface of the rotors. In equations 221 to 238

coordinates $X_{p.equi}$ and $Y_{p.equi}$ are used in place of coordinates X_p and Y_p so that a real cutter blade capable of cutting practical rotors with a known clearance results.

G.3 The Equidistant Helical Surface Method

The inter-rotor clearance is obtained in this case by modifying the cutter blade, that is, the real cutter blade is the equidistant blade of the zero clearance blade.

As **N** is the normal vector of the cutter rotary surface, it has the same direction as the normal vector of the rotor helical surface at any contact point between the rotor and its cutter, so that it can be calculated by the following equation:

$$\begin{aligned}\mathbf{N} &= \frac{\partial \mathbf{r}}{\partial \tau} \times \frac{\partial \mathbf{r}}{\partial t} \\ &= \begin{vmatrix} \mathbf{i} & \mathbf{j} & \mathbf{k} \\ \mp Y & \pm X & p \\ \frac{\partial X}{\partial t} & \frac{\partial Y}{\partial t} & 0 \end{vmatrix} \\ &= -p\frac{\partial Y}{\partial t}\mathbf{i} + p\frac{\partial X}{\partial t}\mathbf{j} \mp \left(X\frac{\partial X}{\partial t} + Y\frac{\partial Y}{\partial t}\right)\mathbf{k}\end{aligned} \tag{240}$$

where,

N Normal vector of a cutter rotary surface.

ε Angle between the vector **N** and the rotational axis of the cutter, [*rad*].

From equations 223 and the above equation, the angle ε can be calculated by the following equation:

$$\begin{aligned}\varepsilon &= \arccos\frac{\mathbf{k}_c \cdot \mathbf{N}}{|\mathbf{N}|} \\ &= \arccos\frac{\mp p\frac{\partial X}{\partial t}\sin\psi \mp \left(X\frac{\partial X}{\partial t} + Y\frac{\partial Y}{\partial t}\right)\cos\psi}{\sqrt{p^2\left[\left(\frac{\partial X}{\partial t}\right)^2 + \left(\frac{\partial Y}{\partial t}\right)^2\right] + \left(X\frac{\partial X}{\partial t} + Y\frac{\partial Y}{\partial t}\right)^2}}\end{aligned} \tag{241}$$

The real cutter blade is calculated using the following equations:

$$\begin{cases} R_{c.equi} = R_c + \delta\cos\varepsilon \\ \quad = R_c + \delta\dfrac{\mp p\frac{\partial X}{\partial t}\sin\psi \mp \left(X\frac{\partial X}{\partial t} + Y\frac{\partial Y}{\partial t}\right)\cos\psi}{\sqrt{p^2\left[\left(\frac{\partial X}{\partial t}\right)^2 + \left(\frac{\partial Y}{\partial t}\right)^2\right] + \left(X\frac{\partial X}{\partial t} + Y\frac{\partial Y}{\partial t}\right)^2}} \\ Z_{c.equi} = Z_c + \delta\sin\varepsilon \\ \quad = Z_c + \delta\sqrt{1-\cos^2\varepsilon} \\ \quad = Z_c + \delta\sqrt{1 - \dfrac{\left[p\frac{\partial X}{\partial t}\sin\psi + \left(X\frac{\partial X}{\partial t} + Y\frac{\partial Y}{\partial t}\right)\cos\psi\right]^2}{p^2\left[\left(\frac{\partial X}{\partial t}\right)^2 + \left(\frac{\partial Y}{\partial t}\right)^2\right] + \left(X\frac{\partial X}{\partial t} + Y\frac{\partial Y}{\partial t}\right)^2}} \end{cases} \tag{242}$$

A zero clearance rotor and its cutter have contact points, all of which form the contact line and define the rotor helical surface and the cutter surface of revolution. At any contact point a zero clearance rotor and its cutter have a common tangent and therefore a common normal line. The real cutter blade defined by equation 228 is the equidistant blade of the zero clearance blade defined by equation 226 and is created by stepping out the same distance along the common normal lines of all the contact points. The new contact line, which is the equidistant contact line of the original zero clearance contact line, defines both the real cutter blade and the real helical surface, which is the equidistant helical surface of the zero clearance surface.

Noticing that equation 240 also describes the normal vector of the rotor helical surface, it can be used to describe the normal vector of the rotor helical surface on the end profile, where τ is equal to zero, so that according to equation 221 on the end profile the following equations exist:

$$\begin{cases} \dfrac{\partial X}{dt} = \dfrac{dX_p}{dt} \\ \dfrac{\partial Y}{dt} = \dfrac{dY_p}{dt} \end{cases} \tag{243}$$

Substituting the above equation into equation 240, the normal vector of the rotor helical surface on the end profile can be represented as follows:

$$\mathbf{N} = -p\frac{dY_p}{dt}\mathbf{i} + p\frac{dX_p}{dt}\mathbf{j} \mp \left(X_p\frac{dX_p}{dt} + Y_p\frac{dY_p}{dt}\right)\mathbf{k} \tag{244}$$

The zero clearance lobe profile has a real profile which results from the equidistant helical surface method of clearance determination. The coordinates of the real profile are calculated by the following equations:

$$\begin{cases} X_{equi} = X_p - \delta \dfrac{-p\dfrac{dY_p}{dt}}{\sqrt{p^2\left(\dfrac{dX_p}{dt}\right)^2 + p^2\left(\dfrac{dY_p}{dt}\right)^2 + \left(X_p\dfrac{dX_p}{dt} + Y_p\dfrac{dY_p}{dt}\right)^2}} \\ Y_{equi} = Y_p - \delta \dfrac{p\dfrac{dX_p}{dt}}{\sqrt{p^2\left(\dfrac{dX_p}{dt}\right)^2 + p^2\left(\dfrac{dY_p}{dt}\right)^2 + \left(X_p\dfrac{dX_p}{dt} + Y_p\dfrac{dY_p}{dt}\right)^2}} \\ Z_{equi} = -\delta \dfrac{\mp X_p\dfrac{dX_p}{dt} \mp Y_p\dfrac{dY_p}{dt}}{\sqrt{p^2\left(\dfrac{dX_p}{dt}\right)^2 + p^2\left(\dfrac{dY_p}{dt}\right)^2 + \left(X_p\dfrac{dX_p}{dt} + Y_p\dfrac{dY_p}{dt}\right)^2}} \end{cases} \tag{245}$$

When the above equations are used to calculate the coordinates it should be noted that the normal vector of the helical surface is directed out of the rotor surface. Substituting the coordinates yielded by equation 245 into equation 221 the following equations which may be used to calculate the coordinates of the real profile are obtained:

$$\begin{cases} X_p = X_{equi}\cos\tau \pm Y_{equi}\sin\tau \\ Y_p = \mp X_{equi}\sin\tau + Y_{equi}\cos\tau \\ \tau = \dfrac{Z_{equi}}{p} \end{cases} \tag{246}$$

BIBLIOGRAPHY

1. **Afgan, N.H.** and **Schunder, E.U.** Heat Exchangers: Design and Theory Sourcebook. *Scripta Book Company*, 1974.

2. **Alday, J.H.** and **Hood, J.A.** A Program for Mathematical Modeling and Analysis of Rotary Screw Compressor Performance. *Proceedings of International Compressor Engineering Conference at Purdue*, Purdue University, U.S.A., 1992, pp.249–258.

3. Амосов, П. Е.: Винтовые Компрессорные машины (Справочник). МАШГИЗ, 1977.

4. **Arbon, Ian M.** The Design and Application of Rotary of Rotary Twin-Shaft Compressors in the Oil and Gas Process Industry. *Mechanical Engineering Publications Ltd, London*, 1991.

5. **Bráblik, J.** and **Praha, Č.** Analytical Model of an Oil-Free Screw Compressor. *Proceedings of International Compressor Engineering Conference at Purdue*, Purdue University, U.S.A., 1982, pp.356–364.

6. **Bennewitz, Christer** Software Support for Screw Rotor Design, Manufacture and Quality Control. *Proceedings of International Compressor Engineering Conference at Purdue*, Purdue University, U.S.A., 1992, pp.431–437.

7. **Buckingham, E.** Analytical Mechanics of Gears. *McGraw-Hill Book Company, Inc.*, 1949.

8. Сакун, И. А.: Винтовые компрессоры. МАШГИЗ, 1960.

9. **Chlumský, V.** Reciprocating and Rotary Compressors. London, 1965.

10. **David, N.** and **Shaw, P.E.** Screw Compressor Control of V_i and Capacity "the Conflict". *Proceedings of International Compressor Engineering Conference at Purdue*, Purdue University, U.S.A., 1988, pp.236–243.

11. **Downing, R.C** Refrigerant Equations. *ASHRAE Transactions*, Vol. 80, Part II, 1974, P158.

12. **Edstroem, S.E.H.** Quality Classes for Screw Compressor Rotors. *Proceedings of IMechE European Conference*, London, U.K., 1989, pp.83–89.

13. **Edström, Sören E.** A Modern Way to Good Screw Rotors. *Proceedings of International Compressor Engineering Conference at Purdue*, Purdue University, U.S.A., 1992, pp.421–430.

14. **Firnhaber, M.A.** and **Szarkowicz, D.S.** Modeling and Simulation of Rotary Screw Compressor. *Proceedings of International Compressor Engineering Conference at Purdue*, Purdue University, U.S.A., 1980, pp.305–308.

15. **Fleming, John S. Tang, Yan** and **Anderson, H.** Optimisation Techniques Applied to the Design of a Refrigeration Twin Screw Compressor. *Proceedings of International Compressor Engineering Conference at Purdue*, Purdue University, U.S.A., 1994, accepted and to be published.

16. **Fleming, John S. Tang, Yan Young, W.** and **Anderson, H.** Leakage Analysis of a Helical Screw Compressor. *Proceedings of I Mech E European Conference on Developments in Industrial Compressors and their Systems*, London, U.K., 1994, pp. 1–8.

17. **Fleming, John S. Tang, Yan Young, W.** and **Anderson, H.** The Calculation and Optimisation of Cutter Blade Shapes for the Manufacture of Helical Screw Compressor Rotors. *Proceedings of IMechE European Conference on Developments in Industrial Compressors and their Systems*, London, U.K., 1994, pp.17–25.

18. **Fleming, John S. Tang, Yan** and **Anderson, H.** Twin Screw Compressor Performance and its Relationship with Rotor Cutter Blade Shape and Manufacturing Cost. *Proceedings of International Compressor Engineering Conference at Purdue*, Purdue University, U.S.A., 1994, accepted and to be published.

19. **Fleming, J.S. You, C.X.** and **Tang, Y.** Rotor Tip Design in Oil Injected Helical Twin Screw Compressors with Respect to Viscous Friction Loss. Proceedings of the Institution of Mechanical Engineers, Developments in Industrial Compressors and Their Systems, European Conference, London, 1994, pp.115–122.

20. **Fujiwara, M., Kasuya, K., Matsunaga, T.** and **Watanabe, M.** Computer Modeling for Performance Analysis of Rotary Screw Compressor. *Proceedings of International Compressor Engineering Conference at Purdue*, Purdue University, U.S.A., 1984, pp.536–543.

21. **Fujiwara, M.** and **Osada, Y.** Performance Analysis of Oil-Injected Screw Compressors and its Applications. *Proceedings of International Compressor Engineering Conference at Purdue*, Purdue University, U.S.A., 1990, pp.51–60.

22. **Fukazawa, Yoshimitsu** and **Ozawa, Utaka** Small Screw Compressors for Automobile Air-Conditioning Systems. *Proceedings of International Compressor Engineering Conference at Purdue*, Purdue University, U.S.A., 1980, pp.323–330.

23. **Haugland, K.** Pressure Indication of Twin Screw Compressor. *Proceedings of the International Compressor Engineering Conference at Purdue*, Purdue University, U.S.A., 1990, pp.450–456.

24. Handbook of Air Conditioning (in Japanese). 1981.

25. **Hodge, J.** Some Aspects of Screw Compressors. *Proceedings of IMechE European Conference*, London, U.K., 1970, pp.153–158.

26. **Holmes, C.S.** and **Munro, R.G.** A Study of Screw Compressor Rotor Geometry with a New Method for the Remote Measurement of Clearances. **VDI** *BERICHTE NR. 859*, 1990, pp.269–279.

27. **Howden Compressors Ltd., Glasgow, UK** Measured Data Books from 1963 to 1994.

28. **Howden Compressors Ltd., Glasgow, UK** Data and Charts for Friction Power of Shaft Seal and Bearings etc. and for Liquid Refrigerants Dissolved in Oil, 1993.

29. **Howden Compressors Ltd., Glasgow, UK** Drawings for Different Compressors from 1970 to 1994.

30. **Howden Compressors Ltd., Glasgow, UK** Data and Charts for Applied Profiles, 1994.

31. **Ignatiev, K.M. Tang, Yan Fleming, John S.** and **Tramschek, A.B.** Thermal Interaction in a Refrigeration Twin Screw Compressor during the Compression Process. *Proceedings of the International Compressor Engineering Conference at Purdue,* Purdue University, U.S.A., 1994, accepted and to be published.

32. **Jonsson, S.** Computer Calculation for Design and Analysis of Screw Compressors. *Royal Institute of Technology, Department of Thermal Engineering*, Stockholm, Sweden, Trita åtk 860907, 1986.

33. **Jonsson, S.** Performance Simulation of Twin-Screw Compressors for Refrigeration Purpose. **VDI** *BERICHTE NR. 640*, 1987, pp.187–207.

34. **Kanyshev, G.A. Vuzhva, A.A.** and **Sapronov, V.I.** Influence of Viscosity of Oil and ist Solubility with Refrigerant upon Characteristics of Screw Compressors. *Proceedings of IIR Congress*, Moscow, 1975, pp.949–956.

35. **Kobayashi, H.** and **Murata, N.** The Effect of Refrigerant Dissolved in Oil on Journal Bearing Reliability. *Proceedings of International Compres-*

sor Engineering Conference at Purdue, Purdue University, U.S.A., 1986, pp.1013–1025.

36. **Laing, P.D.** and **Perry, E.J.** Development of Oil-Injected Screw Compressors for Refrigeration. *Proc. Instn. Refrigeration*, 1964.

37. **Lysholm, A.J.R.** New Rotary Compressor. *Proc. Instn mech. Engrs*, 1943, **150**, pp.11–16.

38. **Martin, F.A.** and **Garner, D.R.** Plain Journal Bearings under Steady Loads: Design Guidance for Safe Operation. *First European Tribology Congress*, LB371/73, I Mech E, London, 1973.

39. **Miyoshi, K.** Analysis of Screw Compressor Performance Based on Indicated Diagrams. *Proceedings of International Compressor Engineering Conference at Purdue*, Purdue University, U.S.A., 1992, pp.259–268.

40. **Mori, H. Kasuya, K. Fujiwara, M.** and **Branch, E.** Single Stage, Oil-Free Screw Compressor with a Compression Ratio of Eight. *Proceedings of International Compressor Engineering Conference at Purdue*, Purdue University, U.S.A., 1986, pp.105–118.

41. **Mugele, R.A.** and **Evans, H.D.** Droplet Size Distribution in Sprays. *Indutrial and Engineering Chemistry*, Vol. 43, No. 6, 1951, pp.1317–1324.

42. **Nutbourne, A.W.** Differential Geometry Applied to Curve and Surface Design (Volume 1: Foundations). *Ellis Horwood Ltd.*, Chichester, 1988.

43. **O'Neil, P.A.** Industrial Compressors, Theory and Equipment. **Butterworth-Heinemann**, Oxford, UK.

44. **O'Neil, P.** and **Beatts, W.** The Oil-Free Screw Compressor. *Proceedings of IMechE European Conference*, London, U.K., 1970, pp.175–182.

45. **Person, J.-G.** Heat-Exchange in Liquid-Injected Screw-Compressors. **VDI** *BERICHTE NR. 640*, 1987, pp.121–135.

46. **Person, J.-G.** Performance Mapping vs'design Parameters for Screw Compressors and other Displacement Compressor Types. **VDI** *BERICHTE NR. 859*, 1990, pp.15–31.

47. **Press, William H., Flannery, Brian P., Teukolsky, Saul A.** and **Vetterling, William T.** Numerical Recipes. The Art of Scientific Computing. *Cambridge University Press*, 1986.

48. **Rinder, L.** Schraubenverdichter. *Springer*, Vienna, Austria, 1974.

49. **Sångfors, B.** Analytical Modeling of Helical Screw Machine for Analysis and Performance Prediction. *Proceedings of International Compressor Engineering Conference at Purdue*, Purdue University, U.S.A., 1982, pp.135–139.

50. **Sångfors, B.** Computer Simulation of the Oil Injected Twin Screw Compressor. *Proceedings of International Compressor Engineering Conference at Purdue*, Purdue University, U.S.A., 1984, pp.528–535.

51. **Singh, Pawan J.** and **Onuschak, Anthony D.** A Comprehensive, Computerized Method for Twin-Screw Rotor Profile Generation and Analysis. *Proceedings of International Compressor Engineering Conference at Purdue*, Purdue University, U.S.A., 1984, pp.519–527.

52. **Singh, Pawan J.** and **Patel, Ghanshyam C.** A Generalized Performance Computer Program for Oil Flooded Twin-Screw Compressors. *Proceedings of International Compressor Engineering Conference at Purdue*, Purdue University, U.S.A., 1984, pp.544–553.

53. **Singh, Pawan J.** and **Bowman, James L.** Heat Transfer in Oil-Flooded Screw Compressors. *Proceedings of International Compressor Engineering Conference at Purdue*, Purdue University, U.S.A., 1986, pp.135–151.

54. **Singh, Pawan J.** and **Bowman, James L.** Effect of Design Parameters on Oil-Flooded Screw Compressor Performance. *Proceedings of International*

Compressor Engineering Conference at Purdue, Purdue University, U.S.A., 1986, pp.71–89.

55. **Sjöholm, L.** Different Operational Modes for Refrigeration Twin-Screw Compressors. *Proceedings of International Compressor Engineering Conference at Purdue*, Purdue University, U.S.A., 1986, pp.89–104.

56. **Sjöholm, Lars** Important Parameters for Small, Twin-Screw Refrigeration Compressors. *Proceedings of International Compressor Engineering Conference at Purdue*, Purdue University, U.S.A., 1986, pp.1129–1142.

57. **Sjöholm, Lars** Variable Volume-Ratio and Capacity Control in Twin Screw Compressors. *Proceedings of International Compressor Engineering Conference at Purdue*, Purdue University, U.S.A., 1986, pp.494–508.

58. **Sjöholm, Lars** and **Short, Glenn D.** Twin-Screw Compressor Performance and Complex Ester Lubricants with HCFC-22. *Proceedings of International Compressor Engineering Conference at Purdue*, Purdue University, U.S.A., 1990, pp.724–733.

59. **Sjoholm, Lars I.** and **Short, Glenn D.** Twin-Screw Compressor Performance and Suitable Lubricants with HFC-134a. *Proceedings of the International Compressor Engineering Conference at Purdue*, Purdue University, U.S.A., 1990, pp.733–740.

60. **Stockholm, J.-G.** Heat-Exchange in Liquid-Injected Screw-Compressors. *VDI BERICHTE NR. 640*, 1987, pp.121–135.

61. **Stošić, N. Kovačević, A. Hanjalić, K.** and **Milutinović, Lj.** Mathematical Modeling of the Oil Influence upon the Working Cycle of Screw Compressors. *Proceedings of International Compressor Engineering Conference at Purdue*, Purdue University, U.S.A., 1988.

62. **Stošić, N.** and **Hanjalić, K.** etc. Mathematical Modeling of Screw Compressor Working Process. *Technic-Science-Engineering*, 20(1989)4, pp.7–13.

63. **Stošić, N.** and **Hanjalić, K.** etc. Computer Aided Design of Screw Compressors. *Technic-Science-Engineering*, 20(1989)4, pp.23–29.

64. **Stošić, N. Milutinović, Lj. Hanjalić, K.** and **Kovačević** Invetigation of the Influence of Oil Injection Upon the Screw Compressor Working Process. *Int. J. Refrig.*, 1992, Vol 15, No 4, pp.206–220.

65. **Tang, Yan** and **Fleming, John S.** Simulation of the Working Process of an Oil Flooded Helical Screw Compressor with Liquid Refrigerant Injection. *Proceedings of the International Compressor Engineering Conference at Purdue,* Purdue University, U.S.A., 1992, pp.213–220.

66. **Tang, Yan** and **Fleming, John S.** Obtaining the Optimum Geometrical Parameters of a Refrigeration Helical Screw Compressor. *Proceedings of International Compressor Engineering Conference at Purdue*, Purdue University, U.S.A., 1992, pp. 221–227.

67. **Tang, Yan** and **Fleming, Johs S.** Computer Aided Geometrical Analysis of the Geometrical Characteristics of a Helical Screw Compressor. *International Compressor Engineering Conference at Xi'an,* Xi'an Jiaotong University, Xi'an, China, 1993, pp.399–407.

68. **Tang, Yan** and **Fleming, John S.** The SRM-D Profile: Its Basic Construction, Analysis and Use in Twin Screw Compressor Design. *Research Report 7*, Nov., 1993.

69. **Tang, Yan** and **Fleming, John S.** Computer Aided Analysis of the Geometrical Characteristics of a Twin Screw Compressor. *Research Report 8*, Dec., 1993.

70. **Tang, Yan** and **Fleming, John S.** Manufacture by Milling of the Rotors of Twin Screw Compressors: Cutter Blade Shape Determination to Combine Increased Thermodynamic Efficiency with Reduced Manufacturing Cost. *Research Report 9,* Dec., 1993.

71. **Tang, Yan** and **Fleming, John S.** Simulation of the Working Process of a Modern Refrigeration Twin Screw Compressor. *Research Report 10*, Feb., 1994.

72. **Tang, Yan** and **Fleming, John S.** The SRM A-Profile and Symmetrical Circular Profile: there Basic Construction, Analysis and Generation. *Research Report 11*, April, 1994.

73. **Tang, Yan** and **Fleming, John S.** Clearances between the Rotors of Helical Screw Compressors: Their Determination, Optimisation and Thermodynamic Consequences. *Proc I Mech E Vol 208 Part E, Journal of Process Mechanical Engineering*, 1994.

74. **Trulsson, I.** A New Development in Rotary Screw Compressor Design. *Proceedings of IMechE European Conference*, London, U.K., 1970, pp.137–143.

75. UK Patent GB 1 197 432.

76. UK Patent GB 2 092 676 B.

77. **Wu, Xu-Tang** Mating Theory of Gears (in Chinese). *Mechanical Industry Book Company*, Bejing, 1982.

78. **You, C.X. Tang, Yan** and **Fleming, John S.** Removing the Non-Return Valve from the Refrigeration System with a Twin Screw Compressor. *Proceedings of International Compressor Engineering Conference at Purdue*, Purdue University, U.S.A., 1994, accepted and to be published.

79. **Zhang, ZhiYou** Refrigeration Principles and Equipments. *Mechanical Industry Publisher*, Bejing, 1989.